



Tasadduq KHAN
Senior Advisor

High Temperature Materials: an Introduction to Onera's Contribution

The third issue of Aerospace Lab is dedicated to high temperature materials. Onera has been at the forefront of research and development for this class of materials for the past five decades, especially for aerospace engine applications. Starting in the mid 1960's, many new materials and processes were invented, and cutting-edge research was carried out during this period. Similarly and concurrently, great progress has been made in mechanical modeling and lifing analysis, but a description of these aspects will require a full separate issue. The focus here is on materials in the hot sections of compressors and turbines. These materials have a wide range of applications.

The purpose of the papers that follow is to illustrate the state-of-the art, the progress made and the future outlook for such materials in propulsion systems.

General introduction

The work presented here is essentially in the form of 'overviews' that describe mainly the in-house efforts and the progress achieved up until now within the broader context of world-wide developments on propulsion materials. Because of its specific role as a research establishment in France, the work undertaken at Onera has traditionally focused on the specific needs of the French aerospace industry, extended lately to some of the requirements of European industry, mainly through collaborative European programmes.

Broadly speaking, the papers in this issue cover a wide spectrum of activities which are based on the short, medium and long-term requirements of industry.

Superalloys and thermal barrier coatings

Onera has been at the forefront of a number of new superalloys for turbine blades and for disc applications which are already being used in French military and commercial aircraft engines, including helicopter engines. In the case of superalloys, the main objective is to satisfy the short-term requirements, and the emphasis in this issue is on the most recent alloy developments addressing various aspects of relationships between the chemistry, microstructure and mechanical

properties. For disc alloys, some of the on-going research on new compositions and processing parameters is presented. An attempt is made to clarify the complex interaction between processing, the microstructure and the mechanical behavior, particularly in creep.

A sustained medium and long-term effort on thermal barrier coating degradation mechanisms and new advanced thermal barriers has been actively pursued over the past twenty years with the objective of both increasing the life times and achieving higher turbine inlet temperatures. Concurrently, additional effort has accompanied this work to develop new bond coats under the thermal barrier coatings. The nature of the approach has been essentially multidisciplinary (the micro and macro 'mechanics of coatings' and the mechanical characterization are not included here).

Lightweight intermetallics, silicides, ceramic composites and ultra- high temperature materials

In terms of long-term research, and depending upon the type of material, various processing approaches are being pursued. The material which is closest to potential applications is currently Titanium aluminide. Here again, the primary effort for many years has been to acquire a basic understanding of complex structures produced through various processing routes and to relate these microstructures to the

mechanical properties. The main objectives are to establish robust processing routes which, when scaled-up, will yield reliable properties and meet the industrial requirements.

Another area of activity in the context of long-term research involving a substantial collaborative effort within Europe has been on materials such as silicides, which could potentially replace some of the rather 'heavy' superalloys with lighter-weight materials. This is a very long-term effort, but still worth pursuing.

Finally, in the same vein, there are alternative materials for certain applications which will require a sustained and patient approach such as eutectic composites, oxide-oxide composites and ultra- high temperature materials for various applications.

This issue will attempt to cover a very wide spectrum of materials with a multidisciplinary research approach and a strong interaction between basic and applied research. ■

D. Locq, P. Caron
(Onera)

E-mail: didier.locq@onera.fr

On Some Advanced Nickel-Based Superalloys for Disk Applications

Recent work performed at Onera on nickel-based superalloys for disk applications is presented. In the first section, disk characteristics and metallurgical routes used to produce these specific aero-engine components are reviewed. Then, two alloy development programs carried out to satisfy the requirements of the industrial partners are detailed. Finally, the results of studies aiming at identifying the complex relationships linking the microstructure and the creep behaviour of disk superalloys are described: influence of the strengthening γ' precipitation on the deformation micromechanisms, and effect of the microstructure on grain boundary sliding.

Introduction

Nickel-based superalloys are mainly used for static or rotating components of the hottest sections of aero engines. These rotating parts are the blades and the disks in the high-pressure compressor (HPC) and turbine (HPT) stages. As far as disks are concerned, nickel-based superalloys are selected for the last HPC (hot) stages while titanium-based alloys are used for the first (colder) compressor stages due to their lower density. In contrast, nickel-based superalloys are systematically used for the high- and low-pressure turbine (HPT or LPT) disks because of the thermal and mechanical requirements (figure 1).

Blade loss can be contained within the engine casing, while the catastrophic failure of a turbine disk could cause puncture of the engine casing by its largest fragments [1]. This event represents a potential fatal hazard to the aircraft and its occupants. Therefore, it is essential to have the best understanding of the current relationships between the alloy chemistry, the production processes, the thermomechanical treatments, the heat treatments, the microstructure, the mechanical properties and finally the service behavior of the disk.

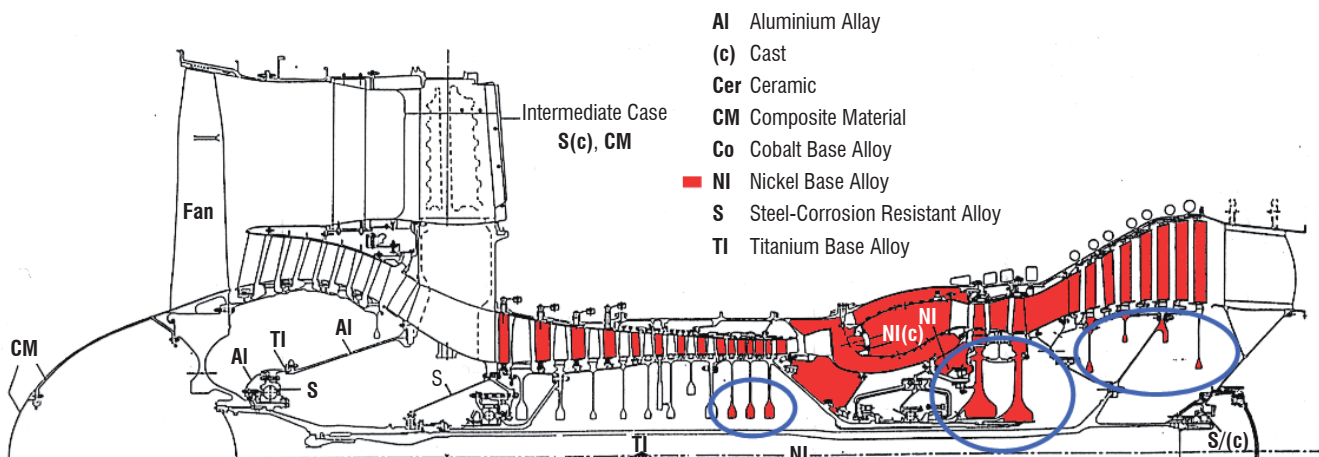


Figure 1 - Half cross section of the PW4000 engine (in red, nickel-based superalloy components and, in circles, nickel-based superalloy disks).

The operating conditions experienced by a typical HPT disk are [2]:

- a temperature within the 200-300°C range in the bore and up to 650°C in the rim;
- a rotational speed higher than 10,000 revolutions per minute (the mechanical stresses generated in the bore region may reach 1000 MPa during take-off);
- an oxidizing/corrosive environment.

In consequence, turbine disk alloys require the following properties:

- high yield and tensile strengths to prevent yield and bursting (yield strength > 1000 MPa and ultimate tensile strength > 1200-1300 MPa in the 400-650°C range);
- ductility and fracture toughness to prevent dramatic fracture and improve defect tolerance;
- high resistance to fatigue crack initiation and low fatigue crack growth rate (in oxidizing environment);
- high creep resistance to avoid creep strain in the rim;
- and finally, a density as low as possible.

Currently, this set of requirements is only met in the case of the nickel (or some nickel-iron)-based superalloys. The high mechanical resistance of the nickel-based superalloys is essentially due to the presence of hardening precipitates in a matrix phase. The matrix phase denoted γ exhibits the face-centered cubic (FCC) structure of the nickel and can contain significant amounts of elements in solid solution such as cobalt, chromium, molybdenum, etc. The structural hardening is provided by precipitates of the coherent stable intermetallic compound denoted γ' (cubic $L1_2$ structure – Ni_3Al). The properties of γ' -strengthened alloys are mainly dependent on:

- volume fraction and size of the different populations of γ' precipitates;
- and solid-solution strengthening of both γ and γ' phases.

Inconel 718 is the most widely used superalloy for the production of compressor and turbine disks. This «old» alloy (1959) is a nickel-iron superalloy (principally strengthened by precipitation of the γ'' phase – Ni_3Nb) and is produced by the conventional cast-and-wrought (C&W) route. For more severe applications, γ' -hardened nickel-based superalloys are used. These superalloys usually hold between 40 and 60 volume % of γ' phase and are processed either by the C&W route or by the powder metallurgy (PM) route. The PM route allows processing of large dimension disks made of superalloys with higher γ' fraction and/or with higher content of refractory metals (Mo, W, Nb, Ta). By this specific processing route, chemical segregations in the disk are minimized and the more uniform deformability of the PM billet allows forging of disks made of highly strengthened superalloys. PM disks were first installed in turbines of military aero engines (Pratt & Whitney F100 engine in 1974). They are now also used in large commercial engines (René 88 alloy in General Electric CF6 and GE90-94B engines [3] and René 104 in Engine Alliance GP7200 engine [4]).

At Onera, investigations on PM disk superalloys started in the late 1970's. In the early 1980's, the French manufacturer of aircraft engines Snecma (now Safran Snecma) launched the development project of the military engine M88 intended to power the Rafale fighter aircraft from Dassault. To meet the severe requirements for several disks of the M88 engine, Snecma wished to use a new PM superalloy. A program of alloy development was therefore conducted in cooperation with Snecma, Imphy S.A., École des Mines de Paris and Onera. This program led to patent application of the N18 superalloy and its use for the production of HPC and HPT disks of the M88 engine [5].

This paper presents two investigations performed at Onera on PM nickel-based superalloys for disk applications. The first one focuses on alloy design studies considering the industrial requirements. The second one is related to the relationship between the microstructure of the superalloy and its high-temperature creep behavior.

Alloy design

Increase of the operating temperature

The N18 alloy is the first French PM superalloy for aero engine applications. This superalloy is designed to withstand high stresses at intermediate temperatures. The maximum temperature of the HPT disk rim of the M88 engine was predicted in the 600-650°C range with possibly short incursions at 700°C. From the late 1980's, the Délégation Générale de l'Armement (DGA: the Defence Procurement Agency) proposed a further research direction for new disk superalloys operating at temperature higher than 700°C (up to 750°C). For disk superalloys, the rise of 100°C in the maximum operating temperature globally results in:

- an appreciable drop in mechanical resistances;
- faster microstructural evolutions;
- stronger interactions with environment.

The chemistry and the standard microstructure of the N18 alloy are designed for applications up to 600-650°C. In this temperature range, fine-grain (5-15 μm) microstructure is globally favorable for high mechanical resistance and microstructural evolutions are rather slow. Initial studies on N18 rapidly showed that this alloy was not a suitable candidate for higher temperature applications. Firstly, this alloy is prone to precipitation of deleterious topologically close-packed (TCP) phases during long-term exposure above 650°C [6,7]. Secondly, the grain size is not easily adjustable in this alloy. Increasing the grain size is one way to improve some time-dependent mechanical properties at high temperature such as creep or crack propagation resistance. The grain growth in these superalloys requires a supersolvus heat treatment (i.e. above the γ' solvus temperature of the alloy). The application of such heat treatments evidenced some problems for the N18 alloy:

- depending on isothermal forging conditions, the supersolvus heat treatment can lead to abnormal grain growth (growth of a few grains to very large sizes up to several millimeters) [8],
- at industrial cooling rates, quench cracking occurred on disk preforms. The propensity for quench cracking in superalloys is related to high γ' volume fractions (higher than 45 % [9]) and N18 alloy is in the 50-55 vol % range which is a high value for disk alloys.

To meet the DGA's objective, a series of experimental superalloys was designed, processed and evaluated at Onera [10]. From the chemical composition of N18 alloy, modifications were made to design alloys free of TCP phases and nevertheless having equal or higher mechanical properties than those of N18. The common features of these experimental alloys and the N18 alloy are:

- Co content maintained close to 15 wt. %;
- Cr content close to 25 at. % in the γ matrix to retain a good environmental resistance at high temperature especially during crack propagation;
- minor elements contents (C, B, Zr and Hf) close to those of N18 alloy. The compositions of NR3 and NR6 alloys are compared with the N18 chemistry in table 1.

Alloy	Ni	Co	Cr	Mo	W	Al	Ti	Nb	Hf	C	B	Zr
N18	Bal.	15.7	11.5	6.5	-	4.35	4.35	-	0.50	0.015	0.015	0.03
NR3	Bal.	14.7	12.3	3.5	-	3.80	5.50	-	0.30	0.020	0.010	0.05
NR6	Bal.	15.1	13.8	2.1	4.0	3.20	4.50	-	0.30	0.020	0.010	0.05
SMO43(N19)	Bal.	12.2	13.3	4.6	3.0	2.90	3.60	1.5	0.25	0.015	0.010	0.05
SMO48	Bal.	14.9	12.3	3.6	4.0	3.20	4.40	0.8	0.30	0.030	0.010	-

Table 1 - Nominal compositions of disk superalloys developed at Onera (wt. %).

To avoid the precipitation of TCP phases, the molybdenum content is lowered to decrease a stability criterion $\bar{M}d\gamma$. This phase stability parameter is defined as follows:

$$\bar{M}d\gamma = \sum_{i=1}^n X_i^{\gamma} (Md)_i$$

where X_i^{γ} is the atomic fraction of the element i in the γ matrix and $(Md)_i$ is the Md value for element i . The Md is the average energy level of d orbitals of alloying transition metals (in eV). These Md levels correlate with the electronegativity and with the metallic radius of each element. The Md values used for the calculation are those given by Morinaga in the New Phacomp method [11]. When the $\bar{M}d\gamma$ value of one alloy becomes larger than a critical value, the matrix phase instability takes place and a second phase precipitates in the γ matrix. This critical value for TCP phase precipitation was determined to be 0.915 by previous experiments.

To counterbalance the loss of solid solution strengthening of the γ matrix resulting from lower Mo content, the Ti/Al (concentrations in at. %) ratio is increased to 0.8 (vs. 0.56 for N18 alloy). This Ti for Al partial substitution is carried out to increase the strength of the γ' phase. For NR6 alloy, the γ' volume fraction is lowered to the 40-45 % range (to avoid quench cracking) and the resulting decrease in mechanical strength is compensated both by Ti/Al ratio increase and by W to Mo partial substitution ($W/Mo \sim 1$, concentrations in at. %). W partitions in both γ and γ' phases while Mo is mainly present in the γ phase. So, in spite of the higher Md value for W, the addition of this element leads to a lower increase of the alloy Md than the same addition of Mo (in at. %). However, substantial W content has a detrimental effect on the alloy density

because of its very high atomic weight (almost twice as much as the one of Mo).

The chemistries of the NR3 and NR6 alloys were balanced by using an Onera program based on the method developed by Watanabe for calculation of the fraction of γ' phase and the composition of the γ and the γ' phases from the alloy chemistry [12].

After a laboratory-scale screening, NR3 and NR6 alloys were characterized in comparison with N18 alloy. All alloys were processed by the industrial PM route:

- vacuum induction melting;
- argon atomization;
- hot extrusion;
- isothermal forging;
- supersolvus solution treatment.

The final sequence of heat treatments leads to a medium grain size (GS) microstructure ($20 < GS < 100 \mu m$) and a bimodal distribution of γ' precipitates: the secondary γ' (or cooling γ') with a mean size of a few hundreds of nanometers and the tertiary γ' (or ageing γ') with a mean size of a few tens of nanometers (figure 2).

Tensile and creep-rupture tests showed that NR3 and NR6 alloys have mechanical properties close to or slightly higher than those of N18 alloy [10]. Samples of the three alloys were aged in the 700-850°C range for times up to 10,000 hours to confirm the stability of the γ matrix in relation to the TCP phase precipitation. Scanning electron microscopy (SEM) or transmission electron microscopy (TEM) observations show that intragranular TCP

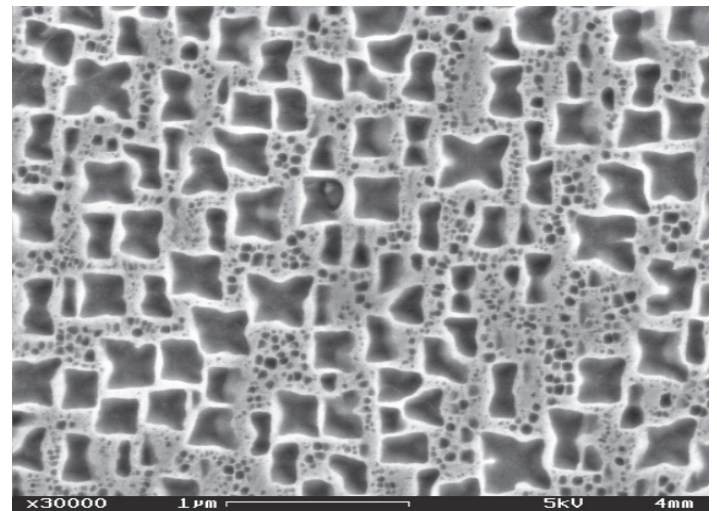
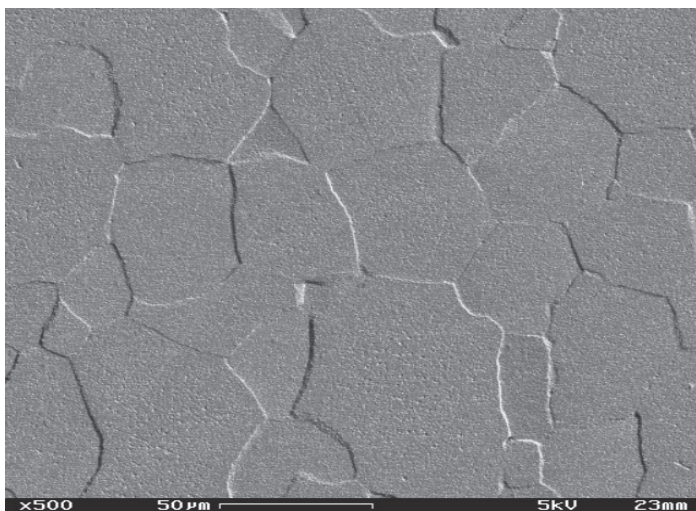


Figure 2 - Typical microstructure of a PM disk superalloy after a supersolvus heat treatment. On the left, grain structure and on the right, the secondary and tertiary γ' precipitates within the grains (SEM images).

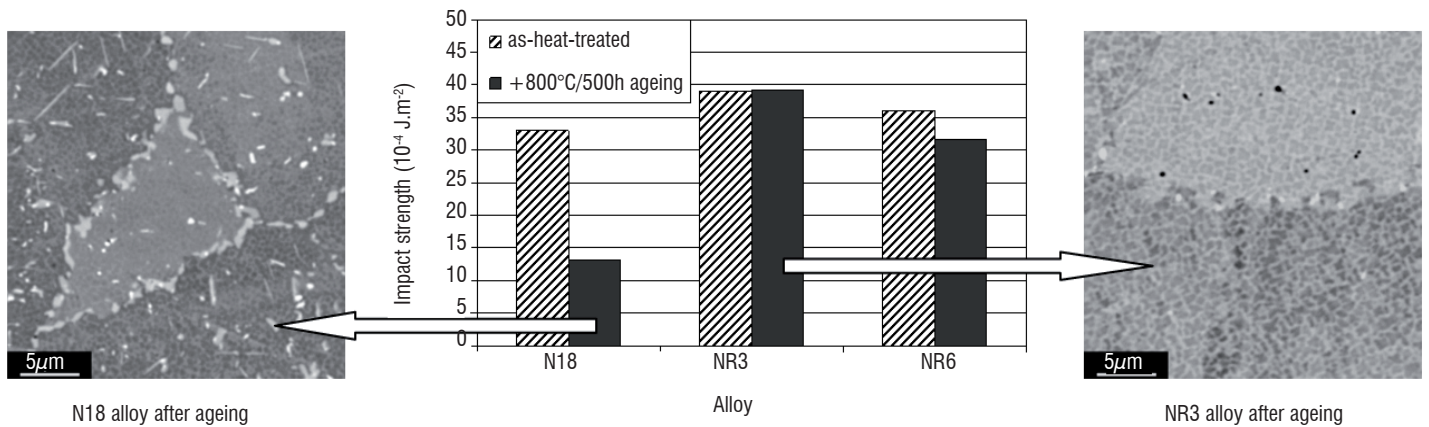


Figure 3 - Effect of long-term ageing treatment (500 hours at 800°C) on microstructure and on impact strength at room temperature for three disk superalloys.

phase particles precipitate in the N18 after 1000 hours at 700°C. No intragranular TCP phases are observed in NR3 or NR6 alloys even after long-term exposure at high temperature (10,000 hours at 750°C). These results confirm the expected stability of the NR3 and NR6 alloys. The detrimental effect of TCP phase precipitation on mechanical properties was also evidenced by impact tests on samples with or without severe ageing heat treatment (500 hours at 800°C). The micrographs presented in figure 3 show the TCP phase precipitation (light gray particles) within N18 alloy while such phenomenon does not occur within NR3 alloy. The significant drop of impact strength related to this unwanted precipitation is also clearly highlighted in figure 3.

This study led to a Snecma-Onera patent application [13]. Till today, the NR3 and NR6 alloys have not been industrialized by Snecma for disk applications but they were intensively used for long-duration creep studies at high temperatures where the absence of TCP phase precipitation makes easier the analysis of creep deformation mechanisms, as detailed in the following.

Increase of service life

In the late 1990's, a cooperative program (Snecma-Onera-Centre des Matériaux de l'École des Mines de Paris) was launched to develop a new PM superalloy grade with these main specifications [14]:

- capability of significant grain size evolutions through thermomechanical and heat treatments,
- metallurgical stability for long term exposures up to 750°C,
- higher creep and fatigue resistance as compared to N18 alloy up to 700°C,
- increased strain hardening ability,
- and a density lower than 8.35 g.cm⁻³.

To meet these requirements, the target γ' fraction of the new N19 superalloy was in the 40-45 % range. This drop in γ' amount in comparison with the value of 55 % in alloy N18 is counterbalanced by both γ and γ' strengthening increases. The γ matrix chemistry is optimized through a careful balance between the Cr, Mo and W elements. The goals are to:

- increase the solid solution hardening of the γ matrix;
- maintain oxidation and corrosion resistances by means of sufficient Cr addition;
- avoid or limit the precipitation of TCP phases;
- and, limit the increase in alloy density.

A special attention is paid to Co content because of its effects on high temperature creep resistance and, above all, on the γ' solvus temperature which generally decreases when the Co level increases. To strengthen the γ' phase, the $[\text{Ti}+\text{Nb}+\text{Ta}]/\text{Al}$ ratio (concentrations in at. %) is increased to about 0.85 (vs. 0.56 for alloy N18). Here again, excessive addition of Ti and/or Nb and/or Ta can have detrimental effects on the microstructure and the mechanical properties. A too high $[\text{Ti}+\text{Nb}+\text{Ta}]/\text{Al}$ ratio can lead to the presence of undesirable acicular plates of intermetallic phases such as η -Ni₃Ti, δ -Ni₃(Nb,Ta). Although Nb has a higher strengthening effect than Ti, excessive Nb content is likely to be deleterious to crack propagation resistance and ductility [15]. Lastly, no particular study is dedicated to the effects of minor elements. For all the experimental alloys, carbon is kept within the 150-320 wt. ppm range and boron is in the 150-200 wt. ppm range, hafnium content is about 0.3 wt. % and zirconium, when added, is in the 600-630 wt. ppm range.

22 experimental alloys and the two reference alloys N18 and René 88 [9] were processed by laboratory PM route. Two out of the experimental alloys were selected for further studies on their mechanical and metallurgical features in comparison with N18 alloy [14]:

- higher tensile properties between room temperature and 700°C and 700°C creep resistance;
- lower γ' fraction and solvus temperature and higher solution window (gap between the incipient melting temperature and the γ' solvus temperature) which are key factors for improving thermal and thermomechanical treatment capabilities;
- higher γ matrix stability (no or little TCP phase precipitation);
- high γ' phase stability (no η or δ phase precipitation).

These two alloys (SMO43 and SMO48) were processed by the industrial PM route and were heat treated to obtain a medium grain size. The mechanical properties of these materials were compared with those of N18 alloy with its reference microstructure as used in the M88 engine, i.e. a fine-grain microstructure (5-15 μm). This comparison allows it to be noted that, in spite of their coarser grain size, these new alloys exhibit tensile strengths and low cycle fatigue (LCF) behaviors close to that of N18 alloy. Moreover, partly due to their coarser grain sizes, SMO alloys show a significantly higher creep resistance (figure 4). Lastly, some fatigue crack growth tests were performed at 550°C and 650°C. It emerges from these tests that SMO alloys present fatigue crack propagation behaviors close to that of N18 alloy. SMO43 was finally chosen for further assessments because of its

slightly higher LCF resistance and its expected better process suitability thanks to its low γ' solvus temperature [14]. Complementary studies are in progress to optimize its mechanical properties (especially through thermomechanical and/or heat treatments).

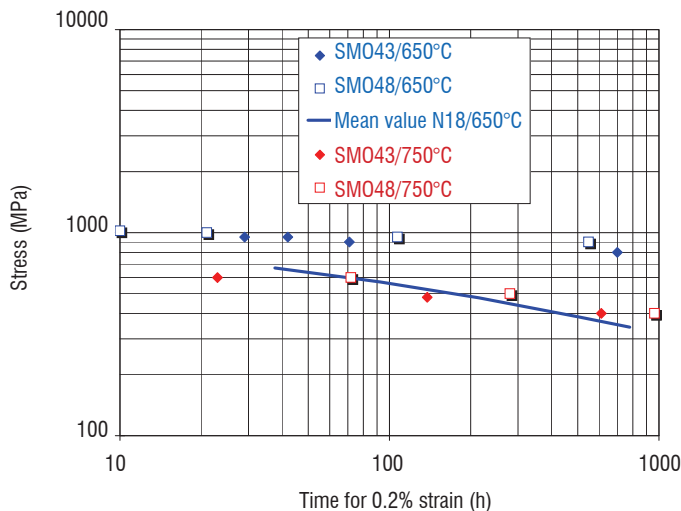


Figure 4 - Time for 0.2 % creep strain of SMO alloys compared with results on N18 alloy.

Microstructure – creep behavior relationship

As for the United States HSCT (High-Speed Civil Transport) research program, the ATSF (Avion de Transport Supersonique Futur: Future Supersonic Transport Plane) program was launched in France in the mid-1990's (200 seats/ 10,000 km range/ Mach 2). The ATSF should be equipped with a MTF (Mid-Tandem Fan) engine developed by Rolls-Royce and Snecma (with a turbine inlet temperature closed to 1650 K during cruise). For subsonic civil missions, the more intensive phases for the engine are the take-off and the landing. For supersonic civil applications, engines are highly stressed during the whole cruise duration (several hours). This point means that microstructural modifications and creep phenomenon in turbine disks have to be taken into account. Long duration creep studies were mainly carried out on the NR3 and NR6 alloys for the reasons previously mentioned. These studies led to the achievement of numerous creep tests in the 650-850°C range and in a large stress range (150 to 1000 MPa depending of the temperature). For these creep tests, the minimum creep rate was in the range 10^{-7} - 10^{-11} s $^{-1}$.

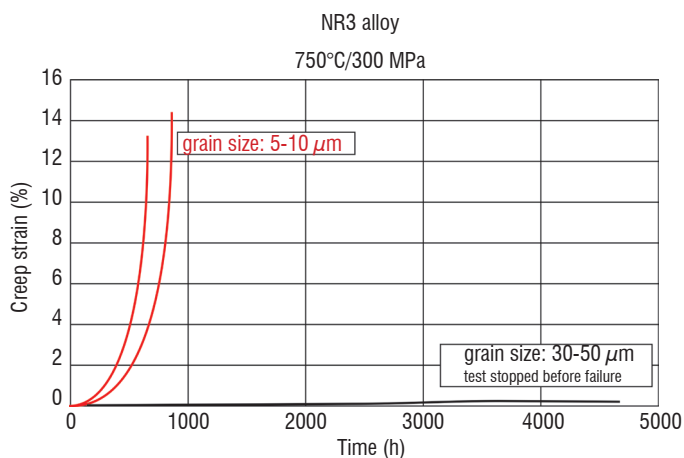


Figure 5 - Influence of the microstructure on creep behavior of NR3 alloy.

This work allows clarification of the typical influence of the grain size on the creep behavior. A small grain size superalloy has a higher minimum creep rate and experiences an earlier increase of the creep rate than a coarser grain size one (figure 5). These phenomena are even more significant when the creep temperature is high and/or the creep stress is low [16].

The effect of the tertiary γ' precipitates and of their evolution on the long duration creep behavior at temperatures above 700°C was also examined. The size and fraction of these very fine particles (a few nanometers to a few tens of nanometers) have a significant influence on the deformation micro-mechanisms and therefore on the macroscopic behavior of the material [17, 18]. This study was carried out closely with the CEMES Toulouse (Centre d'Élaboration de Matériaux et d'Études Structurales) [19, 20, 21]. The TEM observations allow it to be established that the absence of tertiary γ' precipitates leads to bypassing mechanism of the secondary γ' precipitates by matrix dislocations (figure 6). On the other hand, the presence of these particles in the γ matrix channels induces different shearing mechanisms depending on the local distribution of the tertiary γ' precipitates in front of the dislocations (figure 7). A new shearing configuration of γ' precipitates has been observed and analyzed during this study (decorrelation of the movement of two partial dislocations in the narrowest matrix channels) [22]. The influence of the tertiary γ' precipitate distribution was studied in small grain size microstructure [23] as well as in coarser grain size one [20]: this effect decreases as the creep rate diminishes too (lower creep temperature and/or stress).

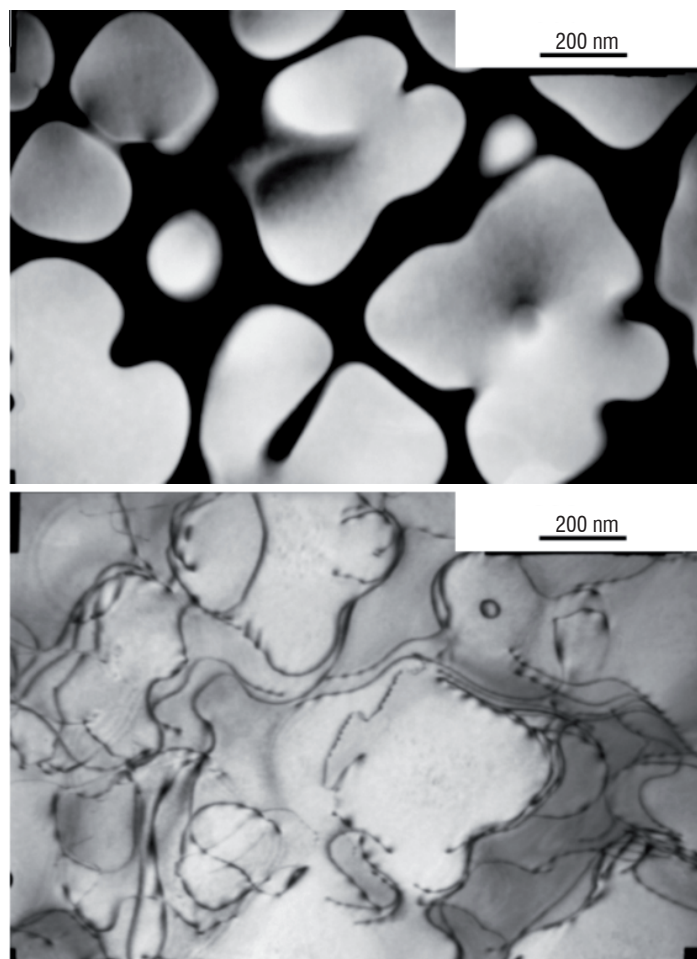


Figure 6 - Microstructure of over-aged NR3 alloy (without tertiary γ' precipitates) and associated bypassing mechanism (TEM images).

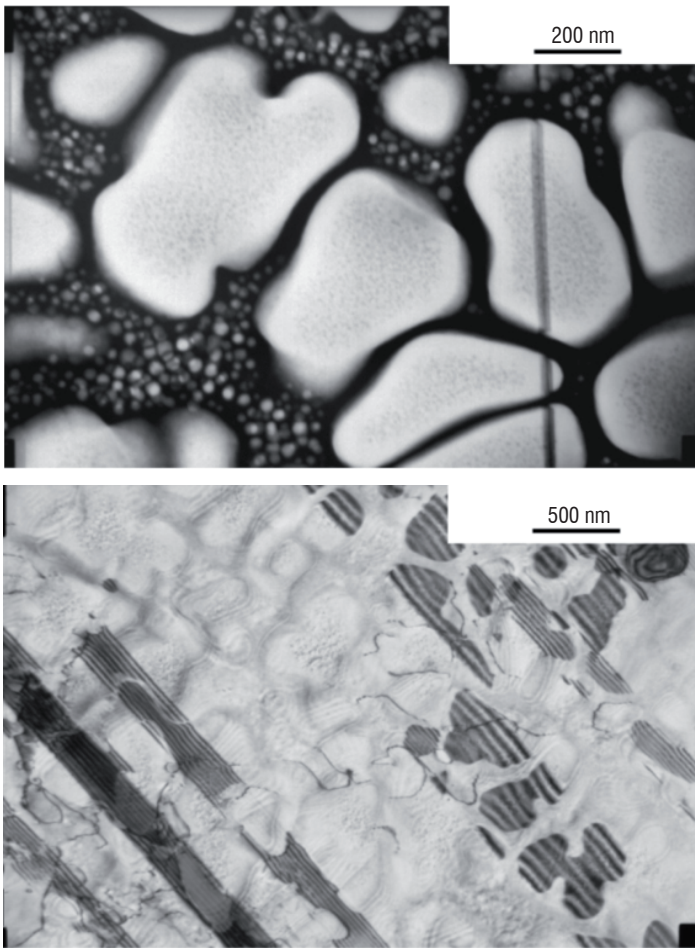


Figure 7 - Microstructure of standard NR3 alloy (with tertiary γ' precipitates) and associated shearing mechanisms (TEM images).

According to these results and those obtained by Dubiez-Le Goff [24] and Raujol [19], it was inferred that grain boundary sliding (GBS) contribution to the overall strain could not be neglected. To quantify the GBS strain during high-temperature creep tests, a specific microgrid extensometry technique was developed [25]. Hafnia microgrids ($318 \times 318 \mu\text{m}^2$ with a $5 \mu\text{m}$ pitch) were deposited on flat creep specimens of the NR6 superalloy which were creep tested in the 700-850°C temperature range for a few hours to a few hundred hours. The creep tests were conducted under high vacuum ($\sim 10^{-4}$ Pa) to avoid excessive oxidation of the superalloy. High resolution SEM images

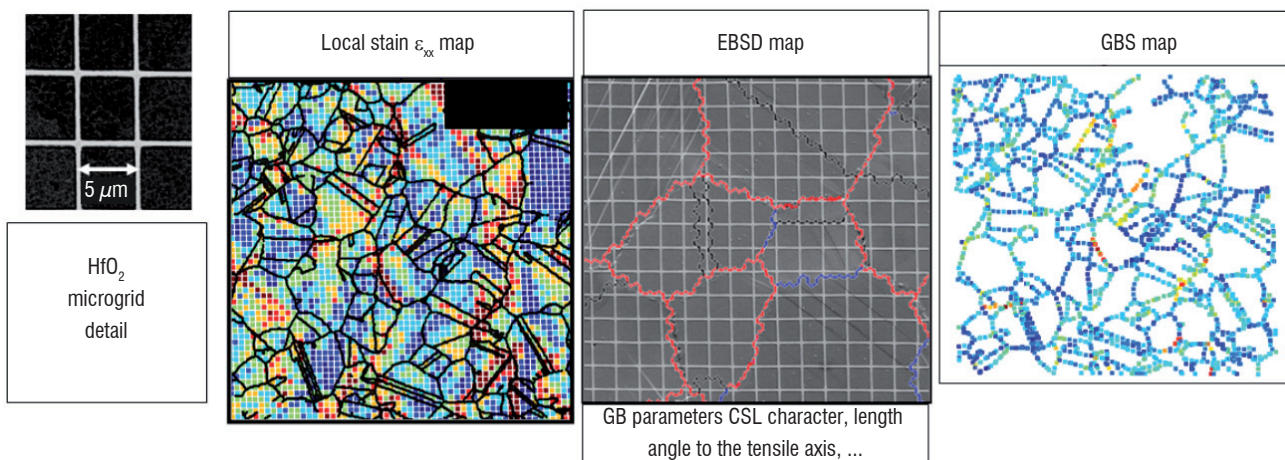


Figure 8 - Microgrid, deformation maps and EBSD map used to study the GBS contribution.

of the grids were recorded before and after the creep tests. Specific image correlation tools were developed to calculate local strain and GBS. These deformation maps were superimposed on EBSD (Electron Backscatter Diffraction) maps to merge the grain boundary parameters with the deformation data [26, 27] (figure 8).

The development of these tools allowed study of the effect of the creep parameters (temperature, stress and deformation ratio) on the GBS contribution to the overall deformation of the superalloy. The experimental results globally show that the GBS contribution increases as the temperature and/or the stress are lowered. In other words, the lower the creep rate, the higher the GBS contribution (Figure 9).

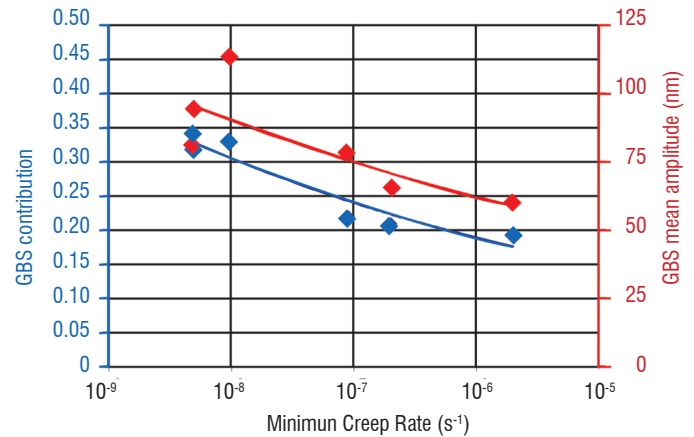


Figure 9 - Dependence of GBS contribution and mean amplitude on creep rate.

The influence of the grain boundary parameters (crystallographic nature using the Coincidence Site Lattice (CSL) model [28], length, orientation with respect to the tensile axis) on the ability to undergo GBS was also assessed. For instance, this analysis brings out the fact that random grain boundaries are more prone to GBS than CSL grain boundaries (especially twin boundaries which are the most resistant to GBS). However, this trend tends to decrease as the creep temperature increases (figure 10).

Creep tests at various temperatures (700-850°C) and stresses (350-700 MPa) were carried out on NR6 specimens and interrupted after 1 % creep strain. For each creep conditions, analyses of the deformation maps completed with TEM observations of the microstructure and of the dislocation structures allow linking microstructural changes to different deformation micro-mechanisms (as previously

seen for NR3 alloy) and also linking these modifications to the GBS contribution. These results are summarized in figure 11.

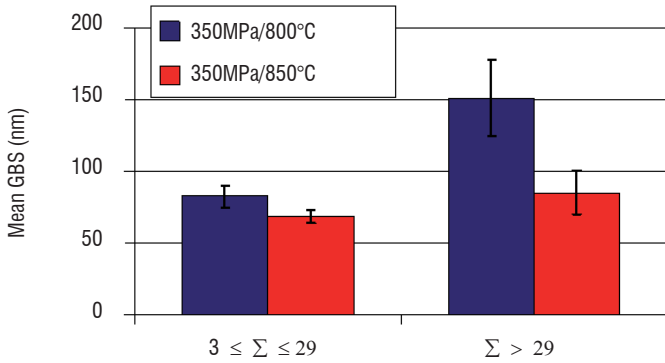


Figure 10 - Influence of creep temperature at 350 MPa on the mean GBS amplitude of two classes of grain boundaries. ($3 \leq \Sigma \leq 29$ = CSL grain boundaries and $\Sigma > 29$ = random grain boundaries).

When the microstructure is stable (a bimodal distribution of γ' precipitates is preserved (blue area in figure 11)), γ' precipitate shearing mechanisms are mainly observed in the grains. The deformation is localized into slip bands and heterogeneously distributed within grains and between adjoining grains. On the other hand, when the precipitation microstructure rapidly changes (to a monomodal distribution of γ' precipitates) because of long exposure at high temperature (800-850°C (red area in figure 11)), a bypassing mechanism is observed and is more homogeneously distributed within grains and between adjoining grains.

For the NR6 superalloy, creep parameters can lead to microstructural changes that can affect deformation micro-mechanisms. The more heterogeneous deformation within grains and between adjoining grains, the higher the GBS contribution. In that case, the local stresses induced by deformation incompatibilities between neighboring grains and by dislocation pile-up at grain boundaries are assumed to assist the GBS phenomenon.

The aim of these studies is to contribute to the understanding of the deformation mechanisms controlling high-temperature creep of poly-

crystalline nickel-based superalloys. This better knowledge is expected to provide solutions to increase disk superalloys resistance (to creep or other mechanical loadings) through grain engineering (optimization of γ' precipitate distribution) and through grain boundary engineering (GBE) (improvement of CSL grain boundary distribution). Concerning the GBE, the challenge consists in finding deformation and thermal cycles compatible with the industrial processing of disk superalloys. Once this issue is solved, the mechanical properties involving the grain boundary environmental and mechanical resistance should be improved (in particular, creep and dwell crack growth resistances).

Conclusion

This article reports studies conducted at Onera in the field of nickel-based superalloys for disk applications. Two research topics are here presented. The first one deals with superalloy design and the second issue concerns the analysis of the microstructure/mechanical property relationships.

Alloy design studies were carried out in collaboration with industrial or research laboratory partners and were mainly based on mutual theoretical and experimental knowledge. The NR3 and NR6 PM superalloys were developed with the aim to increase the high temperature capability of such alloys above that of the N18 alloy today used in the M88-2 engine of the Rafale fighter. More recently, the N19 PM alloy was designed to improve the LCF strength as compared to N18 in order to increase the disk life. A specific alloy design methodology has been developed to meet the industrial application requirements. In house laboratory-scale equipments allowed production of experimental superalloy grades by the PM route. Microstructural studies and basic mechanical assessment were carried out on these materials to screen the most promising ones. The selected alloys were then processed by our industrial partners using the industrial PM route. Further studies were finally undertaken to optimize the microstructure (and so the mechanical behavior) of the materials by adjustment of the last processing step parameters (thermomechanical and/or heat treatments). At this stage, studies on the relationships between the process parameters, microstructure and mechanical behavior gives helpful information to reach the objectives more efficiently.

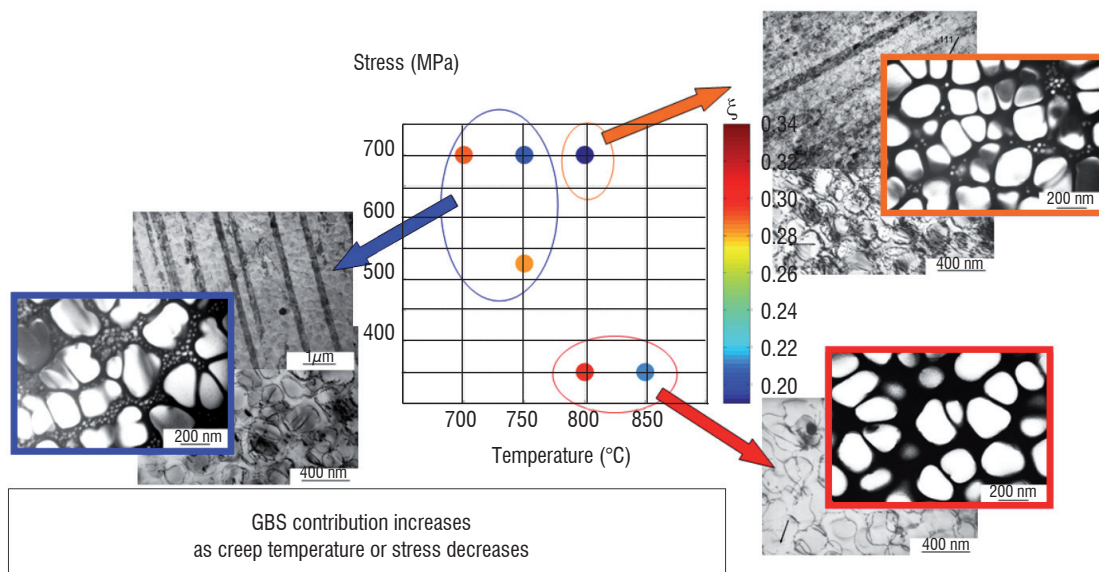


Figure 11 - Relationships between microstructure, straining micro-mechanisms and the GBS contribution ξ as a function of creep temperature and stress.

Identification of the deformation mechanisms operating during creep of NR3 and NR6 alloys was carried out to analyze the effects of microstructural changes on the creep behavior. TEM investigations allow understanding of the dislocation/strengthening precipitate interactions at the nanoscopic and microscopic scales. Moreover, calculation of local strain and GBS maps thanks to displacement measurements of a new high-temperature resistant microgrid provides

valuable information on the relative contributions of intergranular and intragranular deformations during creep of such materials. By combining strain maps with EBSD data, the correlation between the GBS and microstructural parameters (grain boundary characteristics and γ' precipitate distribution) is demonstrated to be possible. This new tool paves the way for microstructure optimization and consequently for mechanical behavior improvement of disk superalloys ■

Acknowledgements

The authors would like to thank:

- their Onera colleagues and in particular, C. Ramusat who is involved in all of these studies and A. Soula (now at Safran Aircelle), D. Boivin, Y. Renollet and D. Mézières for their contribution to GBS studies;
- their CNRS colleagues from CEMES Toulouse, F. Pettinari-Sturmel, N. Clément, J. Douin and A. Coujou for their productive participation to deformation micro-mechanism studies;
- L. Nazé and J.-L. Strudel from École des Mines de Paris for our continuous collaboration on superalloy design and optimization.

They are also grateful to J.-Y. Guédou (Safran Snecma) for his scientific, technical and financial support. Thanks to DGA, DGAC and Ministère de la Recherche for financial support.

References

- [1] L. WITEK - *Failure Analysis of Turbine Disc of an Aero Engine*. Eng Fail Anal, 13, pp. 9-17, 2006.
- [2] R.C. REED - *The Superalloys – Fundamentals and Applications*. Cambridge University Press, Cambridge UK, 2006.
- [3] G. RAISSON - *Evolution of PM Nickel Base Superalloy Processes and Products*. Powder Metall, 51, 1, pp. 10-13, 2008.
- [4] The GP7200 - *Power from Joined Forces*. Airliner World, pp. 53-57, Aug. 2010.
- [5] C. DUCROCQ, D. LESTRAT, B. PAINTENDRE, J.H. DAVIDSON, M. MARTY, A. WALDER - *Superaliage à matrice à base de nickel notamment élaboré en métallurgie des poudres et disque de turbomachine constitué en cet alliage*. French patent 2593830, 1986.
- [6] J.-Y. GUÉDOU, J.-C. LAUTRIDOU, Y. HONNORAT - *N18, PM Superalloy for Disks: Development and Applications*. Superalloys 1992, TMS, Warrendale, PA, USA. (S.D. Antolovich et al., eds), pp. 267-276, 1992.
- [7] S.T. WLODEK, M. KELLY, D. ALDEN - *The Structure of N18*. Superalloys 1992, TMS, Warrendale, PA, U.S.A. (S.D. Antolovich et al., eds), pp. 467-476, 1992.
- [8] M. SOUCAIL, M. MARTY, H. OCTOR - *Development of Coarse Grain Structures in a Powder Metallurgy Nickel Base Superalloy N18*. Scripta Mater, 34, 4, pp.519-525, 1996.
- [9] D.D. KRUEGER, R.D. KISSINGER, R.G. MENZIES, C.S. WUKUSICK - *Fatigue Crack Growth Resistant Nickel-Base Article and Alloy and Method for Making*. US Patent 4957567, 1990.
- [10] D. LOCQ, A. WALDER, M. MARTY, P. CARON - *Development of New PM Superalloys for High Temperature Applications*. EUROMAT, Intermetallics and Superalloys Vol. 10, WILEY-VCH Verlag GmbH, Weinheim, Germany (D.G. Morris et al., eds), pp. 52-57, 2000.
- [11] M. MORINAGA, N. YUKAWA, H. ADACHI, H. EZAKI - *New Phacomp and its Applications to Alloy Design*. Superalloys 1984, TMS-AIME, Warrendale, PA, USA (M. Gell et al., eds), pp. 523-532, 1984.
- [12] R. WATANABE, T. KUNO - *Alloy Design of Nickel-Base Precipitation Hardened Superalloys*. T Iron Steel I Jpn, 16, pp. 437-446, 1976.
- [13] C. DUQUENNE, J.-C.-H. LAUTRIDOU, M. MARTY, S. SOUCAIL, A. WALDER - *Superalliages à base de nickel stables à hautes températures*. French patent 2737733, 1995.
- [14] J.-Y. GUÉDOU, I. AUGUSTINS-LECALLIER, L. NAZÉ, P. CARON, D. LOCQ - *Development of a New Fatigue and Creep Resistant PM Nickel-Base Superalloy for Disk Applications*. Superalloys 2008, TMS, Warrendale, PA, USA (R.C. Reed et al., eds), pp. 21-30, 2008.
- [15] A. WALDER, M. MARTY, J.-L. STRUDEL, E. BACHELET, J.H. DAVIDSON, J.-F. STOHR - *N18, a New High Strength, Damage Tolerant PM Superalloy for Turbine Discs Application*. ICAS 1988 Congress, Jerusalem, Israel, 1988.
- [16] D. LOCQ, P. CARON - *Étude du comportement en fluage d'un superalliage pour disques de turbomachines élaborés par MdP*. Rapport Technique Onera n°67/1931 M, september 2000.
- [17] G.B. VISWANATHAN, P.M. SAROSI, M.F. HENRY, D.D. WHITIS, W.W. MILLIGAN, M.J. MILLS - *Investigation of Creep Deformation Mechanisms at Intermediate Temperatures in René 88 DT*. Acta Mater, 53, pp. 3041-3057, 2005.
- [18] T.P. GABB, J. GAYDA, J. TELESMA, A. GARG - *The Effects of Heat Treatment and Microstructure Variations on Disk Superalloy Properties at High Temperature*. Superalloys 2008, TMS, Warrendale, PA, USA (R.C. Reed et al., eds), pp. 121-130, 2008.
- [19] S. RAUJOL - *Influence du vieillissement sur le comportement en fluage d'un superalliage pour disques de turbine*. PhD Thesis. INSA, Toulouse, 2004.
- [20] D. LOCQ, P. CARON, S. RAUJOL, F. PETTINARI-STURMEL, A. COUJOU, N. CLÉMENT - *On the Role of Tertiary γ' Precipitates in the Creep Behaviour at 700°C of a PM Disk Superalloy*. Superalloys 2004, TMS, Warrendale, PA, USA (K.A. Green et al., eds), pp. 179-187, 2004.
- [21] S. RAUJOL, F. PETTINARI, D. LOCQ, P. CARON, A. COUJOU, N. CLÉMENT - *Creep Straining Micro-Mechanisms in a Powder-Metallurgical Nickel-Based Superalloy*. Mater Sci Eng, A387-389, pp. 678-682, 2004.
- [22] B. DÉCAMP, S. RAUJOL, A. COUJOU, F. PETTINARI-STURMEL, N. CLÉMENT, D. LOCQ, P. CARON - *On the Shearing Mechanism of γ' Precipitates by a Single $(a/6)\langle 112 \rangle$ Shockley Partial in Ni-Based Superalloys*. Phil Mag, 84, 1, pp. 91-107, 2004.

- [23] D. LOCQ, M. MARTY, P. CARON - *Optimisation of the Mechanical Properties of a New PM Superalloy for Disks Applications*. Superalloys 2000, TMS, Warrendale, PA, USA (T.M. Pollock et al., eds), pp. 395-403, 2000.
- [24] S. DUBIEZ-LE GOFF - *Comportement et endommagement d'un superalliage élaboré par compression isostatique à chaud*. PhD Thesis. École Nationale Supérieure des Mines de Paris, 2003.
- [25] A. SOULA, D. LOCQ, D. BOIVIN, Y. RENOLLET, P. CARON, Y. BRÉCHET - *Quantitative Evaluation of High Temperature Deformation Mechanisms: a Specific Microgrid Extensometry Technique Coupled with EBSD Analysis*. J Mater Sci, 45, pp. 5649-5659, 2010.
- [26] A. SOULA, Y. RENOLLET, D. BOIVIN, J.-L. POUCHOU, D. LOCQ, P. CARON, Y. BRÉCHET - *Grain Boundary and Intragranular Deformations During High Temperature Creep of a PM Nickel-Based Superalloy*. Superalloys 2008, TMS, Warrendale, PA, USA (R.C. Reed et al., eds), pp. 387-394, 2008.
- [27] A. SOULA - *Étude de la déformation intergranulaire au cours du fluage à haute température d'un superalliage à base de nickel polycristallin*. PhD Thesis. Institut Polytechnique de Grenoble, 2008.
- [28] V. RANDLE - *The Role of the Coincidence Site Lattice in Grain Boundary Engineering*. The Institute of Materials, London, UK, 1996.

Acronym:

HPC (High Pressure Compressor)
 HPT (High Pressure Turbine)
 LPT (Low Pressure Turbine)
 FCC (Face-Centered Cubic)
 C&W (Cast and Wrought)
 PM (Powder Metallurgy)
 DGA (Délégation Générale de l'Armement)
 TCP (Topologically Close-Packed)
 GS (Grain Size)

SEM (Scanning Electron Microscopy)
 TEM (Transmission Electron Microscopy)
 LCF (Low Cycle Fatigue)
 HSCT (High-Speed Civil Transport)
 ATSF (Avion de Transport Supersonique Futur)
 MTF (Mid-Tandem Fan)
 CEMES (Centre d'Élaboration de Matériaux et d'Études Structurales)
 GBS (Grain Boundary Sliding)
 EBSD (Electron Backscatter Diffraction)
 CSL (Coincidence Site Lattice)
 GBE (Grain Boundary Engineering)

AUTHORS



Didier Locq received his Engineering Diploma in Metallurgy from the Conservatoire National des Arts et Métiers, in 1993. He joined Onera in 1986 and is now senior scientist in the Metallic Materials and Structures Department. His work mainly concerns nickel-based superalloys for disk applications (alloy design, mechanical properties in relation with processing and microstructural parameters...).



Pierre Caron received his doctoral degree in Metallurgy from the University of Paris XI - Orsay in 1979 and his Habilitation Degree in 2000 from the same University. Since 1980, he has been involved in various studies on superalloys and high-temperature materials including alloy design and studies of the relationships between chemistry, microstructure and mechanical behaviour. He is currently a senior scientist and special advisor in the field of superalloys in the Metallic Materials and Structures Department.

P. Caron, O. Lavigne
(Onera)

E-mail: pierre.caron@onera.fr

Recent Studies at Onera on Superalloys for Single Crystal Turbine Blades

Recent alloy development works conducted at Onera for single crystal turbine blade applications succeeded in identifying specific nickel-based superalloys suited for very high temperature applications in aircraft engines and for land-based gas turbine applications in a highly corrosive environment. Various studies concerning the mechanical behavior of such single crystal superalloys showed significant effects of the chemical, microstructural and physical characteristics on the deformation mechanisms, as well as on the creep, tensile and fatigue strength of these materials. Finally, the interactions between some SC superalloys and their protective coatings were investigated, in order to evaluate their influence on the mechanical properties and on the microstructural changes in the coated alloy.

Introduction

Single crystal (SC) turbine blade technology is widely used today in modern high performance aero-engines and land-based gas turbines. The use of SC high pressure turbine blades and vanes made of nickel-based superalloys contributes efficiently to the continuous performance increase of these engines in terms of power and thermal efficiency. For thirty years Onera has actively accompanied the French aero-engine manufacturers Snecma and Turbomeca in the introduction of single crystal blade alloys into their new engines, through the development of new superalloy compositions and by performing a number of studies aimed at improving the understanding of the complex relationships between the chemistry, the process, and the properties of these alloys. This paper gives some examples of the recent work performed at Onera in these domains over the last ten years.

Alloy development

MC-NG, a fourth generation superalloy for very high temperatures

Since the introduction in late 1970s of the first SC turbine blades in the high pressure section of aircraft gas turbine engines, the compositions of the nickel-based superalloys suited for these applications

have continuously evolved with the aim of increasing their mechanical strength and temperature capability. The chemistries of the first generation alloys were derived from those of existing nickel-based superalloys previously designed for conventional casting or directional solidification processes, leading to equiaxed or columnar grained microstructures respectively. The suppression of the grain boundaries, preferential $\langle 001 \rangle$ crystallographic growth orientation and optimized chemical compositions were the main factors for the significant improvement of the creep and fatigue properties, which determine the life of the components. During the 1980s, Onera has participated in, or conducted, several alloy development programs leading to the introduction of first generation SC superalloys in Snecma and Turbomeca gas turbine engines. The AM1 superalloy (table 1) is now used in the M88-2 Snecma engine that powers the Rafale fighter as material for high pressure gas turbine blades and vanes, as well as in the TP400 engine of the Airbus A400M military airplane and in the SaM146 engine that powers the Sukhoi Superjet 100 regional airplane. AM3 and MC2 alloys were successively chosen by Turbomeca for manufacturing the high pressure SC turbine blades of helicopter engines.

Box 1 - Single crystal nickel-based superalloy microstructure

Single crystal blades made of high performance nickel-based superalloys are produced by investment casting in a directional solidification furnace and by using a grain selector or a seed of desired crystallographic orientation placed at the bottom of the mold. After solution and aging heat treatments, the microstructure of a SC nickel-based superalloy is made of an austenitic nickel rich γ matrix strengthened by a high volume fraction (up to 70 vol.%) of γ' -Ni₃Al ordered precipitates with a cubic L1₂ structure. The γ' precipitates are homogeneously distributed in the γ matrix and have sizes of less than 1 μm (figure B1-01). The γ' phase is highly coherent with the γ matrix, however with a small mismatch between the lattice parameters of the two phases defined as $\delta = 2(a_{\gamma'} - a_{\gamma}) / (a_{\gamma'} + a_{\gamma})$, where $a_{\gamma'}$ and a_{γ} are the respective lattice parameters of the γ' and γ phases. The high volume fraction of precipitates associated with the strong solid solution strengthening of both γ and γ' phases, due to multiple alloying, confer to these alloys their outstanding mechanical strength over a wide range of temperatures.

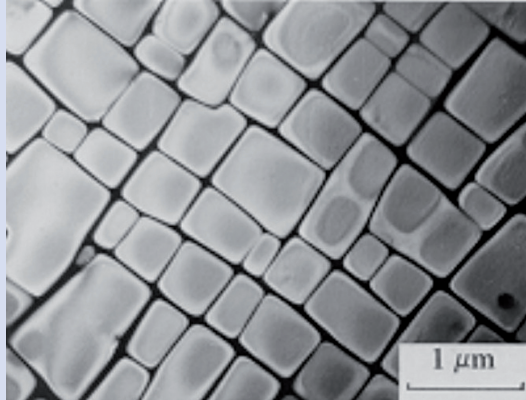


Figure B1- 01 - γ - γ' microstructure of a nickel-based SC superalloy.

The first original modification of the SC superalloy chemistry was the introduction of rhenium (Re). This refractory element introduces significant creep advantages over first generation alloys due to solid solution strengthening effects, but above all due to its low diffusion rate, which slows down all the thermally activated mechanisms controlling the high temperature deformation and damage mechanisms. Typical second generation SC superalloys containing about 3 wt.% Re, are René N5, CMSX-4 and PWA1484, which were respectively developed in the USA by General Electric, the Cannon Muskegon Corporation and Pratt & Whitney. These three alloys are widely used today as turbine blade and vane materials in a variety of aircraft engines, as well as in land-based gas turbine engines for power generation. Further increase of the Re concentration, up to values close to 6 wt.%, led to the development of third generation SC superalloys such as René N6 by General Electric and CMSX-10 by the Cannon Muskegon Corp. [1]. However, the addition of Re is not a panacea, since it entails some drawbacks, such as a high cost, limited availability, proneness to casting defects, increase of the density and higher proneness to deleterious topologically close-packed (TCP) phase precipitation.

An alloy development program was thus undertaken in the 1990s at Onera, in order to identify a material with high temperature properties equivalent to those of third generation single crystal superalloys, but with a lower density and no propensity to form TCP phase precipitates. Such an alloy was thought to be particularly well suited for applications in small helicopter engines, where an emergency regime could occur and cause rapid temperature increase for a short time, but at temperatures above 1150°C. Under these conditions, the blade material must have sufficient creep strength to avoid excessive lengthening of the airfoil. In order to attain these objectives, the deci-

sion was made to develop new alloy compositions with rhenium, but also adding ruthenium (Ru), a refractory element with a density of half that of rhenium [2, 3].

Since the strengthening γ' phase dissolves progressively when the temperature increases above 1000°C, a challenge when designing new alloys was to raise the temperature at which the γ' phase completely disappears, i.e. the γ' solvus temperature. More than twenty experimental alloys were thus defined, then melted and cast as SC bars in order to assess their physical, mechanical and environmental properties. Alloy design was performed by taking into account the data bases and the experience previously acquired at Onera. Thus, time-saving formulae deduced from the analyses of these data bases were used to estimate the γ' solvus temperature for the alloy composition, as well as the density and the lattice parameter mismatch between the γ and γ' phases. The New PHACOMP method, devised on the basis of molecular orbital calculations of the electronic structure [4], was used to predict the formation of TCP brittle phases. An additional objective was to achieve an acceptable resistance to the combustion gas environment, which is highly oxidizing and corrosive. Small contents of hafnium (Hf) and silicon (Si) were thus added to the experimental alloys, in order to improve their high temperature oxidation resistance, as previously shown for the AM1, AM3 and MC2 alloys [5]. Moreover, the levels of molybdenum (Mo) and titanium (Ti) were kept low, in order to preserve the environmental resistance. The chemical compositions of three of the most relevant experimental alloys, MC534, MC544 and MC653, are reported in table 1, together with those of the reference first generation MC2 superalloy and the third generation CMSX-10M and René N6 SC alloys.

Alloy	Ni	Co	Cr	Mo	W	Re	Ru	Al	Ti	Ta	Others
MC2	Bal.	5	8	2	8	-	-	5	1.5	6	-
MC653	Bal.	-	4	4	5	3	4	5.8	-	6	0.1 Si; 0.1 Hf
MC544 (MC-NG)	Bal.	-	4	1	5	4	4	6	0.5	5	0.1 Si; 0.1 Hf
MC653	Bal.	-	4	1	6	5	3	5.3	1	6.2	0.1 Si; 0.1 Hf
CMSX-10M	Bal.	1.75	2	0.4	5.4	6.5	-	5.78	0.24	8.2	0.08 Nb
René N6	Bal.	12.5	4.5	1.1	5.7	5.3	-	6	-	7.5	0.15 Hf; 0.05 C; 0.004 B
AM1	Bal.	6.5	7.8	2	5.7	-	-	5.2	1.1	7.9	-
MC-NG-LGP	Bal.	-	4	1	5	4	4	5.52	0.46	4.6	0.1 Si; 0.1 Hf
MC-NG-Mod	Bal.	-	4	1	4	4	5	4.8	1.2	7.7	0.1 Si; 0.1 Hf
MC-NG-Co	Bal.	10	4	1	5	4	4	6	0.5	5	0.1 Si; 0.1 Hf

Table 1 – Compositions of SC superalloys (wt. %)

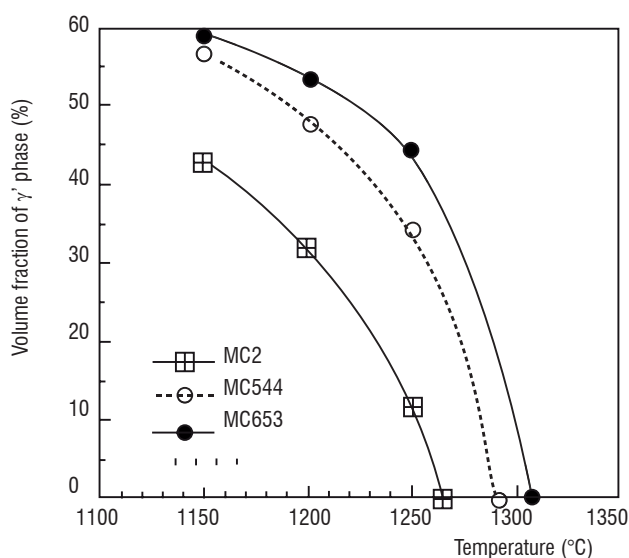


Figure 1 - Changes with temperature of the γ' volume fraction in three SC superalloys.

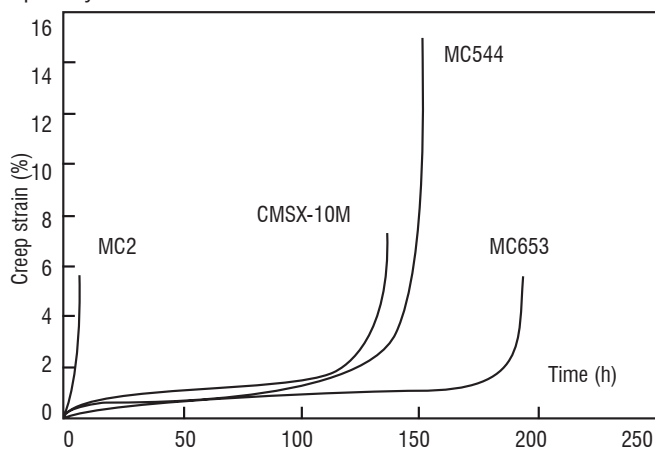


Figure 2 - Typical creep curves of $\langle 001 \rangle$ single crystal superalloys at 1150°C and 100 MPa.

The objective of increasing the γ' solvus temperature compared to MC2 was successfully attained, as illustrated in figure 1 for the MC544 and MC653 alloys. At 1150°C, the residual amount of the γ' phase is still more than 55% in the new alloys, whereas it decreased below 45% in MC2. This increase in the residual fraction of the γ' phase is thought to be the main reason for the corresponding dramatic improvement in creep strength at 1150°C, illustrated by the creep curves of single crystal specimens oriented within 5° of a $\langle 001 \rangle$ crystallographic direction (figure 2), even if this does not exclude other beneficial effects resulting from high concentrations in refractory elements. For rotating components, such as turbine blades, the alloy density is a crucial parameter and the creep strength must be considered on a specific strength basis, to evaluate properly the potential of the new alloy. An effort was therefore made, when developing the new alloys, to limit their density. A good balance of the Re and Ru content was shown to be an efficient way to attain this objective, while maintaining a specific creep strength comparable to that of third generation alloys, but with a lower density. The MC544 was further selected for a more complete evaluation on an industrial scale at Snecma and Turbomeca, under the name of MC-NG (MonoCristal-Nouvelle Génération) [6]. This alloy shows a unique combination of properties, with a reasonable density of 8.75g.cm⁻³, a satisfying environmental resistance and no propensity to form brittle TCP phase precipitates after exposure to high temperatures. This work shows that there is a promising alternative to the third generation superalloys for increasing the temperature capability of the SC turbine blade without being penalized by an excessive density or by microstructural instabilities.

Box 2 - High corrosion resistant SC superalloys for land-based industrial gas turbines

SC turbine blades made of nickel-based superalloys are also frequently used today in land-based industrial gas turbine (IGT) engines for power generation. It has thus been recognized that the use of SC blades and vanes in such engines would bring similar advantages to those obtained for aero-engines [7] in terms of temperature capability. However, the alloys developed for aircraft applications are not suitable for IGT applications, where the environment is much more corrosive due to the use of low-grade fuels containing large amounts of sulfur and vanadium. Specific alloy compositions with high levels of chromium are therefore needed to promote the formation of a protective Cr_2O_3 oxide scale, which is very efficient against corrosion attacks.

The SC16 alloy developed by Onera during the late 80s was evaluated within the COST501-2 European program on "Advanced Blading for Industrial Gas Turbine" [8]. However, whereas the sulfidation resistance of SC16 was shown to be satisfactory in laboratory tests, the corrosion resistance aimed for was not attained in severe industrial environments. A joint European Research project coordinated by Onera and gathering together Turbomeca, EDF, ALSTOM UK (now SIEMENS UK), Howmet UK and the Hahn Meitner Institut Berlin was therefore conducted, to design alloys for demanding IGT applications. The alloy design program driven by Onera took into account a number of criteria to satisfy the needs of the industrial partners. Apart from the specific corrosion resistance requirements, the aim was to make the volume fraction of the strengthening γ' phase as high as possible, in order to satisfy the creep strength objectives, while avoiding precipitation of TCP phases due to excessive concentration of chromium in the γ matrix. The alloys had to show a good castability and to be suitable for complete microstructural homogenization through simple heat treatment procedures. Lastly, the density had to be less than 8.4 g.cm^{-3} , to limit the centrifugal stress acting on the turbine disk. Two target alloys, suited for SC castings, were thus identified successfully, satisfying different operating requirements [9]. The SCA425 alloy containing about 16 wt.% of chromium was designed to operate in the most corrosive environments and offers a creep temperature advantage of about 50°C compared to the reference IN6203DS superalloy with a columnar grain structure, while maintaining corrosion resistance in synthetic ash comparable to that of the conventionally cast IN738LC reference superalloy [10]. The SCB444 alloy containing about 12 wt. % of chromium is suited for applications involving higher stresses and temperatures than SCA425, but for operation with relatively clean fuels and in a relatively clean environment [11]. Both alloys were therefore considered as serious candidates for large SC turbine blades in future engines, with improved thermal efficiency and reduced fuel consumption. SIEMENS has recently pursued some alloy development studies based on the SCA425 alloy, in order to improve its oxidation resistance. The resulting SCA425+ alloy is thus today a candidate for the SIEMENS SGT-800 gas turbine [12].

Mechanical behavior and deformation mechanisms

In order to satisfy the increasing mechanical strength requirements for advanced SC blades, the nickel-based superalloys tailored for these applications must have adequate tensile, creep and fatigue behaviors. It is therefore of the utmost importance to carefully analyze the influence of various chemical and microstructural parameters on these properties, to efficiently develop new alloy compositions, to optimize their microstructures and to have a good description of the mechanical behavior of these materials under various stress and temperature conditions. A number of studies have thus been conducted at Onera in this field of research, addressing various aspects of the relationships between the chemistry, microstructure, physical properties and mechanical behavior of different SC superalloys.

Creep behavior at an intermediate temperature

Even though knowledge of the high temperature ($T > 900^\circ\text{C}$) creep behavior of such materials is essential, since it concerns blade airfoils subjected to the highest thermal solicitations, the intermediate temperature creep behavior ($T \approx 750^\circ\text{C}$) was also investigated, since it concerns parts of the blade such as the platform and the bottom of the airfoil, where localized stress concentration due to geometrical effects (cooling channel system, sharp section changes) may induce local creep damage. Figure 3 compares the tensile creep curves obtained at 760°C and 840 MPa for SC specimens of the AM1, MC534, MC-NG, CMSX-10M and René N6 superalloys [13]. All the SC specimens have orientations within 5° of a $\langle 001 \rangle$ direction. The differences in creep behavior between the various alloys cannot therefore be attributed to an anisotropy effect. MC534 is an experimental new

generation alloy containing Re and Ru additions and a relatively high level of Mo, in order to obtain a large lattice parameter mismatch (table 1) [2]. MC-NG, CMSX-10M and René N6 creep curves are characterized by high amplitude of the primary creep deformation, which varies from about 3 to 10%. The secondary creep rate increases with the primary creep strain and the creep curves end with a short tertiary stage. The primary creep amplitude is dramatically smaller for AM1 and MC534, less than 0.25%. The secondary creep stage is quite short and the main part of the creep life corresponds to a long tertiary creep stage. However, the creep rupture life of AM1 is about ten-time longer than that of MC534. All of these alloys have similar γ/γ' microstructures, but with various chemistries, γ' precipitate sizes and lattice mismatches. The effects of these parameters have therefore been analyzed, in order to explain the differences in creep behavior.

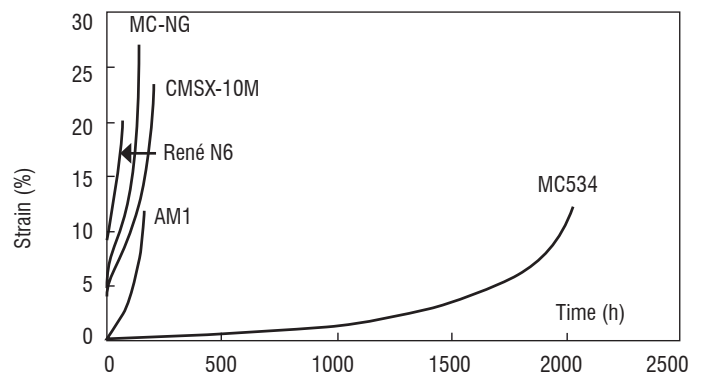


Figure 3 - Creep curves at 760°C and 840 MPa of various nickel-based $\langle 001 \rangle$ SC superalloys.

At 760°C and 840 MPa, AM1 exhibits optimal creep strength with a γ' precipitate size of 480 nm (figure 5a). Decreasing the γ' precipitate size induces an increase in the primary creep extent and a reduction in stress-rupture life. Such a phenomenon, previously observed for the CMSX-2 SC alloy [14], is associated with a change in the deformation mechanism. For a given γ' phase volume fraction, the mean distance between the precipitates, i.e. the γ matrix channel width, decreases with the γ' precipitate size. By-passing of γ' particles by the Orowan mechanism, which controls bowing of perfect $a/2\langle 110 \rangle$ matrix dislocations between the precipitates, becomes more difficult when the γ channel width decreases and the γ' cutting mechanism by $a/3\langle 112 \rangle$ superpartial dislocations is therefore promoted. The cutting mechanism, which operates in a heterogeneous manner, leads to a faster creep rate and a higher primary creep amplitude than the more homogeneous mechanism involving multiple $a/2\langle 110 \rangle\{111\}$ slip within the γ matrix. However, increasing the γ' size, and then the γ channel width too much, facilitates the bowing of matrix dislocations between the precipitates and therefore decreases the creep strength. The effect of γ' size variation is somewhat different in the case of MC-NG, where $\langle 112 \rangle\{111\}$ slip operates during primary creep for γ' sizes within the range 220-480 nm, but with different levels of heterogeneity. The larger the γ' size is, the wider the γ channel, the more homogeneous the deformation and the smaller the primary creep amplitude.

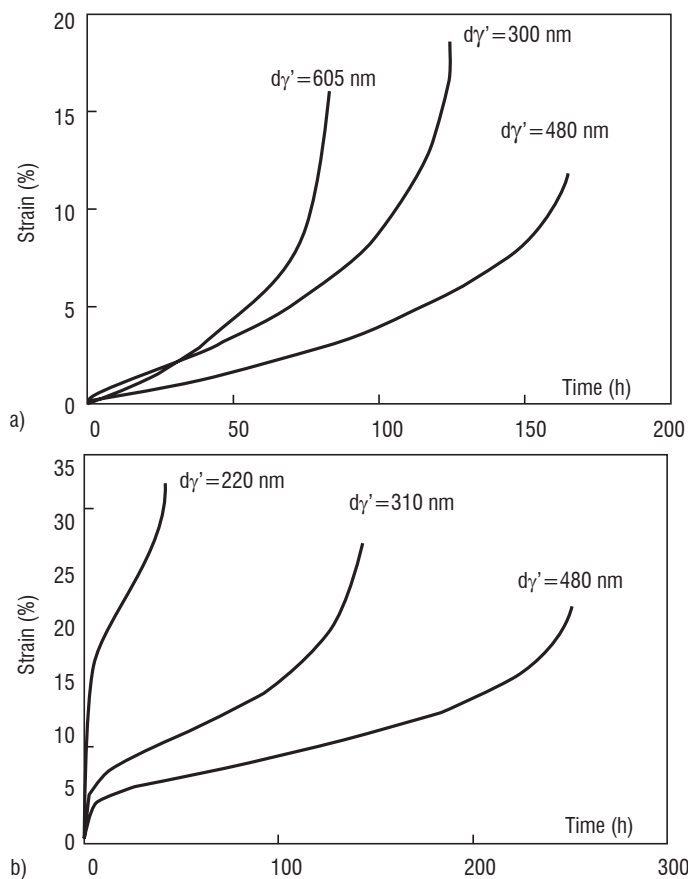
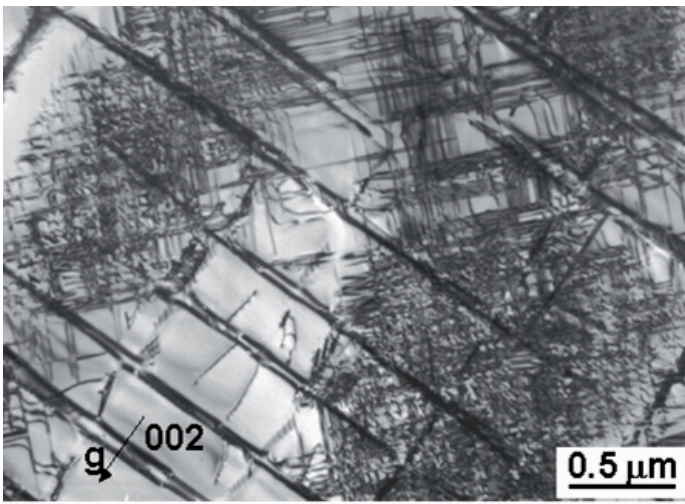


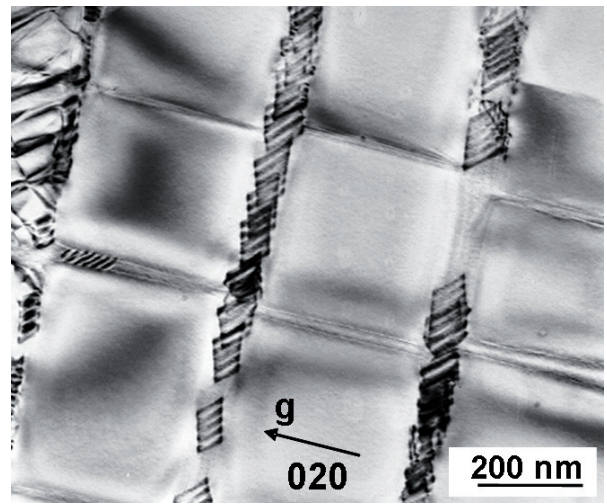
Figure 4 - Creep curves at 760°C and 840 MPa for a) AM1 and b) MC-NG $\langle 001 \rangle$ single crystals with various γ' precipitate sizes.

However, the effect of the γ' size cannot explain the differences in creep behavior at 760°C observed between AM1 and MC-NG alloys with the same size of γ' precipitates, i.e. 480 nm or 300 nm (figure 4). Analysis of the solid solution strengthening effect in both phases of the two alloys shows that the γ phase is stronger in MC-NG than in AM1 and inversely that the γ' phase is stronger in AM1 than in MC-NG [13]. Moreover, the γ' phase of AM1 is characterized by a higher value of the antiphase boundary (APB) energy than that in MC-NG, due to its higher level of Ti and Ta. This makes the shearing of the γ' precipitates by matrix dislocations more difficult. All these differences combine to promote an easier $a/2\langle 110 \rangle$ dislocation glide in the γ channels of AM1 and to facilitate the shearing of γ' precipitates in MC-NG instead of matrix deformation, as observed experimentally [13].

The difference in creep behavior at 760°C between MC-NG and MC534 alloys was inferred to be due to the high amplitude of the lattice mismatch, measured at -14.2×10^{-3} for MC534 at 760°C, in comparison to the value of -0.5×10^{-3} measured for MC-NG [13]. The γ - γ' mismatch measurements were performed by means of high-energy X-ray diffraction at the beam line ID 15A of the ESRF (European Synchrotron Radiation Facility, Grenoble, France). This high value of δ in MC534 results mainly from the much higher level of Mo, which partitions preferentially to the matrix and significantly increases its lattice parameter. Calculations showed that the coherency stresses generated by this misfit add to the applied stress in the channels normal to this external stress [15]. In MC534, transmission electron microscopy (TEM) observations show that the spreading of the matrix dislocations is strongly promoted in the horizontal channels as soon as the external stress is applied, leading to a high density of dislocations at the γ - γ' interfaces normal to the stress axis (figure 5a). At the same time, the mobility of the matrix dislocations is much lower in the vertical channels, where the applied stress is not assisted by the coherency stresses, as is evidenced by the decorrelated movement of Shockley partial dislocations, with the creation of numerous stacking faults (figure 5b) [16]. Stacking faults in the γ phase were also observed in other Ru-bearing alloys [17-19]. These observations suggest that Ru addition decreases the stacking fault energy (SFE) of the γ matrix. However, no stacking faults were observed within the γ channel of MC-NG, which shows that an analysis based only on SFE considerations cannot explain the difference in creep behavior between the MC534 and MC-NG alloys. In any case, the dense dislocation networks rapidly formed at the γ - γ' interfaces act as obstacles to the motion of dislocations in the matrix and also against the shearing of the precipitates, which explains the very limited extent of primary creep for this alloy in comparison to MC-NG. High amplitude of deformation during the primary creep stage, as observed for MC-NG, René N6 or CMSX-10M, penalizes their stress-rupture life in comparison to that of MC534, since the level of stress at the beginning of the secondary creep stage increases proportionately to the primary creep strain.



a) Dislocation networks at the γ - γ' interfaces normal to the stress axis



b) Stacking faults within the vertical γ phase channels

Figure 5 - Dislocation structures in MC534 after creep at 760°C and 840 MPa (foil normal to the [001] stress axis, $t = 4.6$ h, $\epsilon = 0.08\%$).

Creep behavior at high temperatures

A strong microstructural change in the SC superalloys during tensile creep at high temperatures ($T > 900^\circ\text{C}$) is the directional coalescence of the γ' precipitates, leading to a rafted γ - γ' microstructure normal to the $\langle 001 \rangle$ tensile axis when the γ - γ' is negative, as is the case for all industrial alloys. This phenomenon results from the combined effects of centrifugal tensile stress, diffusion, γ - γ' coherency stress and γ - γ' elastic modulus misfit. The rate of transition between the cuboidal and the rafted morphology of the γ' particles, as well as the stability of the γ - γ' rafted microstructure, therefore depend on the alloy chemistry and influence the creep behavior. Typical tensile creep curves obtained at 1050°C and 150 MPa for $\langle 001 \rangle$ oriented SC specimens of MC2 and MC-NG alloys are compared in figure 6 [20]. The stress-rupture times are almost comparable but the shapes of the curves differ in several points. Primary creep occurs for MC2 as soon as the load is applied while the creep for MC-NG starts with a low creep rate incubation period before primary creep happens. The secondary creep stage is dramatically shorter for MC-NG than for MC2 and the tertiary creep stage therefore begins much earlier. Tertiary creep is however longer in the case of MC-NG, which makes the stress-rupture lives comparable for both alloys.

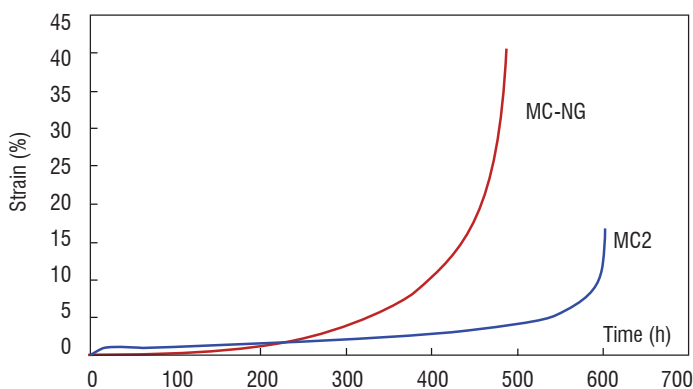
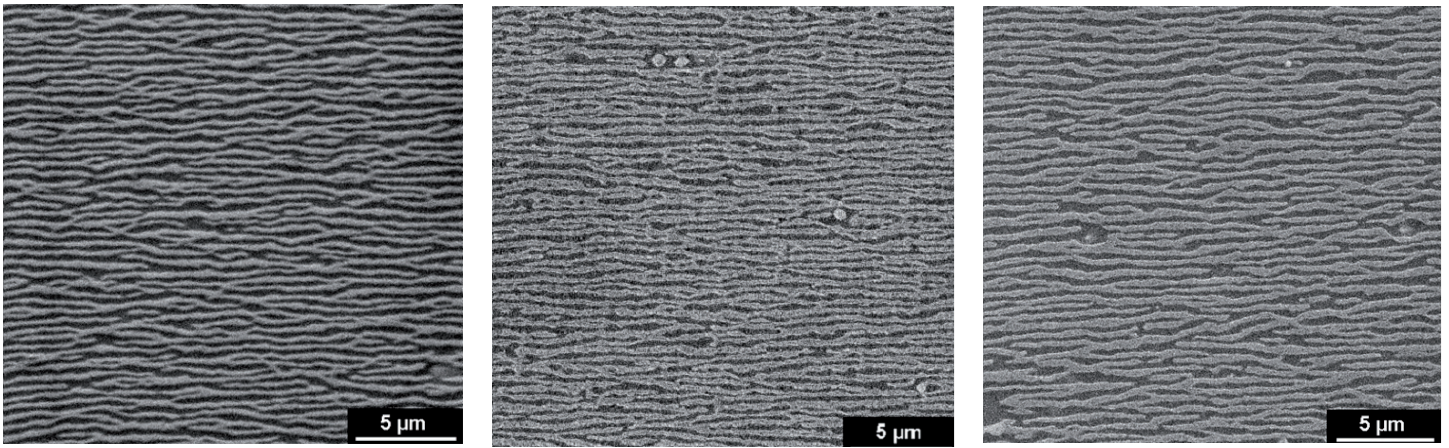


Figure 6 - Creep curves of $\langle 001 \rangle$ MC2 and MC-NG SC alloys at 1050°C and 150 MPa.

After 20 hours of creep, scanning electron microscopy (SEM) observations of longitudinal sections of SC specimens show that the γ - γ' rafted microstructure is well established in MC2 (figure 7a), whereas there is no significant change in the initial structure for MC-NG (figure 8a). The primary creep is associated with the cube-raft morphology transition, which is inhibited, or at least delayed, in MC-NG. Correlatively, TEM observations of the dislocation structures show an intense deformation activity in the matrix of MC2 leading to the formation of dense dislocation networks at the γ - γ' interfaces, while very few dislocations are observed in the γ matrix channels of MC-NG. These observations confirm that the oriented coalescence of γ' precipitates is promoted by plastic deformation. After about 120 hours, the secondary creep stage is attained for both alloys, where regular γ - γ' rafted microstructures are stabilized (figure 7b and 8b). After 310 hours, the creep curve of MC-NG has largely entered into its tertiary stage, while the secondary creep stage is still running for MC2. Whereas the γ - γ' rafted microstructure is still regular in MC2 (figure 7c), it is totally destabilized in MC-NG (figure 8c) where a complete γ - γ' topological inversion has occurred. The γ phase, which surrounded the γ' precipitates before the creep test was started, becomes progressively surrounded by the γ' phase as soon as the tertiary creep stage occurs. At the same time, TEM observations show an increased dislocation activity within the γ' phase, parallel to the γ phase deformation. The continuous increase of the creep rate during tertiary creep of MC-NG is associated with the growing activity of the deformation mechanisms in both the γ and γ' phases, resulting from the γ - γ' topological inversion. On the other hand, the long secondary creep stage in MC2 is related to the stability of the γ - γ' rafted microstructure, where the dislocation activity is mainly confined in the γ matrix. Some authors have concluded that the stability of the rafted structure of SC nickel-based superalloys, during creep at high temperatures, increases with the amplitude of the negative γ - γ' mismatch [21, 22]. This argument cannot however be retained to explain the better stability of the γ - γ' microstructure during creep of MC2, compared to that of MC-NG, since the amplitude of the γ - γ' mismatch at 1050°C is slightly higher for MC-NG than for MC2 [20].

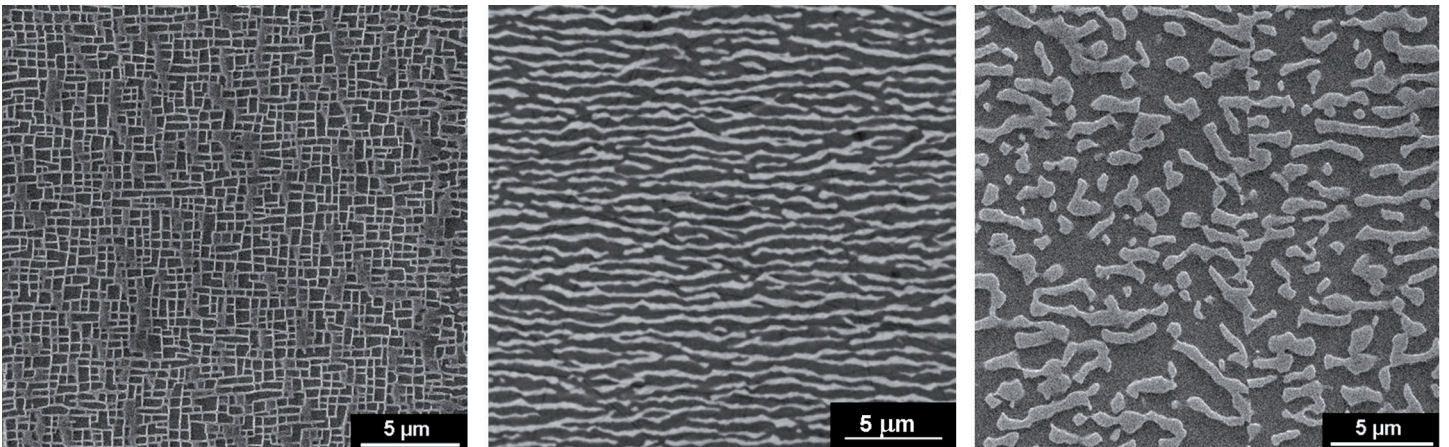


a) $t = 20 \text{ h}, \epsilon = 0.51\%$

b) $t = 123 \text{ h}, \epsilon = 0.8\%$

c) $t = 314 \text{ h}, \epsilon = 0.89\%$

Figure 7 - Changes in the γ - γ' microstructure during creep at 1050°C and 150 MPa of $\langle 001 \rangle$ MC2 SC specimens (sections cut parallel to the tensile axis; the darkest phase is the γ' phase).



a) $t = 21 \text{ h}, \epsilon = 0.06\%$

b) $t = 120 \text{ h}, \epsilon = 0.65\%$

c) $t = 310 \text{ h}, \epsilon = 4.45\%$

Figure 8 - Evolution of the γ - γ' microstructure during creep at 1050°C and 150 MPa of $\langle 001 \rangle$ MC-NG SC specimens (sections cut parallel to the tensile axis; the darkest phase is the γ' phase).

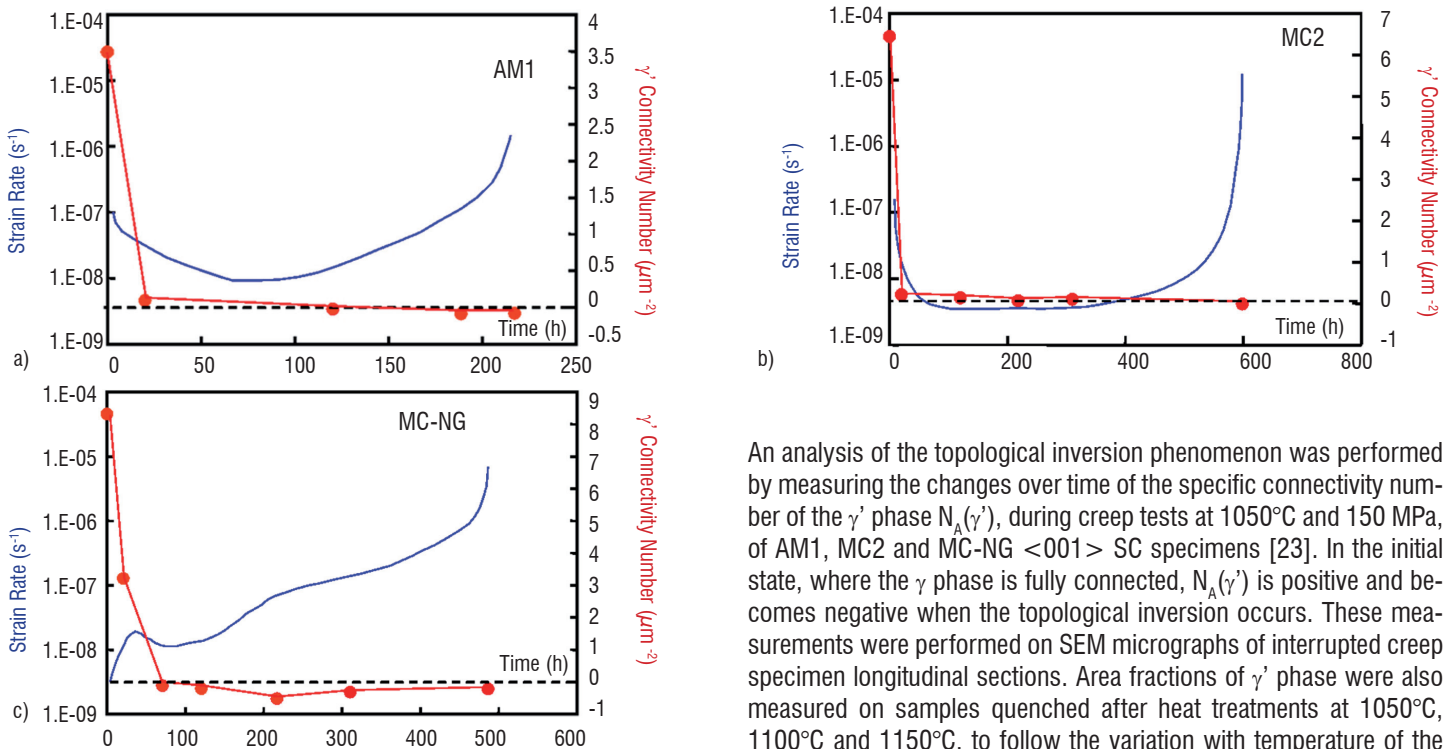


Figure 9 - Evolution of $N_A(\gamma')$ and strain rate during creep at 1050°C and 150 MPa.

An analysis of the topological inversion phenomenon was performed by measuring the changes over time of the specific connectivity number of the γ' phase $N_A(\gamma')$, during creep tests at 1050°C and 150 MPa, of AM1, MC2 and MC-NG $\langle 001 \rangle$ SC specimens [23]. In the initial state, where the γ phase is fully connected, $N_A(\gamma')$ is positive and becomes negative when the topological inversion occurs. These measurements were performed on SEM micrographs of interrupted creep specimen longitudinal sections. Area fractions of γ' phase were also measured on samples quenched after heat treatments at 1050°C, 1100°C and 1150°C, to follow the variation with temperature of the γ' volume fraction. Variations of $N_A(\gamma')$ with creep time are plotted in figure 9, together with the respective creep strain rates.

	T=1050°C		T=1150°C	
Alloy	$F_A(\gamma')$ (%)	$N_A(\gamma')$ (μm^{-2})	$F_A(\gamma')$ (%)	$N_A(\gamma')$ (μm^{-2})
AM1	52.0	-0.081	42.5	+0.105
MC2	44.5	-0.015	39.9	+0.265
MC-NG	62.4	-0.221	48.6	+0.127
MC-NG-LGP	40.4	+0.080	nd	nd
René N6	61.1	-0.093	46.4	+0.133
CMSX-10M	67.3	-0.115	55.2	+0.094

Table 2 - Area fraction and specific connectivity number of the γ' phase after rupture, during creep at 1050°C and 150 MPa and at 1150°C and 100 MPa (nd : not determined).

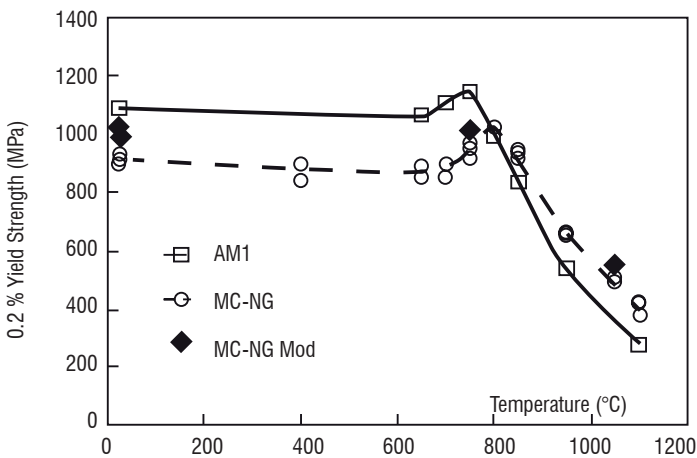


Figure 10 - Variation with temperature of the YS of AM1, MC-NG and MC-NG Mod SC alloys.

In AM1 and MC-NG, the onset of the strain rate increase corresponds to the topological inversion, i.e. to the moment at which $N_A(\gamma')$ becomes negative. In MC2, topological inversion is observed only in the ruptured specimen and is not very pronounced, both γ and γ' phases remaining strongly interconnected. Creep tests have been performed at 1150°C and 100 MPa to check whether γ - γ' topological inversion still occurs under these conditions. The stress rupture life of MC-NG is dramatically longer than that of AM1 and MC2 (about 150 hours instead of less than 20 hours) but, above all, the creep curve of MC-NG at 1150°C has the same shape as those of AM1 and MC2 at 1050°C [23]. Microstructural analyses of stress-ruptured specimens show that $N_A(\gamma')$ remains positive up until rupture in these three alloys, which means that the γ' phase particles are still completely surrounded by the γ phase (table 2). Additional creep tests were performed at 1050°C and 150 MPa on SC of the experimental MC-NG-LGP (low Gamma Prime) alloy, with reduced contents in γ' -former elements compared to MC-NG. This alloy, with a γ' phase fraction close to 40% at 1050°C, did not experience γ - γ' topological inversion at this temperature. Moreover, the comparison of $N_A(\gamma')$ values and the fraction of γ' phase for different alloys shows a strong relationship between the increase in the γ' phase and the growing tendency for topological inversion of the γ - γ' microstructure (table 2).

These experimental results, associated with an analysis of results published in the literature, therefore demonstrate unambiguously that topological inversion of the γ - γ' microstructure of SC nickel-based superalloys during creep at high temperature is inhibited under conditions where the fraction of the γ' phase is lower than about 50%. In alloys where topological inversion occurs, the higher the fraction of the γ' phase is, the earlier this phenomenon occurs during the creep life. This analysis can yield some precious indications for alloy design for a given application, depending on the temperature regime that must be favored, at least as far as creep strength is concerned. Increasing the γ' phase fraction to promote a high creep strength at very high temperatures ($T > 1100^\circ\text{C}$) is not necessarily the most efficient solution to obtain a low creep rate in the high temperature regime ($1000^\circ\text{C} < T < 1100^\circ\text{C}$), where the stability of the rafted structure plays an important role. On the other hand, a high volume fraction of the γ' phase may be preferred in the intermediate temperature range (850 - 950°C), where the γ - γ' microstructure changes slowly and the Orowan resistance governs the creep rate. In any case, it is a huge challenge to optimize the chemistry and the microstructure of such SC superalloys, which must satisfy creep strength requirements over a very large temperature range, typically 700 - 1150°C , covering the different parts of a turbine blade.

Tensile behavior

The tensile properties of the SC superalloys are not only dependent on their microstructure, but also on their chemistry. Indeed, a survey of the literature reveals that significant tensile strength differences may exist between one alloy and another, especially within the low temperature regime ($T < 800^\circ\text{C}$). An analysis of the influence of the chemistry on the tensile yield strength (YS) of various alloys has therefore been performed, to identify the role of pertinent alloying elements [24]. The tensile yield strengths of $\langle 001 \rangle$ AM1, MC-NG and MC-NG Mod SC alloys have been compared within the temperature range 20 - 1150°C (figure 10). The MC-NG Mod alloy was derived from MC-NG by increasing the Ti and Ta contents at the expense of Al, in order to reinforce the γ' - $\text{Ni}_3(\text{Al}, \text{Ti}, \text{Ta})$ phase, where these alloying elements partition preferentially (table 1). All alloys were aged to produce similar γ' precipitate sizes close to 300 nm, in order to discriminate between possible effects of chemistry and microstructure. The YS of AM1 is significantly higher than that of MC-NG from room temperature up to 750°C and the opposite is observed at temperatures above 800°C . At room temperature and 750°C , the YS of MC-NG Mod is intermediate between those of MC-NG and AM1, which shows the efficiency of increasing the Ti and Ta levels. At 1050°C , the MC-NG Mod YS is slightly higher than that of MC-NG. In the low temperature regime, the matrix dislocations first move through the γ channel by $a/2\langle 110 \rangle \{111\}$ slip, but then the high Orowan strength forces these dislocations to cut the γ' precipitates as pairs bounded by an APB. TEM analyses have shown numerous γ' precipitate shearing events in MC-NG and AM1 tensile specimens after 2% plastic deformation at room temperature, together with a high density of matrix dislocations in the γ channels [25]. In the high temperature regime ($T > 800^\circ\text{C}$), the matrix dislocations propagate between the γ' precipitates by thermally activated glide/climb processes and only few γ' shearing events are observed, which promotes a homogeneous deformation. Under these conditions, the tensile strength is therefore essentially linked to the mobility of the matrix dislocations between the precipitates. Variations in the Orowan stress and in the γ - γ' mismatch were excluded to explain the difference in YS between AM1 and MC-NG in the low temperature regime, since the γ channel width

and the lattice mismatch are comparable in both alloys. The higher YS of AM1 in comparison to that of MC-NG was attributed to the better resistance of the γ' precipitates against shearing. The higher strength of the γ' phase in AM1 compared to MC-NG results from the increased levels of Ti and Ta, which substitute for Al in the γ' phase and which are known to increase its APB energy [26], thus rendering more difficult the shearing of γ' precipitates by pairs of matrix dislocations. The higher YS of MC-NG Mod alloy, which shows Ti, Ta and Al contents close to that of AM1, is in agreement with this conclusion. In the high temperature regime, the better tensile strength of MC-NG compared to that of AM1 was attributed partly to a higher Orowan stress, since γ' solutioning is postponed when the temperature increases, which determines a narrower γ channel in the fourth

generation alloy. At 1050°C, typically, the Orowan stress was estimated to be 26% higher for MC-NG than for AM1, taking into account the respective residual amounts of the γ' phase at this temperature. The presence of Re in the MC-NG matrix is also advantageous, since this alloying element has been shown to be the one characterized by the lowest diffusion rate among nickel-based superalloys [27]. This is beneficial for slowing down the climb rate of matrix dislocations, compared to AM1. Finally, the higher solid solution strengthening effect estimated for the MC-NG matrix compared to that of AM1 is an additional argument to explain its greater YS in the high temperature range. Comparison of the data obtained for AM1 and MC-NG with that available for other third and fourth generation SC superalloys confirms our hypotheses.

Box 3 - Impact of γ - γ' rafting on the mechanical properties of SC nickel-based superalloys

Since the γ - γ' microstructure of the SC superalloys changes significantly during creep at high temperatures, it is of the utmost importance to evaluate the impact of such a phenomenon on the other mechanical properties. As an example, MC2 <001> SC specimens were crept during 200 hours at 1050°C and 80 MPa to develop a regular γ - γ' rafted structure before carrying out tensile and low cycle fatigue tests. An effect of the rafting process is to decrease the tensile yield strength (YS) at room temperature (figure B3-01) [28, 29]. TEM observations of unaged and aged tensile specimens tested at room temperature show planar deformation bands with numerous stacking faults within the γ' precipitates (figure B3-02). Outside these bands, deformation operates by $a/2$ <110> dislocation bypass of the γ' particles by the Orowan process. The critical Orowan stress that must be attained to move the matrix dislocations between the precipitates before cutting them is obviously lower in the aged material where the mean spacing between γ' rafts was found to be close to 270 nm, than in the unaged alloy where the γ channel width is about 30 nm. This explains the YS decrease observed at room temperature after aging at 1050°C. A preliminary stress-aging treatment was also shown to decrease the number of cycles to rupture during low cycle fatigue (LCF) tests of MC2 SC specimens at 650 and 950°C [30]. The reduction in YS and easier crack propagation within the γ - γ' rafted microstructure were suggested to be the causes for reduction of the fatigue life of pre-rafterd MC2 alloys, compared to the same material containing cuboidal γ' particles.

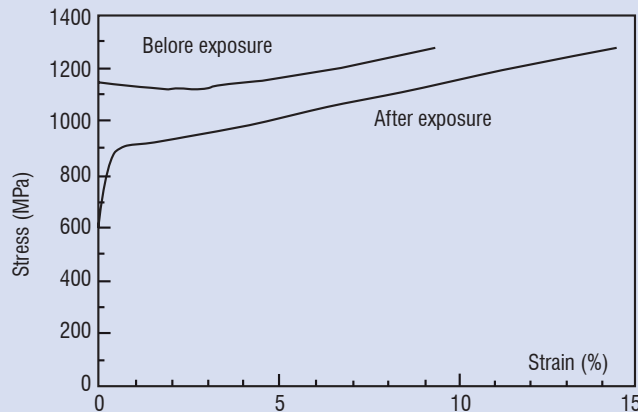


Figure B3-01 – Effect of a 200-hour exposure at 1050°C and 80 MPa on the tensile behavior of the MC2 SC alloy at room temperature.

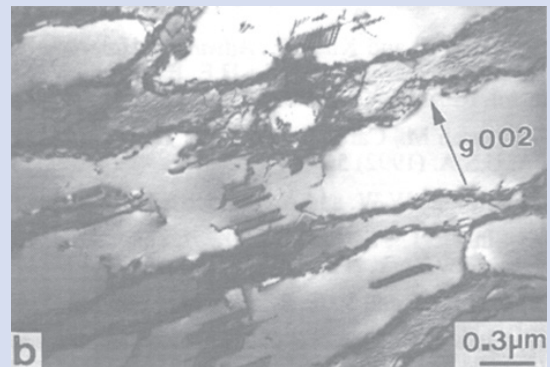


Figure B3-02 – Dislocation structures in tensile MC2 <001> SC specimens strained to 2% at room temperature: a) unaged material, b) aged material.

Interactions between single crystal superalloys and protective coatings

The most advanced high pressure SC turbine blades are protected by a thermal barrier coating (TBC) based on porous ceramic that reduces the temperature of the superalloy substrate and are protected in between by an intermetallic bond coat that ensures a good oxidation resistance and the ceramic coating spallation resistance.

In coated first and second generation SC nickel-based superalloys (Re content between 0 and 3wt. %), interdiffusion phenomena between the substrate and Pt-modified nickel aluminide bond coat create an intermediate zone with a β -NiAl(Pt) matrix, containing precipitates rich in refractory elements (figure 11). In third and fourth generation alloys containing high levels of elements such as Mo, W, Ta, Re and possibly Ru, a deeper secondary reaction zone (SRZ) may develop in the alloy under the primary diffusion zone [31]. Such a SRZ was observed to form in the MC-NG alloy protected by a NiAlPt bondcoat (figure 12) [32]. The SRZ microstructure is cellular with a γ' phase matrix containing elongated γ particles and intermetallic TCP phase precipitates. The driving forces for SRZ formation were suggested to be:

- local changes of composition due to aluminum diffusion towards the superalloy and of nickel and refractory alloying elements in the opposite direction;
- residual stress resulting from the alloy surface preparation prior to coating. Electron backscattered diffraction (EBSD) analysis shows that the cellular transformation leading to the characteristic γ'/γ /TCP phase SRZ microstructure occurs together with the recrystallization of the superalloy affected zone.

Elongated recrystallized grains grow normally to the surface with misorientation relative to the original SC substrate within the $[20^\circ, 60^\circ]$ range (figure 13) [32]. Such high angle misorientations also occur between the grains themselves. The formation of high angle boundaries, on the one hand between the unaffected superalloy and the SRZ and on the other hand between adjacent SRZ grains, is likely to be a weak point in the system with respect to mechanical properties. Moreover, SRZ can extend up to $160 \mu\text{m}$ into the superalloy (MC-NG aged at 1100°C for 300 hours), thus significantly reducing the alloy load bearing section. Due to its specific microstructure, the SRZ strength is indeed inferred to be much lower than that of the substrate γ - γ' microstructure.

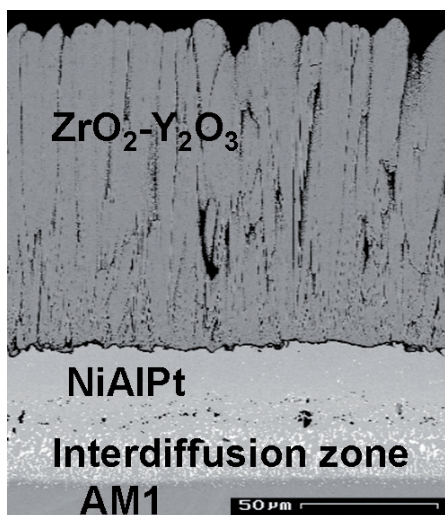


Figure 11 - TBC system on the AM1 SC superalloy: NiAlPt bond coat and $\text{ZrO}_2\text{-Y}_2\text{O}_3$ EB-PVD (Electron Beam-Physical Vapor Deposition) topcoat.

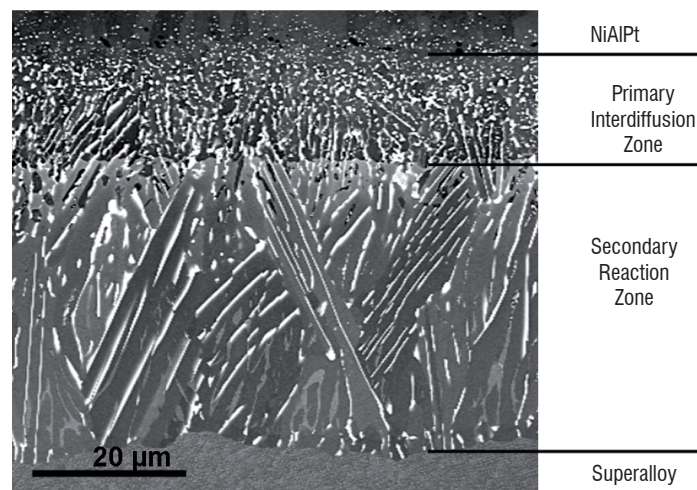


Figure 12 - Microstructure of the diffusion zone in as-coated MC-NG.

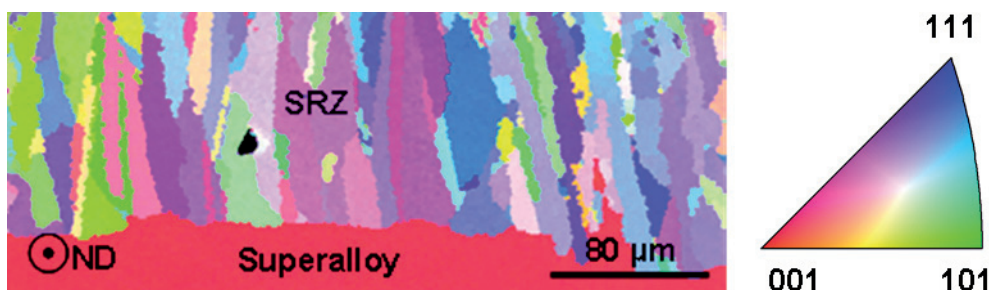


Figure 13 - EBSD inverse pole figure of the SRZ in NiAlPt-coated MC-NG after exposure for 300 hours at 1100°C (ND: sample normal direction) (from [32]).

To estimate the effect of SRZ formation on the creep strength, comparative tests have been performed at 950°C and 300 MPa, at 1050°C and 150 MPa and at 1150°C and 100 MPa, on bare and NiAlPt-coated <001> MC-NG SC specimens. The applied load was determined by taking into account the section of the specimen gauge before coating. The thickness of the SRZ was about 40 μm in the as-coated material and increased to about 75 μm after 204 hours at 950°C. After creep at higher temperatures, it becomes difficult to discriminate between the primary diffusion zone and the SRZ. The total depth of the diffusion zone has increased from 50 μm to 140 μm after 199 hours at 1050°C, and to 110 μm after 62 hours at 1150°C. Considering that the creep resistances of both primary and secondary diffusion zones are significantly lower than that of the γ-γ' microstructure, the true stress acting on the load bearing unaffected alloy was determined at the beginning and at the end of the creep tests, by taking into account the total thickness of the interdiffusion zone. The stress-rupture lives of coated MC-NG are reported in the Larson-Miller diagram presented in figure 14, as a function of the nominal stress (without any section correction) and also as a function of the stress acting on the unaffected alloy section at the beginning and at the end of the corresponding tests. For the sake of comparison, a Larson-Miller curve for the bare MC-NG alloy is reported in this diagram. Without any stress correction, it appears clearly that the presence of the coating significantly reduces the stress-rupture life of MC-NG. With the corrected values of the stress, the stress-rupture life of the coated material is comparable to that of the bare alloy.

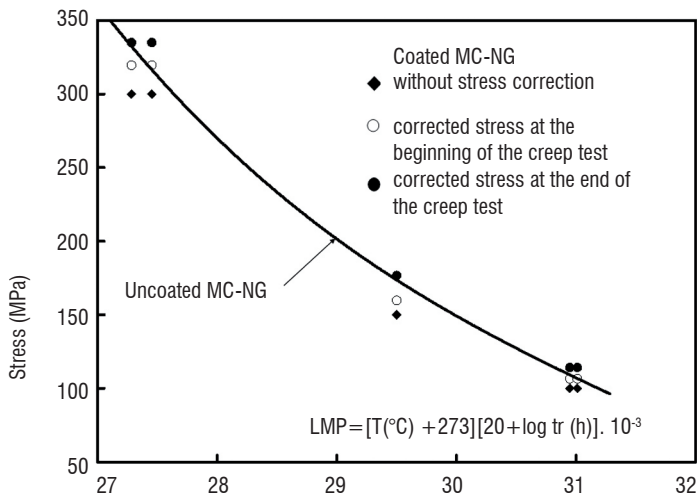


Figure 14 - Larson-Miller diagram for stress-rupture life of MC-NG.

The SEM micrograph in figure 15 illustrates the damage experienced in the SRZ after 199 hours of creep at 1050°C and 150 MPa. Microcracks initiate and propagate within the SRZ, along the grain boundaries. Except for the region very close to the fracture surface, i.e. in the necked portion of the specimen, these cracks never propagate into the unaffected superalloy. The SRZ is therefore a poor strength zone, which is penalized by its recrystallised structure rather than by its cellular microstructure or by the presence of TCP phase particles. The SRZ depth is the pertinent parameter required to estimate the deleterious effect of this microstructural instability. Depending on the local section of the single crystal blade, this phenomenon can have a more or less significant effect on the creep behavior of the component.

The strain-controlled LCF behavior of NiAlPt-coated MC-NG <001> SC specimens was investigated at 650 and 950°C, to check whether SRZ can initiate cracks causing premature failure of the material,

compared to the bare case [32]. At 650°C, the number of cycles to failure is adversely affected by the presence of the aluminide coating, especially at the lowest applied stress level (figure 16). The reduction of the load bearing cross section due to SRZ formation is not sufficient to explain this LCF strength decrease. Actually, cracks start in the brittle NiAlPt layer and not in the SRZ, then follow the grain boundaries within the SRZ and continue within the superalloy (figure 17). This explains the resulting loss of LCF strength. At 950°C, i.e., above its ductile-to-brittle transition temperature, the aluminide coating is no longer brittle and is able to accommodate the strain by creep deformation. The cracks leading to the rupture start at casting porosity, as typically observed in uncoated specimens. In this case, the slight decrease in the LCF strength was shown to be mainly due to the reduction in the load bearing cross section. Under severe laboratory test conditions, the NiAlPt layer was strongly deformed and therefore contained numerous cracks propagating within the SRZ. Contrary to what was observed at 650°C, the cracks did not cross the boundary separating the SRZ and the γ-γ' superalloy, but rather split along this interface (figure 18). This explains the limited deleterious effect of SRZ on the LCF strength of coated MC-NG at 950°C.

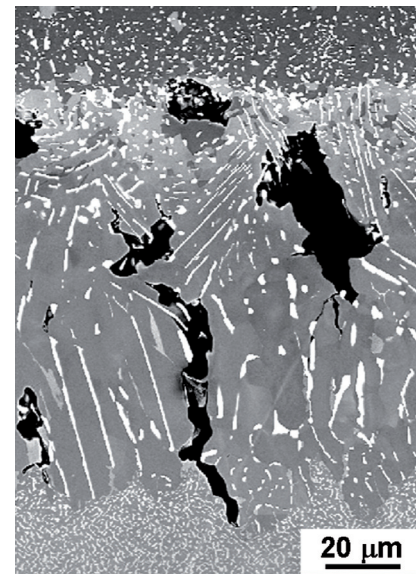


Figure 15 - Secondary reaction zone in coated MC-NG after 199 hours of creep at 1050°C.

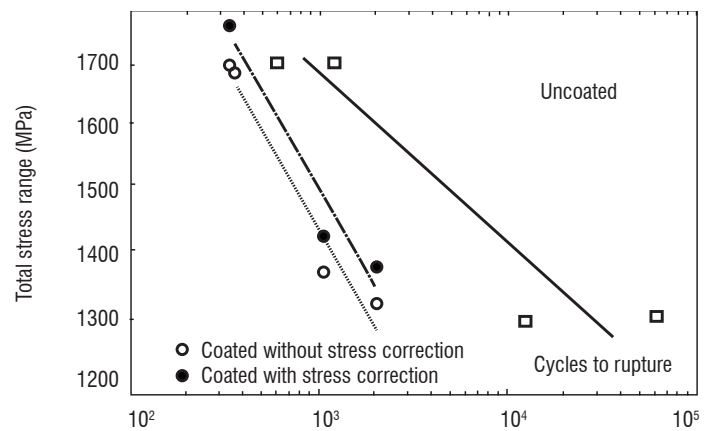


Figure 16 - LCF strength at 650°C of <001> SC specimens of the MC-NG alloy (R = -1; f = 0.33 Hz).

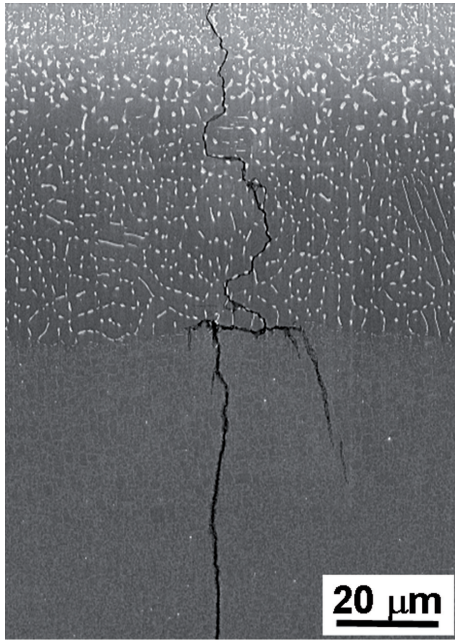


Figure 17 - Crack propagation through the SRZ and the γ - γ' structure of a NiAlPt-coated MC-NG LCF specimen having failed at 650°C (1070 cycles) (longitudinal section; SEM in backscattered electron mode).

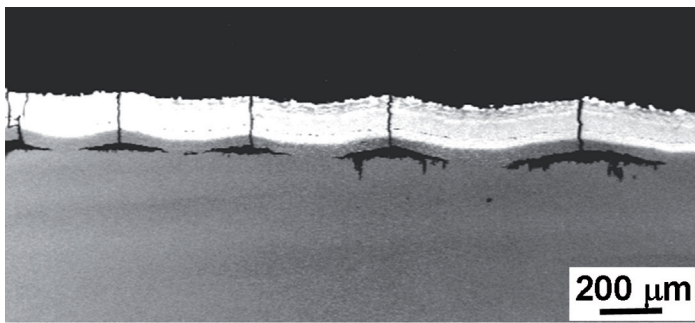
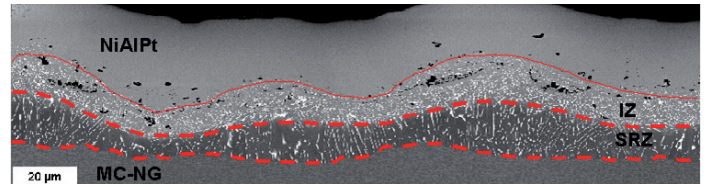
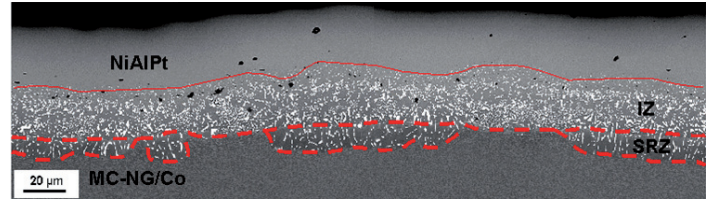


Figure 18 - Secondary cracks within the coating layer of a MC-NG LCF specimen having failed at 950°C (7010 cycles) (longitudinal section; SEM in backscattered electron mode).

One solution generally considered for reducing SRZ proneness is to adapt the alloy substrate chemistry to the bond coat. Analysis of the results obtained for various superalloys (AM1, MC-NG, CMSX-4, CMSX-10M, Alloy 5A, René N6 and Alloy 11) coated with a platinum modified aluminide, puts forward hypotheses about the role of some elements in the SRZ occurrence frequency [33]. Thus, the presence of rhenium seems to be necessary, but not sufficient, for SRZ development. On the contrary, cobalt is inferred to play an inhibitive role. In addition, this element is known to improve the microstructural stability of rhenium-bearing superalloys, by reducing their sensitivity to precipitation of brittle intermetallic phases [32]. In order to validate this alleged effect of cobalt on SRZ mitigation and to analyze the corresponding mechanisms, a modified version of the MC-NG alloy was prepared by replacing 10 wt. % of nickel by the same amount of cobalt, an element that was originally absent from the alloy (table 1) [33, 35, 36]. SC samples were fully solution heat-treated prior to coating. Comparison between the base alloy and the modified one, both having been coated with a γ -NiAl(Pt) single phase coating, indeed shows a very significant decrease of the SRZ amount when cobalt is present in the substrate (figure 19).



a)



b)

Figure 19 - Interaction zones between: (a) the reference MC-NG superalloy or (b) the Co-modified one and a NiAlPt coating (IZ: primary interdiffusion zone; SRZ: secondary reaction zone).

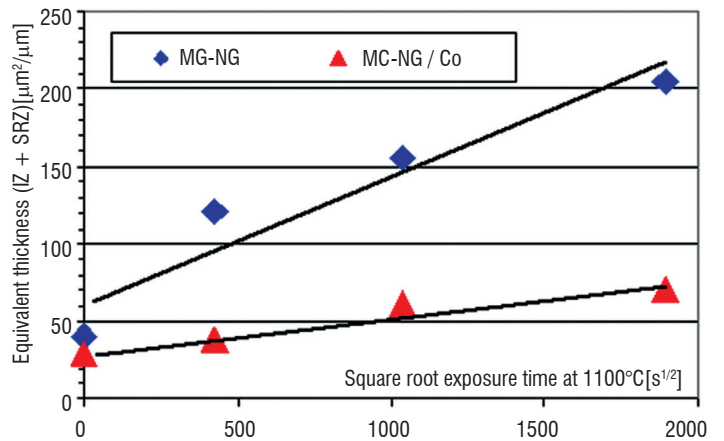


Figure 20 - Changes in the interdiffusion zone thickness over time, at 1100°C, in reference and Co-modified MC-NG alloys.

Moreover, microstructural assessments of the interdiffusion zones after aging treatments, at temperatures within the 950-1100°C range, in an argon atmosphere, show that the SRZ growth rate as a function of temperature or of time is slower in the cobalt-bearing alloy (figure 21). This growth rate is controlled by diffusion as shown by the linear dependence of the SRZ thickness on the square root of time. The estimated diffusion coefficient is about 6.10^{-15} [m².s⁻¹] for the MC-NG alloy, which is very close to the value obtained for Alloy 5A [28]. This is about one order of magnitude lower for the Co-modified MC-NG alloy.

Conclusions

Various studies on nickel-based superalloys for SC turbine blade applications have shown the complex relationships between the chemistry, the physical characteristics, the microstructure and the mechanical behavior of such materials in a wide temperature range. In particular, the creep behavior is highly dependent on the size and morphology of the strengthening γ' precipitates, which in turn depend on the chemistry and change with time and temperature. Accurate

analyses of deformation mechanisms and microstructural changes through the use of both SEM and TEM techniques make it possible to propose hypotheses to explain the observed effects. Since these single crystal turbine blades need to be protected against environmental and thermal attacks by using adequate coatings, attention was also paid to the interactions between the substrate and a diffusion protective coating. The microstructure modifications due to the inter-

diffusion processes were shown to be significant in the highly-alloyed single crystal superalloys recently developed for high temperature applications. This has a deleterious impact on creep strength, but the phenomenon can be reduced by modifying the alloy chemistry. All these studies therefore provide precious information useful for designing new superalloy compositions suited for specific applications in aircraft or land-based gas turbine engines ■

Acknowledgements

The authors are grateful to the French Ministry of Defense and to Snecma for partial funding of this work. The authors would like to thank C. Ramusat, D. Boivin, S. Drawin, F. Diologent and J. Benoist for their precious contributions.

References

- [1] P. CARON, T. KHAN - *Third Generation Superalloys for Single Crystal Turbine Blades*. Materials for Advanced Power Engineering 1998 - Part II, Forschungszentrum Jülich GmbH, Jülich, Germany (J. Lecomte-Beckers, F. Schubert and P.J. Ennis, eds), pp. 897-912, 1998.
- [2] P. CARON - *High γ' solvus New Generation Nickel-Based Superalloys for Single Crystal Turbine Blade Applications*. Superalloys 2000, TMS, Warrendale, PA, USA (T.M. Pollock et al., eds), pp. 737-746, 2000.
- [3] P. CARON, J.-L. RAFFESTIN, S. NAVEOS - *Superalloye monocristallin à base de nickel à haut solvus γ'* . French patent, N°98 08 693, 7 July 1998.
- [4] M. MORINAGA, N. YUKAWA, H. ADACHI and H. EZAKI - *New PHACOMP and its Application to Alloy Design*. Superalloys 1984, TMS-AIME, Warrendale, PA, USA (M. Gell et al., eds), pp. 523-532, 1984.
- [5] P. CARON, S. NAVEOS and T. KHAN - *Improvement of the Cyclic Oxidation Behaviour of Uncoated Nickel Based Single Crystal Superalloys*. Materials for Advanced Power Engineering 1994 - Part I, Kluwer Academic Publisher, Dordrecht, Holland (D. Coutouradis et al., eds), pp. 1185-1194, 1994.
- [6] D. ARGENCE, C. VERNAULT, Y. DESVALLEES and D. FOURNIER - *MC-NG: A 4th Generation Single-Crystal Superalloy for Future Aeronautical Turbine Blades and Vanes*. Superalloys 2000, TMS, Warrendale, PA, USA (T.M. Pollock et al., eds), pp. 829-837, 2000.
- [7] R.F. SINGER - *New Materials for Industrial Gas Turbines*. Mat. Sci. Techn., Vol. 3, pp. 726-732, 1987.
- [8] T. KHAN and P. CARON - *Development of a New Single Crystal Superalloy for Industrial Gas Turbine Blades*. High Temperature Materials for Power Engineering 1990, Kluwer Academic Publishers, Dordrecht, Holland (E. Bachelet et al., eds), pp. 1261-1270, 1990.
- [9] P. CARON, A. ESCALE, G. MCCOLVIN, M. BLACKER, R. WAHI and L. LELAIT - *Development of New High Strength Corrosion Resistant Single Crystal Superalloys for Industrial Gas Turbine Applications*. PARSONS 2000 - Advanced Materials for 21st Century Turbines and Power Plant, IOM Communications Ltd, London, UK (A. Strang et al., eds), pp. 847-864, 2000.
- [10] P. CARON, M. BLACKLER, A. ESCALE, G. MCCOLVIN, P. WAHI and L. LELAIT - *Nickel-Based Superalloy Having a Very High Resistance to Hot-Corrosion for Monocrystalline Blades of Industrial Turbines*. European Patent Application EP 1 211 335 A1, 30 November 2000.
- [11] P. CARON, M. BLACKLER, A. ESCALE, G. MCCOLVIN, P. WAHI, L. LELAIT - *Nickel-Based Superalloy Having a High Resistance to Hot-Corrosion for Monocrystalline Blades of Industrial Turbines*. European Patent Application EP 1 211 336 A1, 30 November 2000.
- [12] A. SATO, Y.-L. CHIU and R.C. REED - *Oxidation of Nickel-based Single-crystal Superalloys for Industrial Gas Turbine Applications*. Acta mater., Vol. 59, pp. 225-240, 2011.
- [13] F. DIOLOGENT and P. CARON - *On the Creep Behavior at 1033 K of New Generation Single-Crystal Superalloys*. Mat. Sc. Eng. A, Vol. 385, N°1-2, pp. 245-257, 2004.
- [14] P. CARON and T. KHAN - *Improvement of Creep Strength in a Nickel-Base Single-Crystal Superalloy by Heat-Treatment*. Mat. Sc. Eng., Vol. 61, pp. 173-194, 1983.
- [15] U. GLATZEL and M. FELLER-KNIEPMEIER - *Calculations of Internal Stresses in the γ/γ' Microstructure of a Nickel-Base Superalloys with High Volume Fraction of γ' Phase*. Scripta Met., Vol. 23, pp. 1839-1844, 1989.
- [16] P. CARON and F. DIOLOGENT - *Effect of the γ/γ' Lattice Mismatch on the Creep Behaviour at 760°C of New Generation Single Crystal Superalloys*. TMS 2008 Annual Meeting Supplemental Proceedings, Volume 3: General Paper Selections, TMS, Warrendale, USA, pp. 171-176, 2008.
- [17] S. MA, L. CARROLL, T.M. POLLOCK - *Development of γ phase stacking faults during high temperature creep of Ru-containing single crystal superalloys*. Acta Mater., Vol. 55, pp. 5802-5812, 2007.
- [18] R.A. HOBBS, L. ZHANG and C.M.F. RAE - *The effect of ruthenium on the intermediate to high temperature creep response of high refractory content single crystal nickel-base superalloy*. Mat. Sc. Eng. A, Vol. 489, pp. 65-76, 2008.
- [19] N. TSUNO, K. KAKEHI and C.M.F. RAE - *Effect of Ruthenium on Creep Strength of Ni-Base Single-Crystal Superalloys at 750°C and 750 MPa*. Met. Mater. Trans. A, Vol. 40A, pp. 269-272, 2009.
- [20] P. CARON, M. BENOUCHEF, A. COUJOU, J. CRESTOU and N. CLEMENT - *Creep Behaviour at 1050°C of a Re-Containing Single Crystal Superalloy*. Proceedings of International Symposium on Materials Ageing and Life management (ISOMALM 2000), Allied Publishers Ltd., Chennai, India, (B. Raj, K.Bhanu, S. Rao, T.Jayakumar, R.K.Dayal, eds) pp. 148-156, 2000.
- [21] H. HARADA, T. YAMAGATA, T. YOKOKAWA and M. YAMAZAKI - *Computer Analysis on Microstructure and Property of Nickel-Base Single Crystal Superalloys*. Proc. 5th Int. Conf. on Creep and Fracture of Engineering Materials and Structures, IOM, London, UK (B. Wilshire, R.W. Evans, eds), pp. 255-264, 1993.
- [22] J.K. ZHANG, T. MURAKAMO, Y. KOIZUMI, T. KOBAYASHI, H. HARADA and S. MAZAKI - *Interfacial Dislocation Networks Strengthening a Fourth-Generation Single-Crystal TMS-138 Superalloy*, Met. Mater. Trans. A, Vol. 33, pp. 3741-3746, 2002.

- [23] P. CARON, C. RAMUSAT and F. DIOLOGENT - *Influence of the γ' Fraction on the γ/γ' Topological Inversion during High Temperature Creep of Single Crystal Superalloys*. Superalloys 2008, TMS, Warrendale, PA, USA (R.C. Reed, K.A. Green, P. Caron, T.P. Gabb, M.G. Fahrman, E.S. Huron, S.A. Woodard, eds), pp. 159-167, 2008.
- [24] P. CARON, F. DIOLOGENT and S. DRAWIN - *Influence of Chemistry on the Tensile Yield Strength of Nickel-Based Single Crystal Superalloys*. Advanced Materials Research, Vol. 278, pp. 345-350, 2011.
- [25] F. DIOLOGENT - *Comportement en fluage et en traction de superalliages monocristallins à base de nickel*. Doctorate thesis, Université Paris XI, France, 2002.
- [26] P. VEYSSIERE and G. SAADA - *Dislocations in Solids*. Vol. 10, Elsevier Sciences (F. Nabarro and M. Duesbery, eds), 1996.
- [27] M. KARUNARATNE, P. CARTER and R.C. REED - *Interdiffusion in the Face-Centred Cubic Phase of the Ni-Re, Ni-Ta and Ni-W Systems between 900 and 1300°C*. Mater. Sci. Eng., A281, pp. 229-233, 2000.
- [28] M. PESSAH, P. CARON and T. KHAN - *Effect of μ Phase on the Mechanical Properties of a Nickel-Base Single Crystal Superalloy*. Superalloys 1992, TMS, Warrendale, PA, U.S.A. (S.D. Antolovich et al., eds), pp. 567-576, 1992.
- [29] M. PESSAH-SIMONETTI, P. CARON and T. KHAN - *Effect of a Long-Term Prior Aging on the Tensile Behaviour of a High-Performance Single Crystal Superalloy*. Journal de physique IV, Colloque C7, supplement of the Journal de Physique III, Vol. 3, pp. 347-350, 1993.
- [30] M. SIMONETTI and P. CARON - *Role and Behaviour of μ Phase During Deformation of a Nickel-Based Single Crystal Superalloy*. Mat. Sc. and Engin., A254, pp. 1-12, 1998.
- [31] W.S. WALSTON, J.C. SCHAEFFER and W.H. MURPHY - *A New Type of Microstructural Instability in Superalloys – SRZ*. Superalloys 1996, TMS, Warrendale, PA, USA (R.D. Kissinger et al., eds), pp. 9-18, 1996.
- [32] O. LAVIGNE, C. RAMUSAT, S. DRAWIN, P. CARON, D. BOIVIN and J.-L. POUCHOU - *Relationships between microstructural instabilities and mechanical behaviour in new generation nickel-based single crystal superalloys*. Superalloys 2004, TMS, Warrendale, PA, USA (K. A. Green et al., eds), pp. 667-675, 2004.
- [33] P. CARON, O. LAVIGNE, C. RAMUSAT, J. BENOIST and C. RIO - *Secondary reaction zones in coated single crystal superalloy*. Superalloys and Coatings for High Temperature Applications, TMS Annual Meeting 2005, San Francisco, CA, USA, 13-17 February 2005.
- [34] S. WALSTON, A. CETEL, R. MACKAY, K. O'HARA, D. DUHL and R. DRESHFIELD - *Joint development of a fourth generation single crystal superalloy*. Superalloys 2004, TMS, Warrendale, PA, USA (K.A. Green et al., eds), pp. 15-24, 2004.
- [35] O. LAVIGNE, J. BENOIST, P. CARON and C. RAMUSAT - *Interactions between 4th Generation Single Crystal Superalloys and an Aluminide Bond Coat*, Turbine Forum 2006: Advanced Coatings for High Temperature, Forum of Technology, Dorsten, Germany, 2006.
- [36] O. LAVIGNE, P. CARON, C. RAMUSAT and D. BOIVIN - *Influence of Cobalt on the Interaction between a Fourth Generation Single Crystal Superalloy and Its Protective Coating*. TMS Annual Meeting 2007, Orlando, FL, USA, 25 February-1 March 2007.

Acronyms

SC (Single Crystal)
 TCP (Topologically Close-Packed)
 IGT (Industrial Gas Turbine)
 APB (Antiphase Boundary)
 ESRF (European Synchrotron Research Facility)
 TEM (Transmission Electron Microscopy)
 SEM (Scanning Electron Microscopy)
 LCF (Low Cycle Fatigue)
 YS (Yield Strength)
 TBC (Thermal Barrier Coating)
 EB-PVD (Electron Beam-Physical Vapor Deposition)
 SRZ (Secondary Reaction Zone)
 EBSD (Electron Backscattered Diffraction)
 IZ (Interdiffusion Zone)
 EDS (Energy Dispersive Spectroscopy)

AUTHORS



Pierre Caron obtained his doctoral degree in Metallurgy from the University of Paris XI - Orsay in 1979 and his Habilitation Degree in 2000 from the same University. Since 1980, he is involved in various studies on superalloys and high-temperature materials, including alloy design and studies of the relationships between chemistry, microstructure and mechanical behaviour. He is currently a senior scientist and special advisor in the field of superalloys in the Department of Metallic Materials and Structures.



Odile Lavigne graduated as a physicist engineer from the Ecole Supérieure de Physique et Chimie Industrielles in Paris and obtained a PhD degree in Material Science from the University of Paris VI. She joined Onera in 1986, where she was successively involved in developing stealth systems and high temperature composite materials for space applications. For the past fifteen years, she has been working as a senior scientist on thermal barrier systems for gas turbine engines.

M.-P. Bacos, J.-M. Dorvaux,
O. Lavigne, R. Mévrel, M. Poulain,
C. Rio, M.-H. Vidal-Sétif
(Onera)

E-mail: odile.lavigne@onera.fr

Performance and Degradation Mechanisms of Thermal Barrier Coatings for Turbine Blades: a Review of Onera Activities

Thermal barrier coatings are used to protect blades and vanes in the hot sections of gas turbines. They consist of a thick porous ceramic layer deposited on a alumina forming metallic bond coat in contact with the nickel-based superalloy substrate. They are designed to prolong the components lifetimes or to increase gas temperature, and therefore efficiency. In service, the structure and composition of the various layers evolve, due to sintering of the ceramic layer, oxidation of the bond coat, and interdiffusion phenomena with the substrate. As a result, the properties of each layer are affected, as is the interfacial toughness. These evolutions, combined with applied external stresses, may lead to bond coat rumpling, crack formation at the bond coat/ceramic interface and the ceramic layer may eventually spall off. In addition to these intrinsic degradation modes, interactions with the environment can accelerate the system degradation. This paper reviews the aging phenomena occurring in thermal barrier coatings at high temperatures and describes their degradation mechanisms, with illustrations from service experience and laboratory tests

Introduction

Thermal Barrier Coatings (TBCs) were developed in the 70's to meet engine manufacturers' requests for improving engine performance and fuel efficiency (increased operating temperatures of turbine section) while reducing emissions and costs (simplified cooling air system, increased component lifetime, reduced maintenance cost, etc.). Today, TBCs are widely used to protect critical metallic parts of aircraft as well as land-based gas turbines (blades, vanes, seals and combustor chambers) from the surrounding hot gases. However TBCs in service are prone to intrinsic and extrinsic degradation phenomena [1] which may considerably restrict their potential. Both academic and industrial research is therefore underway to improve TBCs' reliability and performance [2]. This paper gives an overview of some activities carried out at Onera in this field over the past ten years in connection with the state-of-the-art. It focuses on TBC systems which are deposited on the most stressed high pressure turbine blades.

TBCs: a multilayer, multifunction system

TBCs are a multilayer system (figure 1) with each layer having a specific function and requirement. The top layer provides thermal insulation and consists of a porous ceramic coating with low thermal conductivity. It must also have a high melting point, good oxidation and corrosion resistance, a thermal expansion coefficient closer to that of the underlying metal in order to reduce thermal mismatch stresses, high toughness and strain tolerance. Yttria partially stabilized zirconia (8 wt. % YPSZ) is commonly used as it is one of the few available materials which satisfies all the requirements. It is deposited on rotating components as a layer of about 150 μm by the EB-PVD process (Electron Beam Physical Vapor Deposition). The resulting columnar microstructure shows high strain compliance and good resistance to erosion, but leads to moderately low thermal conductivity ($\sim 1.5 \text{ W}\cdot\text{m}^{-1}\cdot\text{K}^{-1}$). A temperature drop of up to 150°C can be achieved through the top layer, thus reducing accordingly the underlying metal temperature.

The ceramic insulating layer is deposited on an oxidation resistant metallic layer (the bond coat) which, during service, forms a protective oxide, mostly alumina. This thermally grown oxide scale (TGO) has to be perfectly adherent to both the top layer and the bond coat in order to insure the chemical and mechanical compatibility of the whole system. The bond coat is for example a diffusion platinum modified nickel aluminide which is obtained by deposition of a thin electroplated platinum layer followed by a vapor phase aluminizing process. The underlying substrate is the first generation nickel-based single crystal superalloy AM1¹ [3].

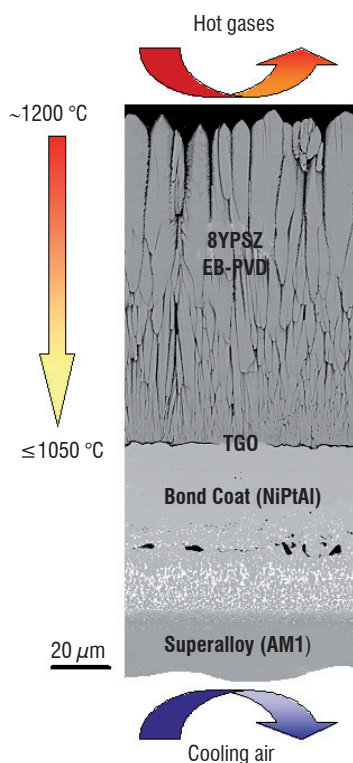


Figure 1 - Typical Thermal Barrier Coating for rotating turbine components

TBCs evolution during service

In service, TBCs are exposed to oxidizing combustion gases and the external surface temperatures can reach about 1200°C. In these conditions, temperature driven phenomena occur such as sintering of the porous ceramic layer, oxidation of the bond coat and interdiffusion with the substrate. Consequently, the structure and composition of the various layers evolve and their properties are affected, as is the interfacial toughness. It will be shown that these evolutions combined with the applied thermal and mechanical stresses may cause the ceramic layer to spall off in the end.

Aging of the ceramic top layer: sintering and phase transformation

Sintering of the top layer occurs rapidly from the first aging times at 1100°C, initially over short length scales and then more slowly over longer length scales. At first, the feather-like edges of the columns are rounded off by surface diffusion and progressively transform into lines of disconnected closed pores. Random bridge formation

between the columns follows (figure 2). These sintering effects are accelerated at higher temperatures. A consequence of these widely documented phenomena [4] is a drop in the top coat strain compliance and thermal insulation capability as illustrated in figure 2 (from [5]). A higher thermal conductivity of the ceramics increases the surface temperature of the metal with deleterious effects on the component life duration. Furthermore an increased Young's modulus of the top coat leads to higher energy stored in the system and can induce anticipated spallation of the TBC (see § Energetic approach of TBC failure, box 3).

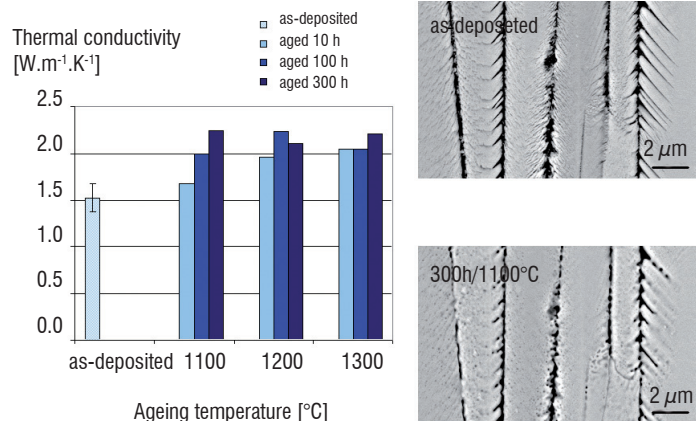


Figure 2 - Effect of sintering on 8YPSZ EB-PVD ceramic top coat microstructure and thermal conductivity (measured at room temperature in air atmosphere with a CO₂ - laser flash technique)

When inter-columnar sintering is sufficiently large, in-plane tensile stresses appear which cause cracks to initiate and grow, giving a mud-like pattern upon cooling [5,6]. These cracks going through the top coat thickness facilitate CMAS infiltration (see § TBC interactions with environment).

Moreover, in the case of YPSZ coatings, crystallographic phase transformations are well known to occur during aging from 1200°C [7]. The initial metastable tetragonal t' phase transforms at high temperature into a mixture of yttria-rich cubic phase and yttria-poor tetragonal phase t which in turn may transform into a monoclinic phase on cooling. As a consequence, cracks due to transformation volume mismatch can appear and the thermal conductivity of the coating may be modified. Nevertheless, Onera work showed [5] from phase fraction estimation by X-ray diffraction and thermal conductivity data as a function of yttria concentration [8] that the phase transformation contributes less than 10% to the evolution of the thermal conductivity of the top coat. This effect is thus of second order compared to the sintering effect.

Bond coat oxidation

In service, the initially β -NiPtAl single phased bond coat loses part of its aluminum content by formation of a highly protective alumina scale which slowly grows according to typical α -alumina growth kinetics, eventually following a transient oxidation period. Nevertheless, some factors can affect the properties of this oxide scale and possibly weaken the resistance of the bond coat / top coat interface, thus contributing to the degradation of the thermal barrier system.

¹ AM1 composition [wt. %] : Ni base, 6.5 Co, 7.8 Cr, 2 Mo, 5.7 W, 5.2 Al, 1.1 Ti, 7.9 Ta

It has been reported that sulfur, present as an impurity in the alloy, dramatically decreases the adherence of the oxide scale [9,10]. If the oxide bonding to the metal is low, growth and/or thermal stresses can induce the spallation of the protective oxide layer or the formation of interfacial voids that is very deleterious for thermal barrier coating systems as shown below. This phenomenon, existing for many alumina-forming alloys, is known as «the sulfur effect».

On β -NiAl, it is widely admitted that the alumina scale grows principally by outward diffusion of aluminum at intermediate temperatures (i.e. θ - Al_2O_3 at $\sim 900^\circ\text{C}$) or by a combination of inward diffusion of oxygen and outward diffusion of aluminum at higher temperatures (i.e. α - Al_2O_3 at $\sim 1100^\circ\text{C}$). Formation of interfacial cavities at the metal/oxide interface was thus observed after the oxidation of NiAl at 900°C . These cavities result from the condensation of metallic vacancies injected in the alloy by the growth mechanism of the oxide or from the nonreciprocal diffusion of the non-oxidized element of the alloy (Kirkendall effect). Studies conducted at Onera [11,12] on NiAl single crystals showed that during the formation of the transient alumina, sulfur segregation at the metal/oxide interface occurs when vacancies are injected during the Al_2O_3 growth. Sulfur segregation is favored at the nickel-rich metallic surface of the interfacial cavities and occurs as long as their surface remains free of oxide, in agreement with Haynes [13] who considered the stabilization of voids by sulfur in a model of cavity growth for a high sulfur content NiAl coating. Once segregated, sulfur remains at the interface at an even higher temperature when the transient cavities are filled by inward anionic growth of the mature α -alumina. Segregated sulfur, trapped at the interface after the θ to α transformation of the scale, weakens the oxide adherence and favors the formation of interfacial voids and the decohesion of the oxide layer under growth and/or thermal stresses (figure 3).

Efforts to limit the detrimental effect of sulfur have focused on different approaches such as desulfurizing the superalloy [10], using low sulfur content superalloys, doping with reactive elements (Y, ...) [13,14] or adding platinum [13]. Indeed platinum was found to reduce sulfur segregation to the free surface [15] and even to eliminate sulfur at the interface [16].

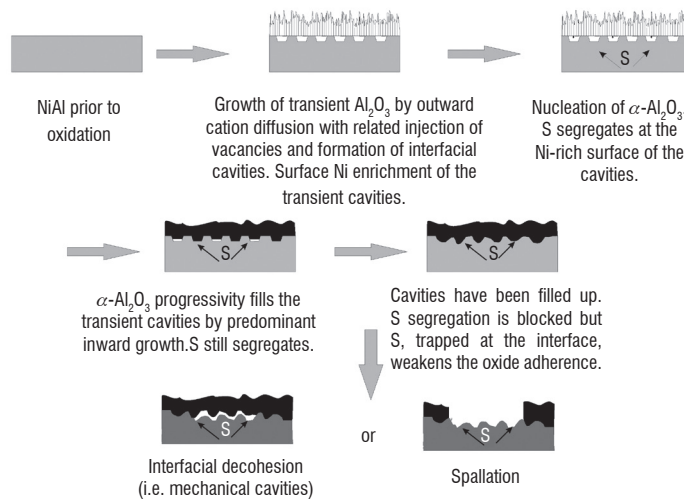


Figure 3 - Model of the sulfur effect at the interface between an aluminide substrate and thermally-grown oxide films (from [12])

The effect of platinum addition on the initial stages of oxidation of cast nickel aluminide intermetallic alloys of low and high sulfur content has been studied at Onera [15]. At 900°C , where a scale of transient alumina θ - Al_2O_3 grows by outward cationic transport, the beneficial effect of platinum is both the size reduction of the interfacial transient cavities and an increase of the transient alumina oxide scale occurrence. This was attributed to an enhancement of the main interdiffusion coefficient of aluminum in the intermetallic by platinum [17]. Therefore adding platinum lowers the oxide-free surface and maintains an Al-rich phase near the surface. According to the Rivoaland model, these two consequences allow for a reduction of the sulfur segregation and consequently an increase in the oxide adhesion.

The transition from θ -controlled to α -controlled kinetics is longer in the presence of platinum in the alloy. This is related to the fact that the growth rate of the transient oxide is still increased (by a factor of 5) by the presence of platinum after initiation of the transition, which leads to the thickening of the oxide scale before formation of a continuous slow-growing α - Al_2O_3 layer. The prolonged transition from

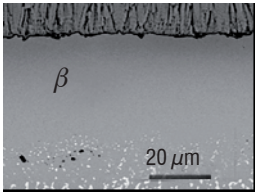
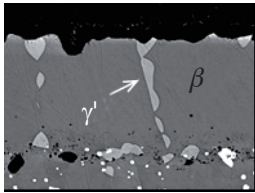
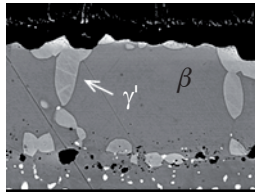
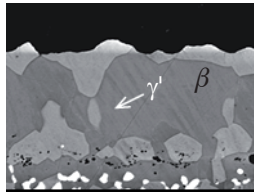
as fabricated	50 cycles at 1100°C		100 cycles at 1100°C		250 cycles at 1100°C	
						
β -NiAl (B2) s: 1.00	β -NiAl (L1 ₀) s: 0.95	γ' -Ni ₃ Al (L1 ₂) s: 0.05	β -NiAl (L1 ₀) s: 0.90	γ' -Ni ₃ Al (L1 ₂) s: 0.10	β -NiAl (L1 ₀) s: 0.75	γ' -Ni ₃ Al (L1 ₂) s: 0.25
B2 : Ni 44, Al 40, Pt 10, Cr 3, Co 3, Ti < 1, Ta < 1 L1 ₀ : Ni 50, Al 30, Pt 8, Cr 6, Co 4, Ti < 1, Ta 1 L1 ₂ : Ni 63, Al 16, Pt 6, Cr 2, Co 5, Ti 1, Ta 6						

Figure 4 - Microstructural evolution of the bond coat as a function of the number of 1h-cycles at 1100°C : different phases surface fraction (s) and chemical composition (at.%)

θ -controlled to α -controlled kinetics observed in the presence of platinum is proposed to favor the stress relaxation in the alumina scale.

Bond coat / superalloy interdiffusion

Besides the oxidation of the bond coat, thermal cycling of the TBC system promotes interdiffusion of various elements between the platinum modified aluminate layer and the underlying superalloy substrate (AM1 in the present case). As a result, the aluminum content of the bond coat becomes lower and lower, so that the initially β -NiPtAl single phase transforms into a γ' -Ni₃Al phase (figure 4). In addition to this inward diffusion of aluminum and platinum, outward diffusion of some elements of the substrate such as cobalt, chromium or titanium also contributes to phase transformation within the bond coat. It should be noted that the chemical composition of these two inequilibrium phases remains constant whereas their volume fraction evolves during thermal cycling: as the initial Al-rich phase is reduced, the aged Al-poor phase extends. Moreover, next to the γ' -Ni₃Al phase (L1₂) a lamellar structure may be observed at room temperature, related to the reverse transformation of the β -NiAl (B2) phase into the martensitic NiAl phase (L1₀) which takes place during the cooling and heating stage of thermal cycling. The occurrence of martensite mainly depends on the Al and Pt content of the bond coat as well as on the nature and content of the diffused elements from the substrate. The phase transformations within the bond coat will have consequences on its mechanical behavior [18].

Intrinsic degradation mechanisms

Stress field and rumpling

As mentioned above, an interfacial stress field develops in thermal barrier systems during thermal cycling, resulting from oxidation growth stresses and thermal stresses due to thermal expansion mismatch between the top coat, the TGO and the bond coat. Piezospectroscopy measurements performed at Onera clearly demonstrate that high compressive in-plane stresses (about 3 GPa) remain at room temperature within the TGO (figure 5, from [19,20]). At the same time, out-of-plane stresses exist because the interface is not flat. They cause the bond coat/TGO interface to deform so that a slight in-plane stress relaxation is observed, due to progressive interfacial roughening, also called rumpling [21]. But resulting out-of-plane stresses also initiate local damage. As a result, geometrical incompatibilities in concave areas combined with voids formation related to oxidation

induce crack interfacial propagation, thus leading to sudden top coat spallation (figure 6). We note that the crack pathway is mixed (going along the TGO/top coat interface or through the TGO) as attested by fracture surface observations.

Large stresses produced in the bond coat by phase transformation, such as the martensitic transformation, may also effectively promote undulation growth. Rumpling is obviously governed by the creep resistance of the bond coat and the mechanical behavior of the highly compressed TGO. The mechanical behavior of the bond coat plays a key role in the relaxation of stresses induced by oxidation and martensitic transformation. In particular, in order to describe the interface progressive roughening, it is essential to know the elastic viscoplastic law of the bond coat in the as-elaborated state and its evolution during thermal cycling linked to the arising phase transformations. An original technique - high temperature instrumented microindentation, up to 1000°C - has been developed at Onera (see box 1) to extract information on the mechanical behavior of the bond coat [22]. The mechanical properties of the different phases (hardness related to yield stress, elastic modulus, creep law) are investigated by means of indentation tests, which enable local measurement within individual phases. For instance, the indentation creep behavior is determined by applying a load of about 0.5 N, and by holding it during several thousand seconds (up to about 1 hour) at different temperatures. An inverse problem analysis is used (analytical approaches and finite element method simulation) to identify the variables of the constitutive law of the materials tested.

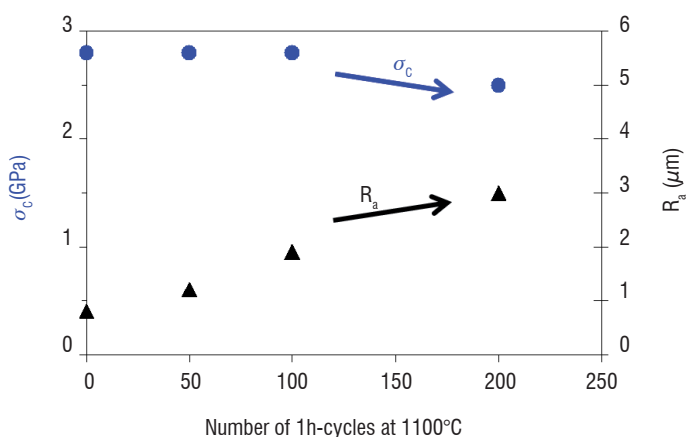


Figure 5 - Evolution of residual compressive in-plane stresses (σ_c) in the TGO and arithmetical mean roughness (R_a) of the bond coat/TGO interface as a function of the number of 1h-cycles at 1100°C

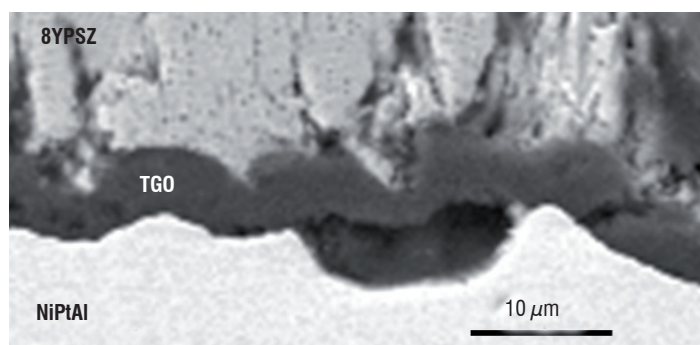
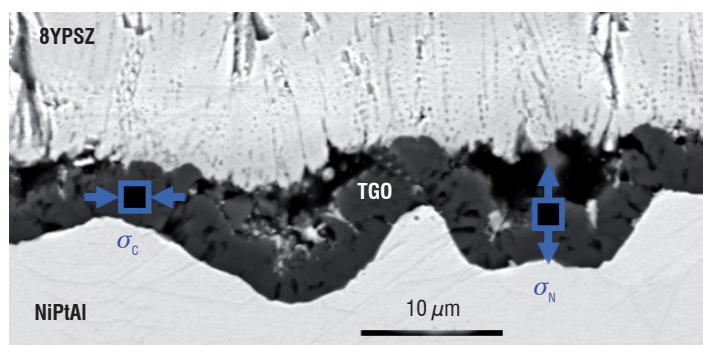


Figure 6 - Interfacial geometrical incompatibilities generated by out-of plane stresses (σ_N) and voids due to oxidation

Box 1 - High temperature instrumented microindentation system

(B. Passilly, Onera – Department of Composite Materials and Structures)

General description - Principle

The vacuum chamber contains two translation stages (horizontal X and Y axis), on which the load sensor, the sample holder, the sample, and a furnace are fixed. This X-Y stage enables the horizontal sample to move from under a microscope to under the indenter. The indenter and the sample are located inside small furnaces which are separately resistively heated up to the test temperature (up to 1000°C). The displacements are measured using a differential capacitive technology.

Time, load and indenter displacement are recorded simultaneously during the loading, holding and unloading phases.

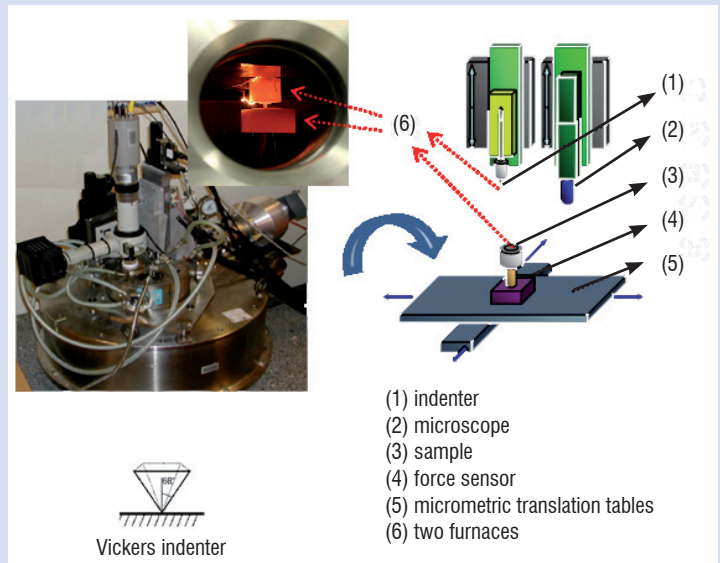


Figure B1-01 - Microindentation equipment

Data analysis

Adapted from the approach by Sargent and Ashby - *Indentation creep*. Mat. Sci. Technol., 8 (1992) 594-601

Norton law
$$\dot{\epsilon} = \dot{\epsilon}_0 \left(\frac{\sigma}{\sigma_0} \right)^n \cdot \exp\left(-\frac{Q}{RT} \right)$$

Penetration depth
$$h_{calc}(t) = \left[h_0^{2n} + B(T) \cdot n \cdot \exp\left(-\frac{Q}{RT} \right) \right]^{\frac{1}{2n}}$$

- fitting experimental curves $h_{exp}(t)$ for different $T \rightarrow n, B(T)$
- variation in $B(T) \rightarrow Q$

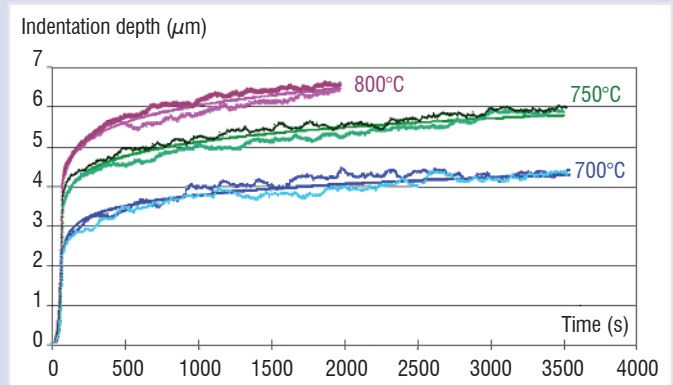
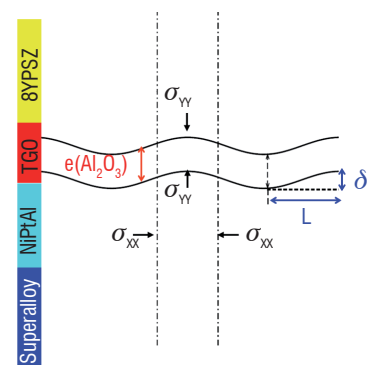


Figure B1-02 - Example: indentation creep (0.5 N load) of NiPtAl bond coat

Interface evolution modeling

In order to better understand the TBC degradation mechanisms, a semi-analytical model describing the interface evolution during thermal cycling is used at Onera. This model, which is based on Hutchinson studies [23], considers the TBC system as a macroscopic multilayered structure, in which complex behavior laws are used for each layer. It has to be specified that the creep law of the bond coat injected into the model is the one determined by high temperature instrumented microindentation and that the interfacial roughness is drawn as a sinusoidal undulation (figure 7). This computation is designed to quantify the interface roughening, related to the in-plane and out-of-plane stress development with the aim of specifying a damage criterion. The model is being validated by comparing its predictions with experimental observation of rumpling. Onera's current work focuses on getting essential data in order to build a physically-based model, able to assess thermal barrier spalling on turbine blades.



Input data of the computation:
Oxidation kinetic, martensitic transformation, hardening, creep laws, thermal expansion coefficients, initial undulation geometry

Output data of the computation:
In-plane and out-of-plane stresses (σ_{xx} and σ_{yy})
Undulation amplification (δ)

Figure 7 - Semi-analytical modeling of the TBC multilayered structure

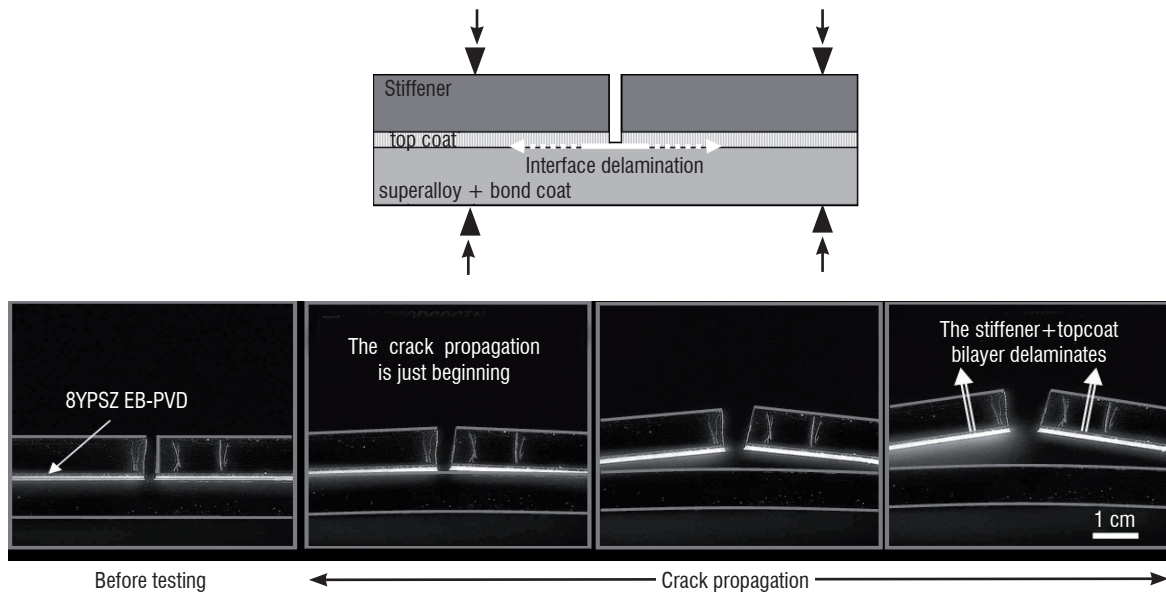


Figure 8 - Four-point bending test

Energetic approach of TBC failure: Lifetime prediction

The sudden failure of TBC systems is due to rapid propagation of interfacial cracks, initiated by complex phenomena linked to the oxidation mechanisms and to the evolution of the interfacial area stress field and intrinsic interface adhesion properties. An energetic model [24,25] was studied at Onera [20] with the aim of proposing a possible guide for predicting TBC system lifetime, which is a goal of prime importance. An energy balance is used for the lifetime assessment, by comparing evolution of the interfacial fracture toughness with the evolution of the stored strain energy in the ceramic layers (top coat and TGO).

To get a quantitative assessment of TBC system adhesion and to better understand how the interfacial strength is damaged by microstructural degradations during thermal cycling, an original approach

was developed based on the design and implementation of a specific test (a modified 4-point bending test – figure 8 [19]).

The whole set of experimental data, particularly the adhesion energy (from the 4-point bending test) and the residual stress assessments (from piezospectroscopy analysis – box 2), allows for a comparison of the energy needed to fracture the interface and the available energy which can induce the interfacial crack propagation (box 3). From this mechanical modeling, a spallation criterion has been defined that gives an estimate of the TBC system lifetime. The predicted lifetime (as the adhesion energy and the available energy intersect) has proved to be consistent with experiments (observed TBC spontaneous spallation). This energetic approach can be used to build a physically-based model, which can assess thermal barrier spallation on turbine blades. This model, developed at Onera, was very recently discussed in the review paper from Hutchinson [26].

Box 2 - Piezospectroscopy analysis

(F. Lepoutre, Onera – Department of Composite Materials and Structures)

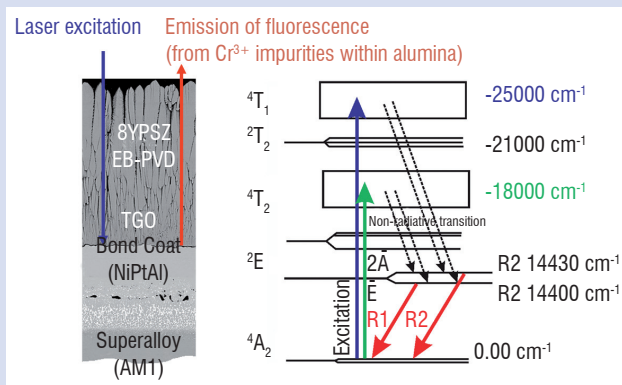


Figure B2-01- Principle

Principle

Piezospectroscopy is a non-contact technique which allows for measurement of the in-plane stresses within the TGO. It uses the spectroscopic displacement of fluorescence lines (R1, R2) emitted after the excitation by a laser of Cr³⁺ impurities in alumina when the stresses relax [27]. The principle of this measurement is similar to the one used in the diamond anvil pressure cell.

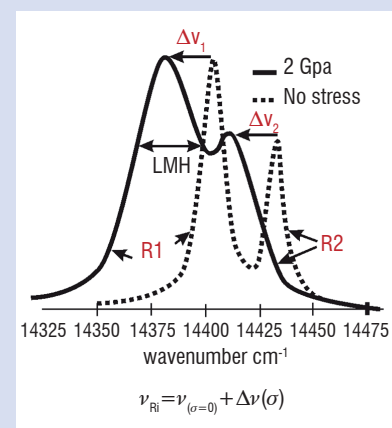


Figure B2-02- Spectroscopic displacement of fluorescence lines

Box 3 - Energetic approach of TBC failure

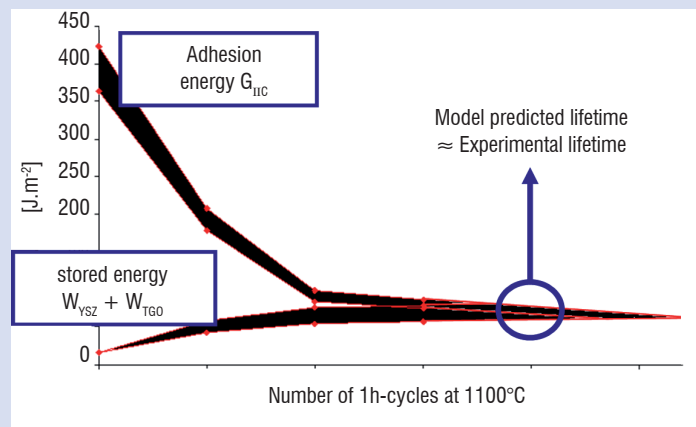


Figure B3-01 - Evolution of adhesion energy (G_{IIc}) and available energy (W) for interfacial crack propagation during thermal cycling at 1100°C

Calculation of the adhesion energy

During the spontaneous buckling and growth of TBC scales, the interfacial loading rapidly tends to pure mode II. The pure mode II values of adhesion energy (G_{IIc} , $\psi = 90^\circ$) can be estimated from our 4-point adhesion values (G_c , $\psi = 40^\circ$) using the empirical relation proposed by [28].

ψ = mode mixity angle = parameter measuring the ratio between mode II ($\psi = 90^\circ$) and mode I ($\psi = 0^\circ$) loadings during the crack propagation.

Influence of experimental data on TBC lifetime prediction

It is to be noted that an experimental uncertainty is attached to the interfacial fracture toughness evolution, and that some parameters used for the elastic stored energy calculation also induce some inaccuracy. In particular, the top coat Young's modulus, which increases during thermal cycling, due to sintering phenomena and environmental interactions (CMAS infiltration) must be precisely quantified in order to refine the lifetime prediction.

Calculation of the driving energy for TBC failure

For each ceramic layer ($i = \text{YPSZ or TGO}$)

$$W_{stored}(i) = (1 - \nu_i^2) \sigma_i^2 e_i / 2 E_i$$

e_i = thickness

E_i = in-plane Young's modulus

ν_i = Poisson's ratio

σ_i = in-plane stresses (assumed to be biaxial and isotropic in the plane of the layer)

TBC interactions with environment

As already mentioned, the surface of TBCs on turbine blades and vanes located in the hottest sections of gas turbine engines can reach temperatures up to 1200°C in operating conditions. At such temperatures, thermal barrier coatings are susceptible to corrosion by molten calcium-magnesium-alumino-silicates (CMAS) resulting from the ingestion of siliceous mineral debris (dust, sand, ash) contained in the hot gases arriving in the turbine. In the literature, few studies [29,30] can be found investigating, on ex-service blades or vanes, the damage resulting from CMAS attack on the TBC, especially when the top coat is elaborated by EB-PVD [31]. The first studies conducted at Onera in this field have thus consisted of microstructural characterizations of the interaction between CMAS and EB-PVD TBC observed on high pressure turbine blades removed from service. The main results of this study are reported below.

The initially white TBC surface is covered after service by a brownish deposit strongly adhering to the blade surface. This deposit is present mainly on the pressure side and leading edge whereas a large part of the suction side surface is free from deposits (figure 9).



Figure 9 – After service high pressure turbine blade: pressure side covered by CMAS brownish deposit

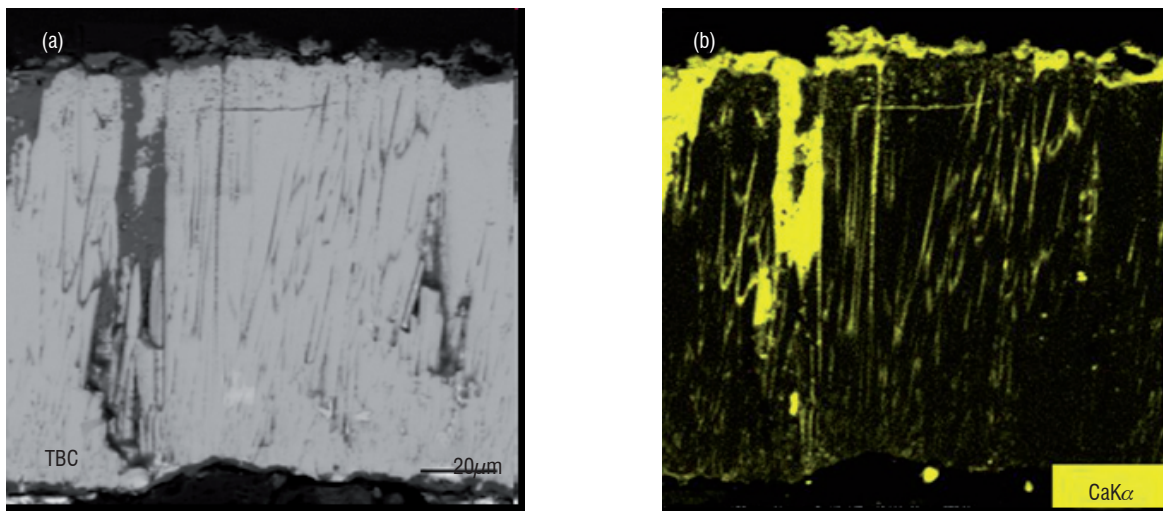


Figure 10 - TBC top coat infiltrated by CMAS (SEM image (a) and corresponding elemental map of Ca ($K\alpha$ line), (b))

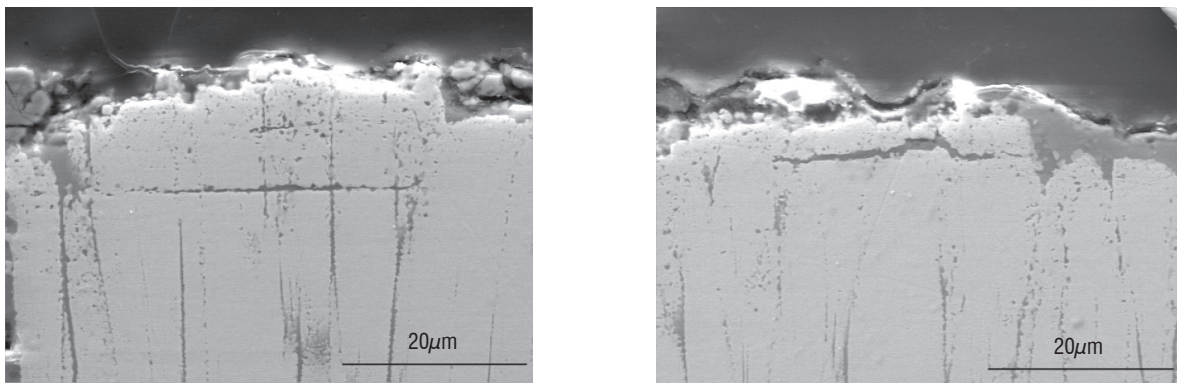


Figure 11 - Delamination cracks in the TBC (pressure side)

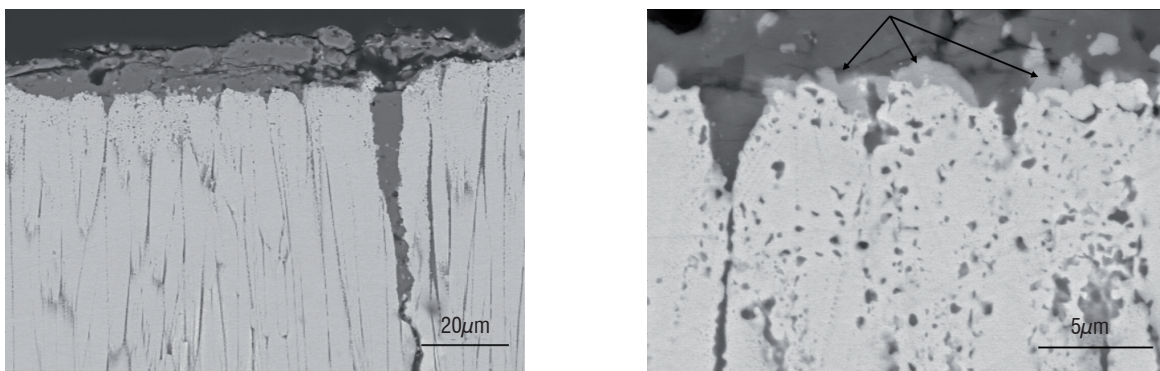


Figure 12 - Degradation of the column tips and formation of a new phase (arrows)

Energy dispersive spectroscopy (EDS) performed on the blade surface reveals the presence of oxides of Ca, Mg, Al, and Si, indicative of CMAS as well as metallic elements Ti, Fe, Ni, certainly originating from debris of metallic turbine components. The deposition of such mineral dust on the blades appears to be detrimental as soon as the TBC surface temperature is high enough to cause such deposits to melt. As a result, significant TBC damage is observed in the hottest zones of the pressure side.

Firstly, when the CMAS becomes molten, its low viscosity enables its infiltration into the TBC intercolumnar gaps, porosity and cracks, down to the TGO layer (figure 10). Such observations have already

been reported in the literature and a failure mechanism has been proposed [30,32]: upon cooling, the melt freezes and the infiltrated TBC becomes rigid, losing its strain tolerance. Delamination cracks can thus develop in the coating leading to progressive TBC spallation during in-service thermal cycling. An illustration of this mechanism is presented in figure 11.

Secondly, a chemical interaction takes place between the molten CMAS and the 8YPSZ top coat ceramic, degrading the column tips and the porous morphology, especially in the upper part of the coating (figure 12). The initially fine-scale intracolumnar porosity and the feather-like porosity are replaced by larger pores filled with CMAS.

Moreover, a new phase is observed at the interface between the CMAS and the TBC (figure 12, right image).

EDS semi-quantitative analysis performed on the CMAS layer on the TBC surface indicates (table 1) that it is mainly constituted of CaO, MgO, Al₂O₃, SiO₂ but also contains a large amount of iron oxide Fe₂O₃. The presence of iron oxide is important to note as it allows, via the formation of low temperature eutectics, for the silicate mixtures present at the TBC surface to have melting points lower than or close to 1200° C, which is the temperature generally supposed for the TBC surface.

	CaO	MgO	Al ₂ O ₃	SiO ₂	TiO ₂	Fe ₂ O ₃	ZrO ₂	Y ₂ O ₃
Composition (wt. %)	25.7	7.5	13.9	34.5	4.5	10.8	2.3	0.7

Table 1 - CMAS chemical composition as observed on ex-service blade

The CMAS also contains minor amounts of zirconium and yttrium suggesting dissolution of 8YPSZ into the molten CMAS. This result, which is of major importance as it identifies the mechanism by which the CMAS acts, has already been observed by Borom [30] and Braue [31] during investigation of ex-service turbine components and by Stott [33] and Krämer [34] during laboratory experiments using synthetic CMAS.

EDS semi-quantitative analysis performed on the interfacial new phase reveals that it is mainly constituted of (Ca, Ti, Fe, Zr) oxide (table 2). The presence of zirconium suggests that this phase results from the interaction between molten CMAS and dissolved zirconia. The formation of a new phase in the interfacial reaction zone has been rarely observed. Only Braue [31] observed and identified a Ca-Zr-Fe silicate on an ex-service first stage high pressure turbine blade. Stott [33] and later Krämer [34] postulate that YPSZ dissolves into the CMAS until the zirconia solubility limit is attained. The excess zirconia is then re-precipitated as a fine grain structure depleted in yttria. It seems that, in our case, the excess zirconia is re-precipitated as a new phase containing Zr and some of CMAS chemical elements.

	Al	Si	Ca	Ti	Fe	Zr	y	Mg	O
Composition (at.%)	0.9	0.6	6.1	12.5	3.2	10.8	2.1	0.3	63.5

Table 2 - New interfacial phase chemical composition

As a conclusion, ex-service blade microstructural characterization has shown that CMAS corrosion occurs more particularly in the

hottest zones of the blade pressure side. Two types of interaction between CMAS and TBC are observed: CMAS infiltration into the TBC microstructure (intercolumnar gaps, pores, cracks) and chemical attack of the TBC according to a dissolution-re-precipitation mechanism. Both interactions lead to the progressive degradation of the TBC top coat, via delamination cracks due to TBC rigidification and loss of column integrity and porous morphology. In order to measure the detrimental effect of CMAS attack, the energetic approach of TBC failure (box 3) can be used: the effect of CMAS infiltration is described as an increase in the top coat Young's modulus. With the hypothesis of a Young's modulus value of 200 GPa for the CMAS infiltrated TBC [32], it can be seen that the predicted life time is clearly reduced (figure 13).

This degradation mode is a growing concern, as in the future, gas temperature in the engine and therefore the temperature at the surface of thermal barrier should increase.

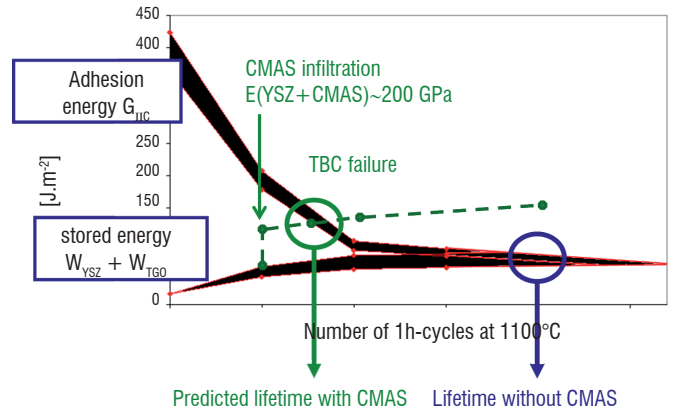


Figure 13 – Predicted effect of CMAS attack on TBC lifetime

Conclusion: towards TBCs with extended working lives

From the above short overview of the aging and degradation mechanisms of a present «standard» TBC system (AM1 single crystal superalloy / NiPtAl bond coat / 8YPSZ EB-PVD top coat), it is clear that advanced thermal barrier systems operating at higher temperatures and/or for very long durations (commercial aircraft applications for example) need further developments. These should involve materials, mechanical and modeling aspects. Examples of possible improvement fields are low thermal conductivity and high stability ceramic top coats, environmental protection, bond coats with optimized TGO formation and controlled interdiffusion, as well as better understanding of failure mechanisms and prediction of lifetime. Some of these points are detailed in a separate paper [35] ■

Acknowledgements

The French Ministry of Defense and Snecma are gratefully acknowledged for financial support and provision of coupons and ex-service blades.

References

- [1] A.G. EVANS, D.R. MUMM, J.W. HUTCHINSON, G.H. MEIER, F.S. PETTIT – *Mechanisms controlling the durability of thermal barrier coatings*. Progr. Mater. Sci., 46 (2001) 505-553
- [2] S. BOSE - *High temperature coatings*. Elsevier (2007)
- [3] P. CARON, O. LAVIGNE - *Recent Studies at Onera on Superalloys for Single Crystal Turbine Blades*. Aerospace Lab issue 3 November 2011
- [4] V. LUGHI, V.K. TOLPYGO, D.R. CLARKE - *Microstructural aspects of the sintering of thermal barrier coatings*. Mater. Sci. Eng. A, 368 (2004) 212-221
- [5] A. AZZOPARDI, R. MÉVREL, B. SAINT-RAMOND, E. OLSON, K. STILLER - *Influence of ageing on structure and thermal conductivity of Y-PSZ and Y-FSZ EB-PVD coatings*. Surf. Coat. Technol., 177-178 (2004) 131-139
- [6] R.G. HUTCHINSON, N.A. FLECK, A.C.F. COCKS – *A sintering model for thermal barrier coatings*. Acta Mater., 54 (2006) 1297-1306
- [7] U. SCHULZ - *Phase transformation in EB-PVD yttria partially stabilized zirconia thermal barrier coatings during annealing*. J. Am. Ceram. Soc., 83 (2000) 904-910
- [8] J.F. BISSON, D. FOURNIER, M. POULAIN, O. LAVIGNE, R. MÉVREL - *Thermal conductivity of yttria-zirconia single crystals determined with spatially resolved infrared thermography*. J. Am. Ceram. Soc., 71 (2000) 255-260
- [9] J.G. SMEGGIL, A.W. FUNKENBUSH, N.S. BORNSTEIN - *A relationship between indigenous impurity elements and protective oxide scale adherence characteristics*. Metall. Mater. Trans. A, 7 (1986) 923-932
- [10] E. J. L. SMIALEK - *Effect of sulfur removal on Al₂O₃ scale adhesion*. Metal. Trans. A, 22 (1991) 739- 752
- [11] L. RIVOALAND, V. MAURICE , P. JOSSO, M.-P. BACOS, P. MARCUS- *The effect of sulfur segregation on the adherence of the thermally grown oxide on NiAl. I: The oxidation behavior at 900°C of standard, desulfurized or sulfur-doped NiAl(001) single-crystal*. Oxidation Metals, 60 (2003) 137-157
- [12] L. RIVOALAND, V. MAURICE , P. JOSSO, M.-P. BACOS, P. MARCUS - *The effect of sulfur segregation on the adherence of the thermally grown oxide on NiAl. II: Sulfur segregation on the metallic surface of NiAl(001) single-crystals and at NiAl(001)/Al₂O₃ interfaces*. Oxidation Metals, 60 (2003) 159-178
- [13] A. HAYNES, B. A. PINT, K. L. MORE, Y. ZHANG, I. G. WRIGHT - *Influence of Sulfur, Platinum, and Hafnium on the Oxidation Behavior of CVD NiAl Bond Coatings*. Oxidation Metals, 58 (2002) 513-544
- [14] B. A. PINT - *Experimental observations in support of the dynamic-segregation theory to explain the reactive-element effect*. Oxidation Metals, 45 (1996) 1-37
- [15] Y. CADORET, D. MONCEAU, M.-P. BACOS, P. JOSSO, V. MAURICE, P. MARCUS - *Effect of platinum on the growth rate of the oxide scale formed on cast nickel aluminide intermetallic alloys*. Oxidation Metals, 64 (2005) 185-205
- [16] P. Y. HOU, K. F. MCCARTY - *Surface and interface segregation in β -NiAl with and without Pt addition*. Scripta Mat., 54 (2006) 937-941
- [17] R. BOUCHET, R. MÉVREL - *Influence of platinum and palladium on diffusion in β -NiAl phase*. Defect Diffusion Forum, 237-240 (2005) 238-243
- [18] I.T. SPITZBERG, D.R. MUMM, A.G. EVANS - *On the failure mechanisms of thermal barrier coatings with diffusion aluminide bond coatings*. Mat. Sci. Eng., A 394 (2005) 176-191
- [19] P.-Y. THÉRY, M. POULAIN, M. DUPEUX, M. BRACCINI - *Adhesion energy of a YPSZ EB-PVD layer in two thermal barrier coating systems*. Surf. Coat. Technol., 202 (2007) 648-652
- [20] P.-Y. THÉRY, M. POULAIN, M. DUPEUX, M. BRACCINI - *Spallation of two thermal barrier coating systems: experimental study of adhesion and energetic approach to lifetime during cyclic oxidation*. J. Mater. Sci., 44 (2009) 1726-1733
- [21] V.K. TOLPYGO, D.R. CLARKE - *Temperature and cycle-time dependence of rumpling in platinum-modified aluminide coatings*. Scripta Mat., 57 (2007) 563-566
- [22] A. VILLEMIANE, B. PASSILLY, P. KANOUTÉ, R. KOUITAT, R. MÉVREL - *Determination of mechanical properties of aluminide bondcoat materials by high temperature instrumented microindentation*. Int. Conf. Metallurgical Coatings Thin Films, San Diego, USA (2008)
- [23] D.S. BALINT, J.W. HUTCHINSON - *An analytical model of rumpling in thermal barrier coatings*. J. Mechanics Phys. Solids, 53 (2005) 949-973
- [24] K. VAIDYANATHAN, E.H. JORDAN, M. GELL - *Surface geometry and strain energy effects in the failure of a (Ni,Pt)Al/EB-PVD thermal barrier coating*. Acta Mater., 52 (2004) 1107-1115
- [25] X. ZHAO, X. WANG, P. XIAO - *Sintering and failure behaviour of EB-PVD thermal barrier coating after isothermal treatment*. Surf. Coat. Technol., 200 (2006) 5946-5955
- [26] R.G. HUTCHINSON, J.W. HUTCHINSON – *Lifetime assessment for thermal barrier coatings: tests for measuring mixed mode delamination toughness*. J. Am. Ceram. Soc., 94 (2011) S85-S95
- [27] D.R. CLARKE, R.J. CHRISTENSEN, V. TOLPYGO - *The evolution of oxidation stresses in zirconia thermal barrier coated superalloy leading to spalling failure*. Surf. Coat. Technol., 94-95 (1997) 89-93
- [28] J.W. HUTCHINSON, Z. SUO - *Mixed mode cracking in layered materials*. Adv. Appl. Mech., 29 (1992) 63-191
- [29] J. L. SMIALEK, F.A. ARCHER, R.G. GARLICK - *The chemistry of Saudi Arabian sand: A deposition problem on helicopter turbine a airfoils*. 3rd Intern. SAMPE Metals Conf. (1992) pp. M63-M77
- [30] M.P. BOROM, C.A. JOHNSON, L.A. PELUSO - *Role of environmental deposits and operating surface temperature in spallation of air plasma sprayed thermal barrier coatings*. Surf. Coat. Technol., 86-87 (1996) 116-126
- [31] W. BRAUE - *Environmental stability of the YSZ layer and the YSZ/TGO interface of an in-service EB-PVD coated high-pressure turbine blade*. J. Mater. Sci., 44 (2009) 1664-1675
- [32] C. MERCER, S. FAULHABER, A.G. EVANS, R. DAROLIA - *A delamination mechanism for thermal barrier coatings subject to calcium-magnesium-alumino-silicate (CMAS) infiltration*. Acta Mater., 53 (2005) 1029-1039
- [33] F.H. STOTT, D.J. DE WET, R. TAYLOR - *Degradation of thermal barrier coatings at very high temperatures*. MRS Bull. 19 (1994) 46-49

[34] S. KRÄMER, J. YANG, C.A. JOHNSON, C.G. LEVI - *Thermochemical Interaction of thermal barrier coatings with molten CaO-MgO-Al₂O₃-SiO₂ (CMAS) deposits*. J. Am. Ceram. Soc., 89 (2006) 3167-3175

[35] M.-P. BACOS, J.-M. DORVAUX, S. LANDAIS, O. LAVIGNE, R. MÉVREL, M. POULAIN, C. RIO, M.-H. VIDAL-SÉTIF - *10 Years-Activities at Onera on Advanced Thermal Barrier Coatings*. Aerospace Lab issue 3 November 2011

Acronyms

TBC (Thermal Barrier Coating)

YPSZ (Yttria Partially Stabilized Zirconia)

EB-PVD (Electron Beam-Physical Vapor Deposition)

TGO (Thermally Grown Oxide)

CMAS (Calcium-Magnesium-Alumino-Silicates)

EDS (Energy Dispersive Spectroscopy)

AUTHORS



Marie-Pierre Bacos graduated from the Ecole Nationale Supérieure de Chimie in Paris (1981) and received a PhD degree in Applied Chemistry from University Paris VI (1983). She joined Onera in 1983 where she has been involved in oxidation and corrosion mechanisms and in the development of innovating coatings and brazing technologies. She is the Head of the Materials and Architecture Research Unit at Onera Châtillon.



Martine Poulain has been working at Onera since 1979, initially in the «Materials» department. She was involved in the development of protective coatings and she received her PhD degree from the University of Paris XI in 1999, on the topic of thermal insulation capabilities of TBCs. Her present research themes in the Metallic Materials and Structure department focus on the damage and life modeling of TBCs, and the coating by design approach.



Dr. Jean-Marc Dorvaux joined the Material Department of Onera as a research scientist in thermal physics. His activities cover both the experimental development of testing and the modelling of heat transfer in materials in harsh environments.



Catherine Rio graduated from the Institut Universitaire de Technologie of Paris XI. She has been working at Onera since 1982 as a specialist in physical measurements, metallography and microstructure characterization on a wide range of high temperature materials and coatings.



Odile Lavigne graduated as a physicist engineer from the Ecole Supérieure de Physique et Chimie Industrielles in Paris and obtained a PhD degree in Material Science from the University of Paris VI. She joined Onera in 1986, where she was successively involved in developing stealth systems and high temperature composite materials for space applications. For the past fifteen years she has been working as a senior scientist on thermal barrier systems for gas turbine engines.



Marie-Hélène Vidal-Sétif graduated as a chemical engineer from the Ecole Supérieure de Physique et Chimie Industrielles in Paris and obtained a PhD degree in Physical Chemistry from the University of Paris XI. She joined Onera in 1987, where she was successively involved in the development of metal matrix composites (MMC), corrosion behavior of MMC and aluminum alloys. For the past 7 years she has been working as a senior scientist on thermal barrier systems for gas turbine engines.



Dr. Rémy Mévrel has a long experience in the field of high temperature protective coatings. His activities combine experimental and theoretical studies, in relation with both academic scientists and industrial partners. He introduced research activities on thermal barrier coatings at Onera in the early 80s and has become rapidly a world known expert in this field.

M.-P. Bacos, J.-M. Dorvaux,
S. Landais, O. Lavigne,
R. Mévrel, M. Poulain,
C. Rio, M.-H. Vidal-Sétif
(Onera)

E-mail: odile.lavigne@onera.fr

10 Years-Activities at Onera on Advanced Thermal Barrier Coatings

Developing thermal barrier coatings operating at higher temperature and/or for very long durations (commercial aircraft applications) is one of the technological and economic challenges for engine manufacturers. This includes the search for (i) low thermal conductivity, high thermal stability and CMAS resistant ceramic top coats, and (ii) alternative low cost bond coats with improved oxidation resistance and chemical compatibility with the substrate. This paper reviews the rationale supporting the choice of new materials for each layer and presents some recommendations to develop more robust and more efficient systems with increased lifetime.

Introduction

Thermal barrier coatings (TBCs) have been used since the 70s to protect metallic parts in the hot sections of gas turbines. TBCs are multilayer systems including a thermal insulating porous ceramic layer, mostly of 8 wt.% yttria partially stabilized zirconia 8YPSZ, deposited on an alumina forming metallic bond coat in contact with the nickel-based superalloy substrate. They are designed to improve engine efficiency by prolonging the component lifetimes and/or increasing gas temperature while reducing emissions and costs. Nevertheless first generation TBCs turned out to be prone to rapid ageing and degradation in service [1]. Demands for advanced thermal barrier systems with enhanced reliability and performance emerged in the early 1990s, especially for applications at higher operating temperatures and/or for very long durations. This paper gives an overview of some activities performed at Onera in this field during the past ten years, with respect to the state-of-the-art. It focuses on the development of low thermal conductivity, high thermal stability and CMAS resistant ceramic top coats and alternative low cost bond coats with improved oxidation resistance and chemical compatibility with the substrate.

New Ceramic Coatings

Low thermal conductivity TBCs

Thermal conductivity at 1200°C of the current state-of-the-art 8YPSZ top coat is typically 1.5 to 1.8 W.m⁻¹.K⁻¹ for EB-PVD coatings with columnar porosity (blades and vanes applications) and 0.8 to 1.0 W.m⁻¹.K⁻¹ for lamellar porosity structured plasma sprayed coatings (combustors and non-rotating or large component applications). Reducing these values to 30-40 % -all other parameters being kept constant- could ensure significant benefits regarding turbine entry temperature, metal substrate temperature, component life duration, cooling rate and specific fuel consumption [2]. Thus increasing the thermal barrier coating insulation capability emerged as a real techni-

cal and economic challenge for engine designers and manufacturers and has been widely documented and patented since the end of the 90s [3,4].

The thermal conductivity of a porous layer depends on the intrinsic thermal conductivity of the bulk material, which is linked with its composition and its structure, and on the architecture of the porous structure, i.e. pore volume fraction, geometry and distribution. Thus, lowering the thermal conductivity of the ceramic layer can be achieved by engineering chemical composition and/or coating microstructure.

Influence of chemical composition

Dense zirconia based materials already exhibit low thermal conductivity (2 – 3 W.m⁻¹.K⁻¹ at 1200°C) which is governed by phonon-phonon and phonon-point defect interactions. In partially and fully stabilized zirconia systems, the point defects acting as phonon scatter centers are stabilizing substitution ions and associated oxygen vacancies [5]. It has been shown [6] that the thermal conductivity of single crystal yttria doped zirconia at room temperature is a decreasing function of the yttria content (i.e. of the defect concentration) at least for relatively low stabilizer contents. Beyond a composition corresponding approximately to 20YFSZ the thermal conductivity increases again, although more slowly [7]. This latter effect was attributed to a short range ordering of the point defects, in particular of the oxygen vacancies [8].

Further thermal conductivity decrease may be achieved with stabilizers having different atomic mass and/or ionic radius. A semi-empirical model based on solid state physics considerations regarding heat conduction mechanisms in disordered oxide ceramics has been developed [9] for calculating the thermal conductivity of zirconia based materials doped with trivalent and pentavalent metallic ions as a function of composition, defect content and temperature.

Thus, replacing yttrium by different rare earth elements such as Dy, Yb or Sm causes the thermal conductivity of partially and fully stabilized zirconia to decrease. It appears that the distortion effect linked with the difference in ionic radius is predominant over the mass effect. Furthermore it has been shown that additional doping of yttria or other rare earth partially or fully stabilized zirconia with wisely chosen amounts of Nb or Ta can significantly lower the thermal conductivity. This semi-empirical approach served as a guideline for preparing dense zirconia based new materials, showing that significant decrease in thermal conductivity (up to 40%) can be achieved, compared to the standard 8YPSZ [9]. Similar conclusions on multiple doping of zirconia ceramics have been obtained in many publications and patents during the past decade [3,4,10,11].

To go beyond this approach, a more physically based model has been developed with reliable descriptions of the fine microstructure via Monte Carlo simulations and non equilibrium molecular dynamic calculations of the thermal conductivity [8]. This method has first been validated for the yttria-zirconia system. Calculations showed a rather good agreement with experimental data, in particular concerning the trends as a function of temperature and yttria content [12]. In a second approach the molecular dynamic methodology has been successfully applied on more complex structures, such as pyrochlores (rare earth zirconates or hafnates) and perovskites [13]. Resulting calculated thermal conductivities turned out to be in good agreement with calculated values of minimum conductivity [3] and experimental data from the literature [14,15,16]. In particular calculations performed on several perovskite structure candidates led to the selection of the high melting hexagonal ordered BMT – $\text{Ba}(\text{Mg}_{1/3}\text{Ta}_{2/3})\text{O}_3$ - which showed a particular low thermal conductivity ($1.4 \text{ W}\cdot\text{m}^{-1}\cdot\text{K}^{-1}$ at 1200°C) associated with a high thermal expansion coefficient ($9\cdot 10^{-6} \text{ K}^{-1}$ between 200 and 1200°C). These calculated predictions tallied with published results [17,18] and were confirmed experimentally on dense BMT synthesized through a solid state route [13,19].

Besides this work on dense materials, alternative compositions deposited by plasma spraying, EB-PVD or PE-CVD [Box 1] have been tested within national or international projects^{1, 2, 3, 4}: simple binary tetragonal or cubic zirconia based coatings [20,21], ternary zirconia systems [22], ceramics with more complex crystallographic structures like pyrochlores [23],... Thermal conductivity as low as half the thermal conductivity of standard 8YPSZ with similar porosity could be achieved for a given coating process [24].

Influence of porous architecture

Another efficient way to decrease the thermal conductivity of a material is to introduce microstructural defects such as pores, voids, microcracks which constitute obstacles against the through-thickness heat transfer. This approach turned out to be very fruitful in case of plasma sprayed coatings by use of specially designed feedstock powders and/or by control of spray parameters¹. In the case of EB-PVD

or PE-CVD coatings [25] a gain in thermal insulation has also been obtained with particular columnar architectures although smaller than the one achieved with optimized chemical composition¹.

Several methods can be found in the literature which attempt to estimate the thermal conductivity of porous materials as a function of microstructural features. Analytical calculations are mostly derived from the earliest electrical models of Maxwell (1898) and Eucken (1932) and are based on a restricted geometrical description of the porosity. Although these models might be relevant for describing trends in particular materials, the oversimplifying assumptions they rely on, singularly restrict their predictive capacity in the case of more complex interconnected porous structures, such as those observed in EB-PVD or plasma sprayed coatings, even if they have been widely used in the latter case [26].

Numerical approaches involving a representation of the actual microstructure are more promising. Finite element methods⁵ turned out to be very costly in terms of meshing and memory storage as far as very small porous features are concerned (inter-lamellar voids in plasma sprayed coatings or intra-columnar porosity in EB-PVD coatings as small as $0.1 \mu\text{m}$). An alternative approach based on a finite difference method has been developed at Onera [27] using no meshing but digitized micrographs of real coating cross sections as input for the thermal conductivity calculation [Box 2]. Several applications on thermal barrier coatings -mainly plasma sprayed ones- have illustrated the possibilities of this approach in its 2-dimensionnal (2D) version [28], such as:

- estimating the contribution of each morphological feature to the thermal conductivity and their role in its evolution as a result of heat treatments (sintering), thus providing a guideline for engine manufacturers for designing more efficient coatings with optimized thermal properties
- determining the various thermal conductivity components of an anisotropic coating and assessing the effective thermal conductivity in the case of multiphase or multilayer materials possibly with thermal boundary resistances
- evaluating the thermal conductivity of materials in conditions where experiments may be very difficult to carry out, i.e. at high pressure and/or high temperature.

In order to improve the reliability of the FDM calculation, which depends strongly on the representativeness of the input images of the microstructure, a 3-dimensional (3D) extension of this approach has been developed [Box 2]. Such application to thermal barrier coatings is still difficult due to poor reliable high resolution 3D representations of such coatings although new techniques such as FIB sectioning or nano computer tomography should make it possible in a near future.

¹ European project HITS: High Insulation Thermal barrier coating Systems, 4th FWP (1997-2002)

² European project TBC+: New Increased Temperature Capability Thermal Barrier Coatings, 5th FWP (2001-2006)

³ EU-US Project HIPERCOAT: Science of High Performance Multifunctional High Temperature Coatings (2002-2005)

⁴ European project TOPPCOAT: Towards design and Processing of advanced, comPetitive thermal barrier COATing systems 6th FP (2006-2010)

⁵ OOF (<http://www.ctms.nist.gov/oof/>): Object Oriented Fine Element Modelling in Materials Science

Box 1 - Plasma Enhanced CVD

Equipment / Principle

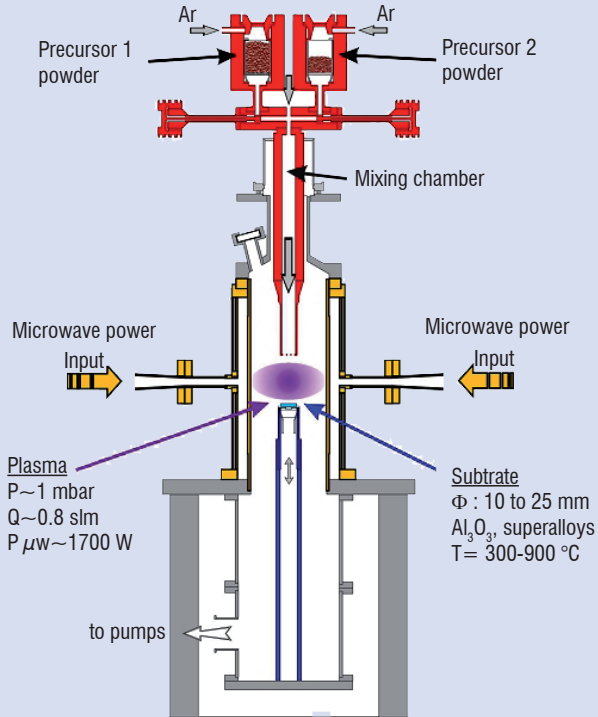


Figure B1-01 – PE-CVD equipment sketch

Equipment characteristics

Gas flow

- coating oxygen stoichiometry
- coating thickness homogeneity

Evaporation or sublimation temperature (100 to 250 °C)

- coating rate (YPSZ: 50 to 250 $\mu\text{m}/\text{h}$)
- coating composition

Deposition temperature (300 to 1000 °C)

- coating porosity (YPSZ: 20 to 50 %)

Precursors (chloride or organo-metallic powders)

- coating composition

Two Onera facilities

Laboratory reactor: coatings on planar substrates (3 cm^2)

Pre-industrial reactor: coatings on turbine blade or vane (50 cm^2)

Coating characteristics

- Columnar structure, similar to EB-PVD
- Complex composition (up to three different oxides), providing available precursors
- Coating on complex shape component (Low line-of-sight process)
- Single or multilayer
- Total cost mostly depends on precursors

Some deposited compositions : 8YPSZ, 20YFSZ, Nd_2O_3 doped zirconia, HfO_2 , La,Gd-garnet, alumina,...

Example

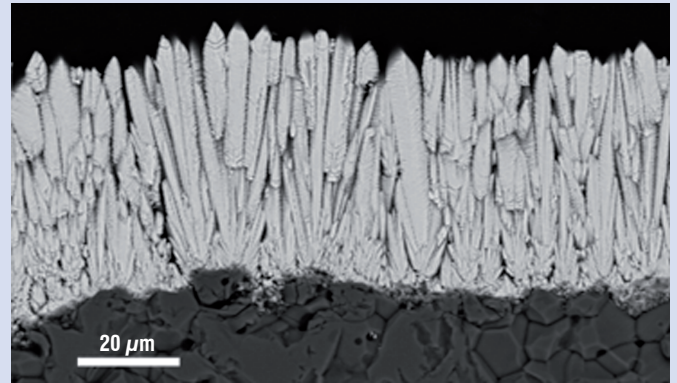


Figure B1-02 – PE-CVD coating microstructure ($\text{ZrO}_2 + 12 \text{ mol.}\% \text{ Nd}_2\text{O}_3$)

Box 2 - FDM calculation of thermal conductivity

2D calculation («TBCTOOL» code): principle

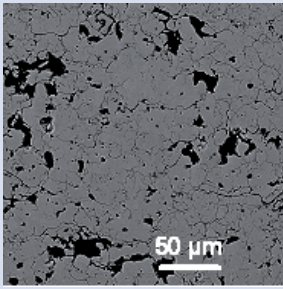


Figure B2-01 – SEM-BSE image of coating cross section (plasma sprayed TBC)

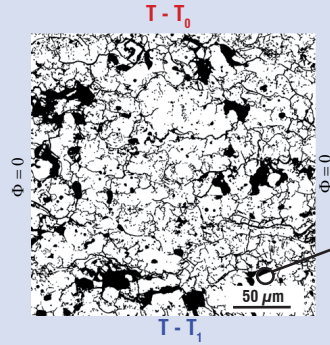


Figure B2-02 – Input data:
 - Threshold binary image
 - Thermal conductivity (K) of the matrix
 - K gas inside the pores

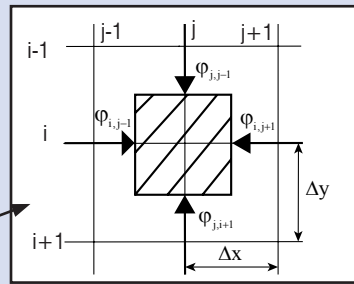


Figure B2-03 – Numerical scheme: resolution of heat equation for each

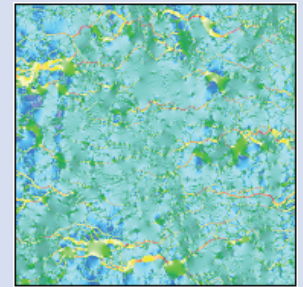


Figure B2-04 – Output data:
 - Effective thermal conductivity tensor
 - Temperature, heat flux, thermal gradient maps

Validation: comparison with FEM calculation

Some tests were done on EB-PVD coating morphologies in order to compare the solutions produced by the Onera TBCTOOL FDM-code and the OOF FEM-code developed at NIST [29]. Due to the very large requirement in memory storage the latter approach was not able to compute directly the conductivity of 1024 x 1024 pixels fields and input images had to be decomposed into slices. The two codes gave close results despite the difference in the computational methods and in the method used to handle boundary conditions.

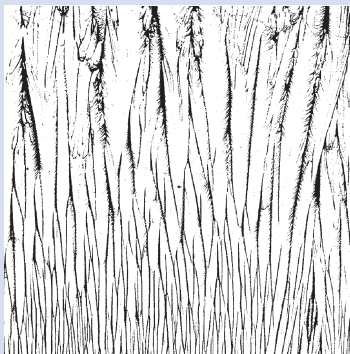


Figure B2-05 – Threshold binary image of EB-PVD TBC cross section

EB-PVD TBC n°	Measured conductivity K [W.m ⁻¹ .K ⁻¹]	K-TBCTOOL whole image [W.m ⁻¹ .K ⁻¹]	K-OOF 4 vertical slices [W.m ⁻¹ .K ⁻¹]	Porosity [%]
1	0.78	0.53	0.59	17
2	0.77	0.52	0.54	22
3	0.61	0.33	0.41	27

Table B2-1 – Measured and calculated (FDM and FEM) thermal conductivity of three different low-thermal conductivity EB-PVD coating microstructures

2D calculation limits:

The reliability of the FDM calculation highly depends on the representativeness of the input images of the microstructure. Plasma sprayed coatings microstructures are generally quite well described with 2D images whereas a 2D approach is of poor relevance for strongly anisotropic EB-PVD coatings. This mainly explains the discrepancies observed between computed and measured values (see table B2-1).

3D calculation (extended “μprop2D”)

A more accurate and competitive 2D-code “μprop2D” has been developed using better FDM schemes, different boundary conditions types and an efficient method of storage for the matrix coefficients so that conductivity of fields as large as 5000 x 3400 pixels could be calculated on a 512 Mb computer.

Then the method was extended to three-dimensional fields. The following results have been computed on a 2Gb memory computer (AMD Athlon 1500) with a time cost of 4h50min for phase conductivity ratio of 0.01. The morphological data (512x512x388 voxels) came from the reconstruction of SEM images of serial slices of an EB-PVD coating.

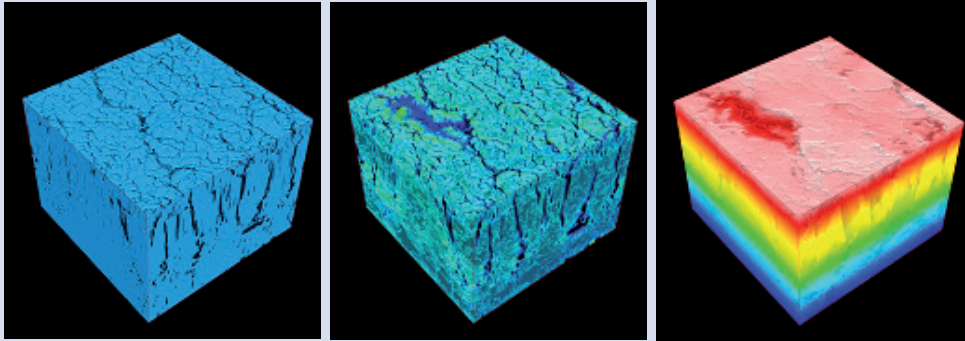


Figure B2-06 – Reconstructed EB-PBD coating morphology

Figure B2-07 – Calculated heat flux

Figure B2-08 – Calculated temperature

Computed thermal conductivity tensor considering periodic boundary conditions and a phase conductivity ratio of 0.01

Some limitations of the 3D calculation

The large volumes of data to be handled may exceed the capacities of an individual ordinary computer. A parallel version of the code should overcome this limitation. Actually it has been demonstrated (EU-US Project HIPERCOAT) that a 1Gvoxels (1024x1024x1024) Laplace problem could be solved on 4x3Gb memory cluster. At the present time a quite common quad core computer with 16Gb of RAM can be used.

Obtaining 3D representations of thermal barrier coatings with suitable resolution and in a reasonable time is still a problem. A 3D volume reconstructed from a series of cross-sections SEM images of an EB-PVD coating has been done once but the method to acquire such images is tricky and time-consuming and can not be widespread. New 3D characterization techniques should provide some solutions.

Additional requirements for the ceramic top coat

TBC long-term stability during service may be of concern, especially with low thermal conductivity coatings as the outer surface temperature is highest or for very long durations, as encountered in commercial aircraft applications. Two main issues are (i) possible phase transformations and (ii) sintering resulting in reduced thermal insulation capability and strain compliance, with TBC system degradation as a consequence [1].

Some low thermal conductivity compositions previously mentioned such as fully stabilized zirconia or zirconates allow the first issue to be avoided. However most of them have to be used as outer layer deposited on an inner layer of 8YPSZ^{6,7}. Actually it is now well established although not yet entirely explained [30] that the longest lifetimes of TBC systems are obtained with 8YPSZ or at least with non transformable t' structured compositions.

Densification of TBCs is a complex phenomenon on account of the constraint imposed by the metallic substrate and the external applied thermomechanical conditions. It depends on the coating microstructure and to a minor extent on its composition. Surface energy is the driving force for sintering and the dominant mechanism at operating temperatures (< 1300 °C) is likely to be surface diffusion. An original method [31] has been adapted at Onera [19] for determining surface diffusion coefficients from grain boundary thermal grooving estimated from atomic force microscopy experiments (Box 3). It appears that some new low thermal conductivity compositions (particularly in the rare earth–zirconia system) are more sintering resistant than standard 8YPSZ.

Currently most research activities regarding top coat compositions are related to an even more critical issue for TBC lifetime, i.e. TBC degradation by CMAS attack.

⁶ European project HITS: High Insulation Thermal barrier coating Systems

⁷ European project TBC+: New Increased Temperature Capability Thermal Barrier Coatings

Box 3 - Surface diffusion coefficient estimation from AFM profile of thermally grooved grain boundaries

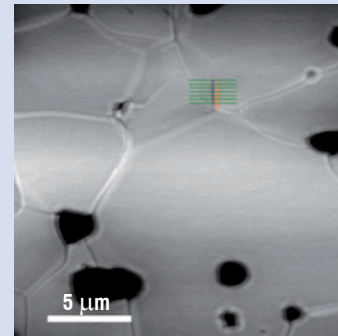
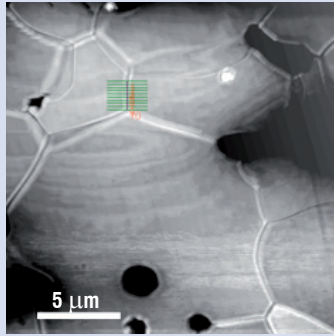


Figure B3-01 – AFM images of the same zone in dense 20YFSZ after annealing at 1300 °C for 12 hours (left) and 96 hours (right)

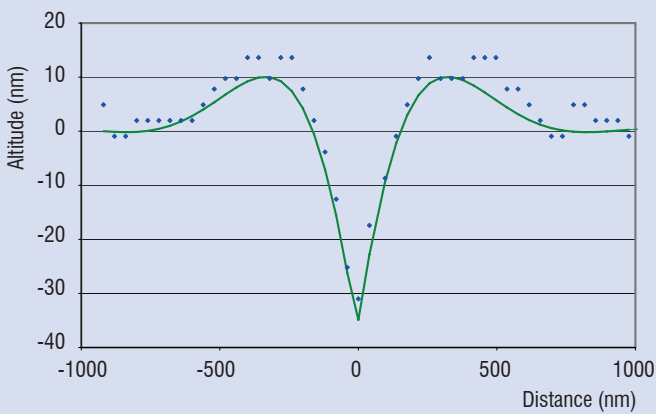


Figure B3-02 –

- ◆ Mean experimental profile of a given grain boundary extracted from AFM image at given (Temperature, time)
- Fit (Matlab) with Mullins equation for surface diffusion [W.W. Mullins – *Theory of thermal grooving*. J. Appl. Phys., 28 (1957) 333-339]

→ **output data:** surface diffusion coefficient and grain boundary equilibrium angle at given (T,t)

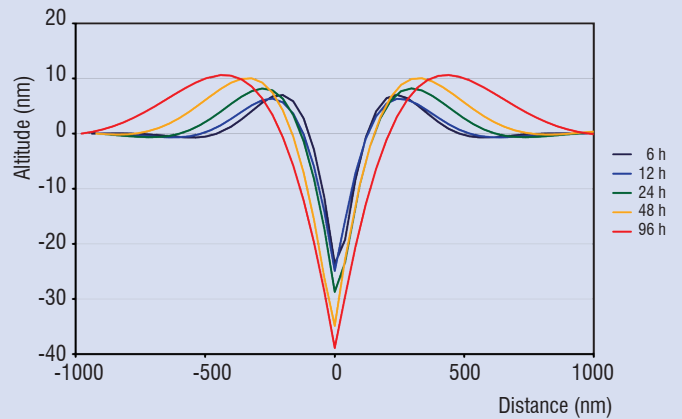


Figure B3-03 – Evolution of the profile (fitted) of the same grain boundary for different annealing times at 1300 °C.

→ **output data:** surface diffusion coefficient as a function of temperature (activation energy of surface diffusion)

Some experimental surface diffusion coefficients obtained at 1300 °C [$\text{m}^2 \cdot \text{s}^{-1}$]: $4 \cdot 10^{-15}$ for 20YPSZ, $4 \cdot 10^{-16}$ for dysprosia fully stabilized zirconia and $4 \cdot 10^{-14}$ for hexagonal ordered BMT – $\text{Ba}(\text{Mg}_{1/3}\text{Ta}_{2/3})\text{O}_3$ perovskite [19].

CMAS resistant coatings

Investigations on blades removed from service in the early 2000s showed that thermal barrier coatings are susceptible to degradation by molten calcium-magnesium-alumino-silicates (CMAS) resulting from the ingestion of siliceous mineral debris (dust, sand, ash) contained in the hot gases arriving in the turbine. Since then various solutions to the problem of CMAS degradation have been attempted. All of them consisted in depositing a protective coating on the surface of thermal barrier coating. Early solutions, most of them published in patents, were divided into three types: impermeable, sacrificial or non-wetting coatings [32,33,34]:

- The impermeable barrier is able to inhibit the infiltration of molten CMAS. It consists in a dense, non-cracked and non porous ceramic or metal outer layer [33]. Examples of such coatings are Pd, Pd-Ag, Pt, SiC, SiO_2 , Sc_2O_3 , SiO_xC_y , Ta_2O_5 , MgAl_2O_4 , and CaZrO_3 .

- The sacrificial coating reacts with CMAS to increase the melting temperature or viscosity of the contaminants thereby inhibiting infiltration [32,33,35,36,37]. Examples are silica, scandia, alumina, chromia, magnesia or calcia layers or alumina particles embedded in a silica matrix.

- The non-wetting outer layer minimizes contact between underlying layers and the molten contaminants. Non-wetting coatings mentioned as especially effective are noble metals as Pd, Pt, Pd-Ag alloy, AlN, BN, SiC, MoSi_2 , SiO_2 , ZrSiO_4 , SiOC [34].

Other solutions, such as an aluminum phosphate layer [38] or Ta_2O_5 layer [39] are also proposed in the patent literature. Though there are a large number of identified protective coating compositions, none of them seems to be effective enough, especially with increasing operating temperatures.

More recently, as a result of studies on low thermal conductivity TBCs (see § Low thermal conductivity TBCs) a solution has been patented consisting in a two layer system [40]. The inner layer is a stabilized zirconia layer such as 8YPSZ and the outer layer, a CMAS resistant zirconia based material doped with an effective amount of rare earth oxides such as Gd, La, Eu, Sm, Nd-oxides. The base material can also be a zirconate $X_2Zr_2O_7$ (pyrochlore structure) where X is a rare earth element. In the open literature, Krämer [41] has shown that a layer of gadolinium zirconate $Gd_2Zr_2O_7$ is effective to arrest CMAS infiltration. Indeed, the high temperature reaction between CMAS and gadolinium zirconate produces a dense crystalline layer consisting of an apatite phase $Gd_8Ca_2(SiO_4)_6O_2$ and fluorite ZrO_2 (with Gd and Ca in solid solution) which rapidly fills the intercolumnar gaps of EB-PVD top coat.

The studies conducted at Onera have investigated the interaction between CMAS and a ceramic from the ZrO_2 - Nd_2O_3 system. The experimental approach adopted was to simulate the CMAS corrosion at laboratory scale, under controlled conditions, using a model synthetic CMAS. Dense materials have been used or EB-PVD coatings deposited on an alumina substrate. Some results are presented below.

Synthetic CMAS interaction with standard 8YPSZ EB-PVD coatings

The first work has consisted in trying to reproduce, in laboratory, the interaction observed between CMAS and 8YPSZ TBC on a high pressure turbine blade removed from service [1]. The model CMAS composition 61.5SiO₂-15Al₂O₃-23.5CaO (wt.%) is the lowest melting eutectic (1170 °C) in the ternary (CaO-Al₂O₃-SiO₂) system. It has been selected on the base of a melting temperature compatible with real thermal barrier surface temperature (≈1200 °C). In a first approach, the effect of Fe or Ti has not been taken into account as Krämer did [42] whose synthetic CMAS composition is 33.2CaO-6.5MgO-11.8Al₂O₃-48.5SiO₂ (wt.%).

The CMAS was prepared by mixing fine powders of the individual oxides and carbonates in de-ionized water, then drying and smelting in a Pt crucible at 1250 °C during 20 hours under air to achieve a homogenized melt. After quenching in water, a transparent and homogeneous glass was obtained which was then crushed in a mortar/pestle for obtaining fine glass powders. In order to study CMAS/TBC interaction, the glass-CMAS powders were deposited at the surface of the TBC specimens (30 mg/cm²) and the CMAS-covered specimens were heat-treated at 1200 °C in air for 4 hours and finally quenched in air.

Figure 1 shows a cross-section SEM image of the TBC specimen which has been exposed to the model CMAS at 1200 °C for 4 hours and the corresponding elemental maps of Ca (K α line). It can be seen that model CMAS completely infiltrates the TBC intercolumnar gaps down to the alumina substrate.

A higher magnification of the upper interaction zone between model CMAS and TBC (figure 2) shows that TBC columns have been attacked by CMAS especially in the periphery (column tips and feathery porosity) resulting in their morphology degradation. Two new crystalline phases are observed at the interface between TBC and CMAS and in the intercolumnar gaps. These new phases have been identified by XRD and EBSD respectively as $Ca_2ZrSi_4O_{12}$ and $CaAl_2Si_2O_8$ (needle-like morphology anorthite). Moreover EDS analysis reveals that the CMAS is enriched with minor amounts (≤ 1 atom %) of Zr and Y. The enrichment is still observed far from the TBC/CMAS interface. This analysis is consistent with the hypothesis of a dissolution solution of the TBC in the molten CMAS.

From these results, it can be seen that the model system gives very good replication of the CMAS corrosion observed on ex-service blades in terms of thermochemical interaction: TBC infiltration, TBC dissolution in the CMAS melt and formation of new crystalline phases.

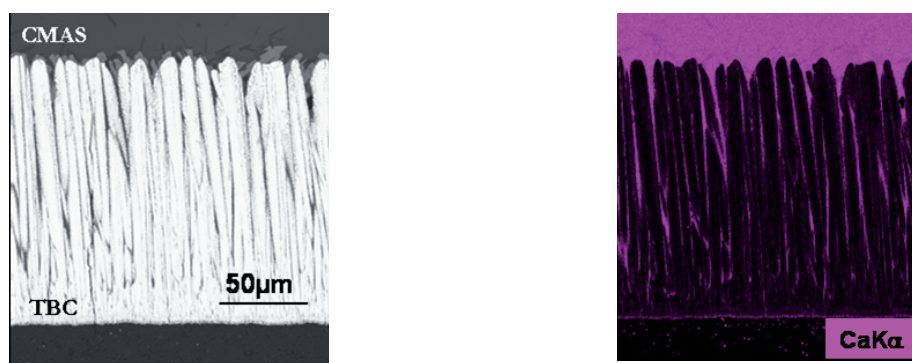


Figure 1 – 8YPSZ EB-PVD top coat infiltrated by synthetic CMAS: SEM image (top) and corresponding elemental map of Ca (K α line) (bottom).

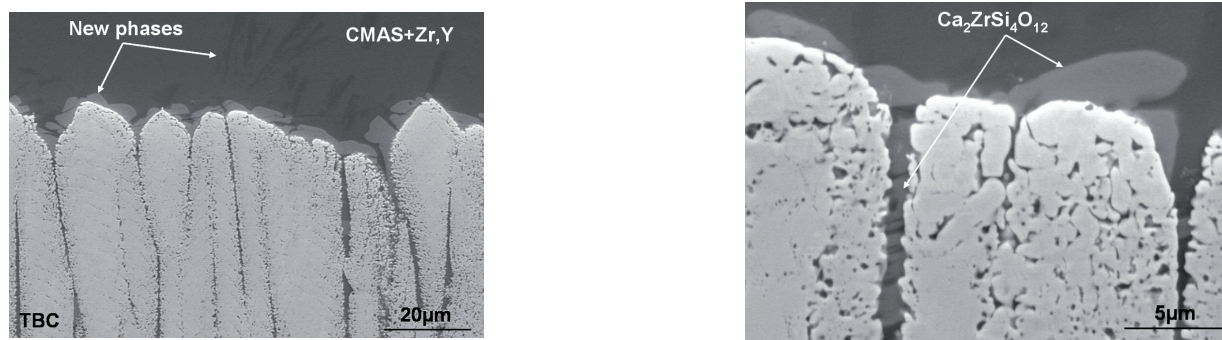


Figure 2 – Reaction zone between synthetic CMAS and TBC after 4 hours at 1200 °C (SEM-BSE image).

Synthetic CMAS interaction with dense ceramics

In a second part, dense ceramic materials have been prepared from pre-alloyed powders by cold isostatic pressing followed by high temperature densification. Two compositions were chosen: $ZrO_2+12 \text{ mol.}\% \text{ Nd}_2O_3$ and $Nd_2Zr_2O_7$ (pyrochlore structure) in order to test their resistance to CMAS infiltration. Dense $ZrO_2+10 \text{ mol.}\% \text{ Y}_2O_3$ was also prepared as a reference for the $ZrO_2\text{-Y}_2O_3$ system. This composition has been preferred to standard $ZrO_2+4.5 \text{ mol.}\%$ (or 8 wt. %) Y_2O_3 as it allows a unique cubic stable phase whatever the heat treatment applied.

After interaction of the yttria doped zirconia dense specimen with the synthetic CMAS at 1200 °C for 4 hours it appears that the CMAS penetration into the dense ceramic is limited to a few micrometers (figure 3). The top region of the ceramic is attacked resulting in the dissolution of yttria doped zirconia into the CMAS associated with the formation of the crystalline phase $Ca_2ZrSi_4O_{12}$. EDS semi-quantitative analysis reveals that the attacked ceramic surface (figure 3 - right) has a lower ratio Y/Zr than the bulk, indicating that a depletion of yttria took place during the interaction of $ZrO_2+10 \text{ mol.}\% \text{ Y}_2O_3$ with CMAS.

Thus the result of the interaction between CMAS and the dense ceramic is the same as for 8YPSZ EB-PVD coating.

Synthetic CMAS interaction with $ZrO_2+12 \text{ mol.}\% \text{ Nd}_2O_3$ and $Nd_2Zr_2O_7$ at 1200 °C for 1 hour presents some similarities with the one observed with $ZrO_2+10 \text{ mol.}\% \text{ Y}_2O_3$, i.e. dissolution of the ceramic in the CMAS, formation of $Ca_2ZrSi_4O_{12}$ in the ceramic top region and depletion of Nd_2O_3 in the attacked ceramic. But a major difference is observed. A dense layer appears (figure 4) between the ceramic grains depleted in Nd_2O_3 and the bulk ceramic. EDS analysis reveals that this layer is mainly constituted of (Zr, Nd, Ca, Si) oxide, suggesting that it is also a reaction product between molten CMAS and the ceramic.

The thickness of this reaction layer increases with the duration of the heat-treatment as seen on figure 5 left for a 25 hours treatment at 1200 °C. At a higher magnification (figure 5 right), the observation of different contrasts in BSE imaging mode indicates that the dense reaction layer is constituted of two interconnected phases. Due to the small size of these phases XRD and transmission electron microscopy should be performed in further work in order to determine the dense layer composition.

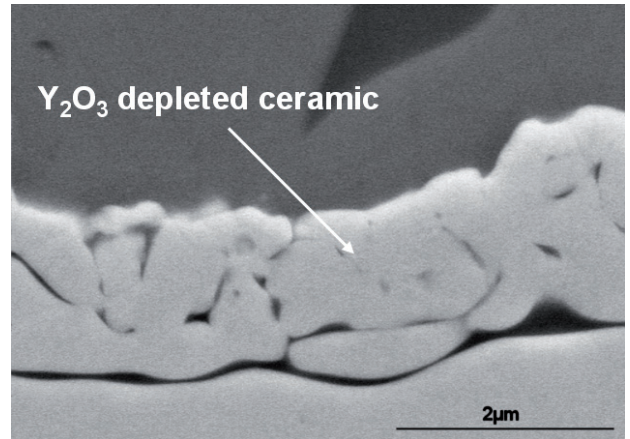
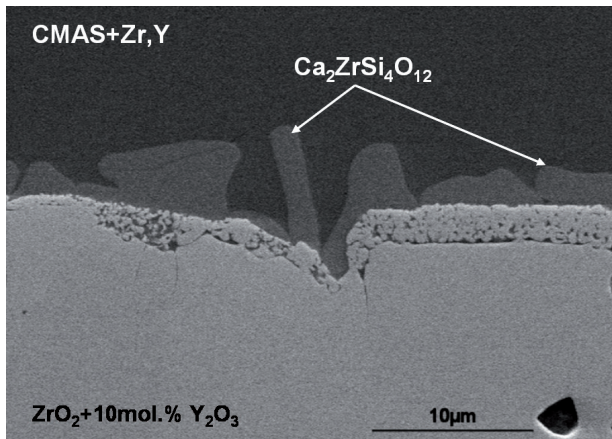


Figure 3 – Reaction zone between synthetic CMAS and dense $ZrO_2+10 \text{ mol.}\% \text{ Y}_2O_3$ after 4 hours at 1200 °C; cross-section SEM micrographs (overview (left), detail (right)).

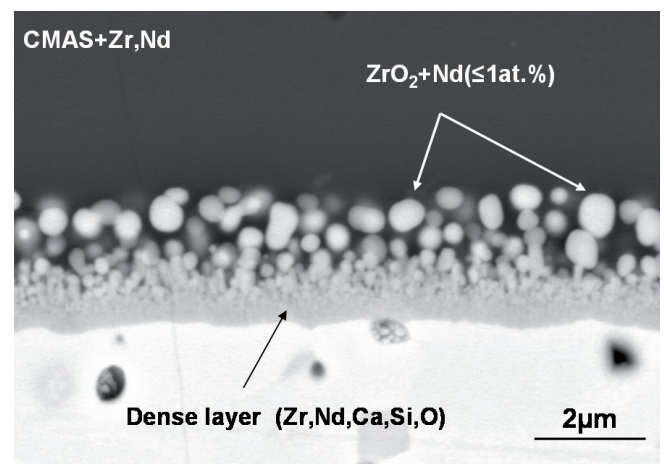
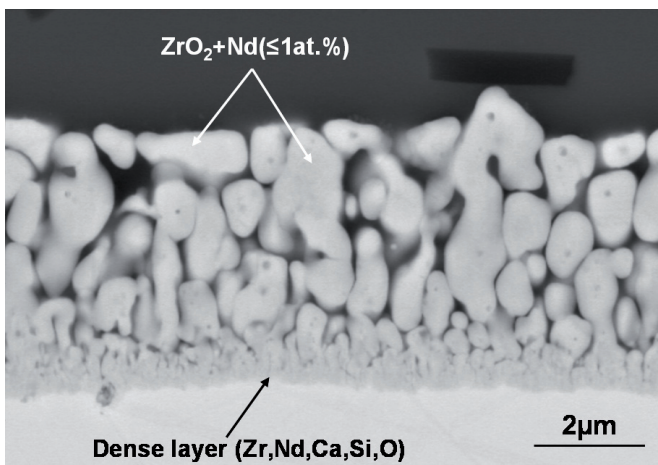


Figure 4 – Reaction zone between synthetic CMAS and dense ceramic after 1 hour at 1200 °C: $ZrO_2+12 \text{ mol.}\% \text{ Nd}_2O_3$ (left), $Nd_2Zr_2O_7$ (right).

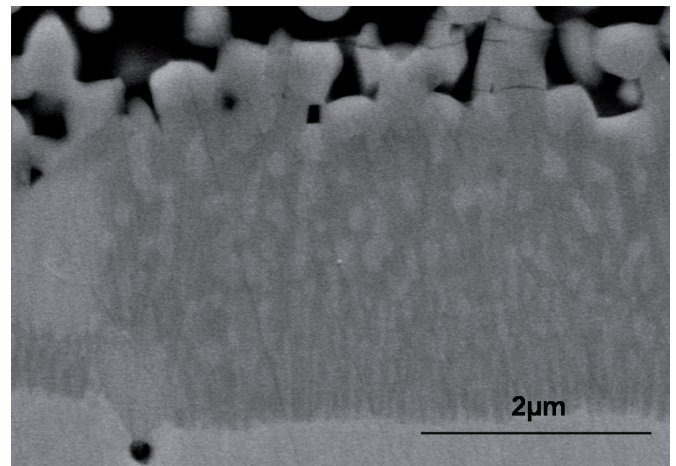
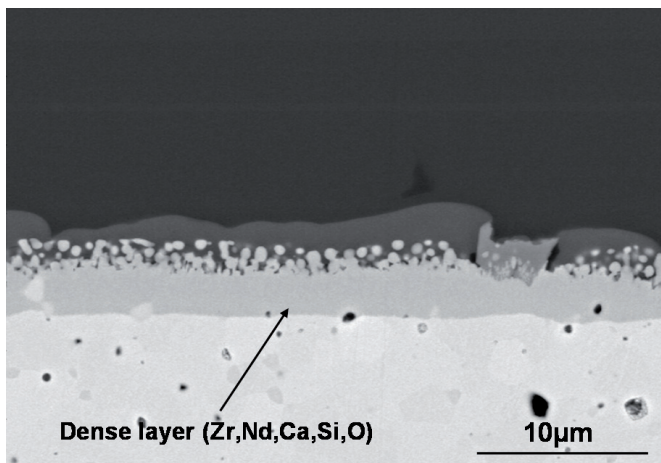


Figure 5 – Reaction zone between synthetic CMAS and $\text{Nd}_2\text{Zr}_2\text{O}_7$ after 25 hours at 1200 °C: overview (left), higher magnification (right).

Synthetic CMAS interaction with a new composition EB-PVD coating

Finally, the thermochemical interaction between a $(\text{La,Nd})_2\text{Zr}_2\text{O}_7$ EB-PVD coating⁹ and the model CMAS has been investigated. After 1 hour at 1200 °C (figure 6 left), the microstructure of the reaction zone between CMAS and ceramic is quite different from the one observed with 8YPSZ EB-PVD coating and very similar to the one obtained with dense $\text{Nd}_2\text{Zr}_2\text{O}_7$. The great difference with 8YPSZ EB-PVD coating is that the model CMAS infiltrated the intracolumnar porosity and the intercolumnar gaps only to a depth $\leq 20\mu\text{m}$ below the original $(\text{La,Nd})_2\text{Zr}_2\text{O}_7$ surface. No evidence of CMAS was found in the rest of the ceramic. Moreover the result of the interaction between the infiltrated CMAS and the ceramic is a dense reaction layer, similar to that observed with the dense $\text{Nd}_2\text{Zr}_2\text{O}_7$ ceramic. EDS analysis reveals that this layer is mainly constituted of (Zr, La, Nd, Ca, Si) oxide. These results suggest that this dense reaction layer, by rapidly filling the ceramic intercolumnar gaps, is responsible for the CMAS infiltration arrest. The same inhibition of CMAS infiltration is still observed after

16 hours at 1200 °C (figure 6 right). These results are in agreement with those obtained by Krämer [41] with the gadolinium zirconate $\text{Gd}_2\text{Zr}_2\text{O}_7$.

As a summary, this work has shown that it is possible to reproduce in laboratory, using a synthetic CMAS, the CMAS corrosion observed on the TBC of a high pressure turbine blade removed from service. The use of dense ceramics in order to test TBC compositions resistant to CMAS has also been validated. Concerning prevention of CMAS infiltration, it seems that $\text{ZrO}_2 + 12 \text{ mol.}\% \text{ Nd}_2\text{O}_3$ and $\text{Nd}_2\text{Zr}_2\text{O}_7$ could be effective to mitigate the CMAS penetration by the rapid formation of a dense reaction layer in the intercolumnar gaps and the intracolumnar porosity of a EB-PVD TBC. Future work will be devoted to elaborate PE-CVD columnar zirconia coatings containing different amounts of Nd_2O_3 (including the zirconate $\text{Nd}_2\text{Zr}_2\text{O}_7$) in order to confirm their ability to arrest CMAS infiltration. Other rare earth doped zirconia coatings will be tried, first using dense ceramics, then PE-CVD coatings, in order to compare their behavior and to select the most effective composition for the mitigation of CMAS infiltration.

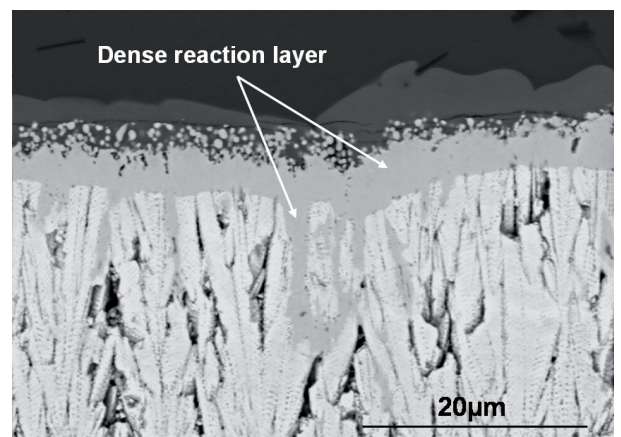
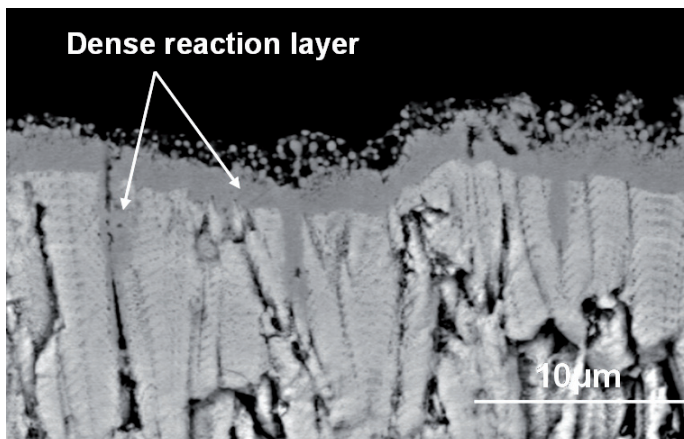


Figure 6 – Reaction zone between synthetic CMAS and $(\text{La,Nd})_2\text{Zr}_2\text{O}_7$ EB-PVD coating after 1 hour at 1200 °C (left), after 16 hours at 1200 °C (right).

⁹ By courtesy of the German Aerospace Center (DLR) – Cologne, within the EU project TBC+ [23]

Alternative bond coats

The search for alternative bond coats to standard platinum modified aluminate is motivated by :

- increasing the adherence of the thermally grown protective alumina scale,
- reducing interdiffusion phenomena between the bond coat and the substrate,
- avoiding phase transitions such as martensite formation,
- increasing creep resistance, in order to minimize surface rumpling and consequently extend the system lifetime,
- reducing the costs.

Zr-doped nickel aluminide

As the addition of reactive elements can have a significant effect on the oxidation behavior of alumina-forming alloys [43], a thermochemical Zr-doping process was developed at Onera [44,45] in order to design Zr-doped NiAl as a bond coat in TBC systems. This non-directional process is well suited for the complex shapes of turbines blades. Moreover there is no need for an electrolytic stage and additionally the use of zirconium instead of platinum decreases the cost of the process.

In this alternative process, zirconium is provided by the $ZrOCl_2 \cdot 8H_2O$ activator (Box 4). The process leads to the co-deposition of Al and Zr on the nickel-base superalloy. Glow discharge mass spectroscopy (GDMS) profile and multi-spectral X-ray maps indicate that zirconium is located far below the coating surface, at the interface between the β -NiAl coating and the interdiffusion zone (figure 7). Total zirconium concentration (reported to the coating volume) may be evaluated to around 400 at. ppm. The zirconium peak localization at the interface indicates that Zr deposition occurs at the beginning of the vapor phase aluminizing deposition process in agreement with the thermodynamic analysis (HSC Chemistry[®]). Indeed results from these calculations suggest that Zr deposition mainly occurs at low

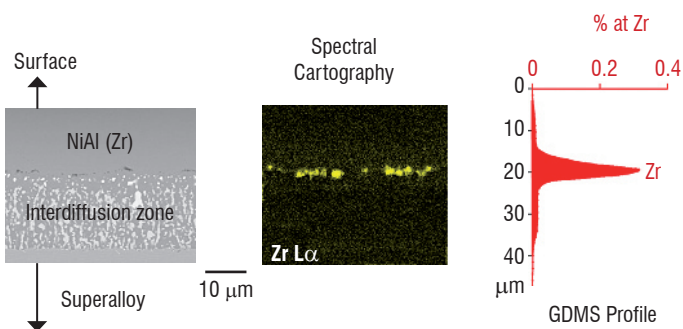


Figure 7 - Zr distribution through alternative Zr-doped aluminide bond coat.

temperatures ($\sim 600^\circ\text{C}$). At higher temperatures ($\sim 1100^\circ\text{C}$) deposition of Al prevails.

Cyclic and isothermal oxidation tests performed at 1100°C showed that adding hundreds of atomic ppm of Zr reactive element in the nickel aluminide improves the adherence of the alumina scale on the NiAl bond coat [46]. Actually NiAl(Zr) coatings deposited on AM1⁹ nickel-based single crystal superalloy presents an oxidation resistance much higher than that of undoped NiAl and comparable to that of NiPtAl coating (Figure 8). The spalled areas revealed the presence of numerous cavities at the metal/oxide interface on AM1/NiAl sample whereas such cavities were never observed on AM1/NiAl(Zr) sample. This absence of voiding in the presence of zirconium is expected to improve thermally grown alumina adhesion on the nickel aluminid.

Isothermal oxidation tests show also that the transient regime of θ -alumina growth lasts shorter with zirconium. Zirconium essentially modifies the transition between the two regimes θ and α but it does not modify the stationary regime of α -alumina growth. However it clearly influences the initial stages of oxide growth and accelerates the transition between the transient and the stationary regimes.

Specific studies using ToF-SIMS experiments show that zirconium, initially located at the interface between the β -NiAl coating and the interdiffusion zone, migrates during oxidation towards the surface leading to a homogeneous depth distribution of zirconium within the whole oxide layer. Zirconium inhibits the formation of cavities at the coating/oxide interface and this could explain the improved spalling resistance observed during cyclic oxidations. This absence of cavities could be due to a shorter transient oxidation, characterized by cationic growth, for NiAl(Zr) coatings, that would prevent cavities growth.

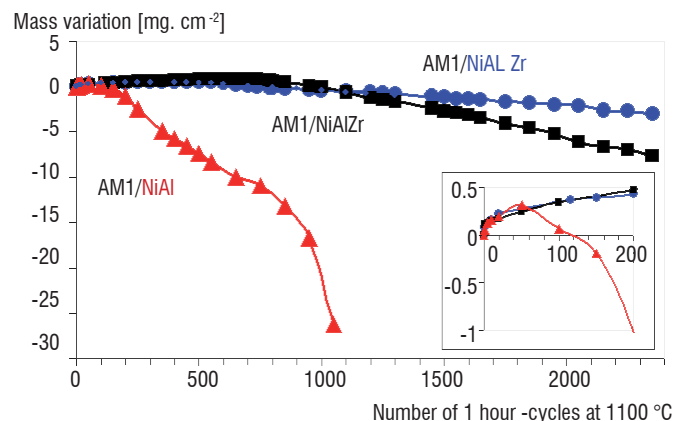
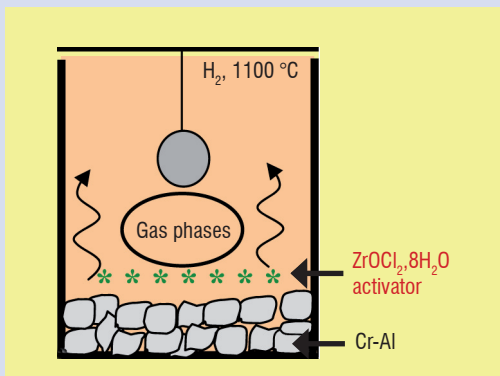


Figure 8 - Cyclic oxidation resistance of different nickel aluminide coatings deposited on AM1 nickel-based single crystal superalloy [47].

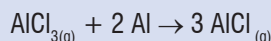
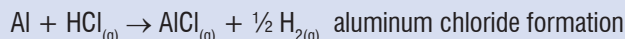
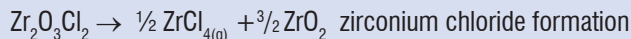
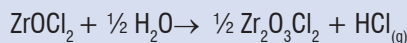
⁹ AM1 composition [wt. %] : Ni base, 6.5 Co, 7.8 Cr, 2 Mo, 5.7 W, 5.2 Al, 1.1 Ti, 7.9 Ta

Box 4 - Zirconium-doped aluminization

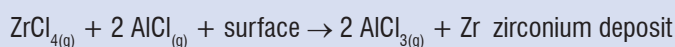
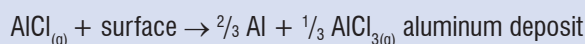
The components to be coated are located in a sealed or semi-sealed retort above a mixture composed of a low aluminum activity cement (Al 30 wt.% Cr 70 wt.%) and a small percentage (from 0.1 to 0.5 wt.%) of a zirconium precursor ($ZrOCl_2 \cdot 8H_2O$) [44,45]. The entire apparatus is placed inside a furnace and heated in a hydrogen atmosphere at high temperature. The duration of the treatment depends on the temperature.



Gas-gas reactions



Gas-surface reactions



Application of NiAl(Zr) as a TBC bond coat

As mentioned above, the NiAl(Zr) coating is as suitable as the NiPtAl one, when considering cyclic oxidation of aluminized AM1 single crystal superalloy. Consequently, both the standard system AM1/NiPtAl/8YPSZ EB-PVD and the alternative AM1/NiAl(Zr)/8YPSZ EB-PVD one have been studied at Onera [47]. Both systems turned out to have quite similar lifetime although the critical microstructural degradations were found to be different (figure 9). The main mechanisms responsible for the standard TBC system failure are rumpling (increasing interfacial roughness induced by out-of-plane stresses) and formation of large cavities related to the oxidation of the bond coat. As a result local decohesions cleavages arise and interfacial cracks propagate along the TGO/top coat or bond coat interface, and possibly through the TGO itself. On the contrary, no interfacial cavities are detected in the case of the NiAl(Zr) bond coat, and its topographical evolution is appreciably less marked so that the top coat and the TGO spall off together. The less pronounced bond coat deformation is probably due to an enhanced yield stress in the case of Zr-doped nickel aluminide and a low propensity towards martensite NiAl (L10) phase formation. Besides, because the TGO/NiAl(Zr) bond coat interface remains rather smooth, the residual in-plane compressive stress level within the TGO is about 1 GPa higher compared to the standard case [47], which is consistent with the well known effect for Zr to increase the creep strength of alumina.

As a conclusion, the NiAl(Zr) bond coat developed at Onera seems to be a good candidate for less expensive thermal barrier coating systems with operational performance comparable to that obtained with NiPtAl bond coat standard system.

Diffusion barriers

In thermal barrier systems exposed at high temperature interdiffusion phenomena occur between the Ni-base superalloy and the nickel aluminide protective coating, which can have fatal consequences for the life duration of the system. Firstly, interdiffusion increases the extent of Al depletion in the coating, which leads to the acceleration of the $\beta - NiAl \rightarrow \gamma' - Ni_3Al$ transformation and to the formation of non-protective oxide scales. Secondly, particular elements from the superalloy diffuse through the aluminide bond coat up to the thermally grown oxide and some have detrimental effects on the oxide scale adhesion. Finally, for coated third or fourth generation Ni-based superalloys, interdiffusion may lead to the formation of detrimental and fast growing secondary reaction zones (SRZ) [48]. In these SRZ, discontinuous precipitation transforms the single crystal γ/γ' superalloy into a weaker polycrystal composed of γ and TCP phases (σ , μ or P) in a γ' matrix. These zones may degrade the mechanical properties of the system by reducing its load bearing section.

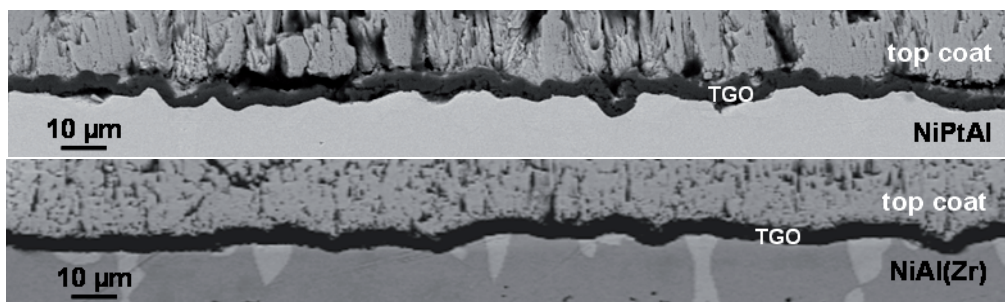


Figure 9 - Interfacial topography after 50 h-cycles at 1100 °C (AM1/NiPtAl/8YPSZ and AM1/NiAl(Zr)/8YPSZ systems)

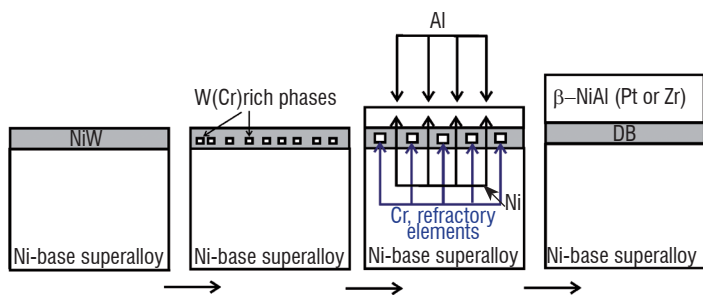


Figure 10 - Principle of a NiW(Cr) diffusion barrier formation after ref [53]

To limit interdiffusion phenomena between the Ni-based superalloy and its protective coating, some authors have introduced diffusion barriers (DB) [49,50]. Onera has developed [51] such diffusion barriers, which were based on a Ni-W electrolytic coating and composed of a dense precipitation of α -W phases after a thermal treatment under vacuum (simple DB) [52,53] or a vapor phase chromization (Cr enriched DB) [55]. These diffusion barriers have been tested under a classical nickel aluminide coating (Pt modified or Zr doped) (figure 10).

Chemical composition measurements (with EDS spectral maps) coupled with the “p-Kp” modeling [54] of the cyclic oxidation kinetics, and the development of the model “p-Kp- β ” at Onera [55] have permitted study of the efficiency of the diffusion barrier as a function of its composition and its ageing at high temperature (figure 11). Isothermal thermogravimetric analysis showed that both as-processed systems without and with NiW diffusion barrier (but without any thermal barrier coating) exhibit similar oxidation kinetics and final mass gains [52].

Finally it has been proved [53] that diffusion barrier modifies the SRZ initiation but not their propagation kinetic, which only depends on the superalloy local composition.

Acknowledgements

The authors are grateful to the French Ministry of Defense and the European Commission for partial funding of this work. The authors would like to thank D. BOIVIN, P. JOSSO, S. NAVÉOS, Y. RENOLLET AND C. SANCHEZ for their valuable contributions.

References

- [1] M. P. BACOS, J. M. DORVAUX, O. LAVIGNE, R. MEVREL, M. POULAIN, C. RIO, M. H. VIDAL-SETIF - *Performance and Degradation Mechanisms of TBCs for Turbine Blades*. Aerospace Lab 03 - November 2011.
- [2] S. ALPÉRINE, M. DERRIEN, Y. JASLIER, R. MÉVREL - *Thermal Barrier Coatings: the Thermal Conductivity Challenge*. AGARD R-823 (1998) 1-1-10.
- [3] D.R. CLARKE - *Materials Selection Guidelines for Low Thermal Conductivity Thermal Barrier Coatings*. Surf. Coat. Technol., 163-164 (2003) 67-74.
- [4] C.G. LEVI - *Emerging Materials and Processes for Thermal Barrier Systems*. Current Opinion Solid State Mater. Sci., 8 (2004) 77-91.
- [5] M. GELL, P.G. KLEMENS - *Thermal Conductivity of Thermal Barrier Coatings*. Mat. Sci. Eng. A, 245 (1997) 143-149
- [6] G.E. YOUNGBLOOD, R.W. RICE, R.P. NIGEL - *Thermal Diffusivity of Partially and Fully Stabilized (Yttria) Zirconia Single Crystals*. J. Am. Ceram. Soc., 71 (1988) 255-260.
- [7] J.F. BISSON, D. FOURNIER, M. POULAIN, O. LAVIGNE, R. MÉVREL - *Thermal Conductivity of Yttria-Zirconia Single Crystals Determined with Spatially Resolved Infrared Thermography*. J. Am. Ceram. Soc., 71 (2000) 255-260.
- [8] M. FÈVRE, A. FINEL, R. CAUDRON, R. MÉVREL - *Local Order and Thermal Conductivity in Yttria-Stabilized Zirconia. II. Numerical and experimental investigations of thermal conductivity*. Phys. Rev. B, 72 (2005) 104118-1-7.
- [9] B. LECLERCQ, R. MÉVREL - *Thermal Conductivity of Zirconia-Based Ceramics for Thermal Barrier Coatings*. Proc. CIMTEC 2002, Firenze Italy, July 14-18 (2002).

¹⁰ MC-NG composition [wt. %] : Ni base, 4 Cr, 1 Mo, 5 W, 3.9 Re, 3.8 Ru, 5.8 Al, 0.5 Ti, 5 Ta, 0.1 Si, 0.1 Hf

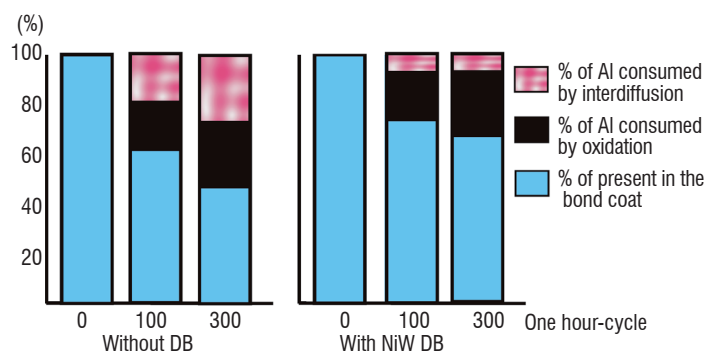


Figure 11 - Efficiency of the diffusion barrier (nickel based superalloy MC-NG¹⁰/simpleDB/NiPtAl system). Repartition of Al content after oxidation at 1100°C (one hour-cycle); after ref [55].

Conclusion

The strong demand from engine manufacturers for improving turbine performance at higher temperature and/or for very long durations has led since the end of the 90s to the development of advanced thermal barrier systems. Onera activities in this field have concerned materials, mechanical and modeling aspects. New compositions and microstructures for a low thermal conductivity, high thermal stability ceramic top coat have been proposed on the basis of thermal conductivity calculations and modeling. Today the search for protective coatings against environment and especially CMAS attack is a priority. Moreover alternative low cost bond coats with improved oxidation resistance and chemical compatibility with the substrate have been developed. Further work will concern the modification of superalloy compositions as recent results proved their strong influence on the TBC system lifetime, through induced changes in the chemical and mechanical properties of the bond coat ■

- [10] X. HUANG, D. WANG, M. LAMONTAGNE, C. MOREAU - *Experimental Study of The Thermal Conductivity of Metal Oxides Co-Doped Ytria Stabilized Zirconia*. Mat. Sci. Eng. B, 149 (2008) 63-72.
- [11] Y. SHEN, R.M. LECKIE, C.G. LEVI, D.R. CLARKE - *Low Thermal Conductivity Without Oxygen Vacancies in Equimolar $YO_{1.5}+TaO_{2.5}$ - and $YbO_{1.5}+TaO_{2.5}$ - Stabilized Tetragonal Zirconia Ceramics*. Acta Mater., 58 (2010) 4424-4431.
- [12] R. MÉVREL, J.-C. LAIZET, A. AZZOPARDI, B. LECLERCQ, M. POULAIN, O. LAVIGNE, D. DEMANGE - *Thermal Diffusivity and Conductivity of $Zr_{1-x}YxO_{1-x/2}$ ($x=0, 0.084$ and 0.179) Single Crystals*. J. Europ. Ceram. Soc., 24 (2004) 3081-3089.
- [13] M.A. PRÉVOST, R. MÉVREL, M. FÈVRE - *New Ceramic Material for Thermal Barrier Coatings*. Intern. Conf. Europ. Ceram. Soc., Berlin, Germany, June 17-21 (2007).
- [14] J. WU, X. WEI, N.P. PADTURE, P. KLEMENS, M. GELL, E. GARCIA, P. MIRANZO, M. OSENDI - *Low-Thermal Conductivity Rare Earth Zirconates for Potential Thermal Barrier Applications*. J. Am. Ceram. Soc., 85 (2003) 3031-3035.
- [15] R. VASSEN, X. CAO, F. TIETZ, D. BASU, D. STOVER - *Zirconates as New Materials for Thermal Barrier Coatings*. J. Am. Ceram. Soc., 83 (2000) 2023-2028.
- [16] M. V. KRISHNAIAH, P. SRIRAMA MURTHI, C. K. MATHEWS - *Thermal Diffusivity and Thermal Conductivity Studies on Europium, Gadolinium and Lanthanum Pyrohafnates*. Thermochim. Acta, 140 (1989) 103-104.
- [17] R. GUO, S. BHALLA, L.E. CROSS - *Ba($Mg_{1/3}Ta_{2/3}$)O₃ Single Crystal Fiber Grown by the Laser Heated Pedestal Growth Technique*. J. Appl. Phys., 75 (1994) 4704-4708.
- [18] R. VASSEN, S. SCHWARTZ-LUCKGE, W. JUNGEN, D. STOEVER - US patent 20050260435 A1 (2005).
- [19] M.A. PREVOST - *Etude de nouvelles céramiques pour barrière thermique*. PhD Thesis Univ. Paris VI, France (2007).
- [20] S. ALPERINE, V. ARNAULT, O. LAVIGNE, R. MEVREL - US patent 6,333,118 (2001).
- [21] U. SCHULZ, B. SAINT-RAMOND, O. LAVIGNE, P. MORETTO, A. VANLIESHOUT, A. BÖRGER - *Low Thermal Conductivity Ceramics for Turbine Blade Thermal Barrier Coating Application*. Ceram. Eng. Sci. Proc., 25 (2004) 375-380.
- [22] B. LECLERCQ, R. MÉVREL, A. AZZOPARDI, A. MALIÉ, B. SAINT-RAMOND - US patent 7,374,821 (2008).
- [23] B. SARUHAN, U. SCHULZ, R. VASSEN, P. BENGTSOON, C. FRIEDRICH, R. KNÖDLER, O. LAVIGNE, P. MORETTO, C. SIRY, F. TARICCO, N. COIGNARD, R. WING. - *Evaluation of Two New Thermal Barrier Coating Materials Produced by APS and EB-PVD*. Ceram. Eng. Sci. Proc., 25 (2004) 363-373.
- [24] U. SCHULZ, C. LEYENS, K. FRITSCH, M. PETERS, B. SARUHAN-BRINGS, O. LAVIGNE, J.-M. DORVAUX, M. POULAIN, R. MÉVREL, M. CALIEZ - *Some Recent Trends in Research and Technology of Advanced Thermal Barrier Coatings*. Aerospace Sci. Technol., 7 (2003) 73-80.
- [25] B. PRÉAUCHAT, S. DRAWIN - *Isothermal and Cycling Properties of Zirconia-Based Thermal Barrier Coatings Deposited by PECVD*. Surf. Coat. Technol., 146-147 (2001) 94-101.
- [26] F. CERNUSCHI, S. AHMANIEMI, P. VUORISTO, T. MÄNTYLÄ - *Modelling of Thermal Conductivity of Porous Materials: Application to Thick Thermal Barrier Coatings*. J. Europ. Ceram. Soc., 24 (2004) 2657-2667.
- [27] J.M. DORVAUX, O. LAVIGNE, R. MÉVREL, M. POULAIN, Y. RENOLLET, C. RIO - *Modelling the Thermal Conductivity of Thermal Barrier Coatings*. AGARD R-823 (1998) 13-1-10.
- [28] M. POULAIN, J.-M. DORVAUX, O. LAVIGNE, R. MÉVREL - *Modelling the Thermal Conductivity of Plasma Sprayed TBCs*. Surface Modification Technol. XIV, ed. T.S. Sudarshan, M. Jeandin, ASM Intern. IOM Commun. Ltd (2001) 495-502.
- [29] M. BARTSCH, E.R. FULLER JR, U. SCHULZ, J.M. DORVAUX, O. LAVIGNE, S.A. LANGE - *Simulating Thermal Response of EB-PVD Thermal Barrier Coating Microstructure*. Ceram. Eng. Sci. Proc., 24 (2003) 549-554.
- [30] D.R. CLARKE, C.G. LEVI, A.G. EVANS - *Enhanced Zirconia Thermal Barrier Coating Systems*. Proc. IMechE, 220 (2006) 85-92.
- [31] A.S. GANDHI, C.G. LEVI - *Surface Diffusion Studies on TBC Materials by Grain Boundary Grooving*. Univ. Santa Barbara, CA (2005) (EU-US Project HIPERCOAT).
- [32] W.C. HASZ, M.P. BOROM, C.A. JOHNSON - US Patent 5,660,885 (1997).
- [33] W.C. HASZ, M.P. BOROM, C.A. JOHNSON - US Patent 5,871,820 (1999).
- [34] W.C. HASZ, M.P. BOROM, C.A. JOHNSON - US Patent n° 6,261,643 (2001).
- [35] R. DAROLIA, B.A. NAGARAJ - US Patent 6,720,038 (2004).
- [36] W.R. STOWELL, J.T. BEGOVITCH, T.W. RENTZ, G.A. MACMILLAN, J.GREENE, J.A. MURPHY, D.P. IVKOVICH Jr, A.J. SKOOG - US Patent 6,465,090 (2002).
- [37] B.A. NAGARAJ, J.L. WILLIAMS and J.F. ACKERMAN - US Patent 6,627,323 B2 (2003).
- [38] B.T. HAZEL, M.GORMAN, B.A. NAGARAJ - US Patent 7,666,528 (2010).
- [39] B.A. NAGARAJ, J.F. ACKERMAN, W.R. STOWELL, C.P. LEE. - US Patent 6,933,066 (2005).
- [40] R. DAROLIA, B.A. NAGARAJ, D.G. KONITZER, M.D. GORMAN, M.FU - US Patent Application 20070160859 (2007).
- [41] S. KRÄMER, J. YANG, C. G. LEVI - *Infiltration-Inhibiting Reaction of Gadolinium Zirconate Thermal Barrier Coatings with CMAS Melts*. J. Am. Ceram. Soc., 91 (2008) 576-583.
- [42] S. KRÄMER, J. YANG, C.A. JOHNSON, C.G. LEVI - *Thermochemical Interaction of Thermal Barrier Coatings with molten $CaO-MgO-Al_2O_3-SiO_2$ (CMAS) Deposits*. J. Am. Ceram. Soc., 89 (2006) 3167-3175.
- [43] B. PINT - *Experimental Observations in Support of The Dynamic-Segregation Theory to Explain the Reactive-Element Effect*. Oxid. Met., 4 (1996) 1-37.
- [44] M.P. BACOS, P. JOSSO, S. NAVÉOS - US patent 7,608,301 (2009).
- [45] S. NAVÉOS, G. OBERLAENDER, Y. CADORET, P. JOSSO, M.P. BACOS - *Zirconium Modified Aluminide by a Vapour Pack Cementation Process for Thermal Barrier Applications: Formation Mechanisms and Properties*. Mater. Sci. Forum, 461-464 (2004) 375-382.
- [46] S. HAMADI, M.P. BACOS, M. POULAIN, A. SEYEU, V. MAURICE, P. MARCUS - *Oxidation Resistance of a Zr-Doped NiAl Coating Thermochemically Deposited on a Nickel-Based Superalloy*. Surf. Coat. Technol., 204 (2009) 756-760.
- [47] P.-Y. THÉRY, M. POULAIN, M. DUPEUX, M. BRACCINI - *Adhesion Energy of a YPSZ EB-PVD Layer in Two Thermal Barrier Coating Systems*. Surf. Coat. Technol., 202 (2007) 648-652.

- [48] W.S. WALSTON, J.C. SCHAEFFER, W.H. MURPHY - *A New Type of Microstructural Instability in Superalloys -SRZ*. Superalloys 1996, ed. R.D. Kissinger et al. (Warrendale, PA - TMS, 1996) 9-18.
- [49] T. NARITA, K.Z. THOSIN, L. FENGQUN, S. HAYASHI, H. MURAKAMI, B. GLEESON, D. YOUNG - *Development of Re-Based Diffusion Barrier Coatings on Nickel Based Superalloys*. Mater. Corrosion, 56 (2005) 923-929.
- [50] J.A. HAYNES, Y. ZHANG, K.M. COOLEY, L. WALKER, K.S. REEVES, B.A. PINT - *High-Temperature Diffusion Barriers for Protective Coatings*. Surf. Coat. Technol., 188-189 (2004) 153-157.
- [51] M.P. BACOS, P. JOSSO - US patent 7,482,039 (2009).
- [52] E. CAVALETTI, S. NAVÉOS, S. MERCIER, P. JOSSO, M.P. BACOS, D. MONCEAU - *Ni-W Diffusion Barrier: Its Influence on the Oxidation Behaviour of a β -(Ni,Pt)Al Coated Fourth Generation Nickel-Base Superalloy*. Surf. Coat. Technol., 204 (2009) 761-765.
- [53] E. CAVALETTI, S. MERCIER, D. BOIVIN, M.P. BACOS, P. JOSSO, D. MONCEAU - *Development of a NiW in-situ Diffusion Barrier on a Fourth Generation Nickel-Base Superalloy*. Mater. Sci. Forum, 595-598 (2008) 23-32.
- [54] D. POQUILLON, D. MONCEAU - *Application of a Simple Statistical Spalling Model for the Analysis of High-Temperature. Cyclic oxidation kinetic data*. Oxidation Metals, 59 (2003) 409-431.
- [55] E. CAVALETTI - *Etude et développement de nouveaux revêtements avec barrières de diffusion pour application sur aubes de turbines à gaz en superalliage à base de nickel*. PhD Thesis, Univ. Toulouse, France (2009).

Acronyms

TBC (Thermal Barrier Coating)
 8YPSZ (8 wt.% Ytria Partially Stabilized Zirconia)
 20YFSZ (20 wt.% Ytria Fully Stabilized Zirconia)
 CMAS (Calcium-Magnesium-Alumino-Silicates)
 EB-PVD (Electron Beam-Physical Vapor Deposition)
 PE-CVD (Plasma Enhanced Chemical Vapor Deposition)
 K (Thermal Conductivity)
 FDM (Finite Difference Method)
 FEM (Finite Element Method)
 FIB (Focused Ion Beam)

AFM (Atomic Force Microscopy)
 GDMS (Glow Discharge Mass Spectroscopy)
 ToF-SIMS (Time-of-flight Secondary Ion Mass Spectroscopy)
 TCP (Topological Compact Phase)
 TGO (Thermally Grown Oxide)
 SRZ (Secondary Reaction Zones)
 DB (Diffusion Barrier)
 SEM (Scanning Electron Microscopy)
 BSE (Back Scattered Electron)
 EDS (Energy Dispersive Spectroscopy)
 XRD (X-Ray Diffraction)
 EBSD (Electron Back Scattered Diffraction)

AUTHORS



Marie-Pierre Bacos graduated from the Ecole Nationale Supérieure de Chimie in Paris (1981) and received a PhD degree in Applied Chemistry from University of Paris VI (1983). She joined Onera in 1983 where she has been involved in oxidation and corrosion mechanisms and in the development of innovative coatings and brazing technologies. She is the Head of the Materials and Architecture Research Unit at Onera Châtillon.



Jean-Marc Dorvaux joined the Material Department of Onera as a research scientist in thermal physics. His activities cover both the experimental development of testing and the modelling of heat transfer in materials in harsh environments.



Stéphane Landais graduated as a materials science engineer from the Conservatoire National des Arts et Métiers in Paris. He joined Onera in 1991 to participate in the development of new ceramic composites. Since 1998, he is in charge of PVD and CVD coating laboratory at Onera-Palaiseau.



Odile Lavigne graduated as a physicist engineer from the Ecole Supérieure de Physique et Chimie Industrielles in Paris and obtained a PhD degree in Material Science from the University of Paris VI. She joined Onera in 1986, where she was successively involved in developing stealth systems and high temperature composite materials for space applications. For the past fifteen years she has been working as a senior scientist on thermal barrier systems for gas turbine engines.



Rémy Mévrel has a long experience in the field of high temperature protective coatings. His activities combine experimental and theoretical studies, in relation with both academic scientists and industrial partners. He introduced research activities on thermal barrier coatings at Onera in the early 80s and has become rapidly a world known expert in this field.



Martine Poulain has been working at Onera since 1979, initially in the "Materials" department. She was involved in the development of protective coatings and she received her PhD degree from the University of Paris XI in 1999, on the topic of thermal insulation capabilities of TBCs. Her present research themes in the Metallic Materials and Structure department focus on the damage and life modeling of TBCs, and the coating by design approach.



Catherine Rio graduated from the Institut Universitaire de Technologie of Paris XI. She has been working at Onera since 1982 as a specialist in physical measurements, metallography and microstructure characterization on a wide range of high temperature materials and coatings.



Marie-Hélène Vidal-Sétif graduated as a chemical engineer from the Ecole Supérieure de Physique et Chimie Industrielles in Paris and obtained a PhD degree in Physical Chemistry from the University of Paris XI. She joined Onera in 1987, where she was successively involved in the development of metal matrix composites (MMC), corrosion behavior of MMC and aluminum alloys. For the past 7 years she has been working as a senior scientist on thermal barrier systems for gas turbine engines.

M. Thomas
M.-P. Bacos
(Onera)

E-mail: marc.thomas@onera.fr

Processing and Characterization of TiAl-based Alloys: Towards an Industrial Scale

This paper highlights Onera efforts focused on the design of new TiAl-based alloys, the development of a commercially-viable route for the manufacture of aero engine components and the optimization of mechanical properties. The alloy G4, with a duplex microstructure, has been developed with an excellent balance of properties for gas turbine applications up to 800°C. Additionally, a series of TiAl-3(Fe,Zr,Mo) alloys have been designed for applications with good ductility requirements. Since these alloys were developed for the casting route, results show that the minimization of subsequent heat treatments is required for property scatter reduction. Alternatively, the Powder Metallurgy (PM) route was explored with the aim of establishing well defined microstructure-property relationships. Moreover, microstructural changes and related phase transformations were fully clarified in the now well known 47-2-2 alloy. This thorough understanding then enabled us to optimize the microstructure of the 47-2-2 alloy via process parameters, in order to meet industrial requirements in terms of tensile, creep, and fatigue properties. Furthermore, in the last three years, alternative PM processing routes, by means of Spark Plasma Sintering and Direct Metal Deposition processes, were found to provide enhanced tensile properties. Finally, structural factors such as the surface-related embrittlement and the formation of oxide scales that occurs on the degradation of mechanical properties, and in turn on the temperature limitations of the TiAl-based alloys, were identified. Different approaches aimed at improving the oxidation/corrosion resistance are then described to achieve a better environmental durability for TiAl-based alloys.

Introduction

Due to requirements for higher thrust-to-weight ratios and enhanced fuel efficiency, TiAl-based alloys have attracted considerable interest among industrial companies for aeroengine applications. Due to their lower weight, high temperature strength, excellent burn resistance and quite good oxidation resistance, these intermetallic alloys are regarded as strong substitute candidates for conventional titanium alloys in the compressor part of aerospace gas turbine engines and also for Ni-based superalloys in the low pressure turbine part. As a significant pay-off for a considerable amount of research activities devoted to developing gamma alloy technology in the last two decades, γ -TiAl alloys are currently being used for turbocharger rotors in automotive engines [1] and have now been introduced for turbine blades in General Electric's GENx engine [2]. The cast Ti-47Al-2Cr-2Nb alloy, which passed the FAR33 certification in 2007 for GENx engines that will power the B787, is regarded as the greatest breakthrough in the TiAl technology up to now.

However, a challenge for successful implementation of a variety of γ -TiAl components, is that, in order to meet the specific requirements for gas turbine applications, the selected alloys must possess

a number of properties: ductility, fatigue strength, creep resistance, fracture toughness and crack propagation as well as high oxidation and corrosion resistance. An additional and necessary requirement concerns the attainment of a strict control of mechanical properties. Therefore, the non-constant size, morphology, proportion and distribution of the constituent phases in γ -TiAl alloys have to be controlled, and the microstructure has to be optimized over different length scales. A number of structural factors, in particular crystal orientations, boundary misorientations and structural inhomogeneities, can be influenced by some processing parameters. This can lead to unfavorable slip transfer conditions and to localized deformation processes which result in some variability of mechanical properties [3,4]. Large efforts were then devoted to compare the processing routes for different industrial applications (aerospace structural parts, automotive engine parts, turbocharger rotors, etc.). Therefore, Onera efforts in the last years were aimed at manufacturing robust engineering materials with efficient processing strategies to achieve optimized properties. The present paper will highlight Onera research work on designing new TiAl-based alloys, developing a commercially-viable route for the manufacture of aero engine components and optimizing mechanical properties. Finally, the temperature limitations in terms of thermal stability, oxidation and corrosion will be addressed.

Historical background

In the eighties, the development of γ -TiAl alloys was initiated in Japan and in the US. Promising results were obtained on tensile ductility based on the addition of specific alloying elements such as Mn [5]. In the meantime, the now well-known General Electric (GE) alloy composed of Ti-(46.5-48)Al-2Cr-2Nb (at%) was designed with the addition of Cr and Nb for ductility improvement and for a better oxidation resistance, respectively [6]. In the next decade, systematic studies were carried out at General Electric to adjust the composition range and to optimize the microstructure via heat treatments for the best balance of mechanical properties. The Al content was maintained in the 46.5-48% range for a good balance between Yield Stress (YS) and ductility. Hot Isostatic Pressing (HIP) at 1185°C for 4 hours was followed by annealing at 1205°C for 2 hours under controlled cooling rate to provide a good compromise in ductility, creep resistance as well as fracture toughness. Large databases were then produced in this annealing condition, including physical properties such as thermal coefficient, specific heat, thermal conductivity, Poisson's ratio, elastic and shear modulus for high specific stiffness applications. In addition, a number of mechanical properties, i.e. YS, Ultimate Tensile Strength (UTS), ductility, crack growth threshold, creep life, Low and High Cycle Fatigue (LCF and HCF) were compared to those of Ni-based superalloys.

However, the 47-2-2 alloy is typical of the first generation alloys, with a very strong solidification texture. The GE alloy is solidified by the $L + \beta \rightarrow \alpha$ peritectic reaction. Under further cooling, subsequent phase transformation occurs by the α (hcp) $\rightarrow \alpha + \beta$ ($L1_0$) $\rightarrow \alpha_2$ (DO_{19}) + γ reaction where nucleation and growth of γ lamellae with the Blackburn relationship is followed by $\alpha \rightarrow \alpha_2$ ordering below the eutectoid temperature. The availability of different TiAl alloy compositions then appears to be a necessary requirement since various applications for automotive, gas and terrestrial turbine components with different stress and temperature regimes are envisaged. For instance, boron-containing TiAl alloys were developed in the early nineties to reduce the cast columnar texture and some investigations are still in progress to understand the underlying mechanisms that makes boron efficient for grain refinement and texture reduction. In the last decade, extensive efforts were focused on $\gamma + \beta$ alloys with the addition of various ternary elements (Nb, Cr, Mo, W, Fe, Ta) that promote the cubic β phase with a higher deformability [7-14].

Results

Alloy development

So far, a number of research activities have been conducted at Onera on alloy development in order to satisfy property requirements in terms of oxidation resistance, thermal stability and of high temperature properties of TiAl-based alloys. For instance, a Ti-47Al-1Re-1W-0.2Si (at%) alloy, namely G4, with a duplex microstructure has been designed as a casting material for high temperature gas turbine applications [15]. Work at Onera concentrated on systematic heat treatment studies to define the most adequate microstructure of this G4 alloy for the best balance of mechanical properties.

Under static load condition, alloy G4 was quite comparable to other commercial γ -TiAl alloys in terms of tensile strength, irrespective of the heat treatment conditions [16]. With regard to HCF, the endurance

limit was found to exceed the yield stress, indicating that alloy G4 may not be very sensitive to such cyclic load conditions. Furthermore, in the low temperature regime up to 800°C, alloy G4 was more creep resistant than nickel-based superalloys on a corrected density basis. However, such creep properties were found to vary quite significantly as a function of heat treatment conditions, with the best condition in the as-HIPed condition, which is not consistent with the observations from the literature concerning the beneficial effect of a fully lamellar structure on creep through sub-transus heat treatment conditions [17]. The Onera study shows that the lamellar structure should not be the key factor controlling the creep rate [16]. Instead, creep in this alloy is controlled by deformation-induced substructures such as percolated interdendritic γ grains enriched in Re. Moreover, an as-HIPed condition like this can satisfy service conditions of most industrial installations. Based upon this attractive set of properties, an increasing temperature capability was then demonstrated with alloy G4 for reliable applications of this material at temperature up to 800°C. However, some difficulties encountered in the very last years, which were related to the supply of fine Re and W powders for the master alloys, do not make it easy to implement alloy G4 for gas turbine applications.

In the last years, alloy development at Onera was also focused on ductility enhancement. Apart from the tendency for ternary elements (V, Cr, Mn, Nb, Ta, Zr, W, Mo, Fe, etc) to be substituted either for Al or for Ti in the γ phase, which contributes to shift the $\alpha_2 + \gamma/\gamma$ transformation line and to change the proportion of lamellar colonies and γ grains, some other intrinsic factors can also be responsible for the plastic behaviour. Addition of Zr tends to increase the a parameter more rapidly than the c parameter, thus diminishing the tetragonality of the γ phase to the benefit of a more isotropic deformation. As mentioned in [18], a Zr atom with an atomic volume that is different from the matrix is expected to introduce elastic effects which result in solid solution strengthening. The presence of Zr also appears to strengthen the directional bonding, but to a lesser extent, which results in a slight increase in the Peierls potential. Consequently, a loss of dislocation mobility is induced and an additional strengthening is expected. In contrast, Fe addition offers a significant electronic effect instead, which reveals a similar intensity for both Ti-Fe et Al-Fe bondings [19]. A lower sensitivity of the Al content with Fe addition can then be anticipated. Finally, Mo offers a beneficial effect in terms of increased deformability by decreasing the lattice friction for the motion of ordinary dislocations and is a well known creep strengthening element [20].

Based on previous theoretical considerations, a number of TiAl-3(Fe,Zr,Mo) alloys were characterized for tensile behavior. Experimental data in terms of room-temperature ductility were found to be quite encouraging in the different alloys investigated, with plastic elongations between 1 and 2%. Consistently with the electronic effect of Fe, properties are not affected by a difference in Al content for Fe-containing alloys. Tensile properties at 800°C revealed a high level of ductility which can bring the required deformability for post-processing operations.

Comparison of processing routes

In view of the industrial requirements for compressor and turbine blade applications, special attention was paid to the influence of the processing and heat treatment conditions on the microstructure and properties. Some results of the two cast and Powder Metallurgy (PM)

processing routes using the same alloy composition TiAl-2Cr-2Nb are reported in this section.

For gas turbine components with complex shapes, the casting texture may not be so regular and axisymmetric. So, property variations are generally observed for different thicknesses of the cast parts and locations of the test specimens whereas, for a jet engine manufacturer, the major concern is to guarantee a minimum value of mechanical properties for every component. Therefore, to control potential cast-induced defects and for a better understanding of the microstructure/property relationship in cast bars, comparative tests were made with respect to the Al content and to the location of the test specimen within the bars. Results in figure 1 demonstrate the predominant effect of the Al content on YS and of the equiaxed-columnar structure transition through the section of the bars on tensile ductility at room temperature. Similarly, both parameters were found to strongly affect the creep behavior (figure 1b).

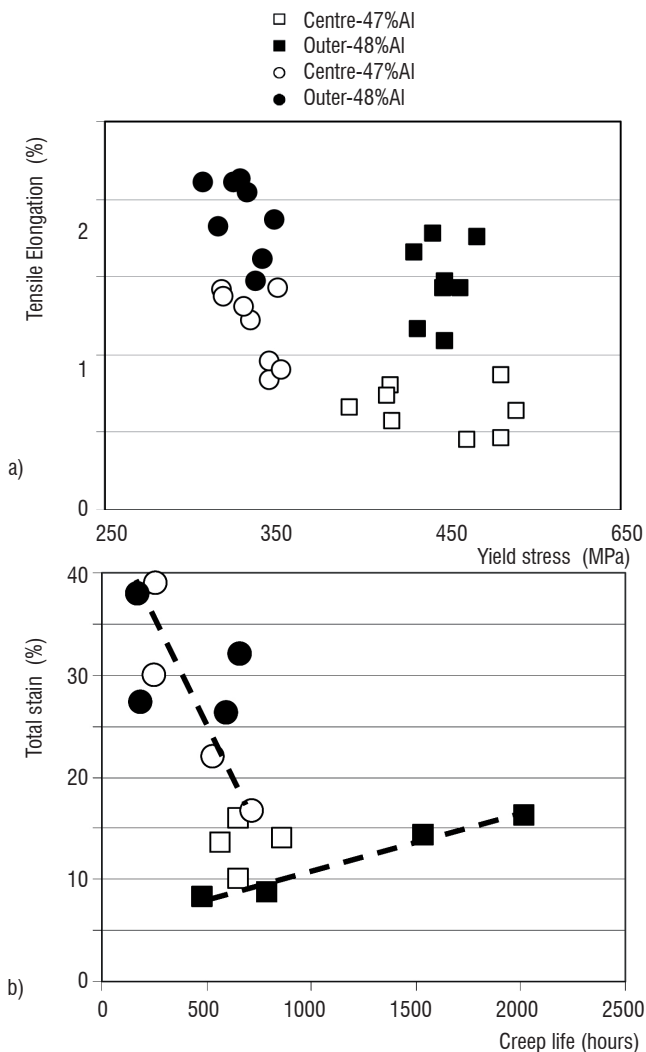


Figure 1 - Effect of Al content and location of the test specimen for heat treated TiAl-2Cr-2Nb alloys. (a) Tensile behavior (after reference 25) and (b) Creep behavior (after reference 26).

Casting is a difficult process to optimize. On one hand, columnar cast structure and chemical inhomogeneities have to be reduced through heat treatments to yield more attractive mechanical properties. On the other hand, property scatter is larger when subsequent heat treatments are carried out in the sub-transus field region, which is indicative of some return to chemical equilibrium counterbalancing a kind of solidification “memory” with cast structural features. To reduce

property scatter, the recommended procedure is to then directly optimize the casting conditions with regard to property requirements, i.e. without post-heat treatments. Furthermore, current cast alloys tend to suffer from the inherent lack of strength associated with the cast structure. Recent cast alloy development efforts have focused on the addition of minor elements (B, C, Si) and of β -stabilizing strengtheners for a better performance [21,22]. Nevertheless, it should be stressed that the centrifugal casting process has already demonstrated that sound parts of a difficult configuration such as low-pressure turbine blades can be obtained [23,24]. On the industrial side, centrifugal casting is sufficiently mature to offer the possibility to manufacture complex shape components.

In order to alleviate inherent crystallographic and morphological texture factors of the γ -TiAl lamellar structure, other processing routes such as PM were explored at Onera. Several main advantages can be stressed regarding the PM route. Full consolidation was obtained for sub α -transus HIP conditions with no evidence of macrosegregation or directionality. Powder compacts exhibit a refined microstructure and are less sensitive to the Al content than cast bars. The next step with PM parts was to establish microstructure-property relationships. For this purpose, an expanded range of microstructures, typically near- γ equiaxed, duplex and fully lamellar, was tailored in samples by varying heat treatment conditions. The tensile behavior was compared for γ -equiaxed and lamellar microstructures by plotting the plastic elongation as a function of the work hardening rate [25]. From figure 2, it is clear that the strategy to improve the tensile ductility is different in both microstructures. It can be seen that the best ductilities are obtained for intermediate work hardening. For lamellar microstructures, the steeper the curves in the plastic domain, the higher the flow stress which rapidly overcomes the critical transgranular cleavage stress and the lower the plastic elongations. This strong work hardening rate dependence of tensile ductility is governed by a homogeneous deformation through the lamellar microstructure. In contrast, γ -equiaxed microstructures exhibit significant strain localization during plastic deformation.

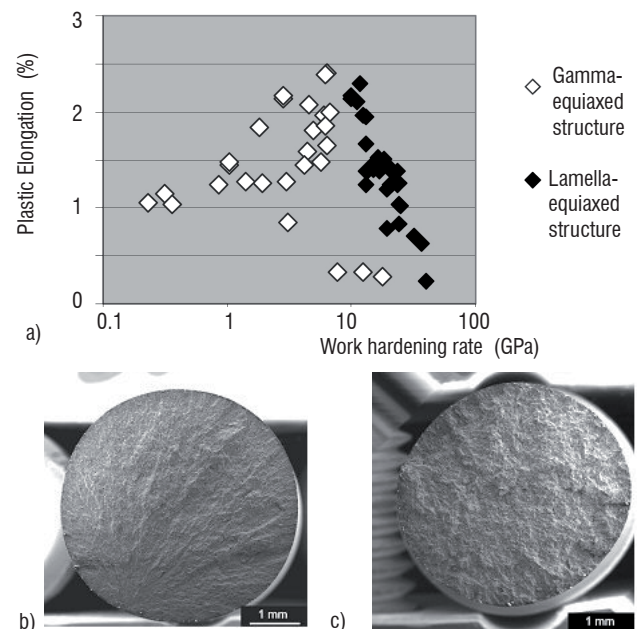


Figure 2 - Tensile behavior for γ -equiaxed and lamellar structures: (a) dependence of tensile ductility on work hardening rate, (b) heterogeneous deformation mode for γ -equiaxed structure, (c) homogeneous deformation mode for lamellar structure (after reference 25).

Phase transformations and microstructural changes

The uniform microstructure obtained for powder compacts after HIPing gave the opportunity to further investigate some microstructural evolutions and related phase transformations in the 47-2-2 alloy. By using specific heat treatment conditions, Onera has identified novel phase transformations in the well-known 47-2-2 alloy [27]. In parallel, coarsening mechanisms for the grain size and lamellar spacing were clarified and are now examined. As already documented in the literature [28,29], heat treatments above the α transus temperature result in fully-lamellar microstructures. Moreover, the holding time is found to control the lamellar colony size while the cooling rate controls the lamellar spacing. However, more unusual is the fact that the lamellar colony size appears to be also cooling rate dependent, whereas the lamellar spacing is also time dependent [27].

Several authors [30-33] have already pointed out the fact that the final grain size is time dependent and not cooling rate dependent since grain coarsening should only occur above the α -transus. However, our quantitative analyses [27] show that over-aged samples still exhibit a significant effect of the cooling rate on grain coarsening. Some authors [34,35] have already noticed that, despite the fact that additional time during cooling seems to be negligible with respect to the holding time, different cooling rates nevertheless lead to significant differences in colony size. However, they assumed that the lamellar colonies produced at a higher cooling rate had a size similar to that of prior α grains, and that slow cooling would enhance some lamellar impingement at colony boundaries leading to substantial colony coarsening.

In the work performed at Onera, Icy Water Quenching (IWQ) provides information about the initial grain size just before cooling. In more detail, the number of small lamellar colonies is higher in the Furnace Cooled (FC) sample than in the IWQ sample and the FC sample has the greatest amount of large colonies in the 400-650 μm range, indicating that larger grains also exhibit coarsening. But, the Intermediate sand Cooled (IC) sample is the one with small grains as the most representative grain size fraction. The overall grain size distributions can then be interpreted by two distinct mechanisms: (i) a nucleation of new grains leading to small lamellar colonies with cooling rate dependence and (ii) a moderate grain growth during furnace cooling. The nucleation of new grains is likely to occur before the onset of lamellar formation, since there cannot be more than one lamellar colony per prior α grain. Continuous Cooling Transformation (CCT) experiments have reported that an undercooling of at least 70°C below the α -transus temperature is necessary for nucleation of lamellae, even for very slow continuous cooling [34]. It is then reasonable to assume that new α grains are formed within this sub-transus temperature range, even though no in-situ experiment was carried out to confirm such a nucleation process. We may assume that a relaxation phenomenon of internal stresses takes place by promoting new α grains, in particular at triple point junctions.

Looking now at the lamellar spacing, Yang [36] suggested that a relationship can be established with the grain size which is controlled by the holding time, the lamellar spacing λ being proportional to $D^{-1/2}$. In the Onera study, the first interpretation given for the inverse relationship between D and λ is related to a decrease in the total grain boundary area per unit volume, owing to grain coarsening. Therefore, larger prior α grains tend to reduce the number of primary γ nucleation sites

and then to decrease the rate of the lamellar transformation. The lamellar transformation is expected to be shifted to lower temperatures with a sufficiently large undercooling to provide the internal energy required to overcome the excess strain energy resulting from the lamellar formation. The second interpretation is related to a difference in interfacial energy at prior α grain boundaries. After only 5 minutes of annealing, the interfacial energy would remain sufficiently high to trigger the lamellar transformation at a relatively high temperature in the sub-transus temperature range. Further, a holding time of 120 minutes would then drastically reduce the interfacial energy through grain coarsening, thus leading to a dramatic delay of the lamellar transformation. Such a lower-temperature homogeneous transformation of fine lamellae is also consistent with the relatively planar morphology of colony boundaries.

Mechanical properties

Heat treatment studies were conducted to optimize the mechanical properties. A relationship has been established between twin and dislocation densities, grain size and interlamellar spacing, and mechanical properties. The microstructure could then be optimized via process parameters in order to meet industrial requirements in terms of tensile, creep, and fatigue. For instance, the yield stress is affected by the lamellar colony size (Φ) and by the interlamellar spacing (λ), which can be described by the following Hall-Petch expression :

$$\sigma_e = \sigma_0 + k_\Phi \cdot \Phi^{-1/2} + k_\lambda \cdot \lambda^{-1/2} \quad (1)$$

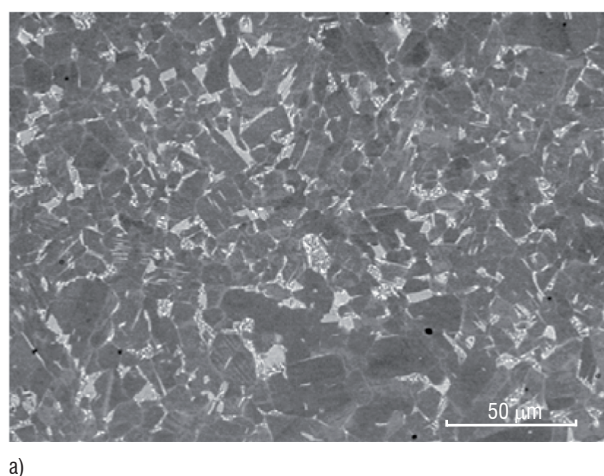
with σ_e the slip system strength, σ_0 the lattice friction stress related to the Peierls-Nabarro stress and solute hardening, and the two empirical constants k_Φ and k_λ related to the critical stresses required for a dislocation to cross a grain boundary and a lamellar interface, respectively. Fatigue behavior and resonant mode behavior are also important properties for component design. In particular, the response from such a material to cyclic deformation during transitional engine speed was found to involve considerable work hardening, which could become deleterious for the component life due to the quite moderate intrinsic ductility of the γ -TiAl alloy.

Onera developed an optimized microstructure that exhibits a significantly lower work hardening rate while preserving the fatigue life of the material. The Cyclic Stress-Strain (CSS) behavior at 20°C and at 500°C of the 47-2-2 alloy showed that an increasing amount of lamellar colonies, a finer lamellar spacing and a smaller γ grain size, can markedly decrease the cyclic strain hardening rate [37]. This is due to enhanced twinning development and then to reduction of the dislocation mean free path which delay the formation of a fully-developed vein-like structure. At 500°C an increased dislocation activity takes place at the expense of mechanical twinning. This replacement of twins by dislocation walls and networks favors the formation of the vein-like structure. Therefore, the CSS behavior at 500°C can be described by two regimes, the first one involving strong hardening which is related to the vein-like structure formation, and the second one which is a saturation regime where a braid-like structure is formed. Finally, the fine fully lamellar microstructure appears to be the optimized microstructure for achieving a lower cyclic strain hardening and a longer fatigue life. For engineering applications, such microstructures are known to be adequate for enhanced creep resistance and fracture toughness properties.

Alternative PM processing routes

Extensive work was carried out by using the Spark Plasma Sintering process (SPS) to consolidate different γ -TiAl alloys. Indeed, the advanced "PM + SPS" processing route is competitive for TiAl implementation in aerospace and automotive applications by reducing the production cost to affordable levels and by ensuring parts with enhanced homogeneity, pore-free microstructures and with suppressed cast mis-runs, melting defects or hot forging cracks. Since the heat inside the material is generated by a Joule effect, whereas the die remains relatively cold, thermal gradients are observed in the parts which involve significant radial structural inhomogeneities. However, uniform microstructures can be achieved either by sintering at elevated temperatures, typically above the α -transus, or by using a boron-containing alloy [38]. In the latter case, the as-SPS alloy displayed the same duplex and uniform microstructures which consist of a mixture of lamellar colonies and γ grains, for sintering temperatures in the 1190-1250°C temperature range. Looking now at the tensile properties, the overall set of tensile data shows a very low scatter for duplicate tests together with a nice balance of yield strength – tensile ductility for the two alloys investigated of the compositions Ti-47Al-2Cr-2Nb and Ti-44Al-2Cr-2Nb-1B [38].

A direct manufacturing technology was employed to produce fully dense parts of 47-2-2 by means of Direct Metal Deposition (DMD). This Onera study was aimed at demonstrating the feasibility of manufacturing TiAl components without hard tooling. In practice, a Computer-Aided Design (CAD) file is used to index the laser and/or the powder supply which is aimed at building 3D parts. DMD is a technique which consists of injecting the powder through a nozzle with helium gas onto the substrate to be molten layer by layer. Because of the high power density used, which leads to very high cooling rate in the order of 10^3 up to 10^4 °C/s, ultra fine and metastable structures are generated. In order to build up dense 3D parts with a good geometrical quality using DMD, a number of key parameters have to be controlled, i.e. the laser power, the powder feeding rate, and the displacement rate. However, when using a single heating source, tensile residual stresses cannot be overcome completely by strong thermal gradients. In order to slow down the cooling rate and relieve the residual stresses, pre-heating of the substrate at a temperature of 300°C and gradual post-heating from external heat source with a low energy density were successfully used to yield crack-free samples



[39]. A concomitant reduction of the feeding rate and a power increase were found to lead to a better dilution and a better coupling with the substrate.

Thermal-induced inhomogeneities were successfully reduced by annealing treatments. A sub α -transus solution anneal at 1250°C appears to be successful in providing a quite uniform duplex microstructure which was then selected for tensile testing. Tensile test results of laser formed 47-2-2 alloy were encouraging since the tensile ductility was even better than that of HIP casting, which is indicative of the fact that post heat-treatments can be successfully used to restore the structural homogeneity and to relieve the residual stresses (figures 3a,b). Comparison of building directions X and Z reveals in average a 30% difference in tensile elongations which is indicative of a moderate anisotropy.

Current status on temperature limitations

Thermal stability after long term exposure

The thermal stability of high-temperature applications of γ -TiAl-based alloys after long term exposure needs to be studied. In the literature, a significant reduction in ductility was reported to occur after exposure at service temperatures such as 650-700°C. Different interpretations were proposed for this material embrittlement: surface oxidation [40] – loss of residual machining stresses [41] – structural instabilities [42,43] – more in-depth interstitial contaminations [44,45] – hydrogen and moisture embrittlement [46,47] – aluminum depletion [48,49] – formation of brittle phase particles [41,50] – nitrogen effect [51].

Attempts were made at Onera to discover the predominant factors causing this reduction in the tensile ductility of the 47-2-2 alloy [52]. Gas atomized powder compacts were used in the as-HIPed condition to yield a near- γ microstructure for the major part of this study because the location of the initiation fracture site is enhanced with such a microstructure, as shown in figure 2. Despite different machining procedures for the unexposed test specimens, YS and UTS values were found to be very close to each other, with tensile elongations between 1.5 and 2%. The deformation mechanisms which were investigated by TEM include a twinning propagation stage through the entire

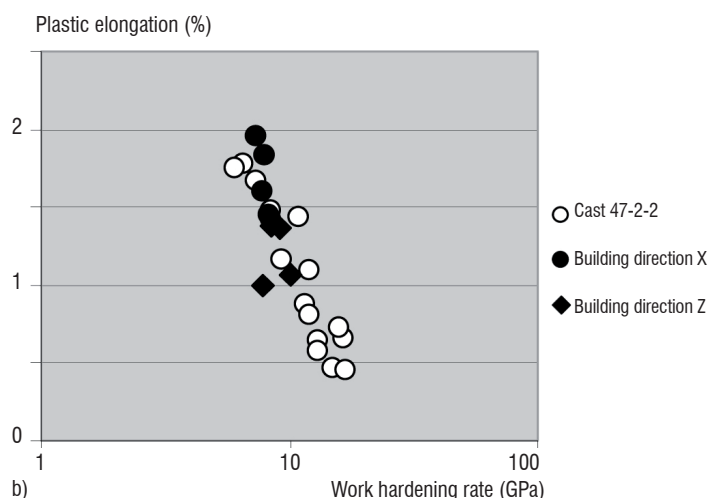
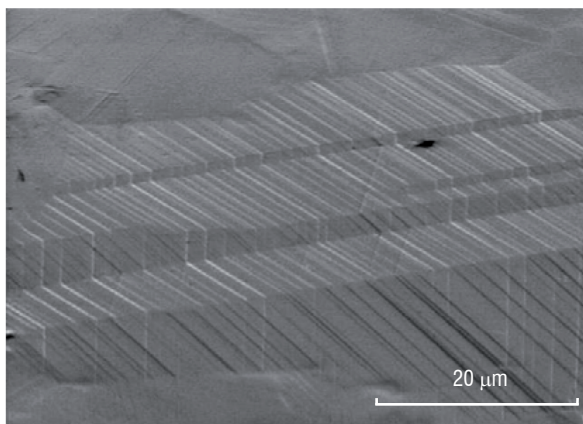


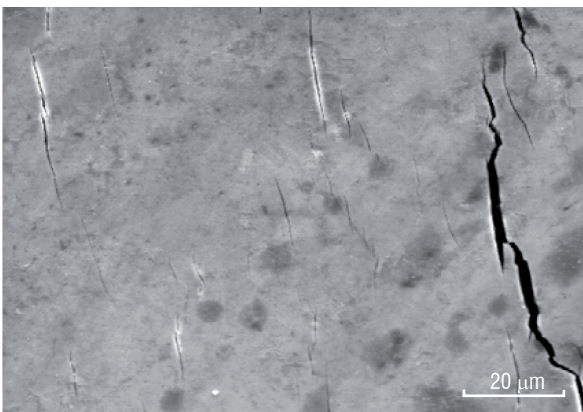
Figure 3 - DMD laser formed 47-2-2 alloy: (a) SEM micrograph of the duplex microstructure, (b) Work hardening rate dependence of tensile ductility for cast and both building directions.

gage length of the specimen, followed by the motion of ordinary dislocations and a build-up of dislocation tangles. Electro-polished gage length surfaces revealed deformation-induced instabilities which can be ascribed to mechanical twinning, as emphasized in Figure 4a. The topographical features which result from cross twinning at the surface do not appear to induce any micro-cracks which might lead to the premature failure of the test specimen.

Blanks and machined test specimens were exposed at 700°C for 400 hours in ambient air, followed by air cooling. When machining the blanks afterwards, the room temperature tensile properties did not seem to differ much from the as-received condition. On the other hand, the exposed test specimens exhibited a pronounced reduction in tensile elongation irrespective of the machining procedure. In our near- γ microstructure, the difference in tensile ductility between surface-removed and surface-retained specimens can definitely be ascribed to a surface-related embrittlement. SEM examinations confirmed this statement since the four specimens actually failed from the surface. The exposure time at 700°C was long enough to enhance the formation of a fine alumina scale with an Al-depletion layer, the composition of which is close to Ti_3Al , both having lower deformation capability than the TiAl subscale.



a)



b)

Figure 4 - SEM micrographs of the electro-polished gage length surface after testing for the near- γ microstructure: (a) unexposed test specimen, (b) test specimen exposed 2 hours at 700°C (after reference 52).

Moreover, a short exposure at 700°C for 2 hours already had a detrimental effect on ductility with strain values between 0.2 and 0.9%, with a fracture originating at the surface. However, no oxide layer was detected at the surface. It was interesting to detect some sub-surface

cracks which could be indicative of a residual stress gradient from the surface towards the interior of the sample generated by air cooling (figure 4b). Moreover, mechanical twinning was not evidenced at the surface, suggesting that a twinning arrest mechanism occurs in the upper layer. It can be concluded that deformation is not accommodated at the surface, thus leading to the build-up of stress concentrations in the sub-scale. Eventually, cracks were found to be generated either from this sub-scale or from the surface. Surface machining was undertaken after short term-exposure to confirm the surface-related embrittlement. When the surface was removed down to 10 μm by mechanical polishing, room temperature tensile elongations were recovered.

Oxidation, corrosion, protection of TiAl

For high temperature applications, such as turbine blades, the oxidation resistance of binary γ -TiAl and also low-alloyed γ -TiAl-based alloys above 700°C still needs to be improved. Indeed at high temperature in air, layers of mixed oxides grow by competitive oxidation of the Ti and Al alloying elements, which prevents the formation of a continuous and dense α -alumina layer that would provide an effective oxidation barrier [53]. On the contrary, γ -TiAl alloys form a continuous alumina scale in pure oxygen up to 1000°C [54].

An XPS and AES investigation of the early stages of oxidation of γ -TiAl (111) surfaces at 650 °C under low O_2 pressure has been carried out at Onera [55,56]. The results show a mechanism of formation of the oxide layers exhibiting three stages [55]. Stage I is a pre-oxidation stage characterized by the adsorption and absorption of oxygen species. When the sub-surface is saturated with dissolved oxygen, the selective oxidation of the alloy leads to the nucleation and growth of ultra-thin (~ 1.2 nm on γ -TiAl) alumina layers characterizing Stage II. The growth of the alumina layers is limited by the transport of Al in the alloy. An Al-depleted metallic phase is formed underneath the oxide. When a critical concentration is reached ($Ti_{82}-Al_{18}$ on γ -TiAl), titanium oxidation occurs characterizing Stage III. Ti(III) and Ti(IV) oxide particles are formed at the surface of the still growing alumina layer, which indicates the transfer, possibly promoted by defects, of titanium cations through alumina layer. The direct atomic-scale observations of the interface between the ultrathin protective alumina grown on a γ -TiAl(111) enabled us to observe, for the first time, nanocavities resulting from the self-assembling of atomic vacancies injected at the interface by the growth mechanism of the protective oxide [56].

The poor oxidation behavior in air, as compared to pure oxygen, is commonly referred as the “nitrogen effect”. Dettenwanger [51] and Lang [57] proposed that the inability of binary γ -TiAl alloys to develop a continuous alumina scale is related to the formation of TiN during the initial stages of oxidation. The formation of these titanium nitrides interrupts the alumina formed at the metal/scale interface and hinders the formation of a continuous and protective alumina layer. As oxidation proceeds, the TiN is subsequently oxidized to form TiO_2 . The process results in the formation of an intermixed Al_2O_3/TiO_2 scale rather than a continuous scale of alumina.

Efforts to improve the oxidation resistance of γ -TiAl alloys have concentrated on different approaches. The first one was based on alloying additions that favored the formation of a highly protective alumina surface layer. Ternary or higher order alloying additions can reduce the rate of oxidation of γ -alloys. In particular, additions of tungsten, tantalum, zirconium, molybdenum, chromium, manganese, silicon,

yttrium, rhenium and/or niobium improve the oxidation resistance by decreasing the growth rate of the intermixed $\text{Al}_2\text{O}_3/\text{TiO}_2$ [58]. Proposed explanations include the decrease of the oxygen vacancies in TiO_2 by doping (valence control rule) [54], an increase of Al/Ti activity to favor Al_2O_3 layer formation [54], the formation of a diffusion layer [58] and the suppression of internal oxidation by reducing oxygen solubility [59]. Niobium effects at the onset of oxidation of $\alpha_2\text{-Ti}_{3-x}\text{AlNb}_x$ alloys were studied at Onera and Chimie Paris Tech by XPS after exposure to pure oxygen and oxygen/nitrogen mixture at 650°C ($P=1.0.10^{-7}$ mbar). Niobium contents were observed to be linked to a poisoning of the entry of $\text{N}_{\text{adsorbed}}$ and a decrease of the nitrogen mobility in the alloys, both being supposed to be responsible for the improvement of the oxidation resistance of these niobium doped alloys [60]. Although further experimental confirmation is needed, these data suggest that niobium addition may reduce the “nitrogen effect” that exists during the $\gamma\text{-TiAl}$ oxidation.

Microalloying with small amounts of halogens can improve the oxidation resistance up to 1000°C [61] which may avoid the potential negative effects on mechanical properties by bulk addition of ternary or quaternary elements. Halogen can be applied in many ways: treatment with diluted halogen liquid or gas, ion implantation. This improvement of the oxidation resistance is based on the selective transport of aluminum via the gas phase from the substrate metal to the oxide scale through pores and micro-cracks by gaseous halogen gas. This leads to the formation of a continuous scale of growing Al_2O_3 . But this positive halogen effect only works in a certain halogen concentration window. A lower value of halogen gas pressure is needed to ensure that the beneficial halogen effect is obtained via the AlCl gas formation, and an upper value must not be exceeded in order to avoid the titanium chloride formation which prevents the select formation of an alumina layer [62]. These limiting values depend on the nature of the halogen.

Other solutions for improving the oxidation/corrosion resistance consist of using surface-modification techniques. Overlay coatings as MCrAlY , CrAlYN or TiAlCr [63] have been studied although with unsatisfactory results due to thermal mismatch between coating and substrate which often resulted in spallation during cyclic oxidation.

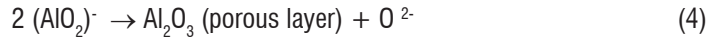
Numerous studies in this field have been conducted with pack-cementation processes – such as siliconizing or aluminizing – to improve oxidation resistance [64-66]. But only a small number of studies concern the corrosion issues [67-69] and the influence of oxidation/corrosion mechanisms on the mechanical properties [41,70,71].

Exposures of TiAl alloys to corrosive atmosphere at temperatures higher than 700-750°C reduced the high temperature tensile strength

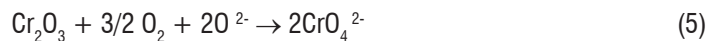
[70,72]. The corrosion mechanisms of $\gamma\text{-TiAl}$ are complex. It is believed [73] that the sulfur released from the sulfate reacts with the alumina layer formed on the alloy surface at the beginning in an O_2 -containing atmosphere according to the following reactions called basic fluxing:



The O^{2-} ions produced in the condensed salt react with the oxide leading to the formation of a porous and non protective alumina layer.



Chromium inhibits the basic fluxing by decreasing the O^{2-} ions concentration in the salt.



In the opposite sense, the presence of an excess of niobium may increase the corrosion rate. In the presence of oxygen, niobium forms an acid oxide Nb_2O_5 that increases local acidity and then induces the acidic dissolution of oxides (particularly chromia) as follows [73]:



The presence of niobium is detrimental during the corrosion process while chromium is beneficial. For alloys containing both chromium and niobium, effects of these two elements cancel each other and there is no internal corrosion while in the case of alloys only containing niobium generalized internal corrosion occurs [70].

Adding NaCl to the sulfate increases the corrosion process. According to [68] the reaction of sodium chloride with titanium and aluminum from the alloy, or their oxides from the scale leads to the formation of TiCl_2 , AlCl_3 , (TiCl_2 formation being favored up to 750°C) and Na_2TiO_3 . The titanium and aluminum chlorides oxidize in mixed layer of titanium oxide and alumina by releasing HCl and Cl_2 gases. These gases go through pores and channels in the oxide scales down to the metal-oxide interface and lead to the formation of new halides TiCl_2 and AlCl_3 by releasing H_2 gas which attacks preferentially the α_2 -phases present at the grain boundaries leading to an intergranular corrosion. This mechanism implies a self-propagating corrosion process that explains why the corrosion phenomenon is more extensive when the NaCl salt content increases [70] (figure 5).

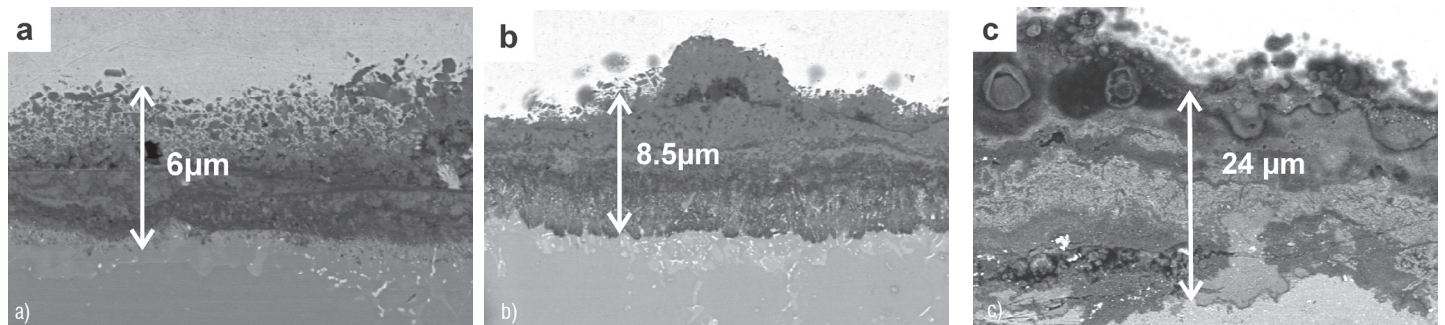


Figure 5 - SEM cross section micrograph of the layers formed at 750°C on corroded Ti46.5Al4 (Cr, Nb, Ta, B) after (a) 1000 1-hour cycles with 97.3 wt% Na_2SO_4 and 2.7 wt% NaCl (b) 1000 1-hour cycles with 75 wt% Na_2SO_4 and 25 wt% NaCl (c) 550 1-hour cycles with pure NaCl, (fig 5b and c after reference 70).

Onera developed coatings to protect γ -TiAl alloys against corrosion [64,72,74]. A typical pack cementation treatment was used to improve the corrosion resistance of the alloy G4 with the composition Ti-47Al-1Re-1W-0.2Si (at%) alloy. Cyclic corrosion tests were performed at 800°C in air up to 800 cycles with a mixture composed of 97.3 wt% of Na₂SO₄ and 2.7 wt% of NaCl. It was shown that the cyclic corrosion resistance of the coated TiAl was improved by aluminizing. The coated specimen firstly exhibited the lowest mass variation but finally cracks appeared during the cyclic corrosion, which were filled with oxide that led to spallation. Nevertheless, at the end of the test, the total corroded bulk area is less developed for the coated specimen than for the uncoated one. No particular creep degradation was observed in terms of mechanical behavior of the different test specimens, neither from the pack cementation treatment nor from the corrosion. It can then be concluded that the alloy G4 is suitable, even without coating, for turbine applications in corroded atmospheres at least up to 800°C.

An Au-based specific coating designed to prevent pure NaCl corrosion of a Ti-48Al-2Cr-2Nb alloy has also been investigated at Onera [72,74]. A two TiAlAu₂ and TiAlAu layers coating, obtained after vacuum heat treatment, was effective in improving NaCl salt corrosion resistance of the coated specimens at 600°C. This good resistance is attributable to the formation of an Al₂O₃ scale on the surface of the coated specimen. During oxidation, or NaCl salt corrosion, the upper TiAlAu₂ layer of the coating transformed in an Al₂O₃ layer on a TiAu₂ layer. The slightly lower creep properties exhibited by the coated specimens are presumably linked to new phases that segregate at grain boundaries during the vacuum heat treatment. The degradation of creep properties after coating and corrosion is believed to be brought about either by the formation of the brittle TiAu₂ phase or by corrosion or oxygen diffusion through the upper scale.

The main factors that can cause the degradation of mechanical properties of the coated γ -TiAl alloys are brittleness of the coating layers and differences in the coefficient of thermal expansion between the coating and the substrate. Onera is involved in the optimization of high corrosion resistance through a "coating by design" approach. Based on microstructural and mechanical characterizations of the different coating layers, and on diffusion and mechanical models, the aim of this work in progress is to optimize the coating process in order to improve the corrosion resistance of the coated alloy whilst minimizing the mechanical property degradation.

Acknowledgements

The authors are grateful to O. BERTEAUX, P. JOSSO, G. HENAFF, A. COURET and C. COLIN for helpful discussion. Thanks are addressed to J.L. RAVIART, A. BACHELIER-LOCQ, F. POPOFF for their technical contribution. The authors are also indebted to J.L. LUNEL, D. REGEN, A. RAFRAY and A. MOREL for material preparation and testing.

References

- [1] T. TETSUI - *Development of a New TiAl Turbocharger for High Temperature Use*. Third International Workshop on γ -TiAl Technologies, Bamberg, Germany, 29-31 May 2006 (unpublished).
- [2] R.E. SCHAFRIK - *A Perspective on Intermetallic Commercialization for Aero-Turbine Applications*. Structural Intermetallics 2001, edited by K.J. Hemker et al, TMS, pp. 13-17, 2001.
- [3] M. YAMAGUCHI, and H. INUI - *TiAl Compounds for Structural Applications*. Structural Intermetallics 1993, edited by R. Darolia et al, The Minerals, Metals & Materials Society, pp. 127-142, 1993.

Conclusions

The status of Onera's work on alloy development, microstructural evolution through heat treatments, mechanical properties and different manufacturing technologies for γ -TiAl-based alloys has been reviewed. Assessment of improved mechanical properties with respect to conventional near- γ alloys was demonstrated with alloy G4. In contrast to the commonly practiced sub-transus heat treatment applied to conventional gamma aluminides to achieve nearly lamellar microstructure, a modified heat treatment condition leading to a duplex microstructure was found to considerably increase the creep resistance and the fatigue behavior of this alloy. Centrifugal casting of γ -TiAl-based alloys appears to be sufficiently mature to offer the possibility of manufacturing complex shaped components. On the other hand, a better repeatability of mechanical properties was successfully achieved by using other processing approaches such as pre-alloyed powder metallurgy which is more tolerant to the alloy chemistry and to the microstructure. The investigation of static and cyclic tensile behaviors in gas atomized powder compacts indicate that three parameters (lamellar colonies, lamellar spacing and γ grain size) are the most relevant microstructural variables that directly influence tensile and fatigue properties. A model of the mechanism of the formation of vein-like structure based on how they are influenced by three microstructural parameters has also been developed. For the different microstructures involved, a correlation between the ability to develop a vein-like structure and the cyclic strain hardening rate has been established. The more prone the microstructure is to develop a vein-like structure, the higher the cyclic strain hardening rate. In another respect, attractive mechanical properties can be achieved by applying alternative Spark Plasma Sintering and laser forming powder technologies. In particular, the feasibility of applying laser forming to the manufacture of γ -TiAl parts has been evaluated on the basis of good geometrical quality, satisfactory metallurgical integrity and the possibility of achieving an optimized microstructure. Finally, tensile ductility degradation after long term exposure is directly related to the brittleness of the surface layers (oxide scales – Al-depletion layer – Nb-rich precipitates). On the other hand, after short term exposure, embrittlement comes from the interactions between several factors: an oxygen-enriched surface, a mechanical twinning propagation which is hindered towards the surface as well as a residual stress gradient generated by air cooling. In terms of environmental durability the titanium aluminides look promising as there are solutions for improving their resistance. In particular, tailored coatings were designed to protect them against oxidation and salt corrosion while retaining good mechanical properties ■

- [4] N. BIERY, M. DE GRAEF, J. BEUTH, R. RABAN, A. ELLIOTT, T.M. POLLOCK and C. AUSTIN - *Use of Weibull Statistics to Quantify Property Variability in TiAl Alloys*. Metall. Mater. Trans. A, vol. 33A, pp. 3127-3136, 2002.
- [5] T. TSUJIMOTO and K. HASHIMOTO - *Structures and Properties of TiAl-Base Alloys Containing Mn*. High-Temperature Ordered Intermetallic Alloys III, edited by C.T. Liu et al, MRS, Pittsburgh, vol. 133, pp.391-396, 1989.
- [6] S-C. HUANG - *Titanium Aluminum Alloys Modified by Chromium and Niobium and Method of Preparation*. US. Patent 4,879,092, Nov. 7, 1989.
- [7] G.L. CHEN, Z.C. LIU, J.P. LIN and W.J. ZHANG - *Strengthening Mechanism in High Nb Containing TiAl Base Alloys*. Structural Intermetallics 2001, edited by K.J. Hemker et al, Warrendale PA: TMS, pp.475-482, 2001.
- [8] V. IMAYEV, R. IMAYEV and A. KUZNETSOV - *Thermomechanical Processing and Tensile Mechanical Properties of β -Solidifying γ -TiAl + α_2 -Ti₃Al Alloys*. Gamma Titanium Aluminides 2003, edited by Y-W. Kim et al, Warrendale, PA: TMS, pp.311-318, 2003.
- [9] F. APPEL, J.D.H. PAUL, M. OEHRING and C. BUQUE - *Recent Developments of TiAl Alloys Towards Improved High-Temperature Capability*. Gamma Titanium Aluminides 2003, edited by Y-W. Kim et al, Warrendale, PA: TMS, pp.139-152, 2003.
- [10] W.E. VOICE, M. HENDERSON, E.F.J. SHELTON and X. WU - *Gamma Titanium Aluminide, TNB*. Intermetallics, vol. 13, pp. 959-964, 2005.
- [11] M.A. MUNOZ-MORRIS, I. GIL and D.G. MORRIS - *Microstructural Stability of γ -Based TiAl Intermetallics Containing β Phase*. Intermetallics, vol.13, pp. 929-936, 2005.
- [12] X. WU - *Review of alloy and process development of TiAl alloys* - Intermetallics, vol. 14, pp.1114-1124, 2006.
- [13] H.F. CHLADIL, H. CLEMENS, H. LEITNER, A. BARTELS, R. GERLING, F.-P. SCHIMANSKY and S. KREMMER - *Phase Transformations in High Niobium and Carbon Containing γ -TiAl Based Alloys*. Intermetallics, vol. 14, 1194-1198, 2006.
- [14] J. LAPIN, Z. GABALCOVÁ, T. PELACHOVÁ and O. BAJANA - *Microstructure and Mechanical Properties of a Cast Intermetallic Ti-46Al-8Ta Alloy*. Materials Science Forum Vols. 638-642, pp. 1368-1373, 2010.
- [15] S. NAKA, M. THOMAS, C. SANCHEZ and T. KHAN - *Development of Third Generation Castable Gamma Titanium Aluminides: Role of Solidification Paths*. Proc. of 2nd Symposium on Structural Intermetallics, edited by M.V. Nathal et al, Seven Springs, PA (USA), September 21-26, pp. 313-322, 1997.
- [16] M. GRANGE, J.L. RAVIART and M. THOMAS - *Influence of Microstructure on Tensile and Creep Properties of a New Castable TiAl-based Alloy*. Met. Trans. vol. 35A, pp. 2087-2102, 2004.
- [17] V. LUPINC, M. MARCHIONNI, G. ONOFRIO, M. NAZMY and M. STAUBLI - *Microstructural Effects on Creep, Low Cycle Fatigue and Crack Propagation Behavior of Ti-47Al-2W-0.5Si*. Gamma Titanium Aluminides 1999, edited by Y-W. Kim et al, The Minerals, Metals & Materials Society, pp. 349-356, 1999.
- [18] A. PONCHEL - *Champs de déformation locaux autour d'éléments d'addition en solution solide dans les alliages ordonnés TiAl+X (X=Cr, Mn, Ni, Zr, Nb). Déterminations expérimentales et théoriques : Application à l'étude de l'interaction soluté-dislocation*. Thèse de doctorat, Université Pierre et Marie Curie Paris VI, 30 octobre 2001.
- [19] Y.L. HAO, D.S. XU, Y.Y. CUI, R. YANG and D. LI - *The Site Occupancies of Alloying Elements in TiAl and Ti₃Al Alloys*. Acta mater. Vol. 47, N° 4, pp. 1129-1139, 1999.
- [20] S. NISHIKIORI, S. TAKAHASHI, S. SATOU, T. TANAKA and T. MATSUO - *Microstructure and Creep Strength of Fully-Lamellar Ti₃Al Alloys Containing Beta-Phase*. Materials Science and Engineering, vol. A329-331, pp. 802-809, 2002.
- [21] M. KRISHNAN, B. NATARAJAN, V.K. VASUDEVAN and D.M. DIMIDUK - *Microstructure Evolution in Gamma Titanium Aluminides Containing Beta-Phase Stabilizers and Boron Addition*. Proc. of 2nd Symposium on Structural Intermetallics, edited by M.V. Nathal et al, Seven Springs, PA (USA), September 21-26, pp. 235-244, 1997.
- [22] J. LAPIN, T. PELACHOVA - *Microstructural Stability of a Cast Ti-45.2Al-2W-0.6Si-0.7B Alloy at Temperatures 973-1073K*. Intermetallics, vol. 14, pp.1175-1180, 2006.
- [23] M. PANINSKI - *Development of a Casting Technology for Complex TiAl Components*. Third International Workshop on γ -TiAl Technologies, Bamberg, Germany, 29-31 May 2006 (unpublished).
- [24] Y. CHEN, Y. CHEN, F. KONG and S. XIAO - *Fabrication and Processing of Gamma Titanium Aluminides - a Review*. Materials Science Forum Vols. 638-642, pp. 1281-1287, 2010.
- [25] M. THOMAS - *Robustness Versus Performance Assessment for Different Gamma-TiAl Processing Routes*. MRS Boston 2010, to be published.
- [26] M. THOMAS, J.-L. RAVIART and F. POPOFF - *Composition and Microstructural Effects upon Creep Strength of Gas Atomized TiAl Alloy Powder Compacts*. Thermec'09, Berlin, 2009 (unpublished).
- [27] O. BERTEAUX, F. POPOFF and M. THOMAS - *An Experimental Assessment of the Effects of Heat Treatment on the Microstructure of Ti-47Al-2Cr-2Nb Powder Compacts*. Met. Trans. A, vol. 39A, n°10, pp. 2281-2296, 2008.
- [28] V. SEETHARAMAN and S.L. SEMIATIN - *Analysis of Grain Growth in a Two-Phase Gamma Titanium Aluminide Alloy*. Metall. Mater. Trans. A, vol. 28A, pp. 947-954, 1997.
- [29] Y. BHAMBRI, V.K. SIKKA, W.D. PORTER, E.A. LORIA and T. CARNEIRO - *Effect of Composition and Cooling Rate on the Transformation of α to γ Phase in TiAl Alloys*. Mater. Sci. Eng. A, vol.424, Issues 1-2, pp. 361-365, 2006.
- [30] G.X. GUO FU'AN - *Influence de la microstructure sur des propriétés mécaniques et des contraintes internes d'un alliage intermétallique biphasé à base de TiAl*. Thèse de doctorat de l'ENSAM Paris, 20 juin 2001.
- [31] G.X. CAO, L.F. FU, J.G. LIN, Y.G. ZHANG and C.Q. CHEN - *The Relationships of Microstructure and Properties of a Fully Lamellar TiAl Alloy*. Intermetallics, vol.8, pp. 647-653, 2000.
- [32] C.E. WEN, K. YASUE, J.G. LIN, Y.G. ZHANG and C.Q. CHEN - *The Effect of Lamellar Spacing on the Creep Behavior of a Fully Lamellar TiAl Alloy*. Intermetallics, vol.8, pp. 525-529, 2000.
- [33] G.W. QIN, G.D. W. SMITH, B.J. INKSON and R. DUNIN-BORKOWSKI - *Distribution Behaviour of Alloying Elements in $\alpha_2(\alpha)/\gamma$ Lamellae of TiAl-Based Alloy*. Intermetallics, vol.8, pp. 945-952, 2000.
- [34] M. CHARPENTIER, D. DALOZ, A. HAZOTTE and E. AEBY-GAUTIER - *Toward a Better Understanding of Chemical and Microstructure Heterogeneities Inherited from Solidification and Solid State Phase Transformations in the Ti-48Al-2Cr-2Nb Alloy*. Matériaux & Techniques, N°1-2, pp. 39-50, 2004.
- [35] T. NOVOSELOVA, S. MALINOV and W. SHA - *Experimental Study of the Effects of Heat Treatment on Microstructure and Grain Size of a Gamma TiAl Alloy*. Intermetallics, vol.11, pp. 491-499, 2003.
- [36] R. YANG - *A Theory of the Formation and Growth of Primary Gamma/Alpha₂ Lamellae in Fully-Lamellar Gamma-TiAl Based Alloys*. International Titanium Aluminide Workshop, Birmingham, UK, 5-7 July 2004 (unpublished).
- [37] O. BERTEAUX, F. POPOFF, M. JOUIAD, G. HENAFF and M. THOMAS - *Microstructure Dependence of the Strain Hardening Rate in a PM Ti-48Al-2Cr-2Nb Alloy*. Third International Workshop on γ -TiAl Technologies, Bamberg, Germany, 29-31 May 2006.
- [38] A. COURET, G. MOLENAT, J. GALY and M. THOMAS - *Microstructures and Mechanical Properties of TiAl Alloys Consolidated by Spark Plasma Sintering*. Intermetallics, vol. 16 n° 9, pp. 1134-1141, 2008.

- [39] T. VILARO, V. KOTTMANN-REXERODT, M. THOMAS, P. BERTRAND, L. THIVILLON, C. COLIN, S. ABED, V. JI, P. AUBRY, T. MALOT and P. PEYRE - *Direct Fabrication of a Ti-47Al-2Cr-2Nb Alloy by Selective Laser Melting and Direct Metal Deposition Processes*. Adv. Mater. Res., 89-91, p. 586, 2010.
- [40] S.L. DRAPER, B.A. LERCH, I.E. LOCCI, M. SHAZLY and V. PRAKASH - *Effect of Exposure on the Mechanical Properties of Gamma MET PX*. Intermetallics, vol. 13, pp. 1014-1019, 2005.
- [41] R. PATHER, W.A. MITTEN, P. HOLDWAY, H.S. UBHI, A. WISBEY and J.W. BROOKS - *The Effect of High Temperature Exposure on the Tensile Properties of γ TiAl Alloys*. Intermetallics, vol. 11, pp.1015-1027, 2003.
- [42] Z.W. HUANG, W. VOYCE and W.P. BOWEN - *Thermal Stability of a Fine-Grained Fully Lamellar TiAl-Based Alloy*. Structural Intermetallics 2001, edited by K.J. Hemker et al, Warrendale, PA: TMS, pp. 551-560, 2001.
- [43] M. BESCHLIESSER, H. CLEMENS, H. KESTLER and F. JEGLITSCH - *Phase Stability of a γ -TiAl Based Alloy Upon Annealing: Comparison Between Experiment and Thermodynamic Calculations*. Scripta Mater, vol. 49, N°4, pp. 279-284, 2003.
- [44] Y-W. KIM - *Recent Advances in Gamma Titanium Aluminide Alloys*. High Temperature Ordered Intermetallic Alloys IV, , edited by J.O. Stiegler et al, MRS, pp. 777-794, 1991.
- [45] T. KAWABATA, M. TADANO and O. IZUMI - *Effect of Purity and Second Phase on Ductility of TiAl*. Scripta Met, vol.22, N°11 pp.1725-1730, 1988.
- [46] C.T. LIU, Y-W. KIM - *Room-Temperature Environmental Embrittlement in a TiAl Alloy*. Scripta Met, vol. 27, n°5, pp. 599-603, 1992.
- [47] A. ZELLER, F. DETTENWANGER and M. SCHÜTZE - *Influence of Water Vapour on the Oxidation Behaviour of Titanium Aluminides*. Intermetallics, vol. 10 pp. 59-72, 2002.
- [48] S.L. DRAPER, G. DAS, I. LOCCI, J.D. WHITTENBERGER, B.A. LERCH and H. KESTLER - *Microstructure and Mechanical Properties of Extruded Gamma MET PX*. Gamma Titanium Aluminides 2003, edited by Y-W. Kim et al, Warrendale, PA: TMS, pp. 207-212, 2003.
- [49] V. MAURICE, G. DESPERT, S. ZANNA, P. JOSSO, M.-P. BACOS and P. MARCUS - *The Growth of Protective Ultra-Thin Alumina Layers on γ -TiAl(111) Intermetallic Single-Crystal Surfaces*. Surface Science, vol. 596, pp. 61-73, 2005.
- [50] G. SCHUMACHER, F. DETTENWANGER, M. SCHÜTZE, A. IBERL and D. REIL - *XRD Investigations of the Phosphorus Effect on the Oxidation of TiAl Alloys by High-Resolution Methods*. Oxidation of Metals, vol. 54 n° 3-4, pp.317-37, 2000.
- [51] F. DETTENWANGER, E. SCHUMANN, M. RÜHLE, J. RAKOWSKI and G.H. MEIER - *Microstructural Study of Oxidized γ -TiAl*. Oxidation of Metals vol. 50 n° 3-4, pp. 269-305, 1998.
- [52] M. THOMAS, O. BERTEAUX, F. POPOFF, M.-P. BACOS, A. MOREL, B. PASSILLY and V. JI - *Effects of exposure at 700°C on RT Tensile Properties in a PM γ -TiAl*. Intermetallics, vol. 14, pp. 1143-1150, 2006.
- [53] J.M. RAKOWSKI, F.S. PETTIT, G.H. MEIER - *The Effect of Nitrogen on the Oxidation of γ -TiAl*. Scripta Metall. et Mater. Vol. 33, n°6, pp. 997-1003, 1995.
- [54] N.S. CHOUDHURY, H.C. GRAHAM, J.W.HINZE - *Properties of high temperature alloys*. Edited by Z.A.Fouroulis and F.S.Pettit (Pennington,N): the Electrochemical Society, pp. 668-680, 1976.
- [55] V. MAURICE, G. DESPERT, S. ZANNA, P. JOSSO, M.-P. BACOS and P. MARCUS - *XPS Study of the Initial Stages of Oxidation of α_2 -Ti₃Al and γ -TiAl Intermetallic Alloys*. Acta Materialia, vol. 55, pp. 3315-3325, 2007.
- [56] V. MAURICE, G. DESPERT, S. ZANNA, M.-P. BACOS and P. MARCUS - *Self-Assembling of Atomic Vacancies at an Oxide/Intermetallic Alloy Interface*. Nature Materials, vol. 3, pp. 687-691, 2004.
- [57] C. LANG, M. SCHÜTZE - *TEM Investigations of the Early Stages of TiAl Oxidation*. Oxidation of Metals, vol. 46 n° 3-4, pp. 255-285, 1996.
- [58] S. TANIGUCHI, T. SHIBAT - *Influence of Additional Elements on the Oxidation Behaviour of TiAl*. Intermetallics, vol. 4 supplement 1, pp. S85-S93, 1996.
- [59] Y. SHIDA, H. ANADA - *Role of W, Mo, Nb and Si on Oxidation of TiAl in Air at High Temperatures*. Materials Transactions, JIM vol. 35, n° 9, pp. 623-631, 1994.
- [60] V. MAURICE, A-G. NOUMET, S. ZANNA, P. JOSSO, M.-P. BACOS and P. MARCUS - *Dual Surface and Bulk Control by Nb of the Penetration of Environmental Elements in TiAl Intermetallic Alloys*. Acta Mater., vol. 56, pp. 3963-3968, 2008.
- [61] A. DONCHEV, E. RICHTER, M. SCHÜTZE and R. YANKOV - *Improvement of the Oxidation Behaviour of TiAl-Alloys by Treatment With Halogens*. Intermetallics, vol. 14, n°10-11, pp. 1168-1174, 2006.
- [62] A. DONCHEV, B. GLEESON and M. SCHÜTZE - *Thermodynamic Considerations of the Beneficial Effect of Halogens on the Oxidation Resistance of TiAl-Based Alloys*. Intermetallics, vol. 11 n°5, pp. 387-398, 2003.
- [63] R. BRAUN, F. ROVERE, P.H. MAYROFER and C. LEYENS - *Environmental Protection of γ -TiAl Based Alloy Ti-45Al-8Nb by CrAlN Thin Films and Thermal Barrier Coatings*. Intermetallics, vol. 18, n°4, pp. 479-486, 2010.
- [64] M.-P. BACOS, M. THOMAS, J-L. RAVIART, A. MOREL, S. NAVEOS and P. JOSSO - *Influence of Surface Modification and Long Term-Exposure on Mechanical Creep Properties of γ -TiAl G4*. Materials at High Temperatures, vol. 26, n°4, pp. 339-346, 2009.
- [65] V. GAUTHIER, F. DETTENWANGER, M. SCHÜTZE, V. SHEMET and W.J. QUADAKKERS - *Oxidation-Resistant Aluminide Coatings on γ -TiAl*. Oxidation of Metals, vol. 59, n°3/4, pp. 233-255, 2003.
- [66] Z.D.XIANG, S.R.ROSE and P.K. DATTA - *Oxidation Resistance of Diffusion Coatings Formed by Pack-Codeposition of Al and Si on γ -TiAl*. J. Mat. Sci., vol. 39, n°6, pp. 2099-2106, 2004.
- [67] Z. TANG, F. WANG, W. WU - *Hot-corrosion Behavior of TiAl-Base Intermetallics in Molten Salts*. Oxidation of Metals vol. 51, n°3-4, pp. 235-250, 1999.
- [68] J.R. NICHOLLS, J. LEGETT and P. ANDREWS. - *Hot Salt Corrosion of Titanium Aluminides*. Materials and Corrosion vol. 48, pp. 56-64, 1997.
- [69] Z. YAO, M. MAREK - *NaCl-Induced Hot Corrosion of a Titanium Aluminide Alloy*. Materials Science and Engineering A; vols. 192-193 part 2, pp. 994-1000, 1995.
- [70] M-P. BACOS, A. MOREL, S. NAVEOS, A BACHELIER-LOQC, P. JOSSO and M. THOMAS - *The Effect of Oxidised and Corroded Long Term Exposure on Tensile Properties of Two Gamma-TiAl Alloys*. Intermetallics, vol. 14, n° 1, pp. 102-113, 2006.
- [71] X.Y. LI, S. TANIGUCHI - *Correlation of High Temperature Oxidation with Tensile Properties for Ti-48Al-2Cr-2Nb and Ti-48Al-2Cr-2Fe Alloys*. Intermetallics, vol. 13, n°7, pp.683-693, 2005.
- [72] M.-P. BACOS, M. THOMAS, J-L. RAVIART, A. MOREL, S. MERCIER and P. JOSSO - *Influence of an Oxidation Protective Coating Upon hot Corrosion and Mechanical Behaviour of Ti-48Al-2Cr-2Nb Alloy*. Intermetallics, vol. 19, pp.1120-1129, 2011.
- [73] R. MORBIOLI, P. STEINMETZ and C. DURET - *Mechanisms of Hot Corrosion of NiAl-Type Aluminide Coatings in Aeronautical Conditions*. Materials Science and Engineering, vol. 87, pp. 337-344, 1987.
- [74] M.-P. BACOS, P. JOSSO - *Procédé pour protéger la surface d'un substrat en alliage intermétallique à base d'aluminium de titane contre la corrosion*. Patent 2918672, 9 July 2007.

Acronymes

AES (Auger Electron Spectroscopy)
CAD (Computer-Aided Design)
CCT (Continuous Cooling Transformation)
CSS (Cyclic Stress-Strain)
DMD (Direct Metal Deposition)
FAR (Federal Acquisition Regulation)
FC (Furnace Cooled)
HCF (High Cycle Fatigue)
HIP (Hot Isostatic Pressing)
IC (Intermediate sand Cooled)
IWQ (Icy Water Quenching)
LCF (Low Cycle Fatigue)
PM (Powder Metallurgy)
SEM (Scanning Electron Microscopy)
SPS (Spark Plasma Sintering)
TEM (Transmission Electron Microscopy)
UTS (Ultimate Tensile Strength)
XPS (X-ray Photoelectron Spectroscopy)
YS (Yield Stress)

Authors



Marc Thomas received his Doctorate (Ph.D) from Sussex University (UK) in 1983. He received his HDR (Research Director Authorization) diploma in 2005, for his research activities on titanium aluminides over the last twenty years. He is currently in charge of the development of structured multifunctional materials at Onera and of additional research projects dealing with powder manufacturing and using innovative processes such as Spark Plasma Sintering and Laser Forming.



Marie-Pierre Bacos graduated from the «Ecole Nationale Supérieure de Chimie de Paris» Paris (1981) and received a PhD degree in Applied Chemistry from University Paris VI (1983). She joined Onera in 1983 where she has been involved in oxidation and corrosion mechanisms and in the development of innovative coatings and brazing technologies. She is the Head of the Materials and Architecture Research Unit at Onera Chatillon.

S. Drawin, J.F. Justin
(Onera)

E-mail: stefan.drawin@onera.fr

Advanced Lightweight Silicide and Nitride Based Materials for Turbo-Engine Applications

Refractory metal silicides and nitride-based ceramics combine two properties that may lead to substantial reductions in aircraft fuel consumption: compared to the most advanced nickel-based superalloys presently used in aeronautical turbines, they can withstand higher temperatures and may have lower densities. Niobium silicide-based alloys and silicon nitride / molybdenum disilicide composites are currently being developed for turbine hot section components for both aircraft engines and land-based turbines. This paper presents the processing techniques, the microstructural features and the mechanical and physical properties at low and high temperatures as well as the oxidation behaviour of these materials. Prospects in composition optimisation, manufacturing processes and control of the microstructure for further improvements are discussed.

Introduction

The performances of aircraft/rotorcraft and land-based gas turbine engines are evaluated using both technical and sociological metrics. Thus not only are the technical needs considered, but the economic and environmental issues are also addressed, the most important ones being: overall power or thrust, specific thrust, fuel efficiency, service reliability (reduced maintenance), emission of CO₂, NO_x and other species (soot, unburnt fuel, CO, etc.), external noise emission and cost.

Hot section components in aircraft/rotorcraft and land-based gas turbine engines differ in size and service conditions and within each group there are very different specifications. In general, for military engines, thrust and thrust-over-mass ratio are privileged, while in commercial airline engines it is rather the operating costs. Several land-based turbine types are in operation, from the low power micro-turbines for local (or distributed) power generation up to the grid-connected 345-MW turbines, for which the regime can go from “peaker” (short duration service cycles to accommodate higher electrical power demands on the grid) to the “baseload” (covering the basic grid power demands). In all cases, the desire to reduce owner costs and operating costs, including fuel consumption and maintenance, are technological driving forces that are becoming more and more important.

These issues have been frequently addressed in advanced engine architecture, new cycle and combustor designs, optimised aerodynamics and new cooling concepts. But the development of hot section materials (especially in the turbine) has clearly made a critical contribution to performance gains in turbo-machinery. However, their still limited

capabilities with respect to the severe operating conditions and the demands of engine designers often limit further improvements in turbine efficiency. A substantial increase in the temperature capability of turbine materials, especially for the airfoil materials which work in the harshest conditions because they are located directly in the hot gas flow coming from the combustion chamber, would allow for significant performance enhancements. High temperature materials represent one major enabler in the long-term for most, if not all, future engine improvements.

Several new material families are being developed to allow for a significant increase (more than 150°C) in airfoil material operating temperatures. The most advanced materials currently used are Ni-based single-crystal superalloys for which the upper operating temperature limit is 1100°C ~ 1150°C.

In addition to the higher temperature capability, low density is crucial for many applications. Besides the component mass reduction which is of high priority for aircraft/rotorcraft turbines, it also allows for the down-scaling of the disk, since the centrifugal forces created by the lighter blades are lower.

Two new material systems, refractory metal (especially Mo and Nb) based silicide multiphase alloys and silicon nitride based ceramics, show promising properties that would allow for their use in future turbines.

The development status will be presented in this paper for both silicide and nitride based materials with a focus on the work carried out at Onera.

Silicide based alloys

Refractory metals (RM), with their outstanding properties (high melting point, good mechanical and creep strength), are currently used as components for ultra-high temperature applications in inert atmospheres. However, RM and RM-alloys suffer from severe oxidation in air. The sublimation of molybdenum oxide, for instance, occurs already at intermediate temperatures ($> 500^{\circ}\text{C}$) which excludes any applications at high temperature in air.

By contrast, RM-silicides can be used in air at higher temperatures and even up to temperatures of 1650°C (e.g. MoSi_2 heating elements). But these compounds also suffer from catastrophic oxidation (pesteing) at intermediate temperatures (ca. $600^{\circ}\text{C} - 800^{\circ}\text{C}$) and exhibit brittleness at ambient temperature. However, the essential objective of the current research on RM-silicide based alloys is to manufacture a composite material that takes advantage of (a) the beneficial oxidation and creep resistance of the silicides and (b) the outstanding mechanical properties of the RM.

RM based metal-intermetallic composites were developed under US impetus in the 1990's. Two systems show the greatest potential [1], Nb-Si and Mo-Si, as metal-toughened intermetallic-strengthened materials with a metallic phase volume fraction between 35% and 60%. The melting points of these multiphase alloys are in excess of 1750°C (Nb-base) and 1950°C (Mo-base), respectively, substantially higher than those of Ni-base superalloys.

Several European universities and research centres, together with major engine manufacturers and a refractory metal supplier, most of them already working on specific aspects of these alloys, pooled their expertise within the European Union funded ULTIMAT project, under the coordination of Onera [2]. This project aimed at providing a sound technological basis for the use of these materials in future turbines, with alloy development focused on the improvement of key properties such as high temperature creep strength, oxidation resistance and room temperature toughness, in connection with semi-industrial scale manufacturing and fabrication processes. In parallel with those of the US and European (France, Germany, UK) teams, investigations on RM-silicide based materials are in progress in Japan, China, India and Brazil.

Mo-silicide based alloys

Berczik [3] first patented Mo-Si-B alloys with compositions in the Mo-rich corner (figure 1) and a manufacturing approach which in essence comprises a rapid solidification step. Boron is added to allow for the formation of a dense protective borosilicate glass.

A typical microstructure yields a matrix of the Mo(ss) solid solution providing good fracture toughness and ductility below 600°C , and embedded intermetallic Mo_3Si and/or Mo_5SiB_2 type compounds (T2 phase) for enhancing both creep and oxidation resistance.

Within the ULTIMAT project, the studied alloys were basically three-phase Mo-9Si-8B alloy (at.%) [4], with addition of solid solution strengthening elements, with volume fractions of about 55% Mo(ss), 30% T2 and 15% Mo_3Si . Although for these alloys the density is comparable or slightly higher than that of superalloys, higher specific mechanical properties make them attractive for many applications.

Manufacturing and microstructures

Due to the very high melting temperatures (in excess of 2000°C) and the heterogeneous microstructures obtained, ingot metallurgy is now seldom used to study and improve the properties of Mo-Si based alloys. Powder metallurgy (PM), on the other hand, is the manufacturing route that has been privileged. Mechanical alloying (MA) in particular can yield supersaturated or even amorphous powders that can be processed to overcome the brittleness exhibited by conventionally solidified ingots or even PM-processed inert gas atomised powders [5]. This has been applied to a Mo-3Nb-9Si-8B alloy in the ULTIMAT project. MA, in a vertical attritor for 10 h, is sufficient to completely dissolve the Nb, Si and B in the Mo matrix. Subsequent heat treatment allows for homogeneous precipitation of the intermetallic phases within the Mo(ss) matrix. The powder was isostatically cold pressed and sintered under H_2 at 1450°C . Finally, billets of 50 mm diameter and 200 mm length were obtained by hot isostatic pressing (HIP) the sintered bars at 1500°C under 200 MPa. The microstructure in the HIP'ed state is shown in figure 2. The expected phases, Mo(ss), Mo_3Si and T2 are present and the residual porosity is below 1%. Some undesired silica inclusions and some larger-scale areas of Mo(ss) are also visible due to a non-optimised MA process.

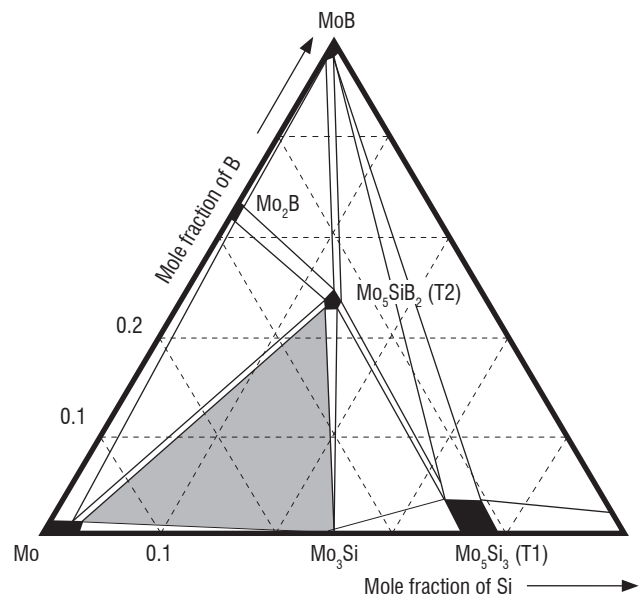


Figure 1 – Mo-rich part of the Mo-Si-B phase diagram at 1600°C . The shaded area is the Mo-Mo₃Si-T2 three-phase region

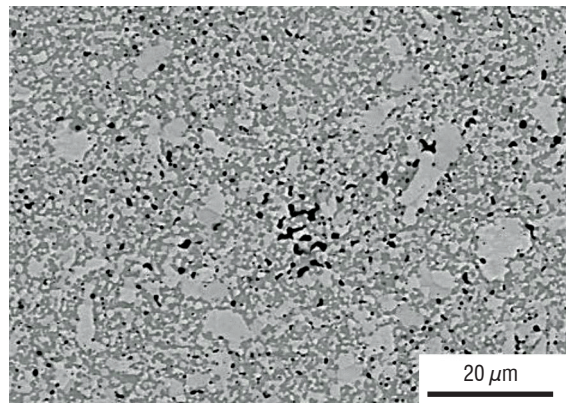


Figure 2 – SEM micrograph of a MA processed and HIP'ed MoNbSiB alloy with Mo(ss) (bright), intermetallics (grey) and undesired silica (black)

Mechanical properties

Tensile tests were performed on Mo-Si-B alloys under vacuum at 20°C to 1600°C [6]. While no significant ductility was measured at temperatures below 1100°C, a total elongation to fracture of about 5% could be observed at 1200°C. The ultimate tensile strength remained close to 500 MPa in the 20°C - 1100°C range. Premature brittle failure within the elastic domain was observed. Crack growth occurred through the continuous network of intermetallics. The ultrafine grained (grain size $\sim 0.8 \mu\text{m}$) and equiaxed microstructure shown in figure 2 exhibited superplastic behaviour: tensile strains to failure of 300% at 1300°C and 400% at 1400°C were obtained for a strain rate of 10^{-4} s^{-1} . This demonstrates the potential for superplastic forming. At present, the applicable forming processes appear limited to lower deformation rates ($< 0.1 \text{ s}^{-1}$) which make conventional (fast) hot forming processes like forging or rolling at even higher temperatures still a critical issue for sound wrought processing. Instead, isothermal forging in closed dies may become realistic to manufacture parts with intricate shapes.

The creep behaviour was evaluated by compression tests in temperature and stress ranges of 1050°C to 1315°C and 100 MPa to 400 MPa. The presence of significant plasticity for Mo-Si-B based alloys above 1100°C indicates poor creep resistance. However, the coarsening of the microstructure by an appropriate heat treatment significantly improved the creep behaviour [4], as shown in figure 3. Annealing at 1700°C for 10 h in a vacuum increased the grain size of Mo(ss) and intermetallic phases by almost a factor ten. The consequence was a decrease of the compressive creep rate by one order of magnitude at all temperatures. The stress exponent remained at a quite low value of $n \sim 2.3$, indicating that grain and interphase boundary sliding processes still play a major role in plastic deformation.

Oxidation resistance

Mo-Si-B alloys tend to form a protective borosilicate scale when exposed to high temperatures. They undergo "peeling oxidation" at intermediate temperatures (600°C-850°C) when excessively slow scale formation kinetics allow Mo to oxidise to volatile MoO_3 . Peeling can however be avoided by a preliminary short high temperature oxidation treatment that builds up the protective scale. Protective coatings are nevertheless needed to increase the Mo-Si-B alloy lifetime. Figure 4 shows that a SIBOR[®] plasma sprayed coating [7] provides excellent protection at intermediate temperatures. The good behaviour of both a SIBOR[®] coating and a pack-cementation FeCrSiB coating was confirmed in a burner rig test at 900°C, 1000°C and 1100°C where lifetimes of over 500 cycles were obtained [8].

Recent developments

The main current research topic is the improvement of the ductility of the Mo-Si-B alloys which exhibit a ductile to brittle transition temperature above 600°C. One direction is better control of the silicon content in the Mo solid solution and the micro-alloying with zirconium or Y_2O_3 particles [9,10].

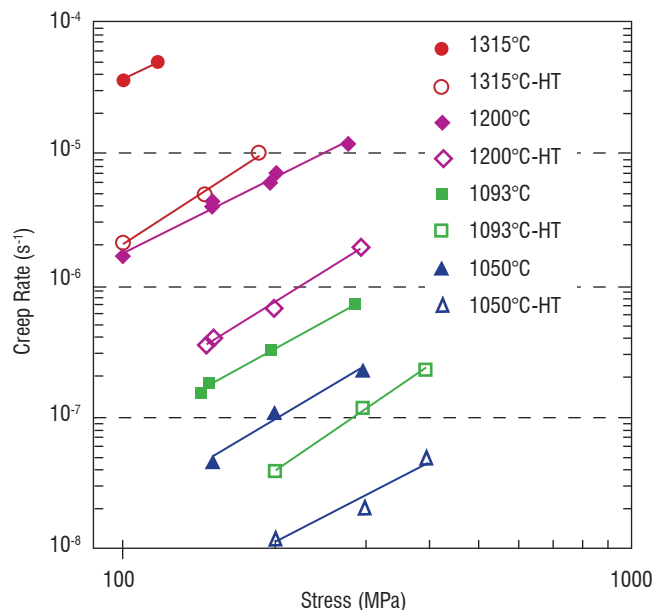


Figure 3 – Steady-state creep rate vs. stress for the HIP'ed (full symbols) and heat-treated (open symbols) MoNbSiB alloy in the 1050°C - 1315°C range

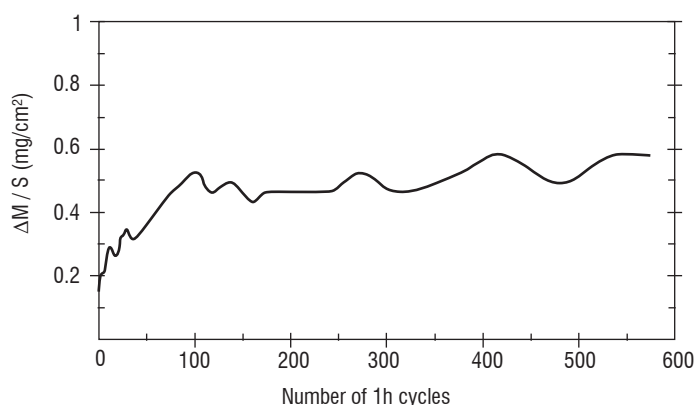


Figure 4 – Cyclic oxidation at 815°C of a SIBOR[®] coated Mo-Nb-Si-B alloy

Nb-base silicides

Alloys in the binary Nb-Si system exhibit good creep resistance, but poor toughness and oxidation resistance. Their properties can be improved by alloying, leading for example to the NbTiHfCrAlSi metal and silicide composites (MASC) family, as developed by General Electric [11,12]. The Nb-Si based materials consist of a metal solid solution M(ss) (M being *e.g.* Nb+Ti+Hf+...) with M_5Si_3 and/or M_3Si silicide phases (figure 5), with densities in the range $6.5 - 7.9 \text{ g/cm}^3$ depending on the composition. Other phases, such as NbCr_2 -type Laves phases in the case of higher Cr content for better oxidation resistance or hexagonal M_5Si_3 (deleterious for creep resistance) in the case of high Ti and/or Hf contents, can also be present.

At high temperatures, M(ss) can be considered as the softest and the silicide as the most creep resistant phase. Improvement of the high temperature mechanical properties (mainly creep resistance) can thus be obtained by enhancing the properties of M(ss) and/or increasing the silicide volume fraction. High silicide contents simultaneously

improve the oxidation resistance, but decrease toughness and ductility at room and intermediate temperatures. Alloys with silicon content of up to 24 at.% have been studied in the ULTMAT project.

Manufacturing and microstructures

Ingot metallurgy (mainly vacuum arc melting, but also Czochralski drawing for directional solidification) is widely used at laboratory-scale to manufacture Nb-Si samples needed for microstructural, mechanical and oxidation characterisations [2,8,11-13]. Unlike Mo-Si-B alloys, complex alloying is required to improve the properties of Nb-Si alloys; the oxidation resistance of the M(ss) phase, for example, is improved by the addition of fairly high amounts of Ti, Cr, Al, which lowers the melting temperature of near-eutectic alloys. The manufacturing of shaped parts by investment casting (figure 6), which requires specific high temperature mould materials with a reduced reactivity with the Nb-Si melt [11, 14], becomes possible as an extension of the manufacturing route developed for Ni-based superalloy components.

It remains difficult to improve the mechanical properties because of the heterogeneous microstructure within the ingot. Metallurgical defects (pores, micro-cracks, etc.) are encountered; for high Si-content alloys – exhibiting high melting points – and despite the small mismatch between the coefficient of thermal expansion (CTE) of the M(ss) and M_5Si_3 phases (e.g. between pure Nb and a MASC alloy: less than $2 \cdot 10^{-6} K^{-1}$), cracking occurs during cool down in the sometimes several hundred micrometer-long silicide dendrites. This significantly reduces the tensile strength compared with the compression strength [11], since the tensile behaviour is controlled here by the defects. Thermo-mechanical treatments of cast alloys only partially succeeded in improving the properties.

The PM approach offers a possibility of refining and better controlling the microstructure and allows for processing at temperatures far below the melting point. First, investigations were carried out on two-phase Nb-Nb₅Si₃ materials obtained by hot uniaxial pressing (HP) and HIP'ing Nb + Nb₅Si₃ powder mixtures [15], or with reactive hot pressing of Nb + Si powder blends [16]. Alloys with more complex compositions with up to nine elements have to be manufactured using pre-alloyed powders obtained either at lab-scale by crushing and milling arc-melted buttons, or by using the rotating electrode process [11], or inert gas atomisation [5,11]; blending of elemental powders followed by sintering and HIP steps can also be used [2]. Pre-alloyed powder compaction is usually done either by extrusion [11,17] or using emerging processes like spark plasma sintering (SPS) [17]. If the microstructure of the as-extruded alloy is relatively fine, it is coarsened by heat treatment, as shown in figure 7. The mechanical properties of these alloys and the optimisation of the microstructure through powder preparation and heat treatment are currently under investigation.

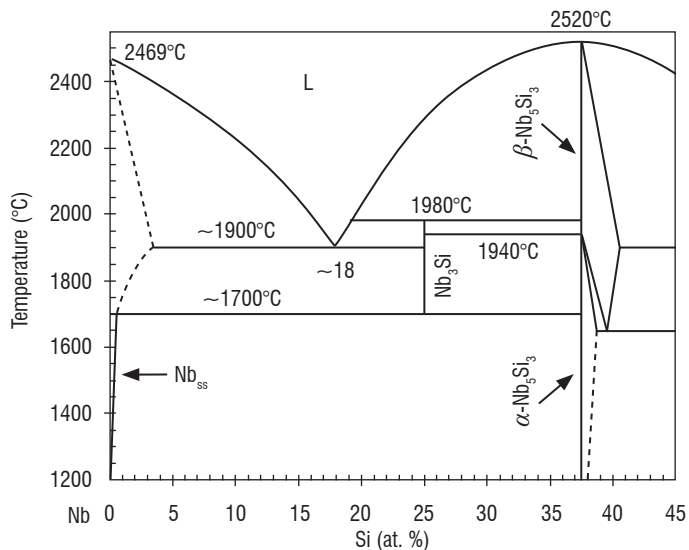


Figure 5 – Nb-rich part of the binary Nb-Si phase diagram



Figure 6 – Investment cast Nb-Si based demo blade (height ~ 120 mm) [2]

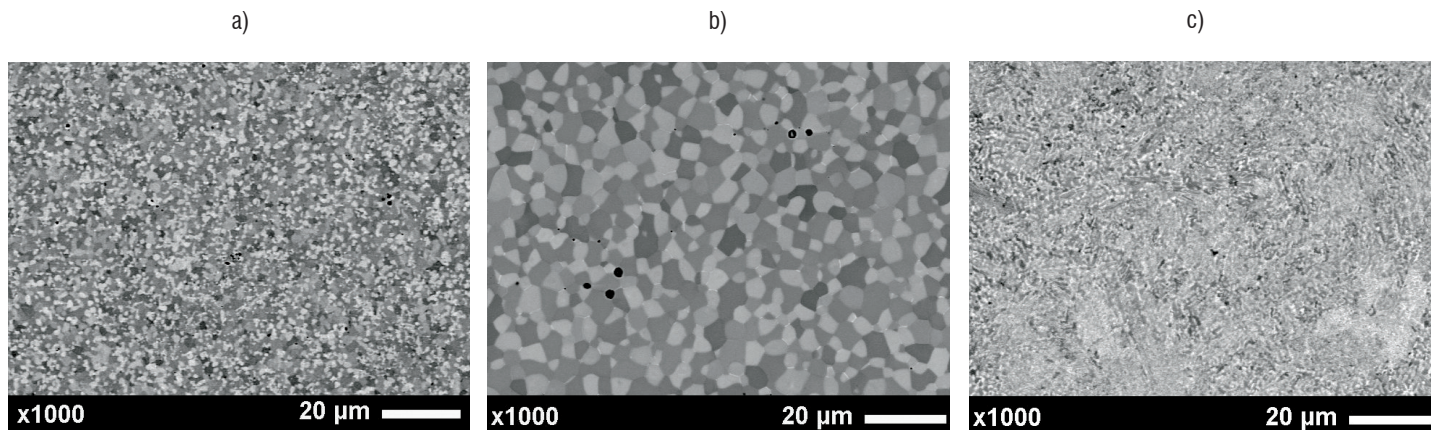


Figure 7 – Microstructure of an Nb-25Ti-8Hf-2Al-2Cr-16Si PM alloy (transverse section) from gas-atomised powders [17]: a) extruded at 1400°C, b) same after heat treatment at 1400°C for 24 h showing an increase of the grain size by a factor 5 to 10, c) as-sintered by SPS at 1325°C

Mechanical properties

The mechanical properties of a range of NbTiHfCrAlSi alloys, including strength, fracture and fatigue behaviour, and creep resistance, were reviewed by Bewlay and co-workers [11,12]. Figure 8 illustrates how alloying improves the fracture toughness of directionally solidified alloys. Alloying with refractory elements results in very high strength and creep resistance. For example, solid solution strengthening of Nb(ss) by Mo and W is very efficient, so that Nb-Mo-(Hf or W)-(16-18)Si alloys exhibit yield strengths at 1400°C higher than 700 MPa in compression [18] (figure 9) and higher than 240 MPa in tension (Nb-18Si-5Mo-5Hf-2C, [19]). These improvements are however obtained at the expense of toughness, ductility (the reported ductile-brittle transition temperatures can be as high as 1200°C [19]) and oxidation resistance.

Creep resistance is one of the major properties to be optimised if high temperature applications for rotating components are the aim. Some results obtained in the ULTIMAT project are presented in figure 10, which shows the effect of an increase in Si content, with respect to the MASC alloy (16 at.% Si), and the addition of refractory elements [8]. An improvement in temperature capability of about 150°C can be obtained over the CMSX-4 single crystal Ni based superalloy.

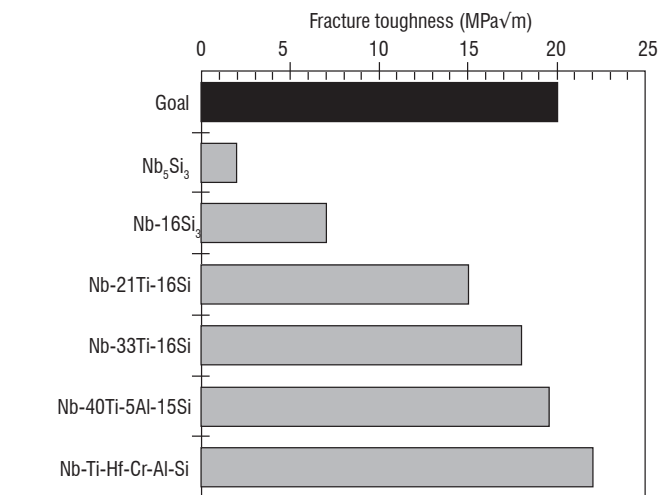


Figure 8 – Fracture toughness of directionally solidified Nb-Si alloys (except Nb₅Si₃), from [12]

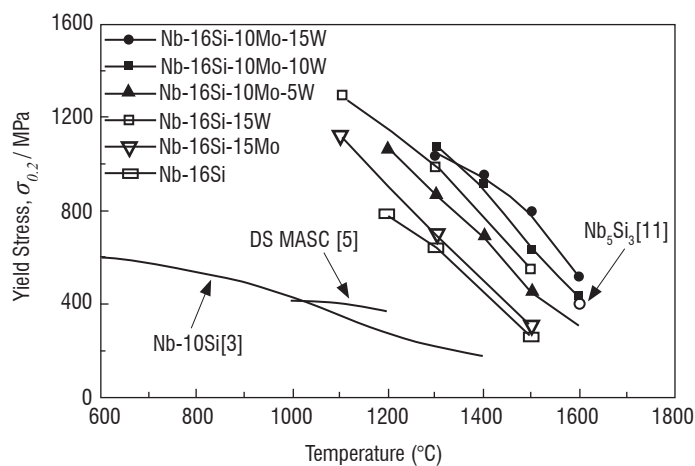


Figure 9 – Compressive yield strength of Nb-16Si-Mo-W cast and heat treated (1700°C, 48 h) alloys compared with single-phase Nb₅Si₃, and two-phase Nb-10Si and Nb-25Ti-8Hf-2Al-2Cr-16Si (MASC) alloys (see references in [18]). Tests were performed in an argon atmosphere

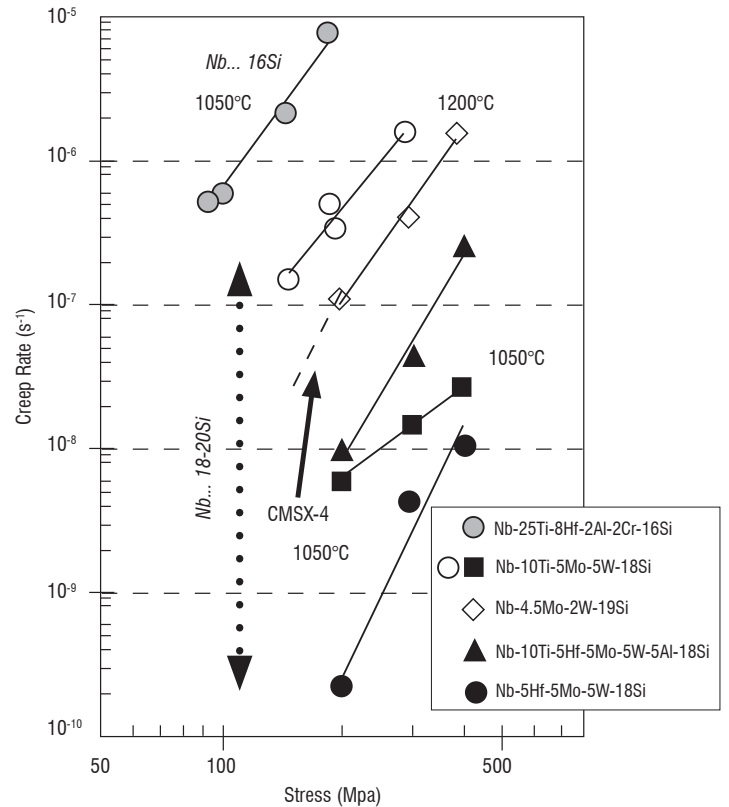


Figure 10 – Compression creep rate as a function of applied stress for Nb-Si based alloys and CMSX-4 [8]

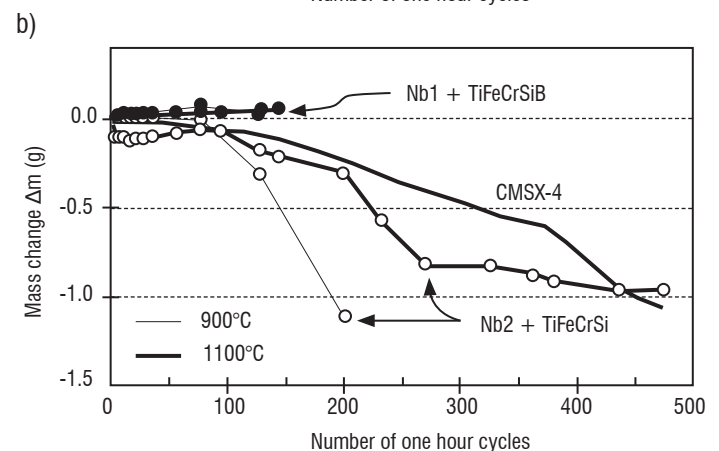
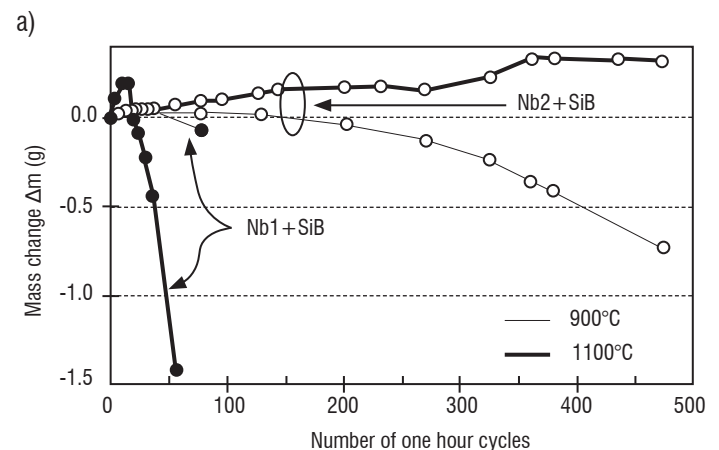


Figure 11 – Mass variation of Nb-Si alloys with various pack cmentation coatings in a burner rig test at 900°C and 1100°C, compared with CMSX-4 at 1100°C (1 g corresponds to ca. 11 mg/cm²) [8]. Nb1 is Nb-10Ti-5Mo-5W-18Si, Nb2 is Nb-25Ti-8Hf-2Al-2Cr-16Si

Oxidation resistance

Niobium does not form any protective oxide scale and suffers from severe internal and external oxidation above 500°C, so binary Nb-Si alloys do not withstand exposure to air at high temperature. Alloying and protection with an adequate coating is thus required. In addition to high temperature oxidation, Nb-Si binary alloys also undergo a “pest” phenomenon in the range 600-900°C, characterised by a rapid disintegration of the material. Both oxidation regimes have been investigated and protective coatings developed [2,8,11-14,20]. Elements like Al, Cr, Ti, Hf but also Sn (specifically for pesting), Ge and B can be added to improve the oxidation behaviour, either in solid solution (*e.g.* for reduction of oxygen solubility and diffusion in Nb, or oxygen scavenging) or for the formation of oxidation resistant phases such as NbCr₂-type Laves phases.

The effect of the microstructure on the high temperature oxidation behaviour has rarely been reported on in the literature. The beneficial effect of a reduced Nb(ss) volume fraction was quickly noticed [12]. It has also been shown that the refined microstructure of PM extruded alloys improves the oxidation resistance at all investigated temperatures (800-1200°C) compared with cast and heat-treated alloys [21].

Conventional cyclic testing in static laboratory air [14] as well as burner rig tests [8] in which samples are exposed to both corrosion by molten salts and oxidation in cyclic conditions have shown in the ULTMAT project that pack-cementation deposited coatings provide excellent protection for both oxidation regimes. The composition of the TiFeCrSiB coating (figure 11) is adjusted to form a continuous glassy borosilicate layer with an adequate viscosity that drastically slows down the ingress of oxygen into the Nb-Si alloy, and is able to fill any crack appearing during cycling.

Recent developments

Current research topics include better control of the microstructure of the Nb-Si based alloys and the simultaneous improvement of the major mechanical properties (creep, toughness, ductility) and oxidation resistance, including the further development of protective coatings. Powder metallurgy-based advanced processes (direct laser fabrication, powder injection moulding, SPS, etc.) are now being considered for the manufacturing of near-net shape components with tailored microstructures. On the European level, the HYSOP project [22] has begun investigating some of these routes and designing advanced coating systems based on multilayer EBC coatings (Environmental Barrier Coatings).

The first applications will probably emerge for intermediate temperatures (900°C – 1000°C) to take advantage of the good specific mechanical properties and the easier handling of the oxidation issues, *e.g.* by the replacement of low pressure turbine Ni based superalloy components by ca. 15% to 20% lighter Nb-Si based components.

Nitride based materials

Nitrides are a wide range of compounds made from nitrogen and others elements (see box). Within this chemical family, only a few of them, such as silicon nitride, are refractory ceramics. As shown in the box, this nitride has many attractive properties, and for this reason it is now used in highly efficient small land-based turbines due to optimisation of the composition, microstructure, processing and coatings. Major manufacturers (Solar Turbines, Ingersoll Rand, Honeywell, General Electric, Pratt & Whitney, Capstone-Microturbines, etc.) have had tens of thousands of service hours of experience with them. However, in

spite of these numerous advantages, Si₃N₄ is not a “miracle material”: it also has some drawbacks, especially difficult and expensive machining due to its hardness and its high electrical resistance (~10¹⁴ Ω.cm), a lack of long term reliability in severe environments, an insufficient level of fracture toughness to overcome the issue of foreign object damage (when used for engine parts), and sensitivity to corrosion in hot gas environments (H₂O in industrial gas turbines for example).

To increase the high-temperature properties of silicon nitride, several additives (SiC, TiN/TiC, BN, ZrO₂, MoSi₂, etc.) have been assessed to form new composite materials. Of these composites, Si₃N₄/SiC and Si₃N₄/MoSi₂ based ceramics seem to be the most promising. With the aim of enhancing engine performance (higher efficiency, weight reduction, pollution decrease, etc.), Onera carried out several studies on Si₃N₄/MoSi₂ materials. According to the literature, these composites could be used at temperatures considerably higher than those attainable with the currently used superalloys (T > 1200°C). This paper is an outline of the work which has been done on these materials in the Composite Materials and Structures Department.

Silicon nitride / molybdenum disilicide composites

According to previous studies, one way to improve the high temperature properties of Si₃N₄ is to combine this ceramic with MoSi₂ [23-26]. Of the non-oxide materials for high-temperature applications, this intermetallic is considered to be one of the most oxidation-resistant at high temperatures (T > 1400°C) [27-29]. This compound has a higher melting point (2030°C) and a lower density (6.2 g/cm³) than the superalloys, and it also has high electrical and thermal conductivities. It exhibits a high toughness above its brittle-ductile transition at around 1000°C. However, due to its brittle nature at low temperatures, inadequate creep resistance above 1200°C, accelerated oxidation around 500°C (a phenomenon called “pest” oxidation [30,31]) and its relatively high CTE (about 8.5 10⁻⁶ K⁻¹), the use of MoSi₂ as a structural material is limited. Fortunately, as mentioned above, these issues may be offset by combining it with another compound as a composite material. This is the case for the Si₃N₄/MoSi₂ composites in particular.

Very interesting properties can be obtained with the synergy of both materials. The addition of about 50 vol.% of Si₃N₄ to MoSi₂ leads in particular to the elimination of its catastrophic pest failure (formation of a Si₂ON₂ protective scale), an increase in the mechanical resistance at room temperature (fracture toughness and compression strength) and high temperatures (creep resistance [25]) and decrease of the CTE [32]. On the other hand, the addition of MoSi₂ to Si₃N₄ yields better Si₃N₄ material properties: improved mechanical resistance and reliability at high temperatures [33], enhanced high temperature fracture toughness [34] and increased electrical conductivity to allow for electrical discharge machining (EDM) [35].

Processing

Commercially available Si₃N₄ and MoSi₂ powders (table 1) were used as precursors, particularly: Si₃N₄ grade M11 and MoSi₂ grade B from H.C. Starck. In order to obtain dense materials, several sintering additives were used in different amounts (MgO, MgAl₂O₄, Y₂O₃, Al₂O₃ and CeO₂). The preparation of the blends involved three successive stages. First, to reduce particle size distribution and promote intimate mixing, the mixtures were ball milled in a liquid for several hours using Si₃N₄ milling media in a high-density polyethylene tank. Then, rotary evaporation was used to dry the mixtures and minimize segregation. Lastly, the powder blends were sieved to avoid agglomeration.

Box 1 - Introduction to nitrides and silicon nitride

Nitrogen reacts with numerous elements to form many different compounds with a wide range of properties. However, the term nitride is only applied to compounds in which nitrogen is linked with elements of similar or lower electronegativity and has a formal oxidation state of -3 (N^{3-} ions). Furthermore, nitrides can be sub-divided into three general classes: ionic, interstitial and covalent nitrides. Ionic or “salt-like” nitrides are formed with the less electronegative elements, *i.e.* alkali metals, alkaline-earth metals and the metals of Group III of the periodic table, including the lanthanide and actinide series (Li_3N , Mg_3N_2 , etc.). Interstitial nitrides formed with the transition metals make up the largest group of nitrides. In these compounds, nitrogen atoms occupy the interstices, or “holes”, in the lattice of close-packed metal atoms. The general formulae of these nitrides are MN , M_2N , and M_4N , although their stoichiometries may vary (TiN , HfN , VN , W_2N , Zr_3N_4 , etc.). As for covalent nitrides, they are formed with the most electronegative elements such as B, S, P, C and Si. They possess a relatively simple crystal structure and an atomic bonding which is less complex than the interstitial nitrides. Their bonding is mostly covalent by the sharing of electrons and is achieved by the hybridisation of the respective electron orbitals (BN , AlN , Si_3N_4 , etc.) [57].

In the categories listed above, only some of the interstitial and covalent nitrides can be qualified as refractory materials (melting point $> 1800^\circ C$ and high chemical stability). This is the case for the nitrides of the early transition metal elements (Groups IV and V) and the covalent nitrides of boron, aluminium and silicon. The refractory nitrides are hard and wear-resistant with high melting points and good chemical resistance. They are important industrial materials and have a significant number of major applications in cutting and grinding tools, wear surfaces, semiconductors, and others.

Among the refractory nitrides, silicon nitride is one of the most interesting. It is also one of the most important non-oxide ceramic materials [58]. This compound has been intensively studied for many years because of its great potential for use in structural applications at room and high temperatures. Thus, many articles have been written about Si_3N_4 [59,60]. It is a hard ceramic with a low density (3.2 g/cm^3), high strength over a broad temperature range, moderate thermal conductivity, a low coefficient of thermal expansion ($\sim 3 \cdot 10^{-6} \text{ }^\circ C^{-1}$), a moderately high elastic modulus, and good fracture toughness for a ceramic. This combination of properties leads to excellent thermal shock resistance, the ability to withstand high structural loads at high temperatures, and superior wear resistance. Si_3N_4 is therefore mostly used in high-endurance and high-temperature applications such as gas turbines, car engine parts, bearings and metal working and cutting tools. Silicon nitride does not melt but dissociates into silicon and nitrogen (N_2 dissociation pressure reaches 1 bar at $1880^\circ C$). It exhibits three crystallographic modifications, α , β and γ . The α and β phases are the most common forms and can be produced under normal pressure conditions.

In industry, the most common sintering technology used for Si_3N_4 is gas-pressure sintering. However, several other methods exist to provide different types of materials: Reaction Bonded Silicon Nitride, Sintered RBSN, Sintered Silicon Nitride (pressureless), Hot-Pressed Silicon Nitride, Sinter HIP'ed Silicon Nitride, HIP'ed Silicon Nitride, etc. Moreover, there is a wide range of compositions and microstructures which are affordable depending on the raw materials, the densification technologies and the manufacturing cycles that are used. It is important to notice that the densification of Si_3N_4 is usually achieved through the acceleration of mass transport by the formation of a liquid phase during sintering [61]. Indeed, Si_3N_4 crystals exhibit a low self-diffusion coefficient due to the high energy of the covalent bonds. This liquid phase is an oxynitride liquid formed by the reaction of the sintering additives with the silica existing on the surface of the Si_3N_4 powder particles [62]. After sintering, the additives are located at the grain boundary and in particular in the triple junctions. The grain-boundary phase, which is an amorphous or partially crystallised phase, significantly influences the material properties.

Starting powder	Grade / supplier	Particle size (μm)	Phase	Purity (%)
Si_3N_4	M11 / H.C. Starck	0.54	$\alpha > 90 \%$	> 98
	SN-E10 / UBE	< 0.50	$\alpha > 95 \%$	> 98
$MoSi_2$	B / H.C. Starck	4.72	tetragonal	> 99
	Mo701 / AEE	$1 < d_{50} < 10$	tetragonal	> 99.8

Table 1 – Grade, size, crystallographic structure and purity of the starting powders

The second phase of the process involved sintering the previous powder blends. Three different methods were used: HP, pressureless sintering and HIP [36-40]. In fact, most of the materials were manufactured by HP, which is a standard process often used during development phases and when very limited numbers of parts are required. On the other hand, pressureless sintering in powder beds was chosen to manufacture complex shaped samples, and HIP to improve material microstructure and properties.

A resistance-heated furnace with graphite dies was used to sinter the blends by HP. After some improvements in the mixture compositions, the densification parameters selected were the following:

- Sintering temperature: $1550 \leq T \leq 1650^\circ C$ (depending on the amount and type of sintering additives)
- Dwell time at high temperature: $t = 90 \text{ min}$
- Uniaxial pressure: $P = 25 \text{ MPa}$
- Atmosphere: nitrogen at atmospheric pressure
- Graphite dies: $36 \times 36 \text{ mm}^2$, $45 \times 45 \text{ mm}^2$ or 6 samples of $50 \times 5.2 \text{ mm}^2$ simultaneously

For pressureless sintered materials, powder blends were first pre-packed at 150 MPa by cold pressing and then machined or directly sintered in powder beds under nitrogen pressure ($1550^\circ C/90 \text{ min}/P_{N_2} \sim 1 \text{ bar}$). Cold pressing at 150 MPa was also used to prepare the samples ($\phi = 20 \text{ mm}$, $L = 30 \text{ mm}$) for HIP'ing in a tantalum can ($1800^\circ C/3 \text{ h}/150 \text{ MPa}$).

Composition	Sintering additives / weight %	Sintering method	Apparent density / g/cm ³	Open porosity / %
50 vols.% Si ₃ N ₄ M11/ 50 vol.% MoSi ₂ B	4 % Y ₂ O ₃ + 3 % Al ₂ O ₃	Pressureless	3.67	0.6
		HP	4.15	0.4
	1 % MgO	HP	4.15	0.6
		7 % Y ₂ O ₃	HP	4.34
	10 % CeO ₂		HIP	4.44
		10 % CeO ₂	HP	4.33
	10 % CeO ₂		HIP	4.51

Table 2 – Densification level of various Si₃N₄/MoSi₂ composites

Microstructure

The density of each material was assessed by the water impregnation method. According to the type and amount of additives and sintering methods used, different apparent density and open porosity values were measured (table 2). For most samples, high densification rates are obtained with open porosity level lower than 1 %. As expected, the lowest values are observed on pressureless sintered materials and the highest on the HIP'ed materials.

Various microstructures have been obtained and in general a fine microstructure with good homogeneity is observed (figure 12). The differences between the microstructures are due to both the type and the amount of sintering aids and to the process used. As already reported in the literature [41], no reaction occurred between MoSi₂ and Si₃N₄. In addition, despite the CTE mismatch ($\alpha_{\text{MoSi}_2} \sim 9.10^{-6} \text{ }^\circ\text{C}^{-1}$ and $\alpha_{\text{Si}_3\text{N}_4} \sim 3.10^{-6} \text{ }^\circ\text{C}^{-1}$), there is good adhesion between the two compounds.

It is important to notice that for HP'ed or pressureless sintered materials, the Si₃N₄/MoSi₂ volume ratio is sometimes modified by reactions of MoSi₂ with the furnace atmosphere (nitrogen). This is of course avoided when sintering occurs in sealed containers (HIP) or under inert gas (argon). Furthermore, for the composites HIP'ed at 1800°C, the growth of acicular β -Si₃N₄ grains is promoted [42,43]; these grains induce crack deflection, so this type of microstructure is often desirable in order to increase the fracture toughness [44].

Materials properties

Machinability

Materials with hard and brittle compounds often involve machining difficulties and high costs. For the materials processed at Onera, thanks

to the low electrical resistivity of MoSi₂ ($\sim 10^{-2} \text{ } \Omega \cdot \text{cm}$), the use of EDM seems perfectly possible [35]. Indeed, with 50 vol.% of the conductive phase, the threshold of percolation is easily reached. However, in our work, EDM was successful only with the HIP'ed materials in which the Si₃N₄/MoSi₂ volume ratio was retained (figure 13). A similar machinability would be obtained on materials sintered by hot pressing under argon in which the volume ratio is also preserved. This good conductivity level is an important advantage compared with basic Si₃N₄ and has allowed for the development of Si₃N₄/MoSi₂ ceramic glow plugs for diesel engines [26].

Mechanical performance

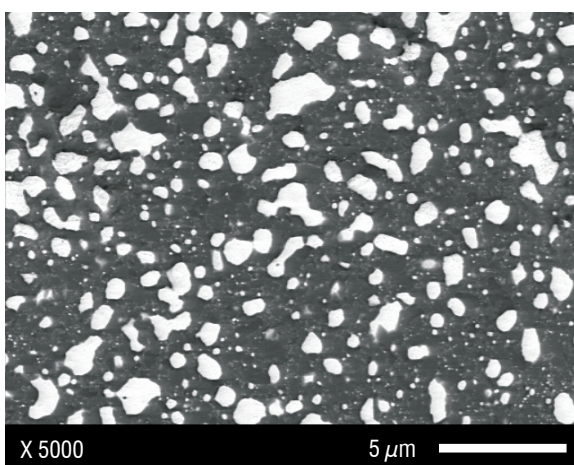
Hardness and fracture toughness

Vickers hardness (*HV*) and toughness (*K_{1c}*) have been evaluated at room temperature by Vickers indentation (with a load *P* = 30 kgf \sim 294 N). The hardness is determined by measuring the surface area *A* of the indentation mark. The fracture toughness is estimated by using the radial crack pattern formed around the indentation mark [45,46]:

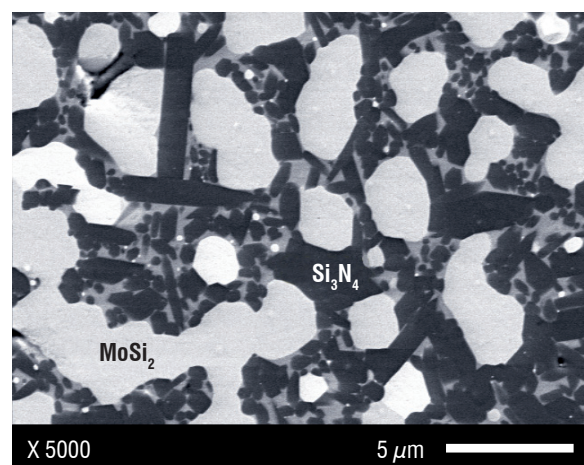
$$HV = \frac{P}{A} = 0.001854 \times \frac{P}{d^2} \quad (1)$$

$$K_{1c} = 0.8854 \times (a \times HV \times E)^{1/2} \times \left(\frac{c}{a}\right)^{-3/2} \quad (2)$$

with *HV* the hardness (GPa), *P* the load (N), *K_{1c}* the toughness (MPa.m^{1/2}), *a* = *d*/2 with *d* the average diagonal indentation mark length (mm), *E* the Young's modulus (GPa) and *c* the crack length from the centre of the indent to the crack tip (mm). Depending on the sintering process and the additives used, different property levels have been recorded (table 3).



Si₃N₄/MoSi₂ with 4% Y₂O₃ + 3% Al₂O₃ (HP'ed)



Si₃N₄/MoSi₂ with 7% Y₂O₃ (HP'ed)

Figure 12 – Microstructure of two types of Si₃N₄/MoSi₂ composites (SEM observations). The phases are MoSi₂ (white), Si₃N₄ (black) and the grain-boundary-phase (intermediate grey level)

Composition	Sintering additives / weight %	Sintering method	HV / GPa	K_{Ic} / MPa.m ^{1/2}
50 vol.% Si ₃ N ₄ M11 / 50 vol.% MoSi ₂ B	4 % Y ₂ O ₃ + 3 % Al ₂ O ₃	HP	15.4 ± 0.4	2.5 ± 0.1
	7 % Y ₂ O ₃	HIP	13.4 ± 0.3	5.2 ± 0.4
	10 % CeO ₂	HIP	12.9 ± 0.3	5.1 ± 0.7

Table 3 – Hardness and toughness of Si₃N₄/MoSi₂ composites (using E ~ 240 GPa; this low value is used to avoid overestimating the fracture toughness performance of the composites)

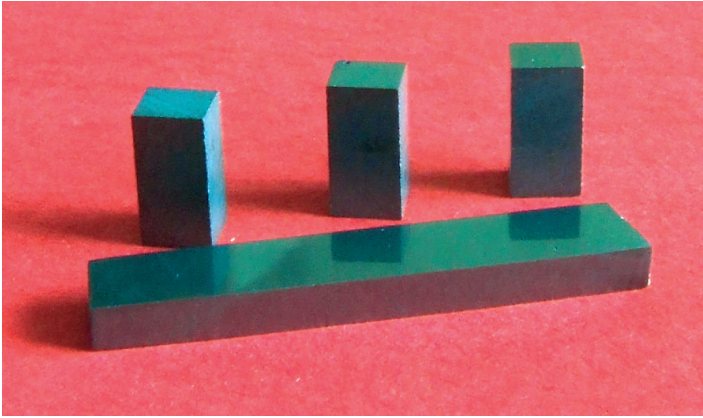


Figure 13 – Pictures of several EDM machined samples after finishing (HIP Si₃N₄/MoSi₂ with 10 wt.% CeO₂)

The Vickers hardness is in good agreement with the values found in the literature on similar materials [44]. Table 3 shows that a significant improvement in fracture toughness is possible when adequate processing methods and sintering additives are used; here HIP'ing has led to the in-situ growth of acicular β -Si₃N₄ grains and thus to increased toughness. For these non-optimised materials (composition, processing cycle, etc.), the room temperature toughness levels achieved are remarkable. Due to the presence of MoSi₂, they will even increase with temperature as reported in the literature (K_{Ic} = 5 MPa.m^{1/2} at 20°C, 7 at 1000°C and 9 at 1200°C) [34].

Several other solutions have also been assessed to form specific β -Si₃N₄ grains containing microstructures to enhance the toughness of Si₃N₄/MoSi₂ composites, such as the introduction of β -Si₃N₄ seeds and various SiC reinforcements (Hi-Nicalon fibers, from Nippon Carbon, with or without BN/SiC CVD coating; Sylramic fibers, from Dow Corning; SA3 fibers, from UBE; SiC platelets, from Millenium Materials Inc., Tokawhiskers, from Tokai Carbon, etc.), but with little success.

Flexural strength

The flexural properties of several composites have been studied by using three-point bending tests from room temperature to 1100°C (in air at atmospheric pressure), yielding values for the flexural stress (σ_f) and the modulus of elasticity in bending (E_f). The specimens, three for each condition, have been tested with a crosshead speed of 0.005 mm.s⁻¹ and a span length of 30 or 38 mm. In table 4, very satisfactory results are shown for a HIP'ed Si₃N₄/MoSi₂/4 wt.% Y₂O₃/3 wt.% Al₂O₃ composite. It is important to notice that at high temperatures the values of the apparent Young's modulus are not really relevant (E_f are manifestly reduced by plasticity).

Composition	Property	Test temperature		
		20°C	900°C	1100°C
50 vol.% Si ₃ N ₄ M11 / 50 vol.% MoSi ₂ B + 4 % Y ₂ O ₃ + 3 % Al ₂ O ₃	σ_f (MPa)	910 ± 135	620 ± 80	510 ± 118
	E_f (GPa)	200 ± 5	150 ± 5	100 ± 5

Table 4 – Three-point flexural strength (σ_f) and modulus of elasticity in bending (E_f)

A high flexural strength is still obtained at 1100°C ($\sigma_f > 500$ MPa). This temperature is above the brittle-ductile transition temperature of MoSi₂ so a decrease in the properties is expected as grain boundary sliding and plastic deformation of MoSi₂ particles begin to operate [47,48]. These mechanisms also explain the observed increase in the flexural strain (ϵ_f = 0.6 % at 1100°C instead of 0.3 % at room temperature).

Creep

Compression creep tests have been conducted in air between 1300 and 1400°C for stresses in the range 50 – 200 MPa on Si₃N₄-MoSi₂ HIP'ed composites with Y₂O₃ or CeO₂ additives (sample dimensions: 3 x 3 x 6 mm³). During the tests, the load was increased in steps after the minimum creep rate was observed at each load. The total strain for each specimen was limited to 10%. The detailed test method was previously reported [49].

The composite containing 10 wt.% CeO₂ was tested at 1300 and 1350°C and the one with 7 wt.% Y₂O₃ at 1300 and 1400°C. For both materials and each temperature selected, the creep rates as a function of stress are shown in figure 14. In addition, in order to compare the previous materials with the literature results, two curves for a HIP'ed Si₃N₄-MoSi₂ composite with 1 wt.% MgO have been added [50].

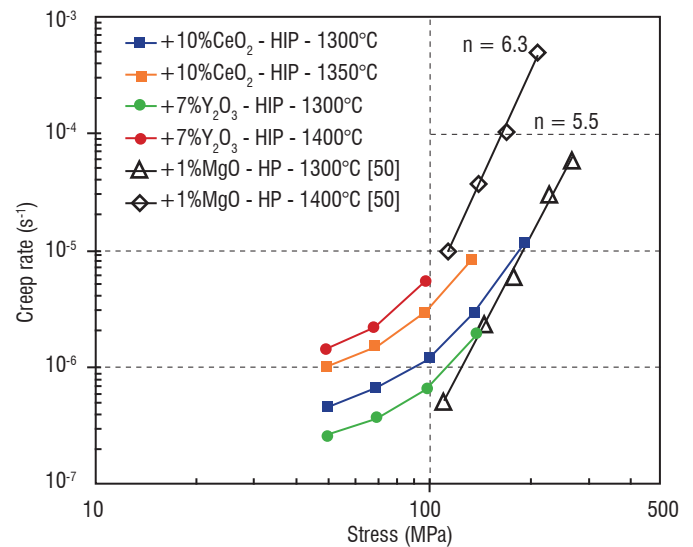


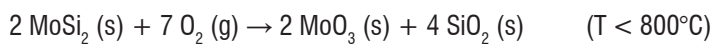
Figure 14 – Stationary creep rate versus stress for various Si₃N₄-MoSi₂ composites in the range 1300-1400°C

These results indicate that the addition of Y_2O_3 leads to lower creep rates than for CeO_2 . In addition, contrary to what is observed on HIP'ed materials, the stress exponents (n) recorded on both HIP'ed composites vary with the applied stress. For the latter, n can increase from 1.01 (at lower stresses) to 3.94 (at higher stresses). In the reference materials, the creep rate is controlled by dislocation creep mechanisms (glide and climb). In comparison, in the HIP'ed composites, for the stress and temperature ranges studied, the creep rates are certainly controlled by a combination of several mechanisms: grain boundary sliding, diffusional creep and dislocation creep mechanisms. However, at higher stress, creep behaviours close to that observed on the reference materials (with constant stress exponent $n \sim 5 - 6$) will probably be found.

It is important to point out that the amount of sintering additive in the HIP'ed materials has not yet been optimised (~ 6 vol.% of the Si_3N_4 - $MoSi_2$ blend) and that it could certainly be possible to enhance the creep resistance of these composites by reducing the fraction of additive.

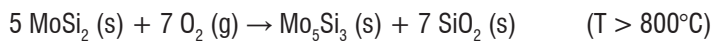
Oxidation and thermal shock resistance

$MoSi_2$ based materials can disintegrate rapidly during oxidation at temperatures around $500^\circ C$ ("pest" phenomenon) [30,31]: the oxidation of polycrystalline $MoSi_2$ leads to the formation of solid MoO_3 and SiO_2 with a substantial volume expansion due to MoO_3 whiskers (or platelets). This results in a mass gain and also in internal tensile stresses which destroy intergranular cohesion:



Above approximately $800^\circ C$, crystalline MoO_3 (melting point: $801^\circ C$) evaporates significantly (a mass loss is recorded) and the oxidation is controlled by diffusion of oxygen through the SiO_2 layer [51].

At higher temperatures (900 - $1100^\circ C$), Mo_5Si_3 is formed and then consumed by further oxidation to form SiO_2 and MoO_3 (g):



However, the SiO_2 layer is a good barrier to oxidation attack because of a low oxygen permeation rate. $MoSi_2$ is hence known to exhibit excellent high temperature oxidation behaviour up to $1600^\circ C$.

In this project, the thermal shock behaviour and the long-term resistance under oxidative atmospheres were assessed at $500^\circ C$ and $900^\circ C$ under static air at atmospheric pressure for cumulative times of up to 400 h. The latter temperature was chosen for the MoO_3 volatilisation regime.

The oxidation rate was estimated by monitoring the material mass variations versus time and the thermal shock resistance by several quick insertions into and withdrawals of the samples from the furnace.

For each material, more than nine insertion/withdrawal cycles (i.e. at least 18 thermal shocks) were achieved with no problems: all of the samples maintained their integrity and no cracks appeared. As expected, all of the compositions exhibited good thermal shock resistance in the tested conditions.

With regard to the oxidation behaviour, the material mass variations recorded on three different HIP'ed composites were reported in table 5 (sample dimensions: $\sim 5 \times 2 \times 20$ mm³). These values are maximum absolute mass variations after 400 h of cumulative treatment.

Regardless of the type of material and the test temperature, the total mass variations are very low ($\Delta M/M < 0.1\%$), showing that the selected materials exhibit good oxidation resistance in the tested conditions, with no "pest" oxidation. This is due firstly to the good densification of the materials (no cracks or pores in the samples) and secondly to the formation of a protective layer.

Outlook

Following up on the previous work, new studies involving the Si_3N_4 - $MoSi_2$ composites are included in the HYSOP project [22] to evaluate the potential of applying Si_3N_4 - $MoSi_2$ composites in aeronautical turbines (blades, vanes and seal segments). The final objectives are to increase the temperature capability of the turbine materials and to reduce the overall mass of the aircraft in order to reduce fuel consumption and emissions, and help to reduce aircraft operation costs. The Si_3N_4 - $MoSi_2$ composite composition will be optimised (nature and quantity of sintering additives, etc.) and advanced processes to manufacture materials with adequate microstructures and properties will be developed (pressureless sintering, Spark Plasma Sintering, HIP). It has already been shown that recent sintering methods (SPS in particular) [52,53] can enhance the mechanical properties of silicon nitride based materials (Si_3N_4 or Si_3N_4/TiN for example). The materials will be characterised (physical, chemical, thermal and mechanical properties, oxidation/corrosion resistance, machinability, etc.) and shaped demonstrators will be manufactured.

It has been demonstrated that one of the major issues for silicon nitride based materials in gas turbines is corrosion resistance [54,55]. Water vapour in particular reacts with the protective silica scale, forming gaseous reaction products such as $Si(OH)_4$. In high pressure and high gas velocity combustion environments, this reaction results in recession of Si_3N_4 based materials. Furthermore, at high temperatures ($\sim 1300^\circ C$), aggressive deposits such as CMAS (Calcium Magnesium Aluminium Silicate glass) further degrade these materials. Thus,

Composition	Sintering additives / weight %	Sintering method	Absolute weight variation	
			at $500^\circ C$	at $900^\circ C$
50 vol.% Si_3N_4 M11 / 50 vol.% $MoSi_2$ B	1 % MgO	HP	0.04 %	0.09 %
	4 % $MgAl_2O_4$	HP	0.01 %	0.03 %
	4 % Y_2O_3 + 3 % Al_2O_3	HP	0.06 %	0.05 %

Table 5 – Material mass variations after oxidative treatments under static air, for 400 h

specific investigations will be carried out in order to estimate and reduce these phenomena and protective coatings may be used to fulfil the requirements [56].

Conclusion

The development of new gas turbine hot section materials with increased high temperature capabilities is crucial for the design of future efficient turbines with low CO₂ and NO_x emission levels. Refractory metal silicide based materials and Si₃N₄-MoSi₂ composites are promising candidates for such applications.

Extensive work in the United States, Europe and the Far East has led to remarkable improvements in both Mo-Si-B and Nb-Si based materials. Over the past decade, the reduction of engine mass has become as important a factor as extended temperature capability, and it is expected that this will be easily achieved. Nb-Si materials are preferred, although specific attractive mechanical properties can be obtained with Mo-Si-B materials. PM processing is a promising approach that not only allows for refined and controlled microstructures but also

considerably alleviates the Si-content limitations encountered in ingot metallurgy (high temperature required for melting, cracking of the silicide dendrites, etc.).

The main tasks that are still to be carried out to ensure the introduction of these silicide based materials into future turbine engines include composition optimisation for simultaneously enhanced mechanical properties and oxidation/corrosion resistance for long service duration, improvement of available protective coatings, control of the microstructure and the implementing of a cost effective industrial manufacturing route.

Silicon nitride based materials have already found applications in small size stationary gas turbines, but their use in turbine engines still requires developments in terms of both mechanical properties and oxidation resistance. The key issues for Si₃N₄-MoSi₂ composites are composition optimisation, especially the nature and amount of the sintering aids which have to be kept as low as possible to improve high temperature mechanical properties, control of the microstructure (beneficial effect of the β-Si₃N₄ phase), the reduction of porosity, all in close connection with the manufacturing processes ■

Acknowledgements

We thank the European Commission for partially funding the ULTMAT project through contract No. AST3-CT-2003-502977.

References

- [1] J.C. ZHAO and J.H. WESTBROOK - *Ultra-high-Temperature Materials for Jet Engines*. MRS Bull. 28(9), 622-627, 2003.
- [2] S. DRAWIN - *Public Executive Summary of the Ultmat Final Activity Report*. www.ultmat.onera.fr.
- [3] D.M. BERCZIK - *Method for Enhancing the Oxidation Resistance of a Molybdenum Alloy, and a Method of Making a Molybdenum Alloy*. US Patent 5,595,616, 1997 - *Oxidation Resistant Molybdenum Alloy*. US Patent 5,693,156, 1997.
- [4] P. JÉHANNO, M. HEILMAIER, H. SAAGE, M. BÖNING, H. KESTLER, J. FREUDENBERGER and S. DRAWIN - *Assessment of the High Temperature Deformation Behavior of Molybdenum Silicide Alloys*. Mater. Sci. Eng. A 463, 216-223, 2007.
- [5] P. JÉHANNO, M. HEILMAIER, H. KESTLER, M. BÖNING, A. VENSKUTONIS, B.P. BEWLAY and M.R. JACKSON - *Assessment of a Powder Metallurgical Processing Route for Refractory Metal Silicide Alloys*. Metall. Mater. Trans. 36A, 515-523, 2005.
- [6] P. JÉHANNO, M. HEILMAIER, H. SAAGE, H. HEYSE, M. BÖNING, H. KESTLER and J.H. SCHNEIBEL - *Superplasticity of a Multiphase Refractory Mo-Si-B Alloy*. Scr. Mater. 55(6), 525-528, 2006.
- [7] H.-P. MARTINZ, B. NIGG, J. MATEJ, M. SULIK, H. LARCHER and A. HOFFMANN - *Properties of the Sibor® Oxidation Protective Coating on Refractory Metal Alloys*. Int. J. Refract. Met. Hard Mater. 24, 283-291, 2006.
- [8] S. DRAWIN, M. HEILMAIER, P. JÉHANNO, D. HU, P. BELAYGUE, P. TSAKIROPOULOS and M. VILASI - *Creep and Oxidation Resistance of Refractory Silicide Based Materials*. 17th Plansee Seminar, International Conference on High Performance PM Materials, L.S. Sigl, P. Rödhammer, and H. Wildner (eds), PLANSEE Group, Reutte, Austria, Vol. 4, paper RM 33, 1-10, 2009.
- [9] M. MOUSA, N. WANDERKA, M. TIMPEL, S. SINGH, M. KRÜGER, M. HEILMAIER and J. BANHART - *Modification of Mo-Si Alloy Microstructure by Small Additions of Zr*. Ultramicroscopy 111(6), 706-710, 2011.
- [10] H. SAAGE, M. KRÜGER, D. STURM, M. HEILMAIER, J.H. SCHNEIBEL, E. GEORGE, L. HEATHERLY, CH. SOMSEN, G. EGGELER and Y. YANG - *Ductilization of Mo-Si Solid Solutions Manufactured by Powder Metallurgy*. Acta Mater. 57(13), 3895-390, 2009.
- [11] B.P. BEWLAY, M.R. JACKSON, J.C. ZHAO, P.R. SUBRAMANIAN, M.G. MENDIRATTA and J.J. LEWANDOWSKI - *Ultra-high-Temperature Nb-Silicide-Based Composites*. MRS Bull. 28(9), 646-653, 2003.
- [12] B.P. BEWLAY, M.R. JACKSON and M.F.X. GIGLIOTTI - *Niobium Silicide High Temperature in situ Composites, in Intermetallic Compounds*. Principles and Practice, Vol. 3, R.L. Fleischer and J.H. Westbrook (eds), J. Wiley & Sons, pp. 541-560, 2011.
- [13] Z. LI and P. TSAKIROPOULOS - *Study of the Effect of Ti and Ge in the Microstructure of Nb-24Ti-18Si-5Ge in situ Composite*. Intermetallics 19(9), 1291-1297, 2011.
- [14] S. DRAWIN - *The European Ultmat Project: Properties of New Mo- and Nb-Silicide Based Materials*. Mater. Res. Soc. Symp. Proc. Vol. 1128, paper 1128-U07-11, 1-6, 2009.
- [15] R.M. NEKKANTI and D.M. DIMIDUK - *Ductile-Phase Toughening in Niobium-Niobium Silicide Powder Processed Composites*. Mater. Res. Soc. Symp. Proc. Vol. 194, 175-182, 1990.
- [16] C.L. MA, A. KASAMA, H. TANAKA, Y. TAN, Y. MISHIMA and S. HANADA - *Microstructures and Mechanical Properties of Nb/Nb-Silicide in-situ Composites Synthesized by Reactive Hot Pressing of Ball Milled Powders*. Mater. Trans. JIM 41(3), 444-51, 2000.
- [17] S. DRAWIN, J.P. MONCHOUX, J.L. RAVIART and A. COURET - *Microstructural Properties of Nb-Si Based Alloys Manufactured by Powder Metallurgy*. Adv. Mater. Res. 278, 533, 2011.

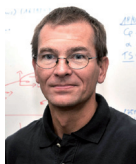
- [18] C.L. MA, Y. TAN, H. TANAKA, A. KASAMA, R. TANAKA, Y. MISHIMA and S. HANADA - *Microstructures and High-Temperature Strength of Silicide-Reinforced Nb Alloys*. Mater. Res. Soc. Symp. Proc. Vol. 646, paper N5.39, 1-6, 2001.
- [19] J.H. KIM, T. TABARU, H. HIRAI, A. KITAHARA and S. HANADA - *Tensile Properties of a Refractory Metal Base in situ Composite Consisting of an Nb Solid Solution and Hexagonal Nb₅Si₃*. Scr. Mater. 48(10), 1439-1444, 2003.
- [20] F. ZAMOUM - *New Niobium- and Molybdenum-Based Materials for Aeronautics: Phase Relationships and Oxidation. Synthesis of New Coatings*. Thèse de doctorat, Université Nancy I, 2008.
- [21] E.S.K. MENON and M.G. MENDIRATTA - *Effect of Powder Processing on High Temperature Oxidation of a Nb-Base Alloy*. Proc. 16th International Plansee Seminar, Kneringer G., Röhdhammer P, and Wildner H. (eds), PLANSEE Holding AG, Reutte, Austria, pp. 857-868, 2005.
- [22] <http://hysop.onera.fr/>.
- [23] H. KLEMM, M. HERRMANN and C. SCHUBERT - *Silicon Nitride Composites Materials with an Improved High Temperature Oxidation Resistance*. Ceram. Eng. Sci. Proc. 18, 615-623, 1997.
- [24] M.G. HEB SUR - *MoSi₂-Base Composites*. Chap.8, Handbook of ceramic composites, N.P. Bansal (Ed.), Kluwer Academic Publishers, 2005.
- [25] K. SADANANDA, C.R. FENG, R. MITRA and S.C. DEEVI - *Creep and Fatigue Properties of High Temperature Silicides and Their Composites*. Mater. Sci. Eng. A261, 223-238, 1999.
- [26] K. YAMADA and N. KAMIYA - *High Temperature Mechanical Properties of Si₃N₄ - MoSi₂ and Si₃N₄ - SiC Composites with Network Structures of Second Phases*. Mater. Sci. Eng. A261, 270-277, 1999.
- [27] K. BUNDSCHUH, M. SCHÜZE, C. MULLER, P. GREIL and W. HEIDER - *Selection of Materials for Use at Temperatures Above 1500°C in Oxidizing Atmospheres*. J. Eur. Ceram. Soc. 18, 2389-91, 1998.
- [28] Z. YAO, J. STIGLICH and T.S. SUDARSHAN - *Molybdenum Silicide Based Materials and their Properties*. J. Mater. Eng. Perform. 8, 291-304, 1999.
- [29] A.K. VASUDEVAN and J.J. PETROVIC - *A Comparative Overview of Molybdenum Disilicide Composites*. Mater. Sci. Eng. A155, 1-17, 1992.
- [30] C.G. MCKAMEY, P.F. TORTORELLI, J.H. DEVAN and C.A. CARMICHAEL - *A Study of Pest Oxidation in Polycrystalline MoSi₂*. J. Mater. Res. 7, 2747-2755, 1992.
- [31] T.C. CHOU and T.G. NIEH - *Pesting of the High-Temperature Intermetallic MoSi₂*. JOM 45, 15-21, 1993.
- [32] T. HSIEH, H. CHOE, E.J. LAVERNIA and J. WOLFENSTINE - *The Effect of Si₃N₄ on the Thermal Expansion Behavior of MoSi₂*. Mater. Lett. 30, 407-410, 1997.
- [33] H. KLEMM and C. SCHUBERT - *Silicon Nitride/Molybdenum Disilicide Composite with Superior Long-Term Oxidation Resistance at 1500°C*. J. Am. Ceram. Soc. 84, 2430-2432, 2001.
- [34] M.G. HEB SUR - *Development and Characterization of SiC₀/MoSi₂-Si₃N₄(P) Hybrid Composites*. Mater. Sci. Eng. A261, 24-37, 1999.
- [35] C.C. LIU - *Wire Electrical Discharge Machining and Mechanical Properties of Gas Pressure Sintered MoSi₂-Si₃N₄ Composites*. J. Ceram. Soc. Japan 108, 469-472, 2000.
- [36] A. EZIS and J.A. RUBIN - *Hot Pressing*. Engineered Materials Handbook Vol. 4, Ceramics and Glasses, 186-193, 1991.
- [37] V. DEMIR and D.P. THOMPSON - *Pressureless Sintering of Si₃N₄ Ceramics with Oxide Additives in Different Packing Powder*. J. Mater. Sci. 40, 1763-1765, 2005.
- [38] P. SAJGALIK and M. HAVIAR - *Pressureless Sintering of Si₃N₄ with Y₂O₃ and Al₂O₃ Additives - Compatibility of Powder Beds*. Ceram. Int. 18, 279-283, 1992.
- [39] H.T. LARKER - *Hot Isostatic Pressing*. Engineered Materials Handbook Vol. 4, Ceramics and Glasses, 194-201, 1991.
- [40] G.E. GAZZA - *Pressure Densification*. Engineered Materials Handbook Vol. 4, Ceramic and Glasses, 296-303, 1991.
- [41] J.J. PETROVIC, M.I. PENA and H.H. KUNG - *Fabrication and Microstructures of MoSi₂ Reinforced-Si₃N₄ Matrix Composites*. J. Am. Ceram. Soc. 80, 1111-1116, 1997.
- [42] S-J. L. KANG and S-M. HAN - *Grain Growth in Si₃N₄-Based Materials*. MRS Bulletin 20, 33-37, 1995.
- [43] F.F. LANGE - *Fracture Toughness of Si₃N₄ as a Function of the Initial α -Phase Content*. J. Am. Ceram. Soc. 62, 428-430, 1979.
- [44] J.J. PETROVIC, M.I. PENA, I.E. REIMANIS, M.S. SANDLIN, S.D. CONZONE, H.H. KUNG and D.P. BUTT - *Mechanical Behavior of MoSi₂ Reinforced-Si₃N₄ Matrix Composites*. J. Am. Ceram. Soc. 80, 3070-3076, 1997.
- [45] A.G. EVANS - *Fracture Toughness, The Role of Indentation Techniques*. Am. Soc. Test. Mater., STP 678, 112-135, 1979.
- [46] B.R. LAWN and D.B. MARSHALL - *Hardness, Toughness and Brittleness: an Indentation Analysis*. J. Am. Ceram. Soc. 62, 347-350, 1979.
- [47] Z. GUOA, M. PARLINSKA-WOJTANB, G. BLUGANA, T. GRAULEA, M. J. REECE and J. KUEBLER - *The Influence of the Grain Boundary Phase on the Mechanical Properties of Si₃N₄-MoSi₂ Composites*. Acta Mater. 55, 2875-2884, 2007.
- [48] D. SCITTI, S. GUICCIARDI and A. BELLOSI - *Microstructure and Properties of Si₃N₄-MoSi₂ Composites*. J. Ceram. Process. Res. 3, 87-95, 2002.
- [49] L. PERRIÈRE - *Élaboration par solidification dirigée et comportement mécanique de céramiques eutectiques à base d'oxydes réfractaires : rôle de la microstructure sur la fissuration et la déformation plastique à haute température*. Thesis Paris XII, 2008.
- [50] C.R. FENG and K. SADANANDA - *Creep Behavior of MoSi₂ with Si₃N₄ Reinforcements*. Mater. Res. Soc. Symp. Proc. Vol. 460, 685-670, 1997.
- [51] Y. T. ZHU, M. STAN, S. D. CONZONE and D.P. BUTT - *Thermal Oxidation Kinetics of MoSi₂-Based Powders*. J. Am. Ceram. Soc. 82, 2785-2790, 1999.
- [52] L. BAI, X. MAO, W. SHEN and C. GE - *Comparative Study of β -Si₃N₄ Powders Prepared by SHS Sintered by Spark Plasma Sintering and Hot Pressing*. J. of Univ. Sci. Technol. Beijing. Vol 14, 3, 271-275, 2007.
- [53] N. AHMAD and H. SUEYOSHI - *Microstructure and Mechanical Properties of Silicon Nitride-Titanium Nitride Composites Prepared by Spark Plasma Sintering*. Mater. Res. Bull. 46, 460-463, 2011.
- [54] H. KLEMM - *Corrosion of Silicon Nitride Materials in Gas Turbine Environment*. J. Eur. Ceram. Soc. 22, 2735-2740, 2002.
- [55] G. BLUGAN, D. WITTIG and J. KUEBLER - *Oxidation and Corrosion of Silicon Nitride Ceramics with Different Sintering Additives at 1200 and 1500°C in Air, Water Vapour, SO₂ and HCl Environments - A Comparative Study*. Corros. Sci.e 51, 547-555, 2009.
- [56] K. N. LEE - *Protective Coatings for Gas Turbines*. The gas turbine handbook, Chap.4.4.2, Edited by NETL, 419-438, 2006.
- [57] H.O. PIERSON - *Handbook of Refractory Carbides and Nitrides*. Noyes Publications, 1996.
- [58] D.W. FREITAG and D.W. RICHERSON - *Opportunities for Advanced Ceramics to Meet the Needs of the Industries of the Future*. DOE/ORO 2076, 1998.
- [59] F.L. RILEY - *Silicon Nitride and Related Materials*. J. Am. Ceram. Soc. 83, 245-265, 2000.
- [60] H. KLEMM - *Silicon Nitride for High-Temperature Applications*. J. Am. Ceram. Soc. 93, 1501-1522, 2010.
- [61] O.H. KWON - *Liquid-Phase Sintering*. Engineered Materials Handbook Vol. 4, Ceramics and Glasses, 285-290, 1991.
- [62] M. HERRMANN, H. KLEMM and C. SCHUBERT - *Silicon Nitride Based Hard Materials*. Handbook of ceramic hard materials, Chap. 6, R. Riedel (Ed.), Wiley-VCH, 2000.

Acronyms

RM (Refractory Metal)
ULTMAT (“ULtra high Temperature MAterials for Turbines” project)
PM (Powder Metallurgy)
HIP (Hot Isostatic Pressing)
MASC (Metal And Silicide Composite)
CTE (Coefficient of Thermal Expansion)
HP (Hot uniaxial Pressing)
SPS (Spark Plasma Sintering)

HYSOP (“Hybrid Silicide-Based Lightweight Components for Turbine and Energy Applications” project)
EBC (Environmental Barrier Coatings)
SEM (Scanning Electron Microscopy)
EDM (Electrical Discharge Machining)
CMAS (Calcium Magnesium Aluminium Silicate Glass)
RBSN (Reaction Bonded Silicon Nitride)

AUTHORS



Stefan Drawin is a Research Engineer in the Metallic Materials and Structures Department at Onera. He received his Engineering degree from the Ecole Centrale de Paris and his doctoral degree in Physics from the Université de Paris-XIII in 1990, and then joined Onera. With a focus on processing and characterisation, he has been working on the development of C/SiC composites, plasma enhanced CVD for the deposition of thermal barrier coatings, and single crystal superalloys. He is now theme leader for the development of new silicide based materials. He is coordinating two European projects, ULTMAT (2004-2008) and HYSOP (2010-2014).



Jean-François Justin is a Research Engineer working within the Thermostructural and Functional Composites unit (CTF) of the Composite Materials and Structures Department (DMSC). He is a graduate of the “Conservatoire National des Arts et Métiers”. Since he joined Onera in 1989, he has been involved in the development of monolithic ceramics and Ceramic Matrix Composites for functional applications (combustion chambers, stealth materials, engine blades, leading edges, air intakes, etc.). He has been also working on improving the CMC processing approaches and CVD coatings. At present, his research is mainly focused on Ultra-High Temperature Ceramics (particularly within the framework of the European ATLLAS and ATLLAS2 projects).

M. Parlier, R. Valle,
L. Perrière
(Onera)

S. Lartigue-Korinek,
L. Mazerolles
(ICMPE- CNRS)

E-mail: michel.parlier@onera.fr

Potential of Directionally Solidified Eutectic Ceramics for High Temperature Applications

Directionally solidified eutectic (DSE) ceramics add new potentialities to the advantages of sintered ceramics: a higher strength, almost constant, up to temperatures close to the melting point and a better creep resistance. The microstructure of melt-growth composites (MGC) of ceramic oxides consists in three-dimensional and continuous interconnected networks of single-crystal eutectic phases. After solidification of binary eutectics, the eutectic phases are alumina and either a perovskite or garnet phase. In ternary systems, cubic zirconia is added as a third phase. For very high temperature structural applications such as turbine blades in future aeronautical turbines or thermal power generation systems, the investigation is focused on both binary ($\text{Al}_2\text{O}_3\text{-Y}_3\text{Al}_5\text{O}_{12}$ (YAG), $\text{Al}_2\text{O}_3\text{-Er}_3\text{Al}_5\text{O}_{12}$ (EAG) and $\text{Al}_2\text{O}_3\text{-GdAlO}_3$ (GAP)) and ternary ($\text{Al}_2\text{O}_3\text{-YAG-ZrO}_2$, $\text{Al}_2\text{O}_3\text{-EAG-ZrO}_2$ and $\text{Al}_2\text{O}_3\text{-GAP-ZrO}_2$) eutectics. Improving the strength and toughness of DSE ceramics being essential for such practical applications, results concerning the mechanical behavior of these eutectics will be reported after a short presentation concerning microstructure and crystallography. This better knowledge of DSE ceramics has led to the development of a specific Bridgman furnace to produce large crystals and investigate possible applications of DSE ceramics to a new generation of very high temperature gas turbines, e.g. hollow non-cooled nozzles, turbine blades or combustor liner panels.

Introduction

Improving the thermal efficiency of aircraft gas turbines and of thermal power generation systems necessitates the development of new ultra high temperature structural materials. In this context, the use of nickel-based superalloys at temperatures beyond 1150°C will be difficult, despite the various studies performed to increase their heat-resistance. For higher temperatures, sintered ceramic oxides or ceramic matrix composites (CMCs) offer many advantages compared to Ni-based superalloys: a lower density and a better resistance to oxidation and abrasion. Unfortunately, sintered ceramics are brittle and their failure strength decreases at high temperature, whereas the use of ceramic fibers in CMCs is limited by grain growth and reaction processes with the matrix and/or the environment at high temperature. On the contrary, melt-growth composites (MGCs), prepared by unidirectional solidification of oxides from the melt, add new potentialities to the advantages of sintered ceramics and CMCs. Studies performed on eutectic compositions between alumina and rare-earth (RE) oxides have led to *in situ* composites consisting in two entangled three-dimensional and continuous interconnected networks of two single-crystal eutectic phases. After solidification, the eutectic phases are alumina and either a perovskite phase REAlO_3 (RE: Gd, Eu) or a garnet phase $\text{RE}_3\text{Al}_5\text{O}_{12}$ (RE: Y, Yb, Er, Dy). In the case of ternary systems, cubic zirconia is added to improve the fracture toughness, this

phase being present as a dispersoid. The binary and ternary systems both exhibit outstanding mechanical properties, such as a flexural strength that is constant up to temperatures close to the melting point (no amorphous phase at the interfaces between the different phases), good creep resistance, stability of the microstructure, no chemical reaction between the constituent phases and intrinsic resistance to oxidation [1-12].

This investigation is focused on both binary ($\text{Al}_2\text{O}_3\text{-Y}_3\text{Al}_5\text{O}_{12}$ (YAG), $\text{Al}_2\text{O}_3\text{-Er}_3\text{Al}_5\text{O}_{12}$ (EAG) and $\text{Al}_2\text{O}_3\text{-GdAlO}_3$ (GAP)) and ternary ($\text{Al}_2\text{O}_3\text{-YAG-ZrO}_2$, $\text{Al}_2\text{O}_3\text{-EAG-ZrO}_2$ and $\text{Al}_2\text{O}_3\text{-GAP-ZrO}_2$) eutectics. These directionally solidified eutectic (DSE) ceramics were grown from the melt using the floating-zone method (arc image furnace). Studies to control the microstructure have been performed, acting on the processing parameters. The mechanical properties have thus been investigated on the small specimens manufactured through this process [13-22]. In this respect, a biaxial testing disc flexure device has been designed to investigate the crack propagation modes in the various phases and in the interfaces [14, 19, 22]. These observations have been correlated to internal stress calculations and piezo-spectroscopy internal stress measurements [14, 16, 19, 22]. Finally, the creep behavior at high temperatures (1450-1600 °C) has been investigated using compression tests [14, 20, 21]. It has been demonstrated that creep mechanisms evolve with the macroscopic

thermomechanical loading (temperature, stress) and a correlation has been established with the deformation mechanisms observed in the entangled microstructure [14, 20, 21].

The next step has been devoted to establish the feasibility of larger crystals using the Bridgman method, which is more appropriate to obtain a homogeneous microstructure in a larger volume. A specific directional solidification furnace has been developed to produce large

crystals with melting temperatures up to 2200 °C and to demonstrate the possibility of direct solidification of turbine blades.

From the very beginning, the entire investigation has been performed in close relation with the CNRS-ICMPE Laboratory [13-22]. This paper is thus aimed at presenting a review of the most representative results obtained in the two laboratories, in order to evaluate the potential of DSE ceramics.

Box 1 - Possible applications of DSE oxides

The possible applications of DSE oxides are based on their high mechanical performances, their specific microstructure and their chemical stability. The main functional applications [3] are aimed at:

- using DSE substrates exhibiting a regular two-phase microstructure, for patterned thin film deposition in the domain of nanotechnology and superconductors,
- manufacturing porous cermets for fuel cells (the porous metallic Ni being obtained through reduction of the NiO phase of binary DSE oxides),
- using an ordered eutectic system as a monolithic bundle of optical waveguides, in the case of optically transparent fibers (selective dissolution of one phase may eventually allow it to be replaced by another material of more suitable optical properties),
- obtaining, through slow solidification, porous bioactive ceramics for human bone replacement ...

In the domain of structural materials for very high temperature applications, the use of DSE oxides is envisaged for a new generation of gas turbines operating with inlet temperatures as high as 1700 °C [12]. The applications could be vanes, hollow non-cooled nozzles, eventually, turbine blades and, in the combustion chamber, liner panels (figure B1-01).

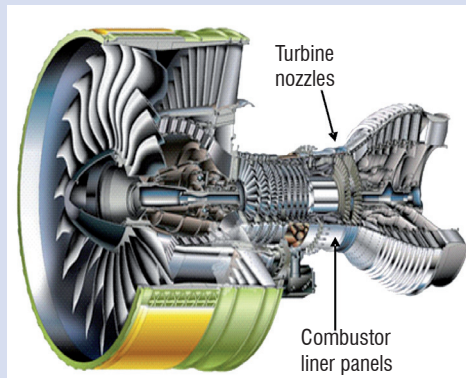


Figure B1-01 - Possible applications for gas turbines: DSE blades, nozzles and vanes, combustor with DSE liner panels. (Although there are no such applications envisaged at present for this type of gas turbine, this picture, available on the Safran-Group Web site, represents the GP 7200 gas turbine designed and developed by Engine Alliance (General Electric and Pratt & Whitney) for Airbus A380, the 9-stage high pressure compressor under the responsibility of Snecma (Safran-Group)).

At the much smaller scale of micro gas turbine engines of power generation machines in the 10 to 100 W electrical power range, the approximately 10 mm in diameter turbine could be machined in DSE oxides [23].

Microstructure and crystallography

Microstructure

Under controlled conditions, solidification from the melt leads to materials free of porosity and with only very few grain boundaries, which are generally at the origin of brittleness in sintered ceramics. The equipment used for the coupled eutectic growth of the oxides consists of high temperature single-crystal growth devices displaying a high thermal gradient. In the present case, rods of oriented eutectics, of about 8 mm in diameter, were grown using the floating-zone translation technique. Solidification runs were achieved in an arc image furnace operating with a 6 kW xenon lamp as a radiation source, at various rates, ranging from 2 to 30 mm h⁻¹.

In most DSE ceramic oxides, coupled growth is mainly controlled by the growth rate. When this rate increases, the eutectic growth undergoes a transition from the homogeneous to the cellular regime that does not correspond anymore to a coupled growth. Scanning Electron Microscopy (SEM) images (figure 1) reveal that the three-dimensional microstructure of the Al₂O₃-YAG eutectic is slightly modified when the growth rate increases; it becomes finer (figure 1 c) and persists up to rates close to 30 mm h⁻¹, before entering into the cellular growth regime (figure 1 d). Similar results were obtained with the other eutectic compositions, thus leading to a selected growth rate of 10 mm h⁻¹.

Box 2 - Coupled eutectic growth

The crucial point leading to the specific microstructure of DSE ceramic composites is the coupled eutectic growth of two (binary eutectics) or three (ternary eutectics) phases from the melt [3]. Let us first consider the **phase diagram** of the Al_2O_3 - Gd_2O_3 system at high temperatures (figure B2-01) [24]. The point corresponding to the **lowest temperature** at which the Al_2O_3 and Gd_2O_3 mixture melts or freezes is called the **eutectic point** (Greek εϋτηκτος easily melted, from: εϋ well and τηκτειν to melt). The corresponding eutectic temperature (T_E) and eutectic composition (C_E) are reported in the phase diagram (figure B2-01). The DSE composite thus obtained through unidirectional solidification is the $\text{Al}_2\text{O}_3/\text{GdAlO}_3$ binary eutectic ceramic composite.

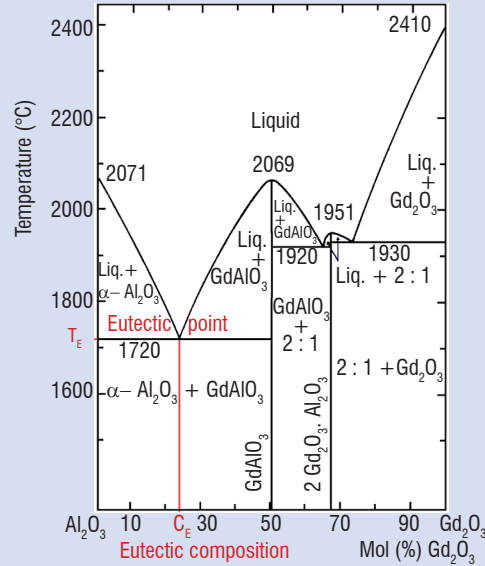


Figure B2-01 - Phase diagram of the Al_2O_3 - Gd_2O_3 system at high temperatures [24].

Coupled eutectic growth avoiding the formation of dendrites is a very complex process [3, 25], which implicates numerous phenomena. The entire process will however be briefly and roughly summarized in order to identify the role of the various involved parameters. For the sake of simplicity, although the DSE eutectics present a 3-D interconnected microstructure, a regular lamellar growth (such as that of the well-known Pb-Sn soldering alloy) will be considered (figure B2-02).

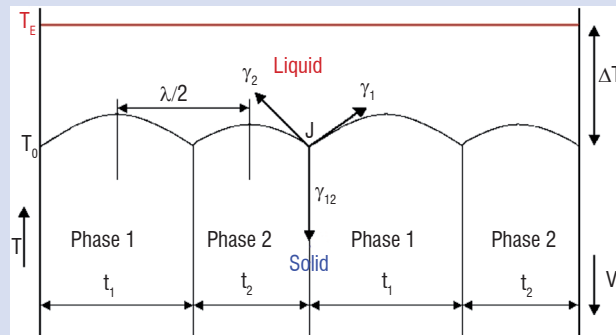


Figure B2-02 – A typical regular lamellar eutectic microstructure growing unidirectionally (V : growth rate)

In this simple case (figure B2-02), the lamellae grow unidirectionally, side by side, and are perpendicular to the planar growth front (solid/liquid interface). Firstly, if the two phases are supposed to grow separately, then long-range diffusion is necessary to ensure **solute transport in the direction of growth**. Secondly, during growth, the solid phase 1 will reject in the liquid phase, atoms corresponding to phase 2 and vice-versa (diffusion coupling), thus leading to a **diffusion flux parallel to the growth front**. The eutectic growth is thus largely governed by **diffusive mass transport**.

At the three-phase junction (J), the **curvature** of the solid phase in contact with the liquid (solid/liquid interface) is determined by the condition of mechanical equilibrium of the **interface forces** (phase 1/phase 2 (γ_{12}), phase 1/liquid (γ_1) and phase 2/liquid (γ_2); arrows in figure B2-02), a phenomenon called **capillarity effects**. In this respect, a specific aspect of ceramics should be emphasized: the capillarity of an oxide such as Al_2O_3 [26] is sufficiently high to allow the growth of commercial sapphire fibers through capillary tubes [27, 28].

These two phenomena, diffusion (through the mean solute undercooling) and capillarity (through the mean curvature undercooling), are the main factors contributing to the ΔT **undercooling** (growth temperature T_0 , as compared to the eutectic temperature T_E ($T_0 < T_E$), figure B2-02). Another consequence of these two factors is that the **lamellar spacing** λ (i.e. the size of the microstructure) varies as a function of the growth rate, V (figure B2-02 and figure 1). Concerning the solidification process, the eutectic behaves like a pure chemical substance; due to **latent heat**, the phase change from liquid to solid occurs with a “thermal arrest” (solidification time) in the cooling curve, the internal energy being higher in the liquid than in the solid. In this respect, another specific aspect of ceramic oxides should be noted: the latent heat (also known as specific melting heat or **enthalpy of fusion**) is very high. For instance, in the case of Al_2O_3 , the enthalpy of fusion is as high as 111.4 kJ/mol (1092 kJ/kg) [29], instead of 7.15 kJ/mol (60.2 kJ/kg) for Sn, 4.77 kJ/mol (23.04 kJ/kg) for Pb or 6.01 kJ/mol (333.55 kJ/kg) for water, which is well-known for its high enthalpy of fusion. Such a high latent heat may have a non-negligible effect on the **kinetic** undercooling, which depends on the **growth rate** V [3] and constitutes a third contribution to the global ΔT undercooling (figure B2-02). Moreover, material characteristics should also be taken into account, essentially the marked tendency of the two phases to grow under **specific crystallographic orientations** (figure 5). Finally, due to the effects of the various parameters mentioned earlier, such as the coefficient of diffusion (D) of solute in the liquid phase, coupled eutectic growth under a given growth rate V can only be obtained if the **thermal gradient** (G_r) in the ceramic ingot attains a sufficient value. Consequently, coupled eutectic growth is only possible if the ratio G_r/V is higher than a critical value $(G_r/V)_{Critical}$

$$G_r/V > (G_r/V)_{Critical} \tag{B2-01}$$

Consequently, in the Bridgman furnace, where the temperature gradient is much smaller than that attained in the floating-zone method, a lower growth rate leads to coupled eutectic growth.

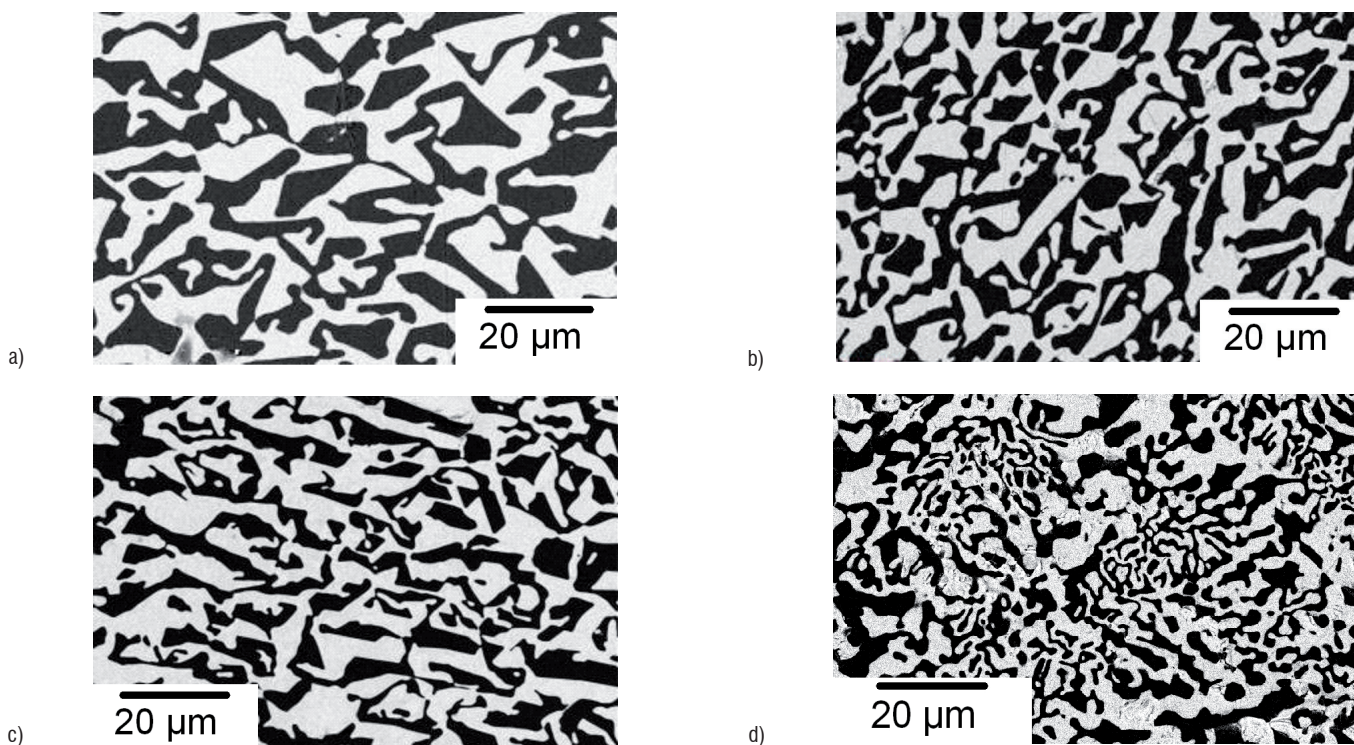


Figure 1 - Back-scattered SEM micrographs of the Al_2O_3 -YAG ($Y_3Al_5O_{12}$) eutectic composite (Al_2O_3 : dark contrast). Morphology of microstructure vs. the solidification rate: 5 mm h⁻¹ (a), 12 mm h⁻¹ (b), 20 mm h⁻¹ (c) and 30 mm h⁻¹ (d).

SEM images of the microstructures in cross-sections perpendicular to the solidification direction of binary eutectics are shown in figure 2. In each case, continuous networks of two single-crystal phases are observed: Al_2O_3 (dark contrast) and a perovskite (P) or garnet (G) phase (bright contrast). The domain mean size of each phase (length of the shortest axis) is similar for the Al_2O_3 -EAG and Al_2O_3 -GAP eutectics (figure 2 b and c), whereas it is much larger for the Al_2O_3 -YAG eutectic composites (figure 2 a). Moreover, the Al_2O_3 -EAG and Al_2O_3 -GAP eu-

tectics exhibit curved interfaces (figure 2 b and c); on the contrary, the Al_2O_3 -YAG eutectic composite displays a faceted microstructure with large planar interfaces (figure 2 a).

The same morphology of continuous networks of two single-crystal phases is observed on sections parallel to the growth direction (figure 3). It should be noted that the phases are not elongated in the growth direction, but perfectly similar in shape and size in sections

parallel or perpendicular to the growth direction, thus revealing the three-dimensional configuration of the microstructure (figure 3). The two phases interpenetrate without grain boundaries, pores or colonies.

Typical microstructures of transverse sections of ternary eutectics are shown in figure 4. First of all, it should be noted that the morphology of the garnet-type phase (YAG or EAG) is modified depending on the rare-earth oxide added to alumina and zirconia. The Al_2O_3 -YAG-ZrO₂ ternary eutectic displays a fine microstructure with curved smooth interfaces

(figure 4 a), instead of the coarser microstructure with large planar interfaces and sharp angles observed in the Al_2O_3 -YAG binary eutectic (figure 2 a). In the Al_2O_3 -YAG-ZrO₂ ternary eutectic, the cubic zirconia phase grows essentially at the interface between Al_2O_3 and YAG. In the case of Al_2O_3 -EAG-ZrO₂ and Al_2O_3 -GAP-ZrO₂ ternary eutectics, zirconia dispersoids are observed, not only at the interfaces, but also in the alumina phase (more clearly evidenced at a higher magnification, in figure 6, reporting crack propagation modes in ternary eutectics).

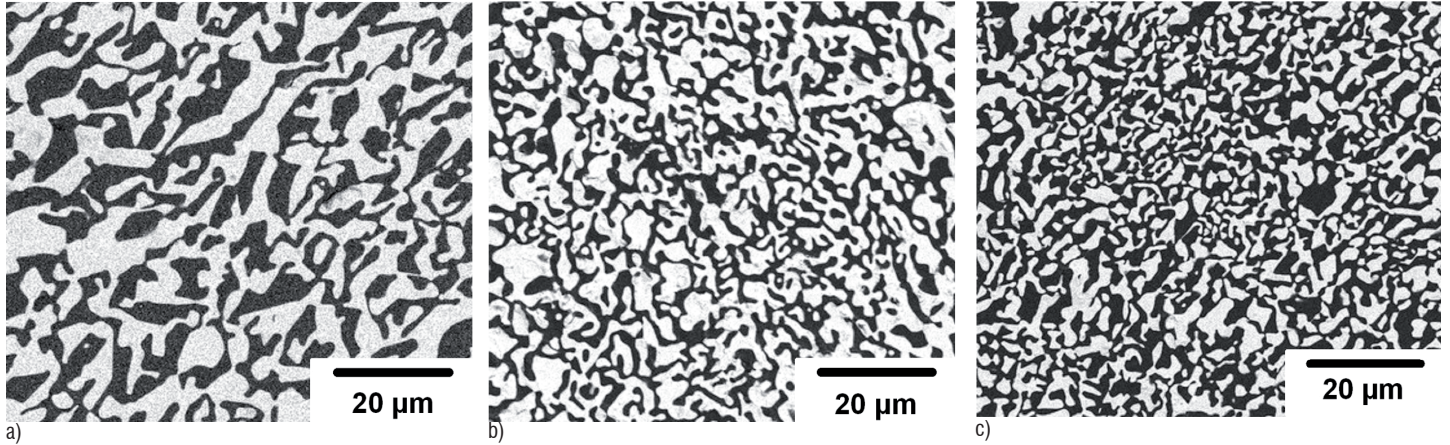


Figure 2 - Back-scattered SEM micrographs of the transverse sections of binary eutectics showing the continuous three-dimensional interconnected microstructure consisting of Al_2O_3 (dark contrast) and: YAG = $\text{Y}_3\text{Al}_5\text{O}_{12}$ (a), EAG = $\text{Er}_3\text{Al}_5\text{O}_{12}$ (b) and GAP = GdAlO_3 (c).

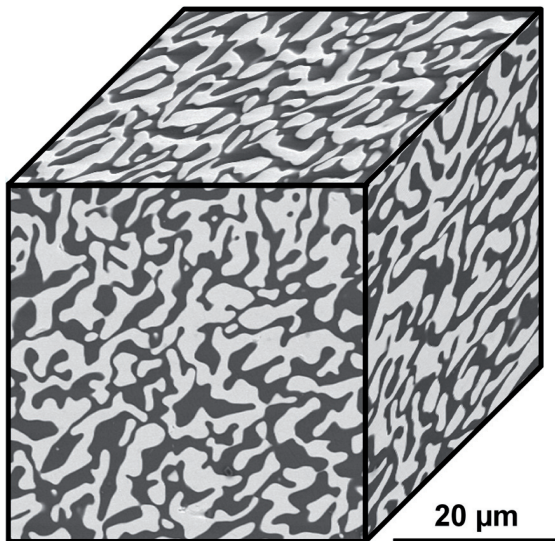


Figure 3 – SEM micrographs revealing the three-dimensional configuration of the microstructure of the Al_2O_3 -GAP eutectic composite. The growth direction is indicated by the vertical arrow.

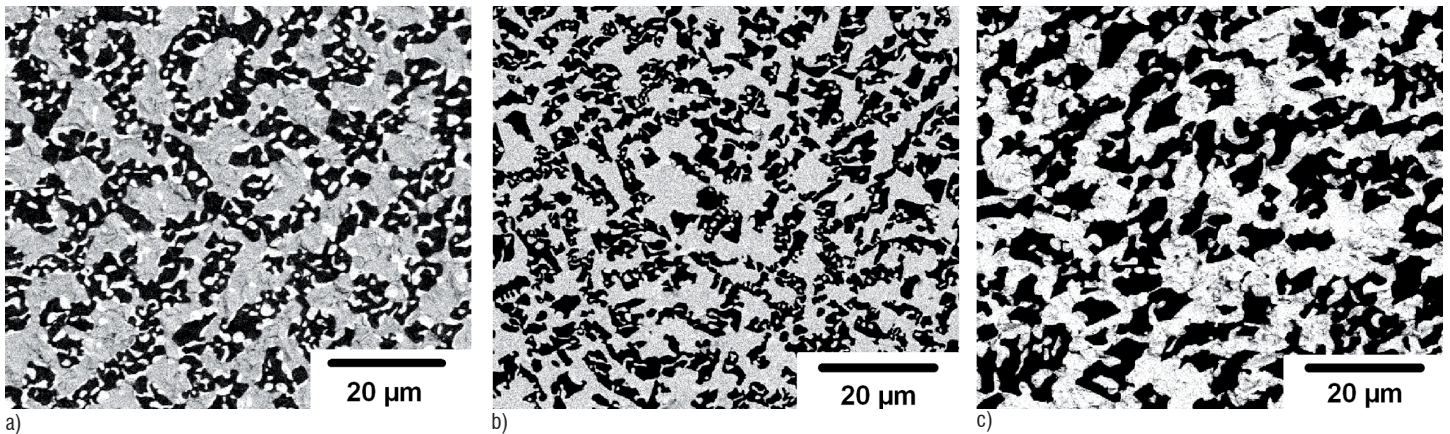


Figure 4 - Back-scattered SEM micrographs of transverse sections of ternary eutectics containing Al_2O_3 (dark contrast), YAG (a), EAG (b) or GAP (c) and zirconia (bright contrast dots).

Crystallography

Aligned eutectic microstructures (lamellae, fibers, etc.), grown by unidirectional solidification, usually consist of single-crystal phases growing preferentially along well-defined crystallographic directions. These directions are not necessarily the directions of easy-growth of the isolated components, but often correspond to minimum interfacial energy configurations between phases. The perfect crystal lattices of each phase are related by orientation relationships which are unique in most systems and produce well-defined interface planes corresponding to dense atomic arrangements in the component phases. Although the DSE do not display 1-D or 2-D aligned microstructures but 3-D interconnected microstructures, electron diffraction studies performed in Transmission Electron Microscopy (TEM) on thin plates cut perpendicularly to the solidification axis reveal growth directions also corresponding to well-defined crystallographic directions (table 1).

Eutectic phases	Al ₂ O ₃ - Perovskite	Al ₂ O ₃ - Garnet
Growth directions	[10 $\bar{1}$ 0] Al ₂ O ₃ // [110] Perovskite	[10 $\bar{1}$ 0] Al ₂ O ₃ // [110] Garnet
Orientation relationships	(2 $\bar{1}$ $\bar{1}$ 0) Al ₂ O ₃ // (001) Perovskite	(0001) Al ₂ O ₃ // ($\bar{1}$ 12) Garnet

Table 1 - Growth directions and orientation relationships of the directionally solidified eutectic composites (TEM).

These results, obtained from Selected Area Electron Diffraction (SAED) patterns correspond to analyzed regions of a few micrometers in size; in order to control the single-crystal homogeneity over larger areas, the Electron Back-Scattered Diffraction (EBSD) technique was used [13, 17, 18]. Figure 5 shows the Pole Figures (PF) and the Inverse Pole Figure (IPF) maps for the Al₂O₃-YAG eutectic ceramics (section perpendicular to the growth direction). The orientation maps presented in figure 5 a reveal the sample texture and the nearly single crystal homogeneity of the sample. Each color corresponds to one crystallographic direction, as indicated in the reference stereographic triangles (figure 5 a, right). For example, if YAG crystals had their $\langle 111 \rangle$ axis normal to the specimen surface, then they would appear as blue and so on. A unique color corresponds to the YAG phase, which thus exhibits only one growth direction (figure 5 a, bottom). Two different colors are visible for alumina (figure 5 a, top); this is due to the fact that the [10 $\bar{1}$ 0] and [01 $\bar{1}$ 0] growth directions are not equivalent in the rhombohedral symmetry, thus resulting in two twin-related variants of Al₂O₃. Moreover, the pole figures (figure 5 b) confirm the orientation relationship between the two phases: (0001)_{Al₂O₃} // ($\bar{1}$ 12)_{YAG}.

Concerning the interfaces between alumina, perovskite, garnet and zirconia, atomic scale High Resolution Transmission Electron Microscopy (HRTEM) investigations have revealed the absence of an interphase layer [1, 2, 17, 20]. The orientation of the interface with respect to the adjacent phases growing in epitaxy and the mismatch between the lattice parameters result in a regular network of intrinsic defects along the interface. However, in each phase, the stress field resulting from such an interface is so local and so faint that it cannot be detected in conventional TEM, thus assessing a minimum energy configuration of the interfaces.

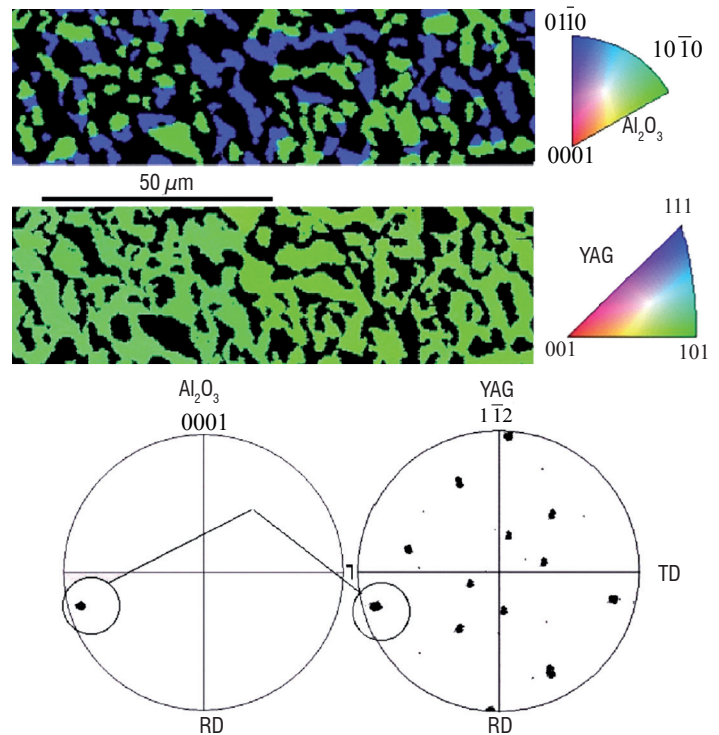


Figure 5 - Inverse Pole Figure maps of Al₂O₃ and YAG phases in a section perpendicular to the growth direction (a) and Pole Figures of 0001_{Al₂O₃} and $\bar{1}$ 12_{YAG} orientations (b). Orientation relationship: (0001)_{Al₂O₃} // ($\bar{1}$ 12)_{YAG} (b).

Mechanical properties

Crack nucleation and propagation modes

Improving the strength and toughness of eutectic ceramics requires a better knowledge of the crack propagation modes in such an interconnected microstructure. In this respect, a biaxial disc flexure testing device has been designed and built at Onera [19]. In the six directionally solidified eutectics [19, 22] investigated, the essential propagation mode is transgranular crack propagation (figure 6). A zigzag crack growth with multiple branches is observed in most cases. However, this type of crack propagation does not only result from deflections of the cleavage crack inside each phase, or when crossing phase boundaries, but more essentially from crack deflection in the interfaces themselves. Interface crack propagation is thus observed between Al₂O₃ and YAG (large black arrow in figure 6 a), Al₂O₃ and EAG (large black arrows in figure 6 b), Al₂O₃ and GAP (large black arrow in figure 6 c), Al₂O₃ and ZrO₂ (white arrows in figure 6 a, b and c), YAG and ZrO₂ (sharp black arrow in figure 6 a) and EAG and ZrO₂ (sharp black arrow in figure 6 b). Crack branching is observed, not only in one of the various phases such as ZrO₂ (split arrow in figure 6 a), but also in the interfaces where crack deflection through debonding has occurred (split arrows in figure 6 c). In most cases, these bifurcation mechanisms lead to stopped cracks (figure 6 a and c).

The various crack propagation modes may be correlated to internal thermal stress measurements and calculations [19]. For instance, the presence of ZrO₂ phases surrounded by a continuous layer of Al₂O₃ (figure 6 b (top right corner) and c (top left corner)) suggests the use of a concentric cylinder model (figure 7 a). The ZrO₂ phases in figure 6 b (top right corner) and c (top left corner) may be

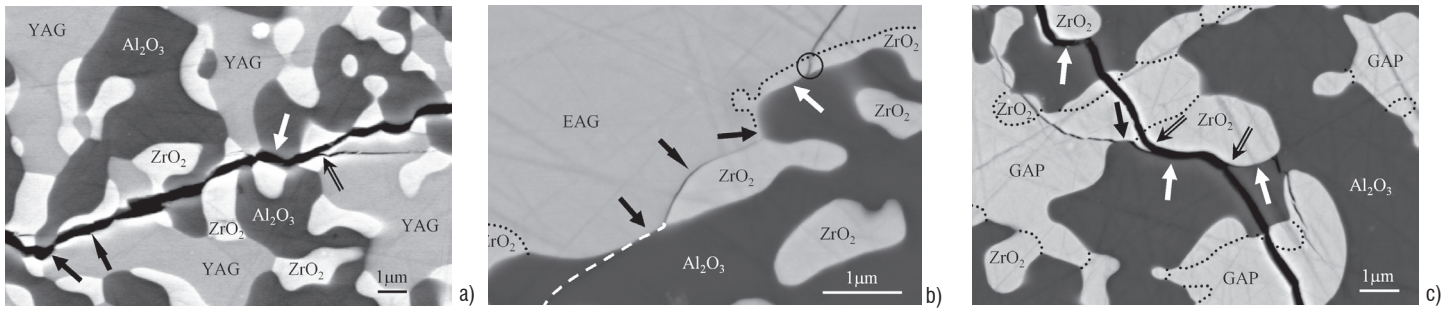


Figure 6 - Crack propagation modes at room temperature in ternary eutectic ceramics subjected to biaxial flexure (Field emission gun (FEG)-SEM, back-scattered electrons): Al_2O_3 -YAG- ZrO_2 (a), Al_2O_3 -EAG- ZrO_2 (b) and Al_2O_3 -GAP- ZrO_2 (c).

represented by a $1 \mu\text{m}$ in diameter ZrO_2 bar, bonded into a $1.5 \mu\text{m}$ thick Al_2O_3 sleeve, surrounded by a $0.5 \mu\text{m}$ thick ZrO_2 sleeve, these three concentric cylinders being embedded into an equivalent homogeneous medium (EHM) having the diameter of the specimen under investigation and the macroscopic thermo-mechanical properties of the bulk Al_2O_3 -EAG- ZrO_2 or Al_2O_3 -GAP- ZrO_2 eutectics, respectively. In the case of the Al_2O_3 -GAP- ZrO_2 eutectics, subjected to a temperature change ($\Delta T \approx 1700^\circ\text{C}$), the normal stress ($\sigma_n = \sigma_r$) acting on the ZrO_2 - Al_2O_3 interface attains $\approx 1000 \text{ MPa}$ (figure 7 b); this high tensile normal stress helps interface crack propagation, as observed in figure 6 c (top left corner). The external ZrO_2 layer is subjected to a high tensile circumferential loading ($\sigma_\theta \approx 1800 \text{ MPa}$) which helps transgranular crack propagation in these phases, as observed in figure 6 b (circle, top right corner) and c (top left corner). As compared to the ultimate tensile strength of such eutectic ceramics [2, 4], the level of these internal thermal stress components is very high, which may explain their essential role in crack nucleation and propagation (e.g. the possibility of crack deflection in the interfaces, in the ternary eutectic ceramics). This high stress level is however in good agreement with the internal stress measurements performed through ruby (Cr^{3+}) fluorescence piezo-spectroscopy [22]. The fact that the observed crack deflection modes are more numerous in ternary than in binary eutectics is in good agreement with the fact that the fracture toughness is improved from the individual constituents, to the binary eutectics ($\approx 7 \text{ MPa m}^{1/2}$) and to the ternary eutectics ($\approx 10 \text{ MPa m}^{1/2}$) [13, 17].

Moreover, factors other than the thermal mismatch stresses, such as the role of the Young's modulus ratio between garnet or perovskite and alumina, as well as the nature of the interfaces, have a non-negligible effect on the crack deflection and propagation modes [22]. Consequently, due to the presence of a two- or three-phase 3-D interconnected microstructure, a highly detrimental crack propagation mode such as transgranular crack propagation in the brittle ceramic phases is drastically limited by energy dissipative crack deflection modes resulting from thermal mismatch stresses, the effects of Young's modulus ratios and the nature of the interfaces between the various phases [19, 22].

Compressive creep behavior

The compressive creep tests performed on the binary and ternary eutectics under consideration were conducted in air within the stress range 50 to 200 MPa and the temperature range 1450 to 1600 °C. The major axis of the parallelepipedic compressive creep specimens was parallel to the solidification direction. After a short primary stage (e.g. strain of about 0.5%), the secondary creep rate is reached [14, 20, 21].

In this investigation, the stress exponent n , and the activation energy Q , which may be derived from equation (B3-01) and are given by equations (B3-02), have been determined through creep tests performed either at a given temperature with load increments or decrements (stress exponent, n), or at a given load with temperature increments or decrements (activation energy, Q). Practically, during a creep test performed on a given specimen at a given temperature, once a secondary stage steady-state regime is attained and the corresponding creep strain rate $\dot{\epsilon}$ is experimentally determined, the applied stress is increased and once a new steady-state regime is attained, the corresponding $\dot{\epsilon}$ is determined. Load increments and decrements are thus applied several times, leading to the determination of strain rates at different stress levels (figure 8 a).

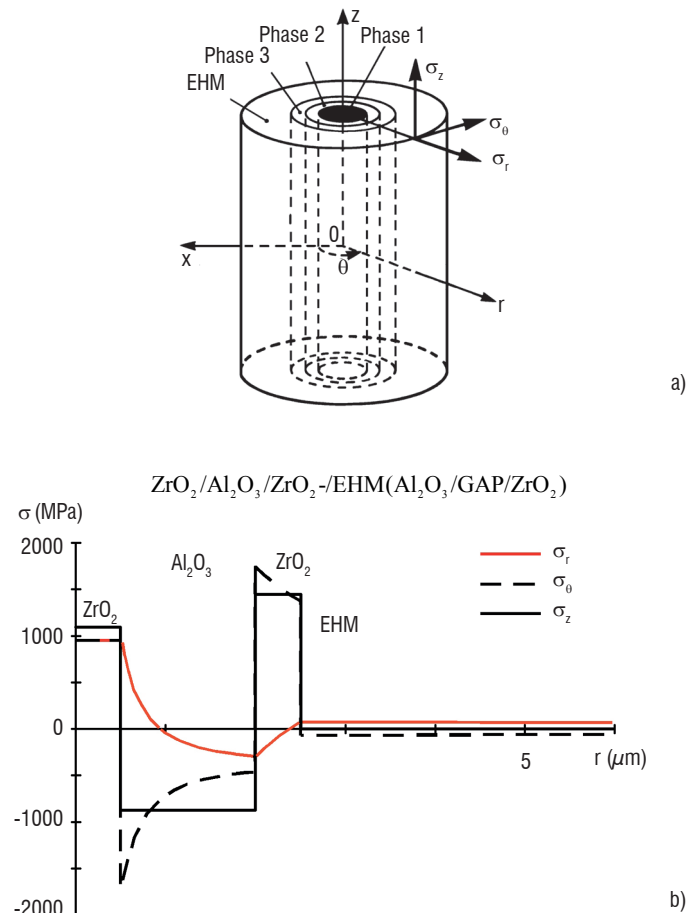


Figure 7 - Internal thermal stresses. The four-phase concentric cylinder model (a), the corresponding stress system (b), where the normal stress σ_n , is given by the radial stress component σ_r .

Box 3 - Creep of ceramics

A good knowledge of the tensile and creep behavior is essential, especially for components subjected to high stresses at high temperatures. Thermomechanical testing of ceramics thus includes tensile tests at various temperatures and high temperature creep tests.

Tensile tests (stress-strain curves) performed at a given temperature and, usually, at a constant strain rate, allow the determination of the elastic and plastic behavior at various temperatures, i.e. Young’s modulus (E), the yield stress (Y), the ultimate tensile stress (UTS) and the fracture stress (F).

Creep tests are performed at a constant high temperature but, contrary to tensile tests, the specimen is subjected to a constant high stress loading (**constant load**) during an **extended time period**. Creep tests are thus representative of essential phenomena such as the deformation of turbine blades subjected to centrifugal loading during service, the resulting length extension being detrimental and even totally unacceptable.

In metals, alloys and superalloys, high temperature stress-strain curves and creep curves are usually obtained with standard specimens having a gauge section between two shoulders (the so-called dog-bone-shaped specimens) subjected to a tensile applied loading. Using such a specimen does not only require a large quantity of material, but also necessitates machining of the shoulders of the test specimen, in order to apply the load to the specimen through the grips of the testing system. Although such a device may be successfully used with DSE ceramics (e.g. threaded specimen ends and tapped DSE grips [30]), due to the brittleness of ceramics, the stress-strain curves are usually obtained through three- or four-point bending tests, whereas the creep behavior is studied through **compression creep** tests, as in the present investigation.

The **creep curve** is the representation, as a function of time, of the cumulated creep strain: the “time-dependent” creep strain (figure B3-01). After linear extension of the specimen (elastic behavior), the shape of the creep curve reveals the three stages of creep (figure B3-01). Firstly, the creep strain rate ($\dot{\epsilon} = d\epsilon/dt$) decreases (transient creep or primary creep), then the strain rate remains constant over a rather long period (steady-state or secondary creep) and, finally, the strain rate increases, leading to creep rupture of the specimen (accelerating creep or tertiary creep).

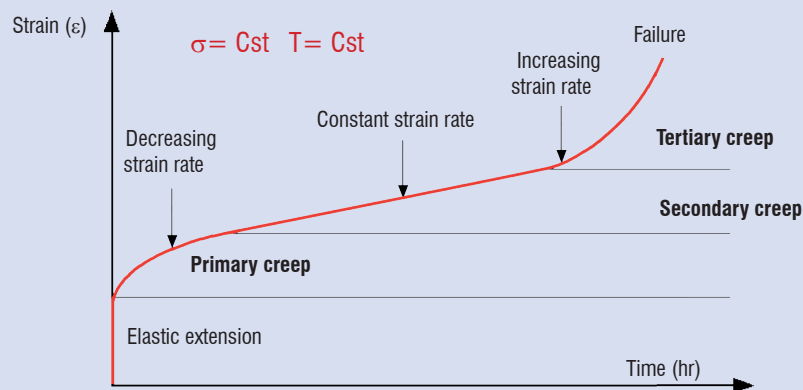


Figure B3-01 – Typical creep curve showing the three stages of the material creep behavior.

In the steady-state (secondary) creep stage, the strain rate ($\dot{\epsilon}$) is proportional to a power of the applied stress (σ) with a thermal activation term

$$\dot{\epsilon} = A \sigma^n \exp - Q/RT \tag{B3-01}$$

where A is a material constant, n is the stress exponent, Q is the activation energy of the creep mechanism and R and T are, respectively, the gas constant and the absolute temperature.

The stress exponent n, and the activation energy Q, are representative of the creep mechanisms responsible of the creep behavior of the material. Determination of these quantities, in close relation with microstructural investigations, will allow these mechanisms to be identified. These quantities may be derived from equation (B3-01) and are given by

$$n = \left. \frac{\partial \ln \dot{\epsilon}}{\partial \ln \sigma} \right)_{T,A} \quad \text{and} \quad Q = -R \left. \frac{\partial \ln \dot{\epsilon}}{\partial 1/T} \right)_{\sigma,A} \tag{B3-02}$$

However, the determination of these quantities necessitates more complex creep tests to be performed. For instance, creep tests performed at a given temperature ($T = \text{Cst}$), with load increments or decrements, will allow the determination of n (figure 8 a), whereas tests performed under a given loading ($\sigma = \text{Cst}$), with temperature increments or decrements, will allow the determination of Q (figure 8 b). In both cases, increments or decrements must only be applied once a steady-state regime is attained; the creep strain rate, corresponding to the steady-state regime of each step, may thus be experimentally determined for a given and constant microstructure, the different steps being attained on the same specimen.

In sintered ceramics, due to the presence of numerous grain boundaries and, in most cases, of an amorphous layer at the grain boundaries, high temperature creep may be essentially attributed to diffusion assisted grain boundary sliding. In DSE oxides, the various mechanisms involved in high temperature creep may include thermally activated dislocation motion in the individual phases (glide, cross-slip and climb), bulk (volume) diffusion, etc.

Similarly, creep tests are performed on another specimen at a given stress level and the creep strain rate is determined for each temperature step (figure 8 b) [14, 20, 21].

Although the eutectics under consideration have been thoroughly tested under compressive creep [14], only the more representative results will be reported in this paper (figure 9).

From the results reported in figure 9 a, which are representative of the investigated Al_2O_3 -Garnet eutectics [14, 21], it should be noted that, at 1450 °C, the stress exponent (n) increases more rapidly, as the applied stress is increased, than at 1525 °C. Under a low applied stress, a value of n such as 1.14 corresponds to a creep strain rate nearly proportional to the applied stress. Such a value of n suggests a diffusion controlled creep mechanism. At a high stress level and/or high temperature, the value of n is higher ($2 < n < 3$), which suggests creep mechanisms controlled by dislocation motion.

The creep strain rate vs. temperature ($1/T$) of the Al_2O_3 -EAG eutectic composite (figure 9 b) is representative of the investigated Al_2O_3 -Garnet eutectics [14, 21]. Concerning the activation energy, the value of $Q \approx 350$ kJ/mol is found only for temperatures lower than 1490 °C and under a low applied stress (70 MPa); the activation energy is

otherwise higher: $Q \approx 600$ kJ/mol. Such a high value of Q may correspond to self-diffusion of oxygen atoms in the alumina phase [31]. It should also be noted that similar values have been reported in the literature [32].

In the case of ternary eutectics, the variation of n as a function of the applied stress is similar to that determined in the binary eutectics [14]. Concerning the activation energy (figure 9 c), the value of $Q \approx 400$ kJ/mol is also found for a temperature lower than ≈ 1500 °C in the only case of Al_2O_3 -YAG- ZrO_2 , a behavior which is similar to that observed in the binary Al_2O_3 -Garnet eutectics (figure 9 b). In the other conditions, an activation energy of $Q \approx 600$ kJ/mol has been determined. Concerning the creep strain rates of the ternary eutectics, it should be noted that the behavior of the Al_2O_3 -YAG- ZrO_2 and Al_2O_3 -GAP- ZrO_2 eutectics is similar to that of the corresponding binary eutectics, whereas that of the Al_2O_3 -EAG- ZrO_2 eutectic is lower [14].

Creep tests performed with the compression loading axis perpendicular to the growth direction have revealed a similar creep behavior [21]. This result is essential for structural parts subjected to tension or compression loadings in different directions.

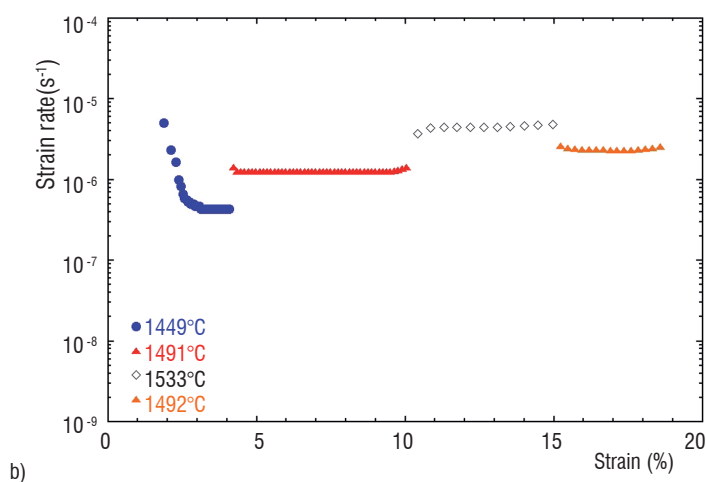
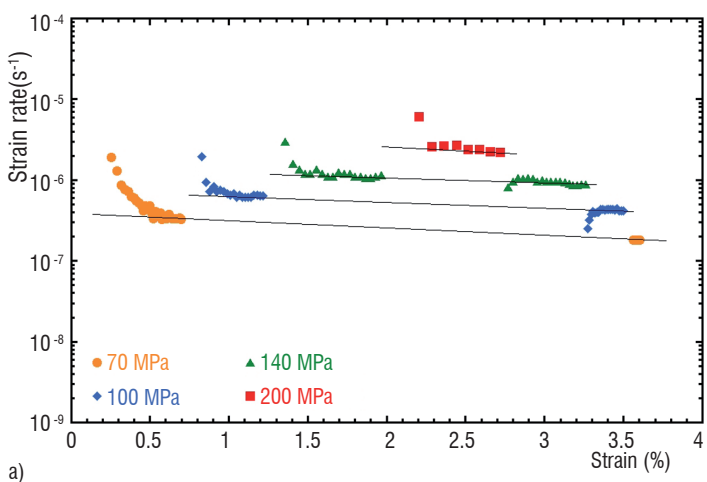


Figure 8 - Compressive creep tests on the Al_2O_3 -YAG eutectic composite. Creep strain rate vs. strain at 1525°C with stress increments and decrements (a) and creep strain rate vs. strain under a 200 MPa loading with temperature increments and decrements (b).

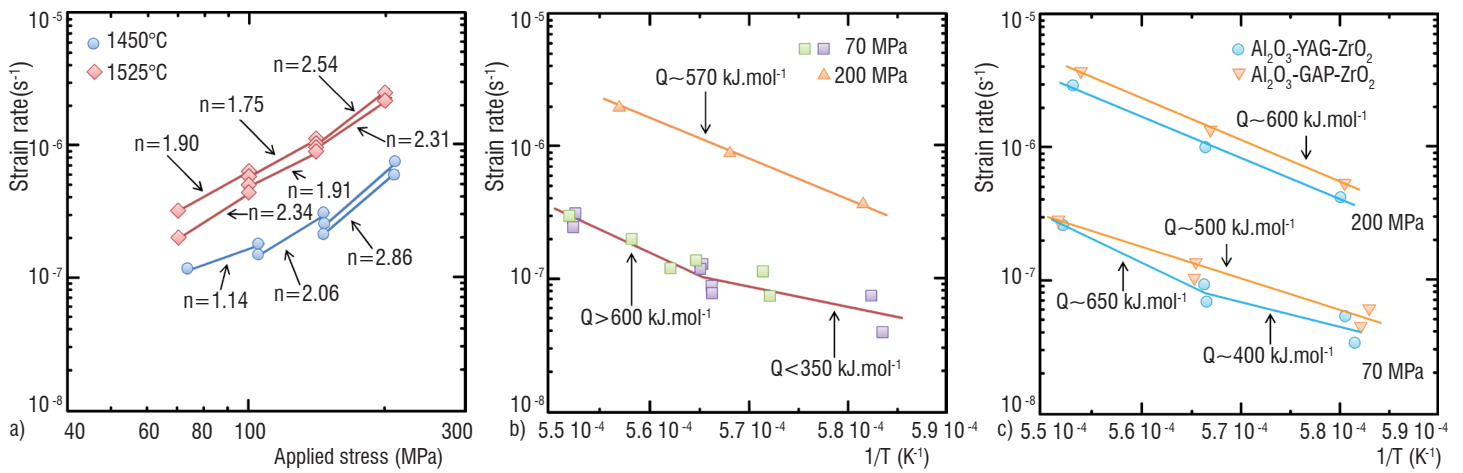


Figure 9 - Compressive creep tests. Creep strain rate $\dot{\epsilon}$ vs. applied stress at 1450 °C and 1525 °C for the Al_2O_3 -YAG eutectic composite (a). Creep strain rate $\dot{\epsilon}$ vs. temperature ($1/T$) under 70 and 200 MPa loadings for the Al_2O_3 -EAG eutectic composite (b). Creep strain rate $\dot{\epsilon}$ vs. temperature ($1/T$) under 70 and 200 MPa loadings for the Al_2O_3 -YAG- ZrO_2 and Al_2O_3 -GAP- ZrO_2 eutectics (c).

In order to identify the creep deformation modes, transmission electron microscopy (TEM) examinations were performed on specimens previously subjected to compressive creep tests [14, 20, 21]. Due to the strong interface bonding between the various phases, interface sliding mechanisms are nearly impossible. Moreover, due to the difficulty for dislocations to cross the interfaces (difference in lattice parameters), the only possibility to transmit plastic deformation from one phase to the other is to activate a dislocation source in one phase, under the stress concentration resulting from the presence of a dislocation pile-up in the other phase. Otherwise, both phases must deform independently in order to accommodate the global creep deformation. In each phase, the gliding dislocations have to bow within the phase width (λ_p). The shear stress τ necessary for this process is given by

$$\tau = Gb/\lambda_p \quad (1)$$

where G is the shear modulus and b the Burgers vector.

Consequently, when the size of the microstructure decreases (e.g. eutectic morphologies reported in figure 2), the activation of dislocation glide requires higher stresses.

In the alumina phase of the Al_2O_3 -GAP eutectics (figure 10 a), the observed dislocations are basal type dislocations ($b = 1/3[2\bar{1}10]$) aligned in parallel (0001) basal slip planes. This is in agreement with the fact that the basal slip system has the lowest critical resolved shear stress at high temperature [33, 34]. A dislocation pile-up has also been observed in the GAP phase (figure 10 b). This pile-up interacts with the GAP-alumina interface at the bottom of the image, and a basal twin is observed in alumina close to the interaction. Mechanical twinning is probably due to accommodation of the stress concentration resulting from the pile-up.

In the alumina phase of the Al_2O_3 -YAG eutectics, rhombohedral dislocations may be observed, thus demonstrating that high stress concentrations may be attained. Thermally activated mechanisms such as dislocation climb have also been observed (figure 10 c, central area). Such a dislocation network, resulting from the reaction of dislocations from the basal and pyramidal slip systems, involves dislocation climb. This diffusion controlled deformation mode was observed in an Al_2O_3 -YAG specimen previously subjected to a creep test, for which an activation energy of $Q \approx 670$ kJ/mol was determined. This last result is in good agreement with reference [31], concerning oxygen diffusion controlled mechanisms in alumina.

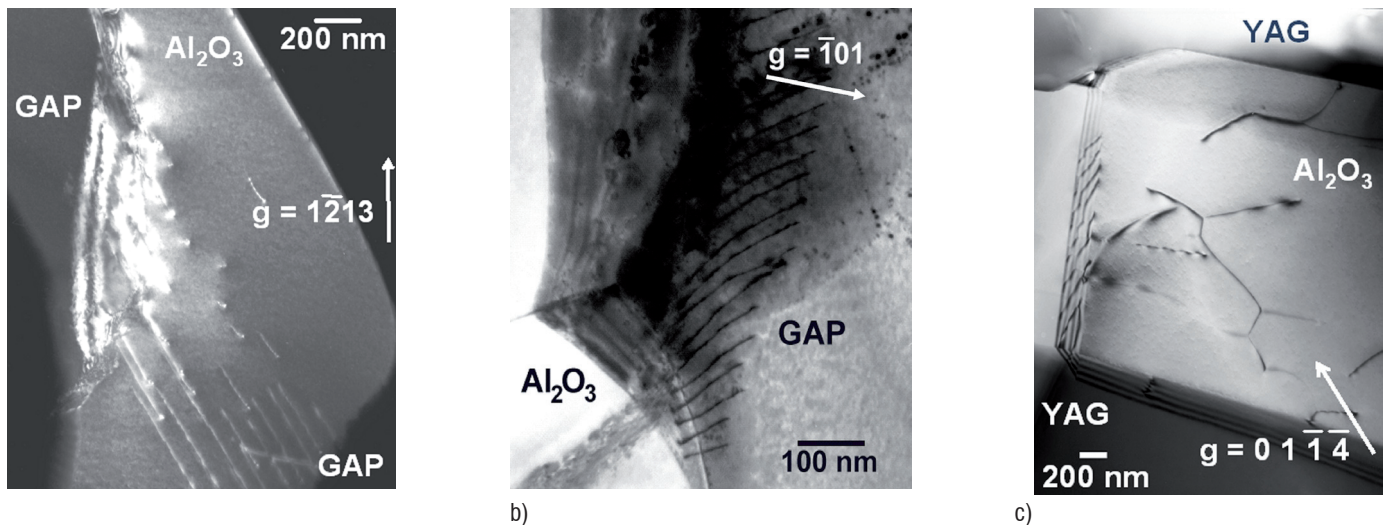


Figure 10 - TEM examinations of compression tested specimens. Dislocation glide in the Al_2O_3 phase of the Al_2O_3 -GAP eutectic composite (a). Dislocation pile-up in the GAP phase of the Al_2O_3 -GAP eutectic composite (b). Dislocation reaction involving climb in the Al_2O_3 phase of the Al_2O_3 -YAG eutectic composite (c).

The TEM examinations have evidenced plastic deformation of the various phases; furthermore, the different deformation modes thus observed are in good agreement with the stress exponents and activation energies experimentally determined.

Feasibility of turbine blades in a large Bridgman furnace

A large Bridgman furnace has been manufactured (Cyberstar, Grenoble, France) according to the specifications established by Onera (figure 11). This device, which includes two superposed radiofrequency heating elements, ensures a melting zone temperature up to 2200 °C ($\pm 1^\circ\text{C}$) and a crystallization zone temperature up to 1600 °C ($\pm 1^\circ\text{C}$). In the liquid/solid transition zone, a thermal gradient in the range 20 °C/cm to 40 °C/cm is attained. This Bridgman furnace operates either under vacuum or under a neutral atmosphere up to 15 bars and allows a growth rate ranging from 5 to 50 mm h⁻¹. The molybdenum crucible allows the directional solidification of large eutectic crystals up to 50 mm in diameter and 200 mm in height.

Studies in progress concern the determination of the solidification parameters, in order to optimize the microstructure of the Al₂O₃-GAP and Al₂O₃-YAG-ZrO₂ eutectics and their thermomechanical characterization, e.g. flexural strength up to 1500 °C. New eutectic compositions without Al₂O₃ phase will be also investigated, in order to improve the resistance to high temperature water vapor corrosion. Finally, the feasibility of making near net shape turbine blades will be investigated.

Conclusion

Ceramic materials prepared by unidirectional solidification of oxides from the melt are under investigation at Onera, for applications in the aerospace field and in particular for gas turbine blades. Studies to control the microstructure of the directionally solidified eutectic ceramics have been performed and the crystallographic orientation relationships between the constituent phases have been identified. The mechanical properties have been investigated with the aim of understanding the toughening mechanisms and the creep behavior at high temperatures. In the ternary eutectic ceramics, the high level of the internal thermal stresses may explain their essential role in crack nucleation and propagation (e.g. the possibility of crack deflection in the interfaces). The fact that the observed crack deflection modes are more numerous in ternary than in binary eutectics is in good agreement with the improvement of the fracture toughness from the individual constituents, to the binary eutectics and to the ternary eutectics. Concerning the creep strain rates of the ternary eutectics, it should be noted that the behavior of the Al₂O₃-YAG-ZrO₂ and Al₂O₃-GAP-ZrO₂ eutectics is similar to that of the corresponding binary eutectics whereas that of the Al₂O₃-EAG-ZrO₂ eutectic composite is lower. The TEM examinations have evidenced plastic deformation of the various phases; furthermore, the different deformation modes thus observed are in good agreement with the stress exponents and activation energies experimentally determined. This better knowledge of the behavior of DSE ceramics subjected to thermomechanical loadings has led to the development of a specific Bridgman furnace to produce large crystals and near net shape turbine blades. New eutectic compositions without Al₂O₃ phase will be investigated to improve the resistance to high temperature water vapor corrosion ■

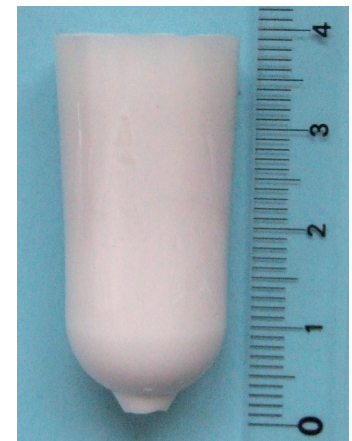


Figure 11 - The Bridgman furnace (a) and an Al₂O₃-GdAlO₃ crystal obtained using this furnace (b).

Acknowledgements

The authors would like to thank M. RAFFESTIN (FEG-SEM investigations), D. BOVIN (EBSD studies), Dr. F. C. LISSALDE (Bridgman furnace, Cyberstar), Dr. L. LIBRALESSO, C. BEN RAMDANE, M. BEJET, J. C. DAUX, S. LALANNE (Bridgman furnace) and Prof. J. CRAMPON for their kind cooperation and fruitful discussions. They would like to express their gratitude to the Regional Council of Île-de-France for the financial support concerning the Bridgman furnace equipment. L. PERRIÈRE would also like to thank the French Defense Research Organization (DGA) for his Doctorate Scholarship.

References

- [1] Y. WAKU, N. NAKAGAWA, T. WAKAMOTO, H. OHTSUBO, K. SHIMIZU, Y. KOHTOKU - *A Ductile Ceramic Eutectic Composite with High Strength at 1873 K*. Nature, Vol. 389, pp. 49-52, 1997.
- [2] Y. WAKU, N. NAKAGAWA, T. WAKAMOTO, H. OHTSUBO, K. SHIMIZU, Y. KOHTOKU - *High Temperature Strength and Stability of Unidirectionally Solidified Al_2O_3/YAG Eutectic Composite*. J. Mater. Sci., Vol. 33, pp. 1217-1225, 1998.
- [3] J. LLORCA, V. M. ORERA - *Directionally Solidified Eutectic Ceramic Oxides*. Prog. Mater. Sci., Vol. 51, pp. 711-809, 2006.
- [4] J. I. PEÑA, M. LARSON, R. I. MERINO, I. DE FRANCISCO, V. M. ORERA, J. LLORCA, J. Y. PASTOR, A. MARTÍN, J. SEGURADO - *Processing, Microstructure and Mechanical Properties of Directionally-Solidified $Al_2O_3-Y_3Al_5O_{12}-ZrO_2$ Ternary Eutectics*. J. Eur. Ceram. Soc., Vol. 26, pp. 3113-3121, 2006.
- [5] S. OCHIAI, T. UEDA, K. SATO, M. HOJO, Y. WAKU, N. NAKAGAWA, S. SAKATA, A. MITANI, T. TAKAHASHI - *Deformation and Fracture Behavior of an Al_2O_3/YAG Composite from Room Temperature to 2023 K*. Comp. Sci. Technol., Vol. 61, pp. 2117-2128, 2001.
- [6] J. MARTINEZ-FERNANDEZ, A. SAYIR, S. C. FARMER - *High-Temperature Creep Deformation of Directionally Solidified $Al_2O_3/Er_3Al_5O_{12}$* . Acta Mater., Vol. 51, pp. 1705-1720, 2003.
- [7] N. NAKAGAWA, H. OHTSUBO, A. MITANI, K. SHIMIZU, Y. WAKU - *High Temperature Strength and Thermal Stability for Melt Growth Composite*. J. Eur. Ceram. Soc., Vol. 25, pp. 1251-1257, 2005.
- [8] J. Y. PASTOR, J. LLORCA, A. SALAZAR, P. B. OLIETE, I. DE FRANCISCO, J. I. PEÑA - *Mechanical Properties of Melt-Grown Alumina-Yttrium Aluminum Garnet Eutectics up to 1900 K*. J. Am. Ceram. Soc., Vol. 88, pp. 1488-1495, 2005.
- [9] Y. WAKU, S. SAKATA, A. MITANI, K. SHIMIZU, M. HASEBE - *Temperature Dependence of Flexural Strength and Microstructure of $Al_2O_3/Y_3Al_5O_{12}/ZrO_2$ Ternary Melt Growth Composites*. J. Mater. Sci., Vol. 37, pp. 2975-2982, 2002.
- [10] J. M. CALDERON-MORENO, M. YOSHIMURA - *$Al_2O_3-Y_3Al_5O_{12}(YAG)-ZrO_2$ Ternary Composite Rapidly Solidified from the Eutectic Melt*. J. Eur. Ceram. Soc., Vol. 25, pp. 1365-1368, 2005.
- [11] Y. WAKU, S. SAKATA, A. MITANI, K. SHIMIZU, A. OHTSUKA, M. HASEBE - *Microstructure and High-Temperature Strength of $Al_2O_3/Er_3Al_5O_{12}/ZrO_2$ Ternary Melt Growth Composite*. J. Mater. Sci., Vol. 40, pp. 711-717, 2005.
- [12] K. HIRANO - *Application of Eutectic Composites to Gas Turbine System and Fundamental Fracture Properties up to 1700 °C*. J. Eur. Ceram. Soc., Vol. 25, pp. 1191-1199, 2005.
- [13] N. PIQUET - *Microstructures interconnectées dans des eutectiques à base d'oxydes réfractaires élaborés par solidification dirigée*. Doctorate thesis, Univ. Paris XII, 2006.
- [14] L. PERRIÈRE - *Elaboration par solidification dirigée et comportement mécanique de céramiques eutectiques à base d'oxydes réfractaires. Rôle de la microstructure sur la fissuration et la déformation plastique à haute température*. Doctorate thesis, Univ. Paris-Est, 2008.
- [15] L. MAZEROLLES, D. MICHEL, M. J. HYTCH - *Microstructures and Interfaces in Directionally Solidified Oxide-Oxide Eutectics*. J. Eur. Ceram. Soc., Vol. 25, pp. 1389-1395, 2005.
- [16] G. GOUADEC, Ph. COLOMBAN, N. PIQUET, M. F. TRICHET, L. MAZEROLLES - *Raman/ Cr^{3+} Fluorescence Mapping of a Melt-Grown $Al_2O_3/GdAlO_3$ Eutectic*. J. Eur. Ceram. Soc., Vol. 25, pp. 1447-1453, 2005.
- [17] L. MAZEROLLES, N. PIQUET, M. F. TRICHET, M. PARLIER - *Microstructures and Interfaces in Melt-Growth $Al_2O_3-Ln_2O_3$ Based Eutectic Composites*. Adv. Sci. Techn., Vol. 45, pp. 1377-1384, 2006.
- [18] L. MAZEROLLES, N. PIQUET, M. F. TRICHET, L. PERRIÈRE, D. BOVIN, M. PARLIER - *New Microstructures in Ceramic Materials from the Melt for High Temperature Applications*. Aerospace Sci. Techn., Vol. 12, pp. 499-505, 2008.
- [19] L. PERRIÈRE, R. VALLE, L. MAZEROLLES, M. PARLIER - *Crack Propagation in Directionally Solidified Eutectic Ceramics*. J. Eur. Ceram. Soc., Vol. 28, pp. 2337-2343, 2008.
- [20] L. MAZEROLLES, L. PERRIÈRE, S. LARTIGUE-KORINEK, N. PIQUET, M. PARLIER - *Microstructures, Crystallography of Interfaces and Creep Behavior of Melt-Growth Composites*. J. Eur. Ceram. Soc., Vol. 28, pp. 2301-2308, 2008.
- [21] L. MAZEROLLES, L. PERRIÈRE, S. LARTIGUE-KORINEK, M. PARLIER - *Creep Behavior and Related Structural Defects in $Al_2O_3-Ln_2O_3$ (ZrO_2) Directionally Solidified Eutectics ($Ln = Gd, Er, Y$)*. J. Eur. Ceram. Soc., Vol. 31, pp. 1219-1225, 2011.
- [22] L. PERRIÈRE, R. VALLE, N. CARRÈRE, G. GOUADEC, Ph. COLOMBAN, S. LARTIGUE-KORINEK, L. MAZEROLLES, M. PARLIER - *Crack Propagation and Stress Distribution in Binary and Ternary Directionally Solidified Eutectic Ceramics*. J. Eur. Ceram. Soc., Vol. 31, pp. 1199-1210, 2011.
- [23] J. GUIDEZ, F. X. NICOU, P. JOSSO, R. VALLE - *Development of a Micro Gas Turbine Engine at Onera*. Proceedings 19th ISABE Conference (Int. Soc. Air Breathing Engines), September 7-11, 2009, Montréal, Canada, Paper n°ISABE-2009-1307, 2009.
- [24] M. MIZUNO, T. YAMADA, T. NOGUCHI - *Phase Diagrams of the Systems $Al_2O_3-Eu_2O_3$ and $Al_2O_3-Gd_2O_3$ at High Temperatures*. Yogyo Kyokai Shi, Vol. 85, pp. 543-548, 1977.
- [25] W. KURZ, D. J. FISHER - *Fundamentals of Solidification*. 3rd Edition, Trans Tech Publications, 1989.
- [26] J. J. RASMUSSEN, R. P. NELSON - *Surface Tension and Density of Molten Al_2O_3* . J. Am. Ceram. Soc., Vol. 54, pp. 398-401, 1971.
- [27] B. CHALMERS, H. E. LABELLE Jr., A. J. MLAVSKY - *Edge-Defined, Film-Fed Crystal Growth*. J. Crystal Growth, Vol. 13/14, pp. 84-87, 1972.
- [28] H. E. LABELLE Jr. - *EFG, the Invention and Application to Sapphire Growth*. J. Crystal Growth, Vol. 50, pp. 8-17, 1980.
- [29] D. A. JEREBTSOV, G. G. MIKHAILOV - *Phase Diagram of $CaO-Al_2O_3$ System*. Ceramics Int., Vol. 27, pp. 25-28, 2001.
- [30] Y. HARADA, T. SUZUKI, K. HIRANO, N. NAKAGAWA, Y. WAKU - *Environmental Effects on Ultra-High Temperature Creep Behavior of Directionally Solidified Oxide Eutectic Ceramics*. J. Eur. Ceram. Soc., Vol. 25, pp. 1275-1283, 2005.
- [31] A. H. HEUER - *Oxygen and Aluminum Diffusion in $\alpha-Al_2O_3$: How Much do we Really Understand?* J. Eur. Ceram. Soc., Vol. 28, pp. 1495-1507, 2008.
- [32] J. RAMIREZ-RICO, A. R. PINTO-GÓMEZ, J. MARTINEZ-FERNANDEZ, A. R. de ARELLANO-LÓPEZ, P. B. OLIETE, J. I. PEÑA, V. M. ORERA - *High-Temperature Plastic Behaviour of $Al_2O_3-Y_3Al_5O_{12}$ Directionally Solidified Eutectics*. Acta mater., Vol. 54, pp. 3107-3116, 2006.
- [33] J. CASTAING, A. MUNOZ, D. GOMEZ GARCIA, A. DOMINGUEZ RODRIGUEZ - *Basal Slip in Sapphire ($\alpha-Al_2O_3$)*. Mater. Sci. Eng. A, Vol. 233, pp. 121-125, 1997.
- [34] M. CASTILLO RODRÍGUEZ, J. CASTAING, A. MUÑOZ, P. VEYSSIÈRE, A. DOMINGUEZ RODRÍGUEZ - *Analysis of a Kink Pair Model Applied to a Peierls Mechanism in Basal and Prism Plane Slips in Sapphire ($\alpha-Al_2O_3$) Deformed Between 200 °C and 1800 °C*. J. Am. Ceram. Soc., Vol. 91, pp. 1612-1617, 2008.

Acronyms

CMC (Ceramic Matrix Composite)
CVD (Chemical Vapor Deposition)
DSE (Directionally Solidified Eutectic)
EAG (Erbium Aluminum Garnet)
EBSD (Electron Back-Scattered Diffraction)
EHM (Equivalent Homogeneous Medium)
FEG-SEM (Field Emission Gun - Scanning Electron Microscopy)
GAP (Gadolinium Aluminum Perovskite)
HRTEM (High Resolution Transmission Electron Microscopy)
IMC (Intermetallic Matrix Composite)
IPF (Inverse Pole Figure)
MGC (Melt-Growth Composite)
MMC (Metal Matrix Composite)
PF (Pole Figure)
SAED (Selected Area Electron Diffraction)
SEM (Scanning Electron Microscopy)
TEM (Transmission Electron Microscopy)
UTS (Ultimate Tensile Stress)
YAG (Yttrium Aluminum Garnet)

AUTHORS



Michel Parlier, holding an Engineering Diploma from ENSCI (Ecole Nationale Supérieure de Céramiques Industrielles) and having graduated in Materials Science from the University of Paris, he received his Doctorate Degree in Metallurgy (Mechanical Behavior of Materials) from ENSMP (Ecole Nationale Supérieure des Mines de Paris) in 1984. Head of the High Temperature Composite Materials Unit at Onera (Composite Materials and Structures Department), he has been involved in the development of sintering techniques of ceramic powders with specific additives (hot-pressing, reaction bonding, hot isostatic pressing); Chemical Vapor Deposition (CVD) for densification of composites and coatings; Ceramic Matrix Composites (CMC) development (glass-ceramics, oxides and silicon carbide); Oxides derived from Sol-Gel; Silicon carbide derived from organosilicon precursors, low density fibrous thermal insulation; Melt-Growth Composites (MGC) processing routes; thermal, mechanical and microstructural characterizations.



Roger Valle, having Masters Degrees (Maîtrises) in Mathematics and Physics, and an Engineering Diploma from the Ecole Nationale Supérieure des Mines de Paris, and having graduated in Theoretical Solid State Physics from the University of Paris, he received his Doctorate Degree (Doctorat d'État ès Sc., Hab. Dir. Rech.) from the University of Lille. From 1973 to 1987, he was in charge of the development of instrumentation and *in situ* experimentation in materials science (electron-solid interaction, plastic deformation, fracture, recrystallization, texture ...) in the High Voltage Electron Microscope Cnrs-Onera Laboratory (LP 12 8714). Since then, he works on the microstructural and mechanical aspects of deformation and failure of Metal Matrix Composites (MMC), Ceramic Matrix Composites (CMC), Intermetallic Matrix Composites (IMC) and Melt-Growth Composites (MGC) subjected to thermo-mechanical loadings (Composite Materials and Structures Department).



Loïc Perrière, obtained his Master's Degree in Materials Science and Engineering and his Engineering Diploma from the Institut National Polytechnique de Toulouse in 2005. He performed his doctorate work at Onera on directionally solidified eutectic ceramics and obtained his PhD from the University of Paris Est - Créteil in 2008. He currently works as a research scientist at the ICMPE (Institut de Chimie et des Matériaux Paris-Est, UMR 7182) on the development and manufacturing of amorphous metallic alloys.



Sylvie Lartigue-Korinek, obtained her PhD in Metallurgy and then her Doctorat d'État ès Sciences Physique-Chimie (Hab. Dir. Rech.) from the University of Paris-Sud (Orsay). Since 1986 she has been a Cnrs researcher and has worked in the field of structure and properties of interfaces, with a particular emphasis on the role of grain boundary chemistry on deformation micromechanisms in metals and ceramics. She currently works at ICMPE (Institut de Chimie et des Matériaux Paris-Est, UMR 7182) in the group "Métaux et Céramiques à Microstructures Contrôlées".



Léo Mazerolles is Director of Research at Cnrs. Graduated as an Engineer from the Ecole Nationale Supérieure de Chimie de Lille (1979), with a PhD degree from University Paris VI (1982) and a Research Habilitation Thesis (Thèse d'État) in Physical Sciences from University Paris VI (1986), he is a researcher in physicochemistry of solids and inorganic materials. One of his main fields of research concerns ceramic oxide materials and more particularly the synthesis and study of microstructures (morphology, size, interfaces). He studies relationships between properties and structural/microstructural features of refractory oxides. Since 2007, he manages the "Metals and ceramics" team at ICMPE (Institut de Chimie et des Matériaux Paris-Est, UMR 7182) in Thiais.

J.F. Justin, A. Jankowiak
(Onera)

E-mail: jean-francois.justin@onera.fr

Ultra High Temperature Ceramics: Densification, Properties and Thermal Stability

Hypersonic flights, re-entry vehicles, and propulsion applications all require new materials that can perform in oxidizing or corrosive atmospheres at temperatures in excess of 2000°C and sometimes over the course of a long working life. Ultra High Temperature Ceramics (UHTCs) are good candidates to fulfill these requirements. Within this family, the ZrB₂ and HfB₂ based composites are the most attractive. The oxidation resistance of diboride-based compounds is better than that of SiC-based ceramics thanks to the formation of multi-oxide scales composed of a refractory oxide (skeleton) and a glass component. Onera is actively involved in several programs to develop such materials for both hypersonic civilian flights and for propulsion systems.

In this paper, we present the ZrB₂-SiC, ZrB₂-SiC-TaSi₂ and HfB₂-SiC-TaSi₂ composites developed in the Onera laboratories for leading edges or air intakes of future hypersonic civilian aircrafts flying up to Mach 6 (T~1100°C-1500°C) with comparisons with the state of the art. Then we discuss new perspectives for higher temperature applications (T>2000°C).

Introduction

Ultra High Temperature Ceramics (UHTCs) are good choices for several extreme applications: thermal protection materials on hypersonic aerospace vehicles or re-usable atmospheric re-entry vehicles, specific components for propulsion, furnace elements, refractory crucibles, etc. This family of ceramic compounds is made of borides, carbides and nitrides such as ZrB₂, HfB₂, ZrC, HfC, TaC, HfN which are characterized by high melting points (table 1), high hardness, chemical inertness and relatively good resistance to oxidation in severe environments.

Historically, this family of ceramic materials was first investigated between the 1950s and 1970s by Russian and U.S. laboratories [1][2], but recent studies to develop hypersonic flight vehicles in particular have led to a resurgence of interest. For hypersonic vehicles with sharp aerosurfaces (engine cowl inlets, wing leading edges and nosecones), there are foreseeable needs for materials that can withstand temperatures of 2000 to 2400°C, operate in air and be re-usable [3]. At present, the structural materials for use in high-temperature oxidizing environments are limited to SiC and Si₃N₄ based materials, oxide ceramics and C/C composites with thermal protection. Silicon-based ceramics and protected C/C composites exhibit good oxidation resistance, but only up to ~1600°C, and their thermal

cycling lifetimes are modest. The development of structural materials for use in oxidizing and rapid heating environments at temperatures above 1600°C is therefore of great importance for engineering.

Material	Crystal structure	Density (g/cm ³)	Melting temperature (°C)
HfB ₂	Hexagonal	11.2	3380
HfC	Face-centered cubic	12.76	3900
HfN	Face-centered cubic	13.9	3385
ZrB ₂	Hexagonal	6.1	3245
ZrC	Face-centered cubic	6.56	3400
ZrN	Face-centered cubic	7.29	2950
TiB ₂	Hexagonal	4.52	3225
TiC	Cubic	4.94	3100
TiN	Face-centered cubic	5.39	2950
TaB ₂	Hexagonal	12.54	3040
TaC	Cubic	14.50	3800
TaN	Cubic	14.30	2700
SiC	Polymorph	3.21	Dissociates 2545

Table 1 – Properties of some UHTCs

Since the 1950s, studies have revealed that diborides of the group IVB were the most resistant to oxidation and among these compounds, HfB_2 was the best, followed by ZrB_2 . However, the use of single-phase materials was not sufficient for high-temperature structural applications. Thus, many additives such as Nb, V, C, disilicides and SiC were evaluated to improve the resistance to oxidation. Of these additives, SiC seemed to be particularly valuable and 20 vol% was judged optimal for hypersonic vehicles by the US Air Force. At present, many groups in the U.S., Japan, China, India and in Europe (especially in Italy) are studying UHTC systems to improve resistance to oxidation [4][5][6][7]. Moreover, in comparison with carbides and nitrides, the diborides have also higher thermal conductivity, which gives them good thermal shock resistance and makes them ideal for many high-temperature thermal applications. For a leading edge for example, a high thermal conductivity reduces thermal stress within the material by lowering the magnitude of the thermal gradient inside the part. Furthermore, it allows energy to be conducted away from the tip of the piece and re-radiated out of the surfaces of the component with lower heat fluxes [8]. Diboride-based UHTCs also exhibit high electrical conductivity (table 2), which is appreciable for manufacturing complex shape components for example (by using Electrical Discharge Machining).

Over the past five years, Onera has carried out several activities on UHTC materials. This paper is an outline of the work which has been done on these materials in the Composite Materials and Structures Department. First, we describe the ZrB_2 -SiC, ZrB_2 -SiC-TaSi₂ and HfB_2 -SiC-TaSi₂ composites developed for leading edges or air intakes of the ATLLAS vehicle (future hypersonic civil aircraft flying up to Mach 6) in comparison with the state of the art. In conclusion, new perspectives and compositions for higher temperature applications ($T > 2000^\circ\text{C}$) are discussed.

Property	ZrB_2	HfB_2
Crystal system space group prototype structure	Hexagonal <i>P6/mmm AB₂</i>	Hexagonal <i>P6/mmm AB₂</i>
a (Å)	3.17	3.139
c (Å)	3.53	3.473
Density (g/cm ³)	6.1	11.2
Melting temperature (°C)	3245	3380
Young's modulus (GPa)	489	480
Hardness (GPa)	23	28
Coefficient of Thermal Expansion (°C ⁻¹)	5.9×10^{-6}	6.3×10^{-6}
Heat capacity at 25°C (J.mol ⁻¹ .°C ⁻¹)	48.2	49.5
Thermal conductivity (W.m ⁻¹ .°C ⁻¹)	60	104
Electrical conductivity (S/m)	1.0×10^7	9.1×10^6

Table 2 – Summary of some properties of ZrB_2 and HfB_2 [9]

Future hypersonic aircraft materials

Context

In 2006, the European Community launched a 3-year project called ATLLAS (Aerodynamic and Thermal Load Interactions with Lightweight Advanced Materials for High Speed Flight) to initiate research on high-

temperature resistant materials for sustained hypersonic flight (up to Mach 6). The project [10], led by ESA-ESTEC, consists of a consortium of 13 partners from industry, research institutions and universities (ASTRIUM, EADS-IW, MBDA, ALTA, GDL, DLR, FOI, ONERA, SOTON, ITR, TUM, UPMC and ESA-ESTEC). Within this program, ONERA DMSC has the objective of investigating and manufacturing materials to allow for the designing of sharp leading edges or air intakes for the ATLLAS reference vehicle [11]. For hypersonic vehicles, performance improvement (lift-to-drag ratio in particular) requires slender aerodynamic shapes with sharp leading edges. However, the thinner the leading edge radius, the higher the temperature. Successful designs for hypersonic aircraft therefore require the development of new materials with higher temperature capabilities.

The first part of the study focused on the choice of suitable compositions to define UHTC solutions for slender aerodynamic shapes. The selection was based on four different criteria: the requirements for these applications (see box 1) taking into account the flight parameters of the ATLLAS vehicle (speed, altitude, etc.) and the shape of the piece (sweep back angle, tip radius, etc.), the processing methods available at Onera, the bibliographical results on similar applications and the thermodynamic stability predictions of the selected compositions. According to these criteria, a preliminary selection of three compositions that are feasible by hot pressing [12] [13] (expected sintering temperature between 1600 and 2000°C), has been done:

- ZrB_2 (60 vol%) + SiC (20 vol%) + TaSi₂ (20 vol%)
- HfB_2 (60 vol%) + SiC (20 vol%) + TaSi₂ (20 vol%)
- ZrB_2 (80 vol%) + SiC (20 vol%)

In these compositions, silicon carbide additives are used firstly to enhance resistance to oxidation, secondly to promote densification by restricting the growth of diboride grains, and lastly to lower their sintering temperature [14]. According to several studies, additions of 20 vol% were judged optimal for our application. For tantalum disilicide additives, the objectives are to increase oxidation resistance and to reduce the sintering temperature of the powder blends [14][15] (the melting temperature of the TaSi₂ is “only” 2400°C). The addition of Ta to the system reduces the concentration of oxygen vacancies and decreases oxygen transport through the growing oxide scale and thus lowers the oxidation rate. Furthermore, Ta additions increase the oxide scale adhesion by phase stabilization. As for the last composition, it is a “classical” ZrB_2 /SiC material. It has been studied in order to provide reference points for comparison with the first two compositions and the results from the literature.

Experimental procedure

To obtain the three selected compositions, commercially available ZrB_2 , HfB_2 , SiC and TaSi₂ powders (table 3) were used as precursors. The preparation of the blends involved three successive stages. First, to reduce particle size distribution and promote intimate mixing, the mixtures were ball milled in cyclohexane for several hours using Si₃N₄ milling media in a high-density polyethylene tank. Rotary evaporation was then used to extract the solvent and minimize segregation during drying. Lastly, the powder blends were sieved to avoid agglomeration. During the study, various improvements were made to this cycle in order to obtain the purest mixtures: a significant decrease of the total duration of attrition, the use of YTZ (ZrO₂) grinding media and optimization of the order of introduction of the constituents.

Box 1 - Some requirements for UHTC materials in ATLLAS application

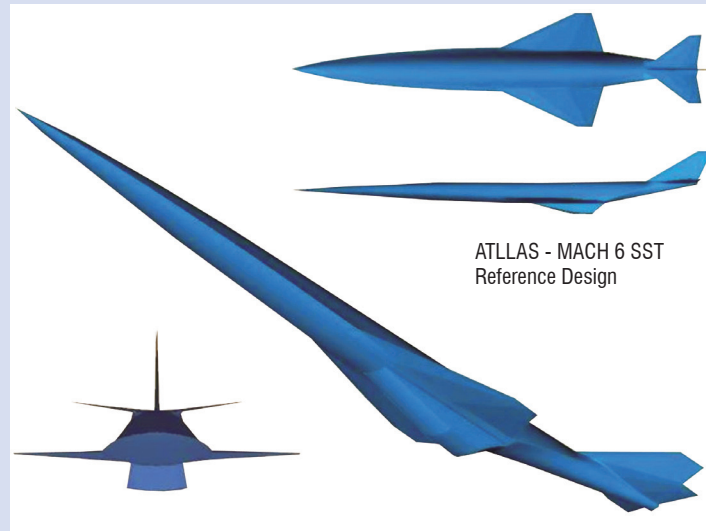
ATLLAS objectives

Future hypersonic civil aircraft for flights at Mach 3 or Mach 6 with a cruising altitude of 30500 m. A minimum of 60 flights should be carried out at maximum speed. With these flight conditions, leading edge (L.E.) and nose temperatures between 980 and 1150°C are expected. The high temperature materials must have a service life of about 40,000 hours with more than 20,000 hours of exposure to the maximum thermal loads.

Details of the ATLLAS vehicle, the flight parameters and the shape of the wing

- Length = 105.1 m
- Wingspan = 29.7 m
- Gross Takeoff Weight = 278 tons (including 110 tons of hydrogen fuel)
- Number of passengers = 200
- Maximum speed = Mach 6
- Cruise altitude = 30 km
- Range = 9300 km (in fact only 7400 km)
- Service life > 25,000 cycles (~ 40,000 h)
- Angle of attack of the vehicle = 4°
- Wing L.E. sweep back angle = 65°
- Radius of curvature at the tip = 1 mm
- Maximum expected temperature = 1150°C (with an emissivity of 0.85)

Design of the reference vehicle



Designing UHTC components for hypersonic applications requires precise knowledge of the values of specific physical, thermal, mechanical and surface properties (density, coefficient of thermal expansion, specific heat, thermal conductivity, Young's modulus, Poisson's ratio, emissivity, catalytic efficiency, surface roughness, etc.) [16].

Starting powder	Particle size (μm)	Grade / supplier	Purity (%)
ZrB ₂	8.17	Z-1031 / Cerac	99.5
HfB ₂	1.99	H-1002 / Cerac	99.5
SiC	0.60	BF12 / H.C. Starck	>98.5
TaSi ₂	6.54	T-1016 / Cerac	99.5

Table 3 – Size, grade and purity of starting powders

The second phase of the process involved sintering the previous powder blends by hot pressing. This standard processing method has been successfully used to manufacture monolithic plates. The making of UHTCs often requires higher cost processes with high temperatures and pressures to obtain complete densification. In our sintering process, a resistance heated furnace using graphite dies was used. After the improvements in the mixture preparation, the selected densification parameters were finally the following:

- Sintering temperature 1700 T 1800°C
- Dwell time t = 2 hours
- Uniaxial pressure P = 27 MPa
- Atmosphere argon at atmospheric pressure after a first step under vacuum
- Graphite dies 36 x 36 mm², 45 x 45 mm² and 68 x 68 mm²

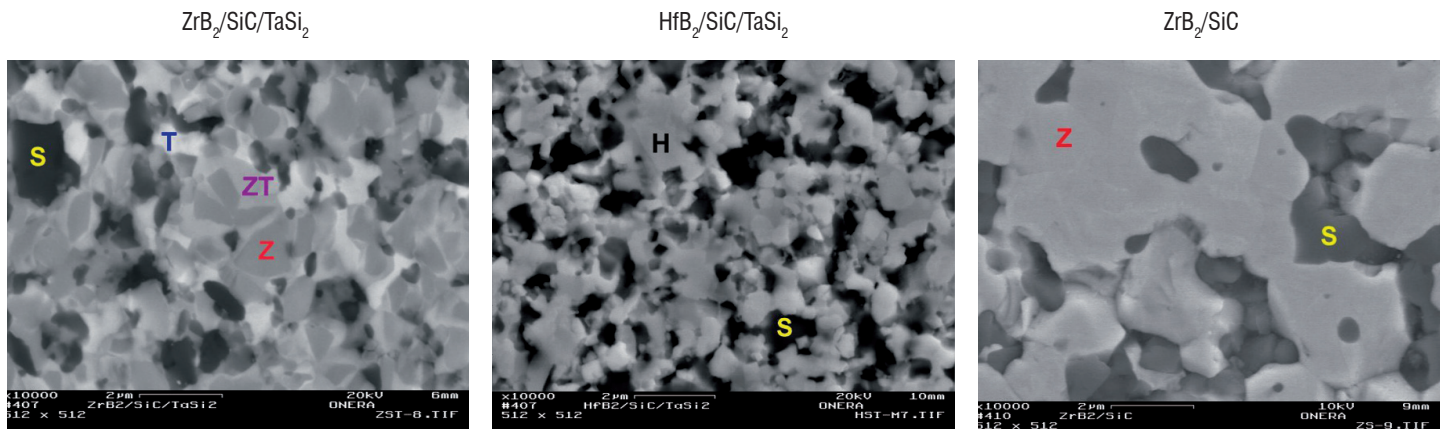
High densification rates are obtained on monoliths. The density of each material has been assessed by Archimedes' method. For the three sintered compositions, the open porosities are lower than 1 % and their densification rates are approximately 98 % of the theoretical value (table 4).

Composition	Apparent density/g/cm ³	Open porosity
ZrB ₂ /SiC	5.36±0.04	0.60±0.33
ZrB ₂ /SiC/TaSi ₂	5.95±0.01	0.30±0.10
HfB ₂ /SiC/TaSi ₂	9.09±0.13	0.38±0.21

Table 4 – Densification level

Furthermore, a very fine microstructure is obtained with good homogeneity and a small grain size (figure 1). In addition, despite the presence of high density compounds ($\rho_{\text{HfB}_2} = 11.2 \text{ g/cm}^3$ and $\rho_{\text{TaSi}_2} = 9.1 \text{ g/cm}^3$), the densest material (HfB₂/SiC/TaSi₂) exhibits a value that is not very far from that of some well-known metal alloys (Inconel 617 for instance, $\rho = 8.4 \text{ g/cm}^3$).

Some X-Ray diffraction analyses were used to identify phases present in these materials. The results indicated the presence of the main constituents as foreseen but also some traces of Ta₅Si₃, ZrO₂, HfO₂ and SiO₂.



Material labels: Z for ZrB₂, H for HfB₂, S for SiC, T for TaSi₂ and ZT for (Zr,Ta)B₂.

Figure 1 – Microstructure of each type of hot pressed material (SEM observations)

Material properties

In order to estimate the capability of the previous monoliths to fulfill the requirements of hypersonic applications, several aspects have been investigated and in particular: machinability, physical, thermal and mechanical properties, resistance to oxidation, thermal shock behavior and resistance under high-enthalpy hypersonic flow (arc jet tests).

Machinability

Materials based on hard and brittle constituents (borides, carbides and silicides) often involve expensive and difficult machining. In our case, thanks to the low electrical resistivity of the compounds which are present in our compositions, the use of Electrical Discharge Machining is perfectly possible ($\rho_{ZrB_2} = 6$ to $10 \mu\Omega \cdot \text{cm}$, $\rho_{HfB_2} = 10$ to $16 \mu\Omega \cdot \text{cm}$, $\rho_{SiC} \sim 105 \mu\Omega \cdot \text{cm}$ and $\rho_{TaSi_2} = 8$ to $46 \mu\Omega \cdot \text{cm}$ [17]). All the selected materials can be easily machined by EDM, and the surfaces are clean and even (figure 2). This is one of the important advantages of these materials. It is important to note that, with EDM, complex shapes can also be made using a die-sinking machine, also known as a ram-type, plunge, or vertical erosion machine [18].

Furthermore, in this work, we have also demonstrated the good behavior of the selected materials for machining with the standard techniques (surface grinding with diamond tools for instance). Several samples

and prototypes were manufactured with this method. In particular, a small piece representing an air intake was made by diamond machining (figure 2). The objective was to test the feasibility of a prototype with a very thin tip. As expected, a small radius was obtained. In fact, the radius was well under the required value for the component (length = 40 mm, width = 40 mm, thickness = 1.9 mm and radius ~ 0.15 mm). Thus, it is clearly possible to obtain very sharp pieces and acute angles.

Mechanical performance

Elastic constants

Nine to twelve samples of each composition were tested with a Grindosonic MK5 apparatus to determine the elastic constants of these materials by impulse excitation of vibration [19]. In fact, due to the dimension of the available samples (bars of $\sim 35.40 \times 5.20 \times 1.75 \text{ mm}^3$), it was only possible to measure the flexural resonant frequencies. Therefore, we were only able to determine the Young's modulus (table 5). The observed values are in good agreement with the expected results [20][21][22].

As for the other elastic constants, we note than similar materials have already been presented in the literature and they generally exhibit shear moduli close to 200 GPa and Poisson's ratios around 0.12 - 0.14 [20] [23].

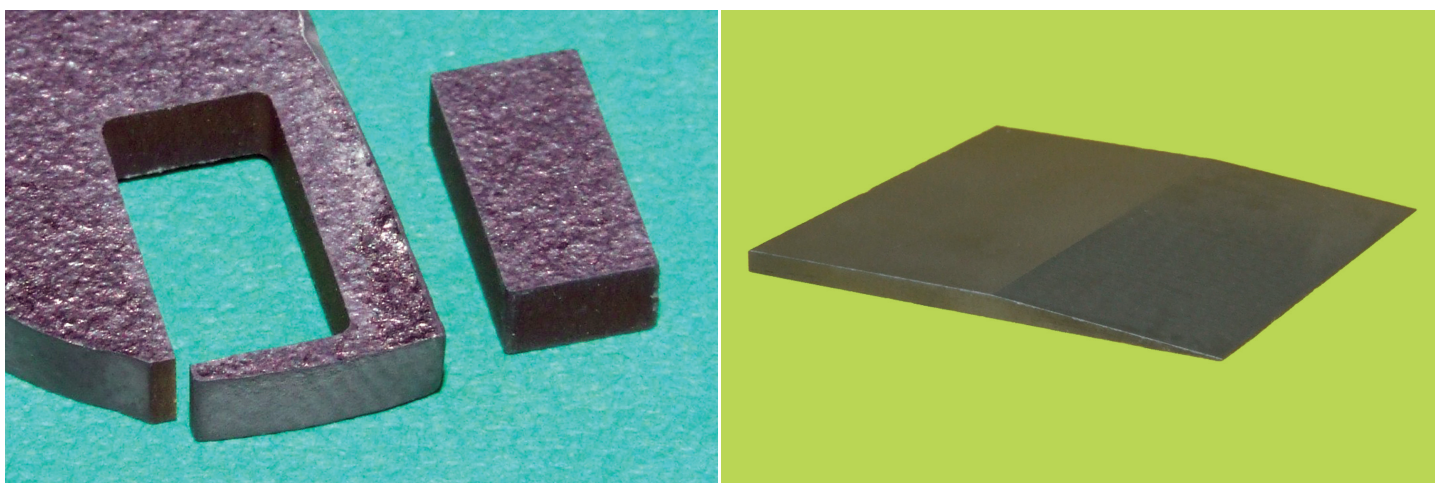


Figure 2 – Wire-cutting EDM trial (left) and a thin air intake prototype made by diamond machining (right)

Hardness and fracture toughness

Vickers hardness (H_V) and toughness (K_{Ic}) have been evaluated at room temperature on $1/4 \mu\text{m}$ polished surfaces of all materials. At least five tests for each composite were carried out by Vickers indentation using a Testwell hardness tester. The hardness is determined by the ratio P/A where P is the force applied to the diamond and A is the surface area of the resulting indentation (in our case, $P = 10 \text{ kgf} \sim 98 \text{ N}$). The fracture toughness (K_{Ic}) is estimated by crack length measurement of the radial crack pattern formed around Vickers indents [24].

$$H_V = \frac{P}{A} = 0.001854 \times \frac{P}{d^2} \quad (1)$$

$$K_{Ic} = 0.0154 \times 10^{-6} \times \left(\frac{E}{H_V} \right)^{1/2} \times \frac{P}{c^{3/2}} \quad (2)$$

with H_V the hardness (GPa), P the load (N), $a = d/2$ with d the average diagonal indentation mark length (mm), K_{Ic} the toughness ($\text{MPa}\cdot\text{m}^{1/2}$), E the Young's modulus (GPa) and c the crack length from the centre of the indent to the crack tip (mm).

Very high levels of hardness and limited levels of toughness have been measured on the three selected compositions (table 5). In fact, all the materials exhibit hardness values close to that of tungsten carbide ($H_V \sim 19.6 \text{ GPa}$) and toughness similar to that of common silicon nitride ($K_{Ic} \sim 3.5 - 6 \text{ MPa}\cdot\text{m}^{1/2}$). SEM observations of the cracks have revealed that both intergranular and transgranular modes of propagation were present. Comparable behaviors are reported in the literature for this type of ceramic [20][21].

Composition	H_{V10} / GPa	$K_{Ic} / \text{MPa}\cdot\text{m}^{1/2}$	E / GPa
ZrB ₂ /SiC	20.9 ± 1.9	4.3 ± 0.2	465 ± 15
ZrB ₂ /SiC/TaSi ₂	18.1 ± 0.4	4.4 ± 0.3	446 ± 9
HfB ₂ /SiC/TaSi ₂	18.1 ± 0.6	4.6 ± 0.2	498 ± 6

Table 5 – Hardness, toughness and Young's modulus of the three sintered materials

In comparison with metallic materials, the hardness of our compounds is considerably greater. For a nickel alloy such as Haynes 242, the H_V is around 2.7 GPa for instance. Moreover, the fracture toughness is also significantly lower: $K_{Ic} = 24 \text{ MPa}\cdot\text{m}^{1/2}$ for the aluminum alloy 7075 for example.

High temperature flexural strength

The three point bending test provides values for the flexural stress (σ_f), the modulus of elasticity in bending (E_f) and the flexural strain (ε_f) of the material. The results shown in table 6 were obtained at different temperatures (20, 1000 and 1150°C), under air at atmospheric pressure, with a test speed of 0.3 mm/min and a support span of

30 mm (average dimension of samples: $\sim 35.40 \times 5.20 \times 1.75 \text{ mm}^3$). For each material (manufactured with the optimized cycle) and each temperature, three to four samples were broken.

Composition	Property	20°C	Test temperature 1000°C	1150°C
		ZrB ₂ /SiC	σ_f (MPa) E_f (GPa) ε_f (%)	451 ± 90 194 ± 6 0.23 ± 0.04
ZrB ₂ /SiC/TaSi ₂	σ_f (MPa) E_f (GPa) ε_f (%)	688 ± 79 211 ± 13 0.32 ± 0.02	801 ± 40 181 ± 14 0.45 ± 0.04	864 ± 96 133 ± 13 0.65 ± 0.02
HfB ₂ /SiC/TaSi ₂	σ_f (MPa) E_f (GPa) ε_f (%)	869 ± 170 245 ± 13 0.36 ± 0.09	882 ± 146 203 ± 24 0.43 ± 0.05	1055 ± 189 178 ± 22 0.56 ± 0.13

Table 6 – Three point flexural strength (average value ± standard deviation)

Except for the reference material, for which some improvements in the manufacturing process are clearly necessary to recover the levels of the literature [21], the measured values are very satisfactory. Indeed, we can observe that for material comprising TaSi₂, increasing temperature leads to higher flexural stresses, a strong increase of flexural strains and a moderate decrease in the flexion modulus. It is important to point out that, with these high levels of flexural stress (values over 1200 MPa have even been measured on HfB₂/SiC/TaSi₂ samples at 1150°C), it is possible to envisage the manufacturing of future high-strength sharp UHTC components.

Thermal and optical properties

Coefficient of thermal expansion

The thermal expansion behavior of the three hot pressed materials has been characterized between room temperature and 1300°C by using an Adamel Lhomargy DI.24 dilatometer (under argon flow). The coefficient of thermal expansion (α tangent in °C⁻¹) is calculated from the following formula:

$$\alpha(T) = \frac{1}{l(T)} \times \frac{dl(T)}{dT} \quad (3)$$

The reference temperature is room temperature (25°C). The recorded values are presented in figure 3. The correlations for the CTE of each composition are given by the following expressions with T in °C units:

$$\text{for ZrB}_2/\text{SiC} \quad \alpha(T) = 4.654676 \cdot 10^{-10} T + 6.844813 \cdot 10^{-6} \quad (4)$$

$$\text{for ZrB}_2/\text{SiC}/\text{TaSi}_2 \quad \alpha(T) = 4.002628 \cdot 10^{-10} T + 7.157354 \cdot 10^{-6} \quad (5)$$

$$\text{for HfB}_2/\text{SiC}/\text{TaSi}_2 \quad \alpha(T) = 1.225332 \cdot 10^{-10} T + 7.216565 \cdot 10^{-6} \quad (6)$$

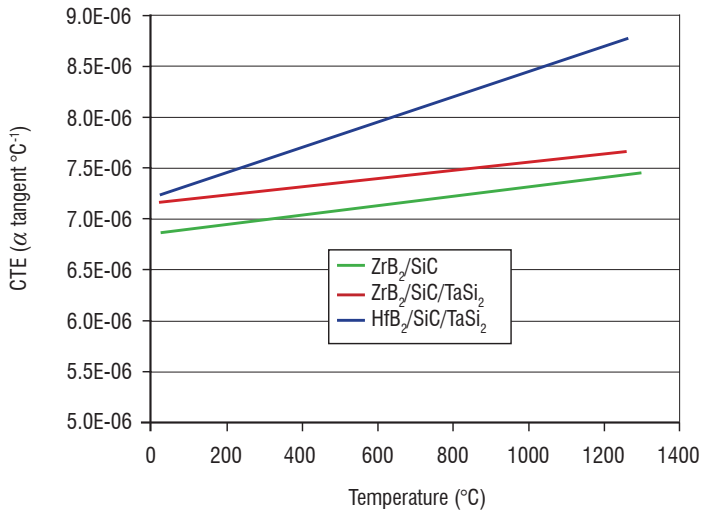


Figure 3 – Coefficients of thermal expansion of the three selected materials

Thus between 25 and 1250°C, the average values of CTE are:

- ZrB₂/SiC ~ 7.1 10⁻⁶ °C⁻¹
- ZrB₂/SiC/TaSi₂ ~ 7.4 10⁻⁶ °C⁻¹
- HfB₂/SiC/TaSi₂ ~ 8.0 10⁻⁶ °C⁻¹

These values are in good agreement with the data available in the literature on similar materials [22][25]. In comparison to advanced CMC (SiC/SiC or C/SiC), these coefficients are quite high and closer to some ceramics like alumina ($\alpha_{0-1000^\circ\text{C}} = 8 \cdot 10^{-6} \text{ }^\circ\text{C}^{-1}$). However, they are twice as low as for metallic materials such as nickel alloys ($\alpha_{25-1000^\circ\text{C}} = 16.3 \cdot 10^{-6} \text{ }^\circ\text{C}^{-1}$ for Inconel 617 for instance).

Thermal conductivity

The thermal conductivity (λ) was calculated from the correlation functions of thermal diffusivity (D), specific heat capacity (C_p) and density (ρ) according to the formula:

$$\lambda(T) = D(T) \times \rho(T) \times C_p(T) \quad (7)$$

The correlations for density were deduced from the CTE measurements. As for diffusivity and specific heat capacity, they were determined by a laser flash technique [26] from room temperature to 1200°C (under argon) on 20 mm diameter and 2 mm thick discs. These characterizations were carried out on the first generation of materials (sintered before the improvements relating to powder blends attrition) and only on monoliths with TaSi₂. The calculated values are presented in figure 4 and the correlations for λ are given by the following expressions (in these formulas, T is in °C units):

- for ZrB₂/SiC/TaSi₂

$$\lambda(T) = 2.6693 \cdot 10^{-8} T^3 - 6.0102 \cdot 10^{-5} T^2 + 3.0995 \cdot 10^{-2} T + 3.6168 \cdot 10^{+1} \quad (8)$$

- for HfB₂/SiC/TaSi₂

$$\lambda(T) = 1.7971 \cdot 10^{-8} T^3 - 3.8412 \cdot 10^{-5} T^2 + 1.6151 \cdot 10^{-2} T + 3.2240 \cdot 10^{+1} \quad (9)$$

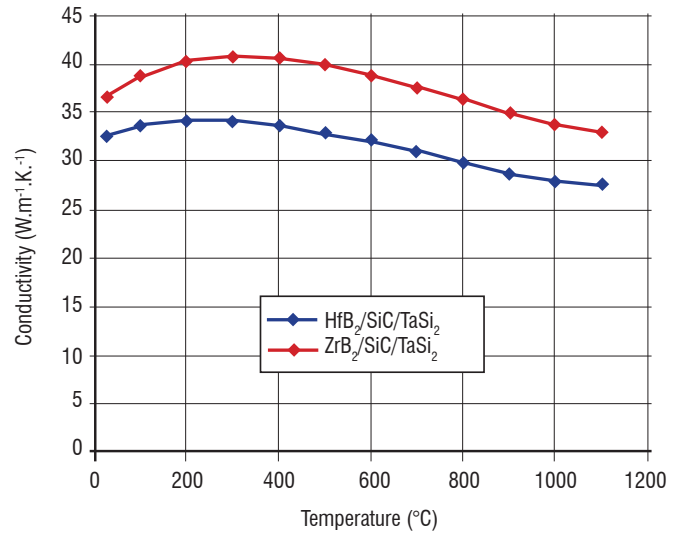


Figure 4 – Thermal conductivity

From 20 to 1200°C, the thermal conductivities of the characterized materials (sintered from non-optimized mixtures) are higher than 25 W.m⁻¹.K⁻¹. In fact, the thermal conductivities of diboride-based UHTC are typically high [27][28], in comparison with those of many other ceramics (table 7) and are a result of both a lattice (vibrations) and an electronic contribution to phonon transport [30]. These values are also higher than for some alloys and CMC (for example: at 300K, $\lambda = 13.6 \text{ W.m}^{-1}.\text{K}^{-1}$ for Inconel 617 and $\lambda \sim 14.5 \text{ W.m}^{-1}.\text{K}^{-1}$ for a standard C/C-SiC). This ability to easily transport heat is one of the most important advantages of these materials. Indeed, their high conductivity allows heat to be conducted from a high heating area to a region of lower heating, where it is then re-radiated into the atmosphere. Furthermore, their high level of conduction gives them good thermal shock resistance.

Material	$\lambda / \text{W/m K}$
Si ₃ N ₄ (Kyocera SN-220)	15.5 (293K) - 13 (1273K)
Al ₂ O ₃ (Kyocera A-479)	24 (293K) - 5 (1273K)
ZrO ₂ (Kyocera Z-701N)	4 (293K) - 3 (1273K)

Table 7 – Thermal conductivity of some different ceramics [29]

Total hemispherical emissivity

As for thermal conductivity, total hemispherical emissivity (ϵ) determinations have been carried out on the first generation of materials and only on monoliths comprising TaSi₂ (total hemispherical emissivity values are deduced from spectral thermal emissivity measurements [31]). The assessment of each material was done on two parallelepiped samples (16 x 8 x 2 mm³), from 200 to 800°C, under argon, before and after an oxidation treatment at 1000°C.

Emissivity values for oxidized materials are presented in figure 5 and the correlations for ε are given by the following expressions (in these formulas, T is in °C units):

- for $ZrB_2/SiC/TaSi_2$

$$\varepsilon(T) = -2.9689 \cdot 10^{-10} T^3 + 2.4882 \cdot 10^{-7} T^2 + 2.3138 \cdot 10^{-4} T + 7.6225 \cdot 10^{-1} \quad (10)$$

- for $HfB_2/SiC/TaSi_2$

$$\varepsilon(T) = -7.5962 \cdot 10^{-10} T^3 + 1.0203 \cdot 10^{-6} T^2 - 2.2331 \cdot 10^{-4} T + 8.3449 \cdot 10^{-1} \quad (11)$$

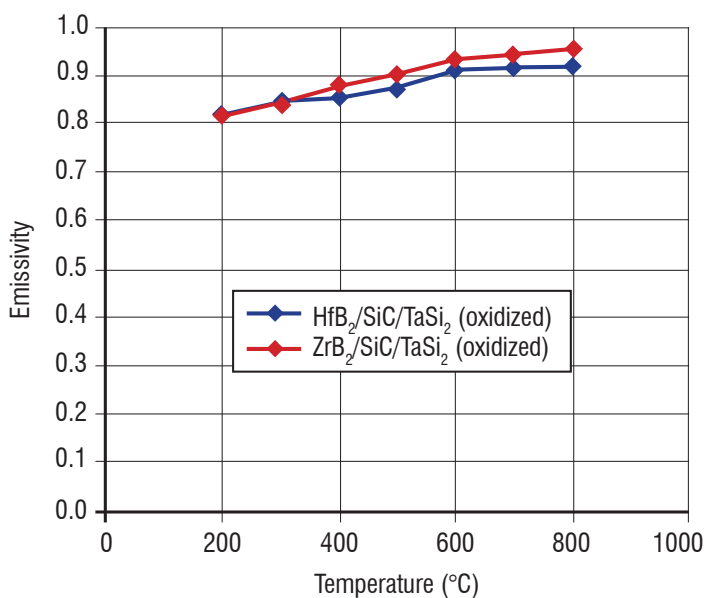


Figure 5 – Total hemispherical emissivity (after oxidation)

In the temperature range studied, oxidized surfaces lead to emissivities higher than 0.8. This level of emissivity is entirely sufficient for the components for which UHTC monoliths are developed (leading edges and air intakes). In these applications, a high emissivity is indeed desirable, as it would reradiate much of the energy from the surface, eliminating some of the energy that the piece would otherwise have to handle. We can add that similar values are generally observed on classical CMC such as C/SiC or SiC/SiC.

Oxidation and thermal shock resistance

Furnace oxidation under stagnant air

The thermal shock behavior and the long resistance time under oxidative atmosphere and at high temperature have been assessed by thermal treatments of several samples at 1000°C under stagnant air at atmospheric pressure. Cumulative times in furnaces of up to 1000 hours were administered on the three selected compositions. The oxidation kinetics were obtained by following material weight variations versus time and the thermal shock resistance was assessed simply by several sudden insertions and extractions of the samples.

For each material, more than 12 cycles of insertion/extraction (*i.e.* at least 24 thermal shocks) were achieved without any problems. In fact, the materials fully maintained their integrity. No cracks

appeared and no destructive oxidation was observed. Thus, under the previous test parameters, all the compositions exhibited good thermal shock resistance. This is due to a large extent to the high thermal conductivity of these materials.

The specific weight changes vs. oxidation time are shown in figure 6. Oxidation kinetics slow down with time and with the samples tested the total weight variations are very limited (< 0.3 % after 1000 h). In addition, as observed by SEM, there is formation of a protective layer on the surface. This protective layer is divided in two parts: a SiO₂ rich glass as the outermost coat (~7 μm thick) and an intermediate layer in the process of being oxidized (~20 μm thick). Very similar behavior has been also observed in samples tested in an arc-jet facility (figure 7).

These results allow us to conclude that the selected materials exhibit good oxidation resistance with the test parameters and conditions of this study.

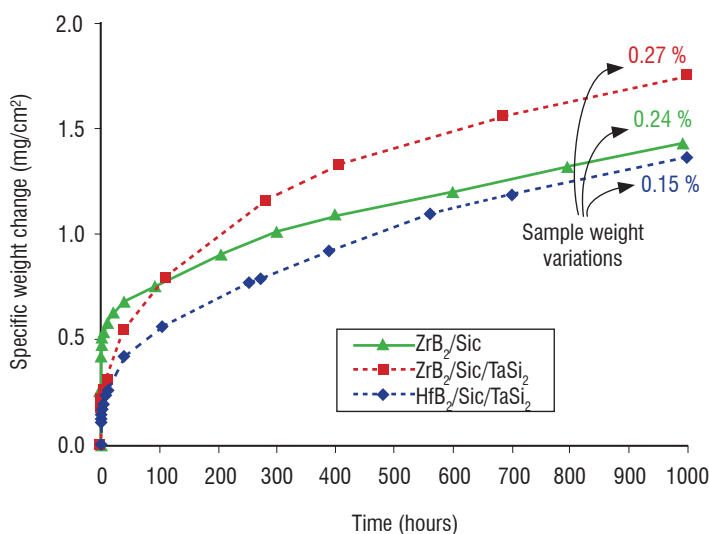


Figure 6 – Oxidation kinetics of the three selected materials

Arc-jet tests

In order to investigate the thermal and chemical resistance of the three selected materials in more realistic conditions (close to hypersonic flight), a test campaign was carried out under high-enthalpy hypersonic flow in an arc-jet facility at DLR Cologne (L2K) [32]. First, four disc-shaped samples (\varnothing 26.5 mm, e = 4 mm) of each composition were machined. Then, with these specific samples, several tests were carried out from 1100 to 1500°C. The test at 1100°C was defined as the baseline test condition with regard to the ATLLAS objectives (hypersonic flights at Mach 6 in Earth atmosphere). Afterwards, higher enthalpy and temperature levels were applied with three other test conditions in order to check the materials' capabilities:

sample A	2 cycles	test of 300 s at 1100°C + test of 600 s at 1100°C
sample B	2 cycles	test of 300 s at 1100°C + test of 600 s at 1300°C
sample C	1 cycle	test of 600 s at 1400°C
sample D	1 cycle	test of 600 s at 1500°C

The samples' resistance to high enthalpy flow was assessed by several measurements (weighing, thickness checking), and by photographs

before and after each test and finally SEM observations of a few samples on both oxidized surfaces and polished cross-sections of discs (figure 7). In addition, videos and photographs were recorded during all of the experiments (see for example figure 8 and video).

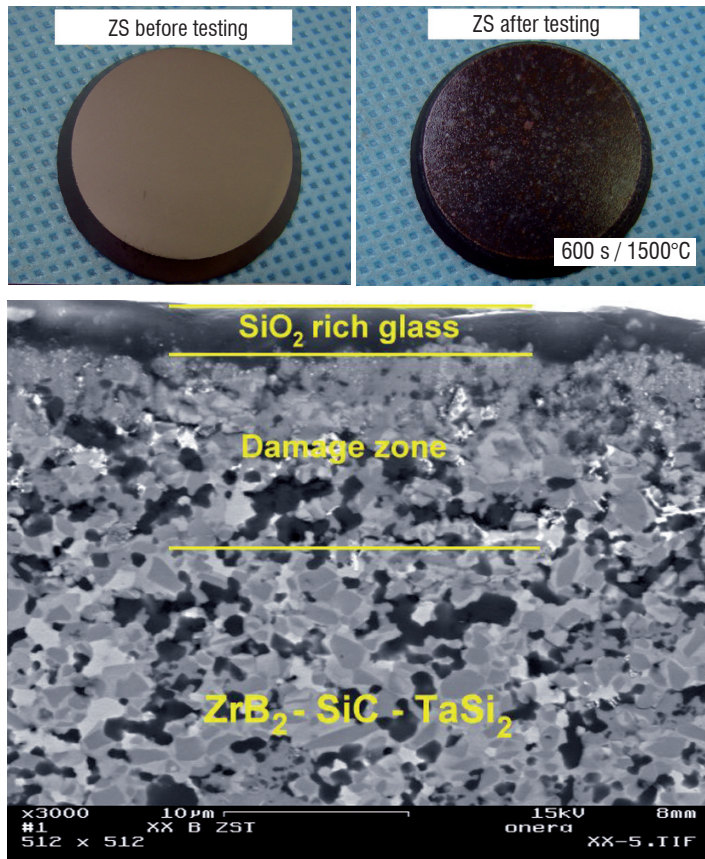


Figure 7 – ZrB_2/SiC disc before and after a test at $1500^\circ C$ (top) and cross-sectioned. $ZrB_2/SiC/TaSi_2$ disc after 2 successive cycles at 1100 and $1300^\circ C$ (bottom)

The results of this test campaign were very satisfactory. For each condition, good material resistance was detected (the most important mass and thickness variations observed during this campaign were quite limited: $\Delta M_{max} = 0.33\%$ and $\Delta e = 50 \mu m$). As previously observed by SEM on oxidized materials (tests under stagnant air), there is again formation of a thin glass layer on the surface and

underneath an intermediate layer in the process of being oxidized (SiC-depleted layer) [33]. Thermodynamically, ZrB_2 , HfB_2 and SiC should oxidize when exposed to air. However, below $1200^\circ C$, it is reported in the literature that the oxidation of ZrB_2 (or HfB_2) is more rapid than that of SiC. Then there is production of a continuous protective oxide layer of B_2O_3 (l) with entrained ZrO_2 (or HfO_2) which prevents ZrB_2 (or HfB_2) from being further oxidized. At higher temperatures, B_2O_3 (l) evaporates due to its high vapor pressure and consequently the rate of SiC oxidation increases, inducing the formation of a SiO_2 rich glass on the surface [6]. Up to $1600^\circ C$, $TaSi_2$ addition improves oxidation resistance because it reduces oxygen vacancy concentration in ZrO_2 . However, it is important to note that Opila et al. has shown that Ta additions are less effective in HfB_2 based materials [15].

In conclusion, under ATLLAS conditions, cumulative durations up to 900 s are performed without any problems (for all the selected compositions). Very good sample-to-sample reproducibility and a lack of sensitivity to thermal load cycling have been demonstrated. In addition, all the selected materials are able to sustain higher thermal loads (up to $1500^\circ C/600$ s). Thus, the requirements for the sharp leading edges and air intakes of the ATLLAS vehicle are well fulfilled. This good thermal-oxidative stability in severe environments is certainly one of the most important results of this work on UHTC materials. It is also interesting to note that several studies have demonstrated the excellent behavior of typical UHTC leading edges under arc-jet testing compared with more traditional composites like C/SiC for instance [34]. However, for long-term use under hypersonic conditions ($\sim 25,000$ cycles), some confirmations of the high resistance of our materials will be necessary to completely validate the solutions.

Possible design of a UHTC sharp leading edge

Due to the high level of properties demonstrated previously, it seems possible to envisage the future making of sharp components based on the best selected UHTC materials. With better knowledge of these specific materials, it should now be easier to design some examples of what could be a leading edge or an air intake of the ATLLAS vehicle. As a matter of fact, the best way to use monolithic UHTC materials for manufacturing sharp components seems to be to combine these materials with others (CMC notably). Thus, the UHTC part would be placed as an insert in front of the structural component in order to use only UHTC pieces of limited size (figure 9). This allows for optimization

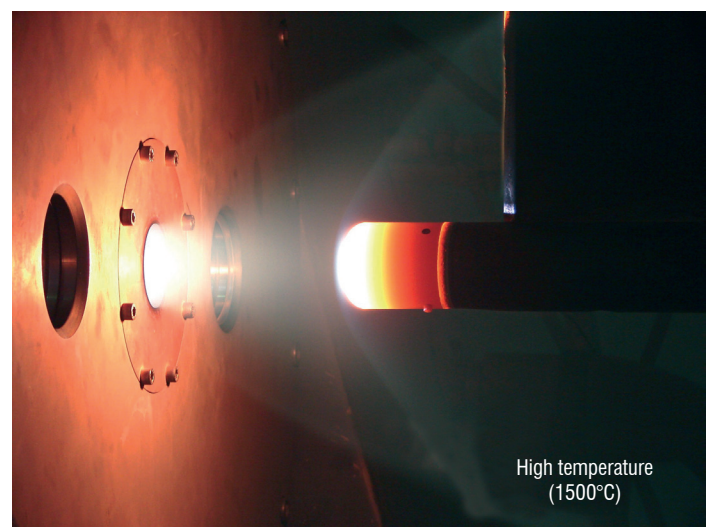
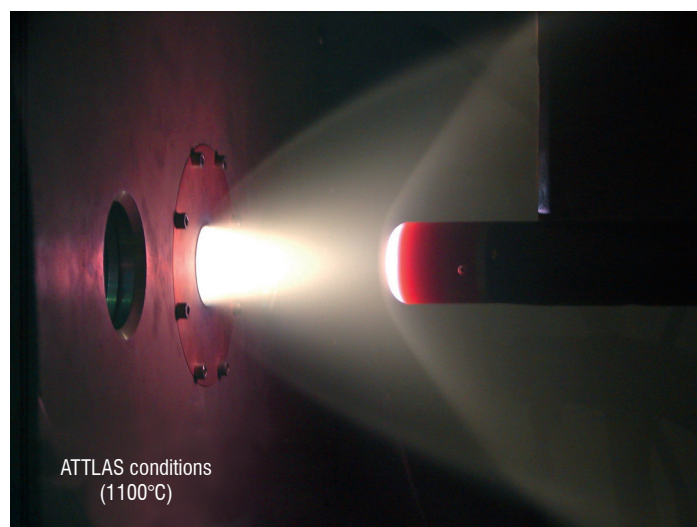


Figure 8 – Flow field around sample holder at different test conditions (shapes of the bow shock and the free stream boundary)
<http://www.aerospace-lab-journal.org/al3/Ultra-High-Temperature-Ceramics>

of the element involved (performance, weight and cost in particular). However, it is important to note that the attachment design needs to be properly addressed to minimize thermal stresses. For example, it would be possible to avoid the contact of the UHTC element with cooler sub-components in the structure in order to reduce bearing stresses at the attachment location [35]. Moreover, in order to avoid possible crack propagation in the UHTC component and also to make the manufacturing easier, the design calls for the leading edge to be comprised of multiple UHTC tiles or segments rather than a one-piece continuous edge [36].

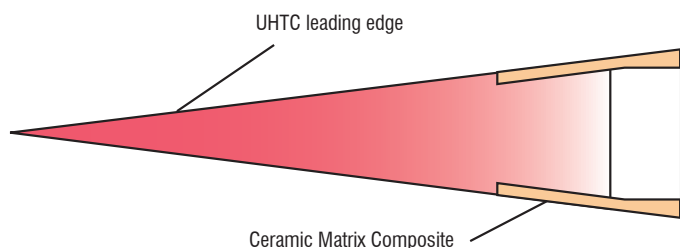


Figure 9 – Possible schematic design of a UHTC sharp component

Outlook: materials for propulsion use

Another major challenge for the future is the development of new materials able to meet the strict requirements of the next generation of propulsion systems for civilian and military uses. These include

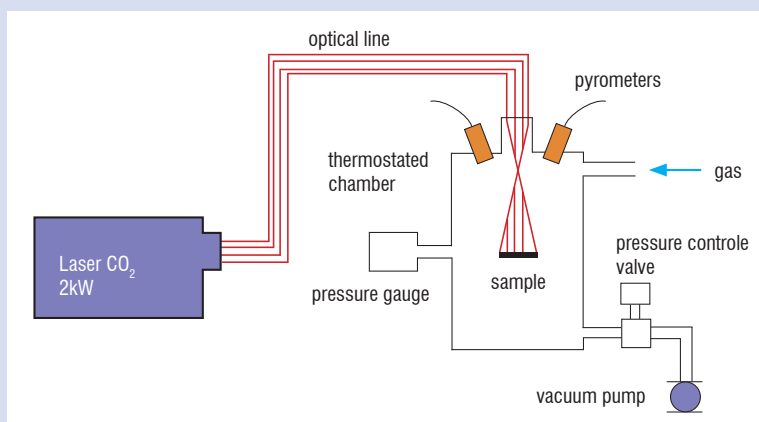
for example specific engine components for hypersonic vehicles (thin uncooled injectors for hydrogen) or elements for high-energy propellant propulsion (hot gas vanes). For this type of application, and for the most rigorous hypersonic uses, there are needs for materials that can withstand 2000 to 3000°C. Onera is therefore involved in several programs (ATLLAS 2 for instance) to assess UHTC materials that could meet these new requirements (with monoliths and composite coatings). Further information regarding ATLLAS 2 can be found on www.esa.int/techresources/atllas_II. In propulsion applications, at temperatures exceeding 2000°C, one of the main problems is the resistance to oxidation and corrosion of the materials which are in contact with combustion gases. These gases contain highly oxidative and corrosive chemical species (water vapor, CO₂, CO and HCl for instance), and we know that low oxidation rate materials, which form pure scales of SiO₂, Al₂O₃, Cr₂O₃, or BeO cannot be used at temperatures above 1800°C due to the disruption of high vapor pressures which arise at the interphase of the base material and the scale [37]. Therefore, diboride/SiC materials with specific additives (rare earth oxides or LaB₆ for example) to improve their resistance to oxidation above 2000°C [38] and new compounds based on oxide blends or carbide/nitride mixtures are currently being studied in our laboratories. In order to evaluate the level of resistance to oxidation of these new materials with relative ease, a custom-designed facility is used: the BLOX 4, which is a 4th generation Laser Oxidation Analysis facility (see box 2). This system simulates the effects of various atmospheres (water vapor for example) on the behavior of UHTC materials at high temperatures.

Box 2 - Laser Oxidation Analysis Facility (BLOX)



Figure B2-01 – BLOX facility at Palaiseau center

The 4th laser oxidation analysis facility (BLOX) is a custom-made device used for thermal characterization of materials at very high temperatures in controlled atmospheres (air, N₂, O₂, Ar, CO₂, water vapor, H₂...) at pressures ranging from a few millibars to 4 bars. The use of a high power CO₂ laser (2kW) can generate temperatures of 2000°C or higher. The sample temperature is measured with pyrometers as seen in the general diagram of BLOX.



Materials can be characterized under intense, continuous or impulse heat flux and the very low thermal inertia allows temperature cycling at high frequencies and very rapid temperature rises.

In addition, due to the selected constituents of the previous UHTC compounds, very high temperatures and pressures would be required to sinter the powders. For this reason, a promising method called Spark Plasma Sintering (SPS) or Field Assisted Sintering Technology (FAST) has been selected to manufacture UHTC monoliths. Using this modified hot pressing process in which electric current runs through the pressing mold and the component, very rapid heating times and short sintering cycles can be achieved [39]. In addition, its operation is easy and it enables ceramics to become fully dense at comparatively low temperatures and with limited grain growth (very fine microstructures are thus possible).

Conclusion

Hypersonic, atmosphere re-entry and rocket propulsion applications provide some unique thermal-structural challenges (sharp leading edges, air intakes, vanes, etc.). In order to fulfill the requirements of these components, some specific materials are compulsory (UHTC). Indeed, thanks to their unique combination of mechanical, thermal and chemical properties, UHTCs are a promising technology for use in a number of high temperature structural applications.

ZrB₂-SiC, ZrB₂-SiC-TaSi₂ and HfB₂-SiC-TaSi₂ were studied for leading edge applications in the ATLLAS project. These compositions were sintered by hot pressing between 1700 and 1800°C and reached 98% of the theoretical density. They possess attractive properties: high hardness, high flexural stress, good machinability, high emissivity. Another attractive feature of these materials is their relatively high thermal conductivity which gives them better thermal shock resistance than most insulating materials and allows heat to be conducted from the leading edge to a region of lower heating, where it is re-radiated into the atmosphere. In addition, these materials exhibit good resistance to oxidation at very high temperatures (>1500°C) due to the formation of a glassy protective layer. Oxygen diffusion is slowed down through this oxide layer and ZrB₂ is then prevented from undergoing further oxidation. All these properties allow these materials to fulfill the requirements to sustain hypersonic flight conditions as demonstrated in the ATLLAS project.

These kinds of materials are also of great value for higher temperature applications (i.e. 2000°C and more). New characterization devices are needed to test them in environments as close to real conditions as possible. A custom-made device is being used in Onera laboratories to reach 2000°C and higher in oxidizing atmospheres ■

Acknowledgements

This work was carried out within the "Aerodynamic and Thermal Load Interactions with Lightweight Advanced Materials for High Speed Flight" project investigating high-speed transport. ATLLAS, coordinated by ESA-ESTEC, is supported by the EU within the 6th Framework Programme Priority 1.4, Aeronautic and Space, Contract n° AST5-CT-2006-030729.

We would like to thank B. Esser and A. Gülhan for the test campaign carried out in the L2K arc jet facility of DLR Cologne [32].

References

- [1] E. CLOUGHERTY, D. KALISH and E. PETERS - *Research and Development of Refractory Oxidation Resistant Diborides*. Technical Report AFML-TR-68-190, 1968.
- [2] G. V. SAMSONOV - *Refractory Transition Metal Compounds: High Temperature Cermets*. Academic Press, New York, 1964.
- [3] M.M. OPEKA, I.G. TALMY and J.A. ZAYKOSKI - *Oxidation-Based Materials Selection for 2000°C + Hypersonic Aerosurfaces: Theoretical Considerations and Historical Experience*. Journal of Materials Science 39, 5887-5904, 2004.
- [4] S.R. LEVINE, E.J. OPILA, M.C. HALBIG, J.D. KISER, M. SINGH and J.A. SALEM - *Evaluation of Ultra-High Temperature Ceramics for Aero propulsion Use*. J. European Ceramic Society 22, 2757-2767, 2002.
- [5] J. HAN, P. HU, X. ZHANG and S. MENG - *Oxidation Behavior of Zirconium Diboride-Silicon Carbide at 1800 °C*. Scripta Materialia 57, 825-828, 2007.
- [6] W.G. FAHRENHOLTZ - *Thermodynamic Analysis of ZrB₂-SiC Oxidation: Formation of a SiC-Depleted Region*. J. American Ceramic Society 90, 43-148, 2007.
- [7] F. MONTEVERDE and A. BELLOSI - *Oxidation of ZrB₂-Based Ceramics in Dry Air*. J. Electrochemical Society 150 [11], B552-B559, 2003.
- [8] D.A. KONTINOS, K. GEE and D.K. PRABHU - *Temperature Constraints at the Sharp Leading Edge of a Crew Transfer Vehicle*. American Inst. of Aeronautics & Astronautics, 2001-2886, 2001.
- [9] W.G. FAHRENHOLTZ, G.E. HILMAS, I. G. TALMY and J. A. ZAYKOSKI - *Refractory Diborides of Zirconium and Hafnium*. J. American Ceramic Society 90, 1347-1364, 2007.
- [10] J. STEELANT - *Atlas: Aero-Thermal Loaded Material Investigations for High-Speed Vehicles*. 15th AIAA International Space Planes and Hypersonic Systems and Technologies Conference, Dayton, Ohio, 2008.
- [11] J.F. JUSTIN - *Investigations of High Temperature Ceramics for Sharp Leading Edges or Air Intakes of Hypersonic Vehicles*. 3rd European Conference for AeroSpace Sciences, Versailles, France, CD-ROM ISBN 978-2-930389-47-8, 2009.
- [12] A. EZIS and J.A. RUBIN - *Hot Pressing*. Engineered Materials Handbook, vol 4, Ceramics and Glasses, 186-193, 1991.
- [13] G.E. GAZZA - *Pressure Densification*. Engineered Materials Handbook, vol 4, Ceramic and Glasses, 296-303, 1991.
- [14] W.C. TRIP, H.H. DAVIS and H.C. GRAHAM - *Effect of a SiC Addition on the Oxidation of ZrB₂*. American Ceramic Society Bulletin, vol 52 [8], 612-616, 1973.
- [15] E. OPILA and S. LEVINE - *Oxidation of ZrB₂- And HfB₂-Based Ultra-High Temperature Ceramics: Effect of Ta Additions*. Journal of Materials Science 39, 5969-5977, 2004.
- [16] T.H. SQUIRE and J. MARSCHALL - *Material Property Requirements for Analysis and Design of UHTC Components in Hypersonic Applications*. J. European Ceramic Society 30, 2239-2251, 2010.
- [17] R. RIEDEL - *Handbook of Ceramic Hard Materials*. WILEY-VCH, 2000.
- [18] N. FAULK - *Electrical Discharge Machining*. Engineered Materials Handbook, vol 4, Ceramics and Glasses, 371-376, 1991.
- [19] ASTM Standard E1876-09 - *Standard Test Method for Dynamic Young's Modulus, Shear Modulus, and Poisson's Ratio by Impulse Excitation of Vibration*.

- [20] S.Q. GUO and al - *Mechanical Properties of Hot-Pressed ZrB₂-MoSi₂-SiC Composites*. J. European Ceramic Society 28, 1891-1898, 2008.
- [21] A.L. CHAMBERLAIN, W.G. FAHRENHOLTZ and G.E. HILMAS - *High-Strength Zirconium Diboride-Based Ceramics*. J. American Ceramic Society 87, 1170-1172, 2004.
- [22] F. MONTEVERDE - *Ultra-High Temperature HfB₂-SiC Ceramics Consolidated by Hot-Pressing and Spark Plasma Sintering*. Journal of Alloys and Compounds 428, 197-205, 2007.
- [23] F. MONTEVERDE, A. BELLOSI and L. SCATTEIA - *Processing and Properties of Ultra-High Temperature Ceramics for Space Applications*. Materials Science and Engineering: A. 485, 415-421, 2008.
- [24] G.R. ANSTIS, P. CHANTIKUL, B.R. LAWN and D.B. MARSHALL - *A Critical Evaluation of Indentation Techniques for Measuring Fracture Toughness: I. Direct Crack Measurements*. J. American Ceramic Society 64, 534-553, 1981.
- [25] A. FRANCESE - *Numerical and Experimental Study of UHTC Materials for Atmospheric Re-Entry*. Dottorato di ricerca in ingegneria aerospaziale, 2007.
- [26] W.J. PARKER, R.J. JENKINS, C.P. BUTLER and G.L. ABBOT - *Flash Method of Determining Thermal Diffusivity, Heat Capacity, and Thermal Conductivity*. J. Applied Physics 32, 1679-1684, 1961.
- [27] R. LOEHMAN, E. CORRAL, H.P. DUMM and al - *Ultra-High Temperature Ceramics for Hypersonic Vehicle Applications*. Sandia Report, SAND 2006-2925, 2006.
- [28] M. GASCH, S. JOHNSON and J. MARSCHALL - *Thermal Conductivity Characterization of Hafnium Diboride-Based Ultra-High-Temperature Ceramics*. J. American Ceramic Society 91, 1423-1432, 2008.
- [29] *Characteristics of Kyocera Technical Ceramics*. http://americas.kyocera.com/kicc/pdf/Kyocera_Material_Characteristics.pdf.
- [30] R. A. CUTLER - *Engineering Properties of Borides*. Engineered Materials Handbook, vol 4, Ceramics and Glasses, 787-803, 1991.
- [31] D. DEMANGE and M. BEJET - *New Methods for Measuring the Thermal Emissivity of Semi-Transparent and Opaque Materials*. 8th International Conference on Quantitative Infrared Thermography, Padova, 2006.
- [32] B. ESSER - *Thermal Characterisation of Onera's Uhtc Materials*. Deliverable D.3.2.6 of ATLLAS project, 2009.
- [33] T. PARTHASARATHY, R. RAPP, M. OPEKA and R. KERANS - *A Model for the Oxidation of ZrB₂, HfB₂ and TiB₂*. Acta Materialia 55, 5999-6010, 2007.
- [34] X. ZHANG and al - *Ablation Behavior Of ZrB₂-SiC Ultra High Temperature Ceramics under Simulated Atmospheric Re-Entry Conditions*. Composites Science and Technology 68, 1718-1726, 2008.
- [35] D.J. THOMAS - *Design and Analysis of Uhtc Leading Edge Attachment*. NASA/CR-2002-211505, Glenn research Center, 2002.
- [36] T. KOWALSKI, K. BUESKING, P. KOLODZIEJ and J. BULL - *A Thermostructural Analysis of a Diboride Composite Leading Edge*. NASA Technical Memorandum 110407, 1996.
- [37] K. UPAHYA, J.-M YANG and W. P. HOFFMAN - *Materials for Ultrahigh Temperature Structural Applications*. The American Ceramic Society Bulletin, 51-56, 1997.
- [38] J. HAN, P. HU, X. ZHANG, S. MENG and W. HAN - *Oxidation-Resistant ZrB₂-SiC Composites at 2200 °C*. Composites Science and Technology 68, 799-806, 2008.
- [39] H.U. KESSEL, J. HENNICKE, J. SCHMIDT, T. WEIßGÄRBER, B. F. KIEBACK, M. HERRMANN and J. RÄTHEL - *"Fast" Field Assisted Sintering Technology - A New Process for the Production of Metallic and Ceramic Sintering Materials*.

Acronyms

UHTC (Ultra High Temperature Ceramic)

ATLLAS (Aerodynamic and Thermal Load Interactions with Lightweight Advanced Materials for High Speed Flight)

ESA-ESTEC (European Space Research and Technology Centre of the European Space Agency)

DLR (Deutsches Zentrum für Luft und Raumfahrt)

SST (Supersonic Transport)

LE (Leading Edge)

YTZ (Yttrium stabilized Zirconia)

HP (Hot Pressing)

CMC (Ceramic Matrix Composite)

C/C (Carbon / Carbon Composite)

C/SiC (Carbon / Silicon Carbide Composite)

SiC/SiC (Silicon Carbide / Silicon Carbide Composite)

EDM (Electrical Discharge Machining)

SEM (Scanning Electron Microscopy)

CTE (Coefficient of Thermal Expansion)

SPS (Spark Plasma Sintering)

FAST (Field Assisted Sintering Technique)

BLOX (Laser OXidation analysis facility)

AUTHORS



Jean-François Justin is a research engineer working within the Thermostructural and Functional Composites unit (CTF) of the Composite Materials and Structures Department (DMSC). He graduated from the "Conservatoire National des Arts et Métiers". Since he joined Onera in 1989, he has been concerned with the development of monolithic ceramics and Ceramic Matrix Composites for functional applications (combustion chambers, stealth materials, engine blades, leading edges, air intakes ...). He has been also involved in the improvement of CMC processing routes and CVD coatings. Currently, his research field is mainly focused on Ultra-High Temperature Ceramics (notably within the framework of the European project ATLLAS II).



Aurélie Jankowiak After graduating from ENSCI in 2005, she received a PhD in Materials Science from the University of Limoges (2008). She has been working since 2009 in the Composite Materials and Structures Department of Onera. Her research field is mainly focused on high temperature materials for functional applications (combustion chambers, engine blades, leading edge).

M. Parlier, M.-H. Ritti, A. Jankowiak
(Onera)

E-mail: michel.parlier@onera.fr

Potential and Perspectives for Oxide/Oxide Composites

The challenge for oxide/oxide composites is to provide an alternative to SiC/SiC composites with the aim of decreasing the cost of manufacture and improving the thermal stability in air at high temperature. Oxide/oxide composites consist of a porous alumina matrix reinforced by fibers of the same nature. Obtaining a controlled rate of porosity in the preparation helps to dissipate the energy associated with the propagation of cracks in the matrix during loading. It follows that the composite is damage-tolerant without requiring a carbon coating on the fibers as in the case of SiC/SiC composites. Using submicron alumina powders and specific additives necessary for shaping and for control of the sintering shrinkage, the first composites were obtained by developing a method of infiltration into fibrous reinforcements. To increase the fiber volume fraction and thus the mechanical properties, processes based on the prepreg molding in a plastic bag of a suspension in a fiber preform were selected. The development of these various processing routes is outlined in relation with the evolution of properties. The development of thermal barrier coatings based on microporous oxide is also presented, in order to extend the thermostructural potential beyond 1200°C.

Introduction

Over the last decades, considerable efforts have been devoted to the improvement of the temperature capability of metallic superalloys, which cannot henceforth exceed 1150°C. For structural applications at higher temperatures under high stresses in oxidizing and corrosive environments, ceramic materials are promising candidates, provided that their brittleness can be overcome by using continuous fiber reinforcements. Since the research performed in the early 80's with the first generation of ceramic fibers, Ceramic Matrix Composites (CMCs) have shown their ability to exhibit a damage-tolerant behavior (Box 1).

Nevertheless, while CMCs have experienced an exceptional development over the last decade, mainly in the short term in the field of aerospace applications (missiles, rocket propulsion) where there is a constant need to increase payloads and working temperatures, efforts are now focused on cost reduction and on the improvement of the life duration. The objective is to use these new materials in gas turbine engines to improve their efficiency and to reduce polluting emissions [1].

Beyond the concept of weak interface composites (WICs) and to overcome the oxidation of the interphase between the fiber and the matrix (see box 1), the challenge was to develop a non oxidizable composite. The first step was to establish the feasibility and the potential of

an oxide/oxide composite for a hot combustor wall. A single crystal alumina fiber (Saphikon, USA)/zirconia (ZrO_2) interphase/alumina matrix has been developed and tested in the frame of the NOXICC Brite/Euram program (Novel OXide Ceramic Composites) [2]. After ageing at 1400°C for 100 and 1000 hours, it has been shown that the mechanical behavior remains comparable to the as-processed composites [3].

To decrease the cost, the next step described in this paper was to develop a weak matrix concept without interphase, using Nextel fibers produced by the 3M Company (USA) to reinforce a porous alumina matrix. The technique to produce the porous alumina matrix, i.e. infiltration of powder followed by sintering, is described in § «Elaboration by infiltration». The mechanical performance and the procedure of improvement of the 2D Nextel 720/ Al_2O_3 composite are then discussed in § «Mechanical behavior» and § «Improvement of mechanical properties, respectively». A potential application concerning hot wall combustor chambers, various thermal barrier coatings (TBCs) are investigated in § «Evaluation of thermal barrier coatings» to increase the working temperature of the composite in hot gas up to 1500°C. Simulation of thermal barrier thickness and ageing behavior are also reported. Finally, to improve the fiber volume fraction and thus the mechanical properties, the first results on 2D Nextel 610/ Al_2O_3 composites produced by prepreg molding in plastic bags are presented.

Box 1 - Damage-tolerant behavior of CMCs

The advent of high temperature components manufactured in CMCs originates from the ability of this class of materials to exhibit a dissipative damage-tolerant behavior, as opposed to monolithic ceramics, which exhibit brittle fracture induced by crack initiation and propagation from the statistical flaw distributions (figure B01-1). This particular property of CMCs is characterized by the development of matrix multicroacking without fiber breaking, a rather unexpected behavior for a material made of two brittle constituents. It is the result of achieving during processing a fiber-matrix bonding sufficiently weak to allow debonding and consequently the relaxation of the stress field at the crack tip and the bridging of matrix cracks by the fibers.

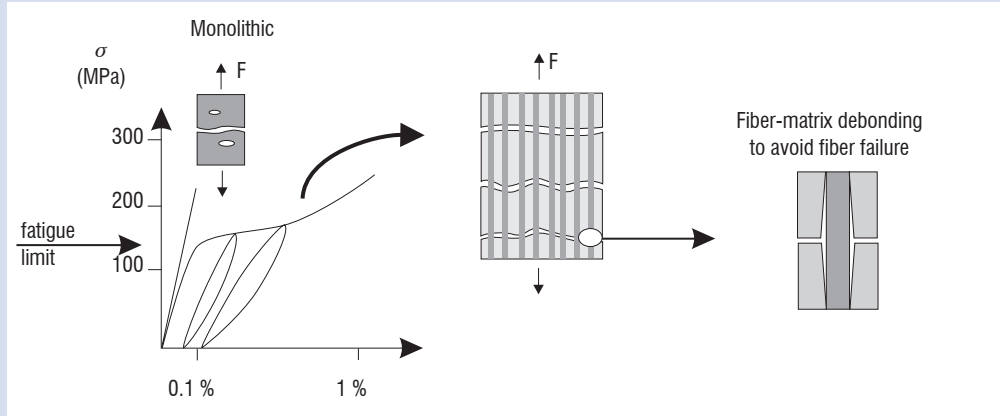


Figure B01-1 – Damage tolerant behavior of CMCs compared to monolithic ceramic

From the well known relationship presented by He and Hutchinson [4], the fracture energy of the interface (Γ_I) for this debonding initiation process can be calculated in relation to the fracture energy of the fiber (Γ_F). A ratio $\Gamma_I/\Gamma_F \leq 0.25$ must be respected to achieve a non brittle behavior when the fiber and the matrix exhibit similar Young's moduli, E_F and E_M , respectively (figure B01-2). For CMCs with dense and crystalline matrices (e.g. SiC, Al_2O_3) surrounding the fiber, the deposition on the fiber of a thin coating called interphase with low cohesion (e.g. pyrolytic carbon or boron nitride, etc.) is required for lowering Γ_I . CMCs of this type are called Weak Interface Composites (WICs). Nevertheless, these coatings may be oxidized at high temperature, thus leading to an increase in the relative fracture energy Γ_I/Γ_F and consequently to a brittle failure of the WIC. In the case of Weak Matrix Composites (WMCs) characterized by a matrix with a fine porosity, the reduced matrix stiffness ($E_M < E_F$) and strength allow a damage-tolerant behavior, even in the case of a strong matrix-fiber interface. Nevertheless, since the matrix is not able to sustain a significant load, the mechanical behavior of WMCs is dominated by the properties of the fibers and a low strength is obtained under compression. Furthermore, brittle failure can be observed if the matrix is excessively densified during the manufacturing step (e.g. infiltration of precursors, sintering of powders, etc.).

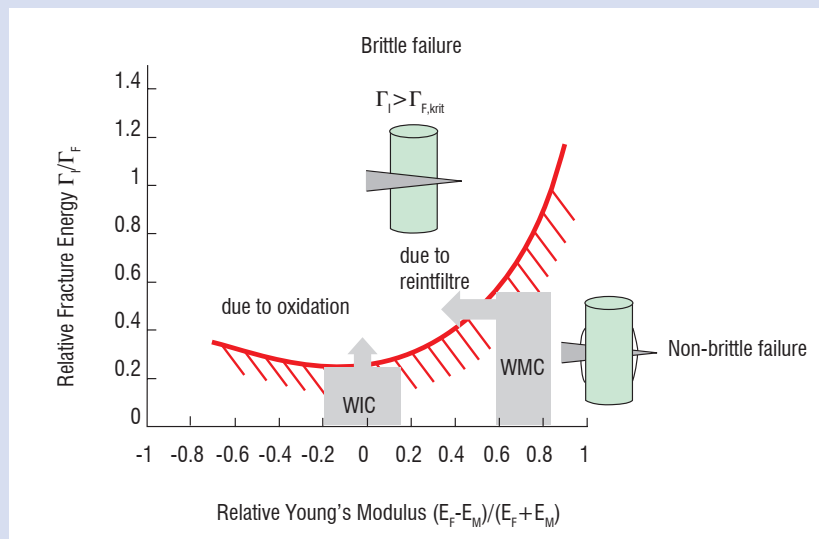


Figure B01- 2 – Boundary curve for non brittle failure of CMCs, taking into account the relative fracture energy Γ_I/Γ_F and the relative stiffness of fiber and matrix [4]. Additionally, the effect of interfacial oxidation and matrix densification are illustrated [5].

Elaboration by infiltration

One way to produce an oxide matrix is to use a Sol-Gel process, where liquid alkoxide precursors are infiltrated into the fiber preform to form a polymeric oxide network (gel) in situ, via hydrolysis and polycondensation reactions. Nevertheless, the first step of the gel formation and its subsequent pyrolysis are globally characterized by a low mass yielding of ceramics, thus leading to a high level of shrinkage (~ 80%). To counterbalance this limitation, a two-step infiltration technique has been developed [5]. The first step consists in an infiltration of the fiber preform by fine submicronic oxide particles using a slurry filtration technique, which allows about 50% of the free volume to be filled. Then, the residual porosity of the powder infiltrated in the fiber preform is filled with an alkoxide followed by in situ hydrolysis/polycondensation and pyrolysis, leading to the formation of an efficient binder. For applications in rocket propulsion, the validity of this processing route has been shown on alumina infiltrated in carbon fiber preforms produced by Snecma (Novoltex®). In this case, a judicious combination of two alkoxides has been selected, firstly, to reduce the shrinkage of the matrix and, secondly, to increase the mechanical properties via the reduction of porosity [6].

The Nextel fibers used in this study are alumina based systems produced by 3M. Nextel 720 is a mixture of alumina and mullite ($2\text{SiO}_2-3\text{Al}_2\text{O}_3$), developed to achieve a compromise between strength and creep with a proven thermal stability up to 1200°C. Nextel 610, mainly composed of alumina, was also used to reach a higher modulus, but its maximum working temperature is limited to 1100°C for long term applications. Since the objective was to moderately densify the matrix, in order to produce a weak matrix composite, the strategy adopted was to select an alumina powder able to sinter at a moderate temperature ($\leq 1200^\circ\text{C}$), with limited shrinkage to avoid matrix multi-cracking. The introduction of Sol-Gel was investigated in a second step § «Improvement of mechanical properties» to check its potential to improve the mechanical performance after ageing.

Sintering behavior of alumina powders

Initially, the objective was to compare the sintering behavior of several alumina powders characterized by a small particle size, to promote their infiltration into Nextel tissues: alpha alumina from the Baikowski Company (France), boehmites AIO (OH) from the Sasol Company (South Africa) (table 1).

Powder	Crystallization	d50 (d20-d90) μm	Specific surface area m^2/g	Size of dispersed particles μm	Green density
A1	Alpha	1.1 (0.7-2.5)	3		1.5
A2	Alpha	0.3 (0.2-0.7)	10		1.9
B1	Boehmite	45	260	0.025	1.2
B2	Boehmite	50	200	0.090	1.5
B3	Boehmite	40	100	0.220	1.4

Table 1- Characteristics of alumina and boehmite powders

The comparison of the sintering shrinkage on pressed pellets (uniaxial press, 60 MPa) is shown in figure 1 as a function of temperature (heating rate of 300°C/h). Both alpha alumina are not sintered very much at 1200°C. However, the A2 powder is characterized by a slightly higher shrinkage, due to its finer particle size. On the other hand, the shrinkage is much more important with boehmites. This behavior is related, firstly, to the loss of hydroxyl groups at low temperatures and, secondly, to the finer individual particle size.

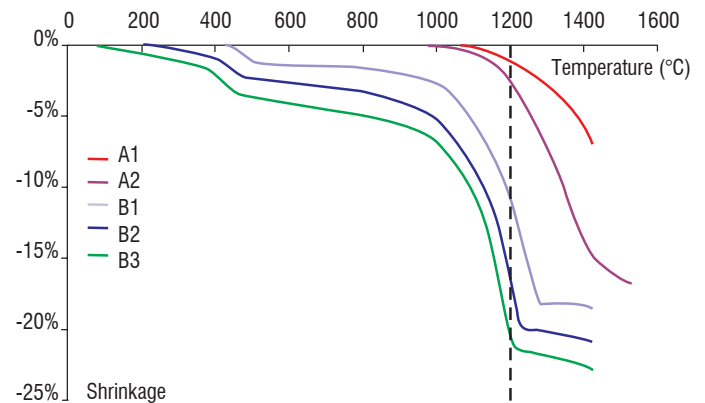


Figure 1 - Evolution of linear sintering shrinkage of alumina powders (300°C/h)

Since the thermostability of Nextel 720 fibers does not exceed 1200°C, the sintering of the composite was deliberately limited to this temperature. Moreover, the presence of the fiber reinforcement (weaving in both directions of the plane) prevents the volume shrinkage of the matrix, thus leading to a severe cracking of the latter. Therefore, only the powders with the lowest shrinkage at 1200°C have been retained in the remainder of the study: alpha alumina A2 and A1, boehmite B3.

Rheology of alumina suspensions

Whatever the processing technique, trials have shown that it is preferable to minimize the amount of water to reduce the level of porosity. However, the rheology of suspensions should be adjusted to get a good infiltration of the powder within the heart of the strands.

To optimize the suspension of A2 alumina powder, viscosity was measured according to the mass concentration of the powder (mass of powder/water) and pH (figure 2). For this, various suspensions in water were prepared, with different additions of concentrated nitric acid or alumina powder to modify the pH and mass concentration, respectively. A viscosimeter with coaxial cylinders (Rheologic International RI:2:L) was used to measure the viscosity, following the DIN 53019 procedure with cylindrical geometry (spindle and sample chamber with a diameter of 14 mm and 15 mm respectively) and shear rate of 10 s^{-1} .

The concentration of 1335 g/l corresponds to the suspension used during the vacuum-pressure infiltration. Its viscosity is very low (4.7 mPa.s). When doubling the concentration by simply adding powder, the pH then increases from 4.7 to 5.6 and the viscosity rises by ten, but the variation is small for pH between 5.6 and 3.9.

Until the concentration of 4000 g/l is attained, the viscosity remains low (60 mPa.s). On the other hand, the viscosity is multiplied by a factor of 4 for an additional increase of 10% in the concentration (210 mPa.s for 4320 g/l).

	Woven fabric	Number of plies	Matrix	Fiber vol. fraction V_f (%)	Density	Porosity (%)	Comment
1	Nextel 440	3	A1	17	1.84	49	Low Vf
2		14		31	1.5	53	Low infiltration yield
3		3	B3	18	1.57	53	Low Vf
4		9		35	1.70	47	High porosity
5	Nextel 720	7	A2	28	2.78	23	Satisfactory densification
6		7		32	2.82	24	
7		8		37	2.81	23	
8		8		37	2.81	23	

Table 2 - Synthesis of infiltration in Nextel fabrics

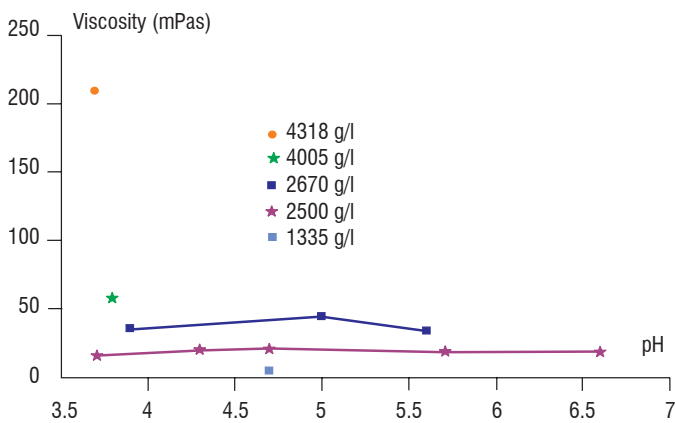


Figure 2 – Change in the viscosity of alumina suspensions versus pH for various concentrations

The viscosity level is not in itself the only criterion to be considered. Indeed, we must also consider the shear stress required to displace the suspension. According to measurements, the shear stress can change very quickly (500 to 3700 mPa) depending on the pH, so that the viscosity is not affected. Moreover, during acidification of suspensions by concentrated nitric acid, hard powder agglomerates are locally formed and they are difficult to re-disperse. This is especially true with a low pH (< 4) and a high concentration.

Thus, the use of concentrated suspensions is possible, but difficult to master as a function of pH, or at least on the way to introduce the acid. These measurements have also shown that prepreg infiltration could certainly be improved by optimizing the concentration and pH.

Infiltration of fabrics

Nextel 720 fabric was supplied by 3M France for the purposes of this study. It is a satin weave of 8 (Ref 720 Nextel XN-513 - Wireless 1500 denier). A similar tissue in Nextel 440 has also been used for a preliminary development.

To infiltrate the layers of fabrics by powders, they are placed on a filter and the thickness of the stack is fixed by a top gate, in order to control the fiber volume fraction. The suspensions consist of water with pH = 3 (addition of nitric acid) and powder in equal proportions

by mass to reach about 2600g/l. To facilitate the migration of the powder suspension within the fabrics, a vacuum under the filter and pressure (0.2 MPa) in the upper assembly are required. The water of the suspension is thus evacuated in the lower part, while the powder is infiltrated between the fibers. After drying, the materials are sintered at 1200°C for one hour.

The results of the infiltration into Nextel 440 and 720 tissue stacks are shown in table 2. The first tests were conducted on the Nextel 440 for economy. For the A1 powder, there is an inadequate infiltration (composites 1 and 2), even with a limited number of plies, which results in a high porosity. For the B3 powder, the lowest particle size is preferable to achieve a better infiltration. Moreover, the decomposition of boehmite (loss of OH radicals) leads naturally to a higher shrinkage and therefore to matrix microcracking induced by the presence of fibers hampering shrinkage (composites 3 and 4). Consequently, the porosity is too high.

On the other hand, the A2 powder, characterized by a low shrinkage and an intermediate particle size, leads to a good infiltration rate and a much lower porosity (composite 5). This result was confirmed with Nextel 720 fabrics (composites 6, 7 and 8). Globally, 2D Nextel 720/A2 composites (66 x 40 x 2.4 mm) are characterized by a fiber volume fraction of about 35% and a porosity of 23%.

Mechanical behavior

Flexural strength up to 1150°C

For 2D Nextel 720/A2 composites consisting of a stacking of 8 or 10 plies with mirror symmetry, some flexural tests (3 point configuration, specimen size: 66 x 7x 2.4 mm, support span: 30 mm, displacement rate : 0.3mm/mn) were performed at room temperature on specimens from different plates. The results of the three-point bending tests are reported in table 3 and table 4.

For three composites (7, 8, 9) with similar morphological characteristics (fiber volume fraction and porosity), a good uniformity of failure stress with an average value of 165 MPa can be noticed, a Young's modulus of 35 GPa and a damage tolerant behavior. A test was also performed on a composite having a higher fiber volume fraction (composite 10). This latter was obtained by adding two

layers of fabric to maintain the mirror symmetry, whereas the same thickness is imposed by the upper grid of the infiltration device. Paradoxically, one specimen exhibits the highest strength, while the other two are among the lowest recorded strengths. A rougher surface and a tendency to delamination of the outer plies can explain these poorer results. A slight relaxation of the more compressed plies is not excluded in this case, but the thickness measurements after sintering are not precise enough to confirm it.

High temperature tests were performed on composites with a stacking of 8 plies of Nextel 720 fabrics (composites 7 and 8). The results reported in table 4 highlight the significant increase in flexural strength with temperature (+ 45% at 1150°C).

	Porosity (%)	V_f (%)	σ_f (MPa)	E_f (GPa)
7	23	37 8 plies	178	36
			145	29
8	23	37 8 plies	182	40
			153	33
9	23	35 8 plies	171	39
			164	36
			157	34
Average			165	35
10	22	43 10 plies	125	32
			184	48
			125	25
Average			145	35

Table 3 – Morphological and mechanical characteristics of 2D Nextel 720/Al₂O₃ composites

Temperature (°C)	σ_f (MPa)	E_f (GPa)
20	178	36
	145	29
	182	40
	153	33
Average	164	34
10000	212	30
	193	27
Average	200	28
1150	224	17
	228	23
Average	225	20

Table 4 – Mechanical properties of 2D Nextel/720 composites as a function of temperature

Flexural strength after ageing

The flexural strength after thermal ageing in air (10 and 100 hours at 1100 and 1200°C) was also determined (composite 9) at room temperature (figure 3). After 100 hours of ageing at 1100°C, the reduction in strength is about 15%, whereas after ageing at 1200°C, it attains 20% after 10 hours of ageing and is slightly above 30% after 100 hours of ageing.

Improvement of mechanical properties

Since the alumina matrix is not fully densified in the composites, further sintering may occur, depending on the conditions of temperature and duration in service. The unavoidable consequence of shrinkage associated with matrix sintering is a decrease in the mechanical properties of the composites, mainly due to degradation of load transfer between fibers and matrix (matrix microcracking, debonding between fiber and matrix). To limit these phenomena, the ATK COI Ceramics company (USA) has adopted the option of introducing colloidal alumina [6], but there is no information available concerning the process. Based on previous work conducted on C/Al₂O₃ composites, addition of zirconia has been taken into account to decrease the risk of sintering in service [7]. The principle is based on the fact that zirconia is more refractory than alumina (melting at 2690 and 2050°C, respectively) which results in a lower sintering (optimum densification at about 70% of the melting temperature).

The zirconia is introduced by infiltration of a zirconium alkoxide precursor in the porosity of the matrix partially consolidated by sintering. After hydrolysis/polycondensation and sintering, the precursor forms submicron zirconia grains arranged on the surface of the alumina grains and on the necks between the sintered grains. Moreover, the effect of silica was also tested on composites to confirm its role in the degradation of the mechanical properties after ageing. The silica is introduced by infiltration of a silicon alkoxide precursor.

Precursor infiltration procedure

The production of composites is divided into several stages. Initially, we proceed to the infiltration of Nextel 720 fabric plies by the alumina powder. The composite obtained after drying is then sintered at 950°C to consolidate the powder, while maintaining the maximum porosity and promoting a damage-tolerant behavior. This step is essential to avoid matrix disintegration during the subsequent infiltration of the porosity by the liquid precursor. The main steps of injection and hydrolysis procedures of alkoxides are the following:

- drying at 120°C of the pre-sintered composite (950°C – 30 min);
- degassing of the hot composite in a dynamic vacuum (~ 2 hours);
- degassing of the alkoxide in a dynamic vacuum;
- introduction of the composite in alkoxide and complementary degassing for one hour in a static vacuum before returning to atmospheric pressure;
- hydrolysis of the composite over a steam bath for one hour;
- drying at 120 °C;
- sintering at 1200 °C for one hour.

Four composites were impregnated with a solution of 70 wt% of zirconium propoxide in propanol (Fluka 96595). Since this solution exhibits a high viscosity, partial infiltration was suspected, particularly in view of the dispersion in the results of the mechanical tests. Two other plates were therefore injected with a diluted solution of 54.5 wt% of zirconium propoxide in propanol. The mass uptake of composites has been difficult to estimate, because there is always a surplus at the surface (between 1 and 2.5 wt%). A plate of Nextel 720/Al₂O₃ composite was impregnated with tetraethoxysilane (TEOS) as a precursor of silica. The porosity of 28% before injection was reduced to 24% after sintering.

Results

After sintering, five specimens were cut in each plate, in order to perform three point bending tests. Two tests were used as a reference and the other three specimens were aged at 1200°C for 10 or 100 hours. The mean flexural strengths are reported in figure 3.

The composite infiltrated with the concentrated precursor is very promising, because the mechanical properties are slightly improved at room temperature and this level is maintained after ageing for 10 hours at 1200°C. However, the dispersion in strength is large, about 100 Mpa, due to the inhomogeneous distribution of zirconia. A more homogenous infiltration is achieved with the diluted precursor, which leads to a higher strength and a smaller dispersion.

The composites reinfiltred with a silica precursor exhibit a lower strength (115 MPa) and a 30% drop in strength after ten hours of ageing at 1200°C.

In conclusion, this early work on the reinfiltred of composites with precursors highlights the advantage of zirconia to improve, not only the reference mechanical properties, but also those measured at room temperature after thermal ageing. A similar approach was adopted by the Zok team at the University of California. The mechanical properties of composites are then improved by decreasing the porosity with an alumina precursor [8].

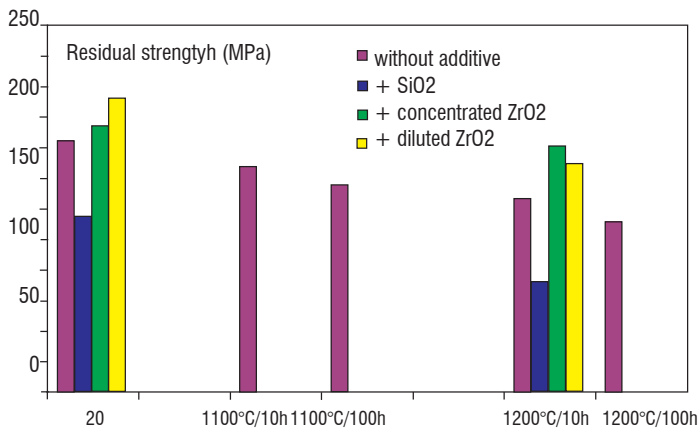


Figure 3 – Average residual flexural strength ($\pm 10\%$ dispersion) after ageing of 2D Nextel 720/ Al_2O_3 composites with and without additives

Evaluation of thermal barrier coatings

For applications with very long durations (> 100 hours), it is preferable to limit the temperature to 1100°C to avoid the strength drop of the Nextel 720 fiber. However, to increase the maximum temperature that can be withstood by the composite, a thermal barrier coating (TBC) can be added, as shown by Solar Turbines (USA) for combustion chambers [9]. Initially, the potential of various TBCs was investigated, via the determination of their thermal conductivity in relation with their morphological and structural evolution. Then, thermal simulations were performed to determine the most efficient TBC for a given thickness.

Alumina and mullite TBCs

The two main criteria to be considered in the selection of a TBC material are the chemical compatibility and thermal expansion agreement

with the composite. As major constituents of the TBC, alumina and mullite were naturally selected. Moreover, thermal conductivity of TBCs being very dependent on the porosity and morphology, various ways of production were taken into consideration to investigate the effect of these factors [10].

The two techniques most commonly used for ceramic coatings are plasma spraying and dipping in a suspension followed by sintering. These techniques were therefore used to produce alumina and mullite coatings. For alumina coating, another possibility is to use a reaction–bonding process based on the oxidation of aluminum /alumina powder mixtures. As described in box 2, this technique leads to porous Reaction Bonded Aluminum Oxide (RBAO) with higher mechanical strength as compared to conventional sintering. Furthermore, a high porosity level can be achieved using a dipping technique to deposit the $\text{Al}/\text{Al}_2\text{O}_3$ slurry previously to the reactive sintering. A similar procedure can be used to produce mullite by reactive sintering from a slurry of polydimethylsiloxane/ $\text{Al}/\text{Al}_2\text{O}_3$ [13]. The characteristics of TBCs and N720/ Al_2O_3 composite are reported in table 5.

	Porosity (%)	CTE (10^{-6}C^{-1})	Young modulus (GPa)	Poisson ratio	Flexural strength (MPa)
N 720/ Al_2O_3	25	6.2	40	0.2	140
RBAO	70	8	34	0.27	10
Mullite	40	5	58	0.27	40

Table 5 – Thermo-mechanical data of TBCs and composite necessary for residual thermal stress calculations

The thermal conductivity K ($\text{W}/\text{m}\cdot\text{C}$) of composites and coatings was determined from measurements of thermal diffusivity D (m^2/s), using a laser flash method. From the knowledge of the density ρ (kg/m^3) and of the variation of the specific heat C_p ($\text{J}/\text{kg}\cdot\text{C}$) with temperature, thermal conductivity is obtained by applying the relation $K = D \cdot \rho \cdot C_p$

Diffusivity measurements were performed on discs, 20mm in diameter, machined in monoliths. For coatings prepared by thermal spraying, the measurements were performed directly on the coated composites taking into account its own thermal diffusivity. The thermal conductivities of the various alumina and mullite are respectively illustrated in figure 4 and figure 5.

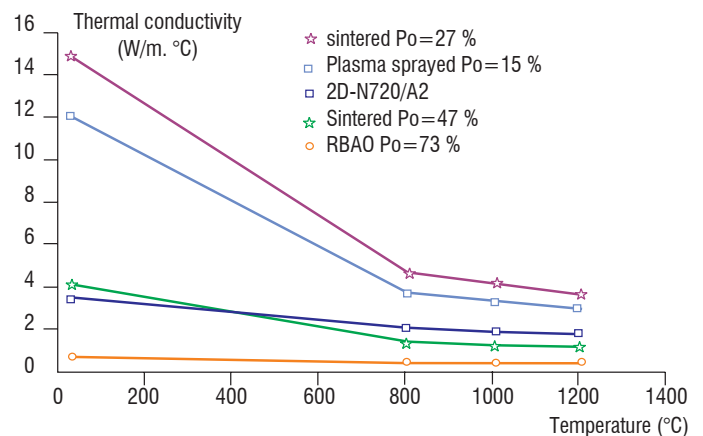


Figure 4 – Thermal conductivity of Al_2O_3 TBC

The thermal conductivity decreases considerably with an increase in the porosity level, for the various sintered alumina. For the plasma-

Box 2 - Reaction Bonded Aluminum Oxide (RBAO)

Another way to form an alumina matrix is the reaction-bonding process, based on the oxidation of aluminum/alumina powder mixtures [11]. The main advantage of this route is the possibility of producing almost net-shaped components, owing to the fact that the sintering volume shrinkage is counterbalanced by the expansion associated with the formation of alumina from aluminum. After investigating the oxidation mechanisms of aluminum powder and then of various Al/Al₂O₃ mixtures, taking into account parameters such as the size of the powders, the thermal treatment and the mixture and pressing modes, it was possible to select a nuance (40/60% in volume) characterized by a close to zero shrinkage (Figure B2-01).

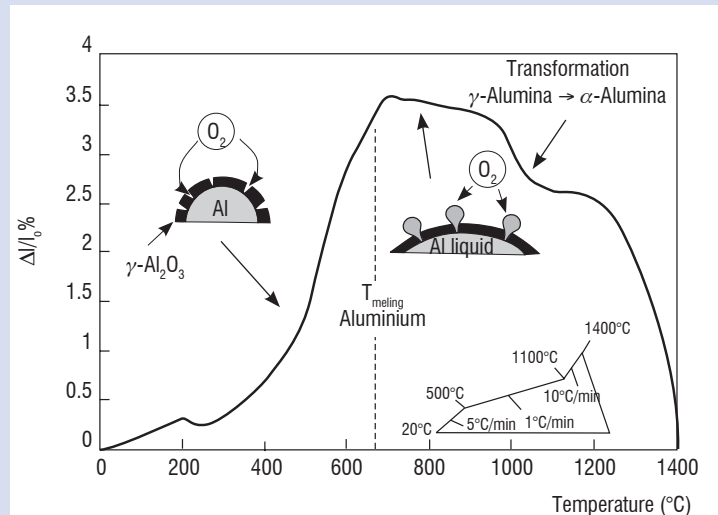


Figure B2-01 – Dimensional variations and oxidation mechanisms of the Al/Al₂O₃ system during the reaction bonding of alumina

The addition of an activator, such as magnesia, improves the sintering kinetics and promotes a better densification at low temperature, despite the formation of vermicular alpha alumina, which is difficult to sinter below 1600°C. In addition, the presence of impurities such as iron leads to a better intergranular cohesion, which, with an equal porosity (34%), results in better mechanical properties (Figure B2-02): 270 MPa (sintering at 1250°C) instead of 175 MPa (sintering at 1400°C) for alumina with a residual porosity of 20% [12].

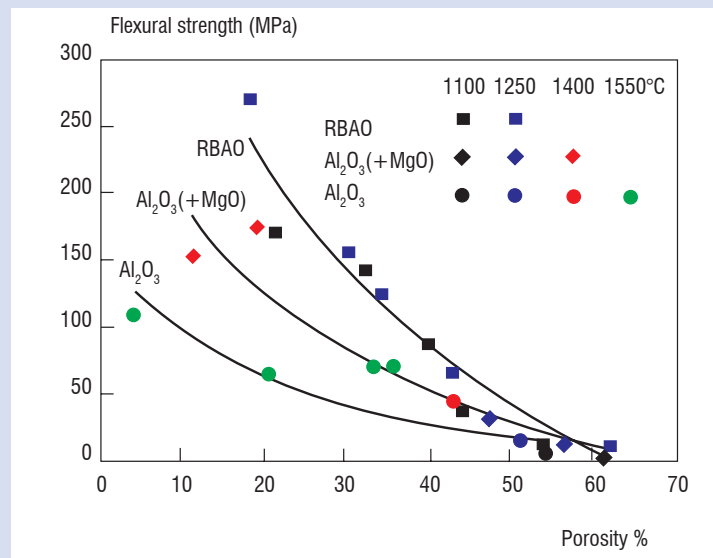


Figure B2-02 – Flexural strength versus porosity of different alumina monoliths conventionally sintered or processed

spayed alumina, the value determined for the composite is not representative, since the coating is completely debonded after the measurement of diffusivity up to 1200 °C. This behavior was correlated with a significant decrease in its porosity (25 to 12%), which is due to densification, as revealed by the morphological observations. The lowest thermal conductivity is obtained with the RBAO coating, which exhibits a very high level of porosity (75%).

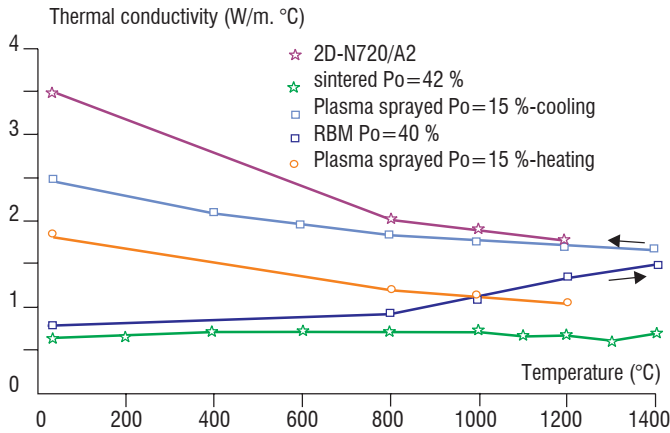


Figure 5 – Thermal conductivity of mullite TBC

For the plasma-spayed mullite, an increase in thermal conductivity is observed during the measurement. In this case, there is no significant reduction in porosity as in the case of thermal-spayed alumina, but there is a significant crystallization of mullite. Contrary to RBAO, the porosity of the reactive-bonded mullite (RBM) is lower (40%) and yttrium silicate has been added to improve the mechanical properties. Consequently, its thermal conductivity is higher than that of the RBAO coating. Finally, the lowest thermal conductivity is achieved with the mullite coating obtained by natural sintering of a submicron powder deposited by dip coating.

From the thermal conductivity measurements, we must bear in mind the very low thermal conductivity of RBAO (0.3 W/m°C) and of sintered mullite (0.7 W/m°C). In both cases, the thermal conductivity is stable, contrary to that of the thermal sprayed coatings, which evolves rapidly during use.

Efficiency of TBC

From these conductivity values, a simulation of thermal barrier thickness was performed, using a thermal code developed at Onera [14]. The calculations reported in figure 6 were conducted in a combustion chamber configuration as follows:

- cylindrical combustion chamber made of 2D Nextel 720/Al₂O₃ composite, with a TBC introduced in the inner part;
- combustion temperature of 1500 °C and exchange coefficient of 1000 resulting in a surface temperature of 1400°C for the TBC;
- external cooling of the composite by air at 600°C and with an exchange coefficient of 10 and an emissivity of 0.7 (common value for oxides at this temperature).

If the temperature at the interface between the TBC and the composite is fixed at 1100°C to avoid matrix ageing, only 1 mm of RBAO is necessary instead of 2.3 mm of sintered mullite. For the mullite obtained using reactive sintering, a thickness of 3.5 mm is required, owing to its higher thermal conductivity. Although it is compulsory to

increase the thickness of the thermal barrier when replacing alumina by mullite, the calculated thicknesses are lower than those used by Solar Turbines in their engine tests [9].

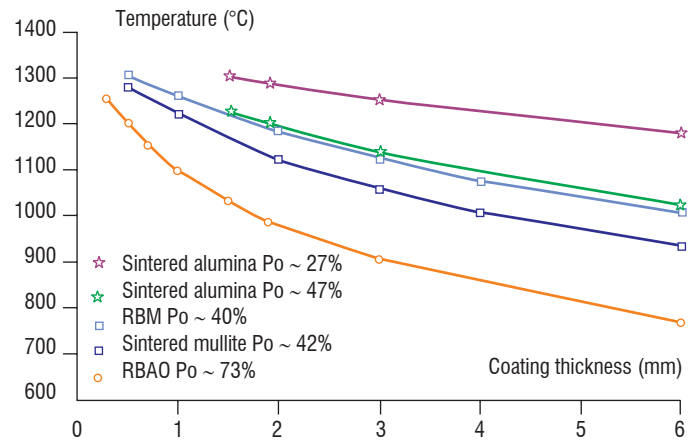


Figure 6 – Prediction of TBC thickness depending on the surface temperature of the composite

Ageing behavior of TBCs

Since RBAO is the most efficient TBC according to thermal simulation, the latter has been selected first to evaluate the ageing behavior of different assemblies. RBAO plates were produced with a porosity level of 75% and a thickness of 1mm. Then, these plates were bonded to alumina monoliths or to 2D Nextel 720/alumina composites using two bonding suspensions: i) alumina A2 powder in water at pH=3, ii) mixture of alumina A2 and silica (mullite proportion) powders in water at pH=3.

In both cases, the suspension was deposited as a thin layer on monoliths or composites. Prior to this, they were soaked in water to prevent premature drying of the surface. As soon as the application of the suspension was completed, the RBAO TBC was deposited onto it and, finally, drying (in air and then in an oven) was performed by maintaining a constant pressure, using clamps to promote contact. Excess suspension was also removed during this operation.

All of the assemblies were sintered at 1200°C for 1 hour. They were then subjected to different thermal ageing treatments: 100 hours at 1100°C, then 100 hours at 1200°C. Following these treatments, we made sure there was no significant change in the microstructure of RBAO, as evidenced by the porosity measurements: 81% after sintering at 1200° C, 80.9% after 100h at 1100°C and 80.1% after 100h at 1200°C.

On monolithic alumina, the RBAO TBC is well joined with an alumina bonding layer after ageing, while a partial separation is observed with a mullite bonding layer. Breaking of the joining is observed in 2D Nextel 720/alumina composites, regardless of the nature of the binder. When the latter is made of alumina, the fracture occurs in this layer. On the other hand, for the mullite bonding, breaking occurs between this layer and the RBAO TBC.

To better identify the origin of the breakdown of RBAO TBC between alumina monolith or composite, their respective coefficient of thermal expansion (CTE) was measured (figure 7). The average CTE difference of about 2.10⁻⁶°C⁻¹ is largely sufficient to induce rupture, due to the development of residual thermal stresses during cooling. Never-

theless, for a mullite TBC, the CTE is lower than that of the composite and the difference is reduced to $1.10 \cdot 10^{-6} \text{ } ^\circ\text{C}^{-1}$. The use of a mullite TBC would be, a priori, a more viable candidate than an alumina TBC, especially since the composite would subject the TBC to compression during cooling.

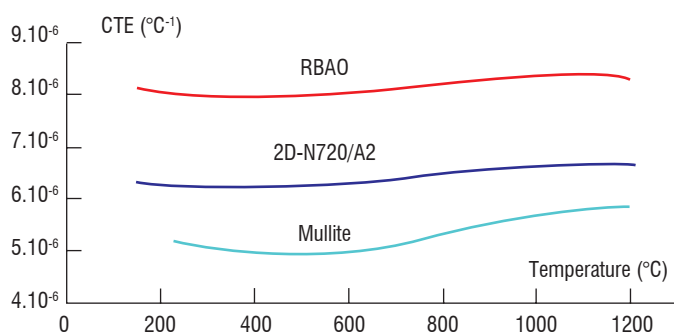


Figure 7 – Evolution of CTE with temperature for 2D Nextel 720 Al_2O_3 and for RBAO and mullite TBC

Consequently, a complementary ageing test was performed on a sintered mullite TBC with a porosity level of 40% and a thickness of 2 mm. This mullite TBC was joined to a 2D Nextel 720/alumina composite using the alumina bond. After ageing at 1200°C for 100 hours, no delamination of the assembly was noticed.

The analytical determination of the stress distribution was then performed in TBC and in composite to explain the behavior of the assembly submitted to ageing. Based on a Timoshenko analysis [15] adapted to a 2D asymmetrical system [16], calculations were performed using the thermo-mechanical data reported in table 5 and a ΔT cooling range of 1200°C . It appears that the stress generated at the interface in RBAO, for the TBC/composite systems submitted to ageing (table 6), is higher than its flexural strength, thus leading to the initiation of cracks normal to the interface which, in turn, may promote debonding from the composite. On the contrary, for the mullite TBC, the rupture flexural strength is not attained on the free surface and the TBC layer near the interface is submitted to a compressive stress.

TBC on 2D N 720/ Al_2O_3	Stress in TBC (MPa)		Stress in composite (MPa)	
	surface	interface	interface	surface
1 mm RBAO / 2 mm composite	1	45	-58	35
2 mm mullite / 2 mm composite	34	-59	37	-15

Table 6 – Residual thermal stresses induced in TBC and in composite for the selected assemblies

Perspectives for oxide/oxide

For a few years now, the elaboration processes generally used for organic matrix composites have been transposed to ceramic matrix composites such as vacuum-molding. Compared to infiltration techniques, these processes are cheaper and they allow the production of more complex shaped parts. Moreover, fiber volume fractions as high as 50% can be achieved. This last point is of great interest to improve

tensile strength and the Young's modulus, as explained in box 1 for Weak Matrix Composites [5], [18], [19], [21]. For all these reasons, new alumina/alumina composites were prepared using prepregs and vacuum molding procedures.

First, the alumina slurry previously used for the infiltration process is now used for impregnation of N610 fabrics (satin weave of 8, Ref 610 Nextel DF-11 - Wireless 1500 denier). Then, $100 \times 150 \text{ mm}^2$ prepreg fabrics are stacked, vacuum bagged having standard bleeders and breathers and a low pressure is applied to reach a fiber volume fraction of 50%. Then, the temperature is raised up to 100°C to allow water evaporation from the composite. After drying, the as-processed plate is sintered at 1200°C with a short dwell time to limit fiber degradation. The final composite with a porosity of 25% exhibits excellent mechanical properties, with damage-tolerant behavior, as shown in table 7 and figure 8.

	Tensile tests	Flexural tests
σ (MPa)	275 ± 15	229 ± 74
ε (%)	0.32 ± 0.02	-
E (GPa)	140 ± 6	122 ± 21

Table 7 – Summary of tensile and flexural properties for vacuum bagged N610/alumina composites

From figure 8, the tensile response is essentially linear with only small inelastic strain, as was usually observed in oxide-oxide composites [19], [20], [17]. Moreover, the mechanical behavior is quite reproducible. Compared to the N610/alumina composites made by Ruggles-Wrenn et al. [17], with an ultimate tensile strength of 117 MPa and a failure strain of 0.09%, the composites of this work are characterized by higher mechanical properties at room temperature.

Since the characteristics (V_f , density) of the two composites are similar, the great difference between the mechanical properties can be explained by the thermal treatment. Indeed, the sintering condition of the composites of Ruggles-Wrenn et al. is 1200°C for 5 hours. Such a long thermal treatment can induce fiber degradation and a decrease in the level of porosity of the matrix leading to a stiffer matrix, thus impeding the debonding process.

Papakonstantinou et al. [21] compared the mechanical properties of some CMCs. Hi-Nicalon (SiC)/SiC composites manufactured by chemical vapor infiltration (CVI) exhibit an ultimate tensile strength of 255 MPa, a Young's modulus of 230 GPa and a failure strain of 0.47%. The tensile strength of the N610/alumina composites produced by vacuum molding is close to that of the SiC/SiC composite, whereas the Young's modulus and failure strain are lower. The elastic moduli of the N610 fiber and the Hi-Nicalon fiber are respectively 373 GPa and 270 GPa [21]. As a consequence, the low Young's modulus of oxide/oxide composites (i.e., a 60% loss compared to fibers) is attributed to the weak matrix. For SiC/SiC composites, the decrease in the Young's modulus between the fibers and the composite is not so large ($\sim 15\%$). This behavior can be explained by the nature of the fiber matrix interface. Indeed, SiC/SiC composites are considered as Weak Interface Composites (box 1) and so, the matrix is stiff but a fiber coating is necessary to allow a debonding mechanism, whereas it is not necessary for Weak Matrix

Composites. This comparison highlights the interest for oxide/oxide composites which are cheaper and less time consuming to manufacture, compared to SiC/SiC composites.

The mechanical properties of oxide/oxide composites can be adjusted, depending on the mechanical constraints required for applications such as exhaust parts or combustion chambers. As an example, to improve failure strain and creep behavior, some authors have coated the N610 fibers with monazite (LaPO_3) [17]. As a result, strain is three times higher, tensile strength is increased but the elastic modulus is decreased and the manufacturing process becomes more expensive.

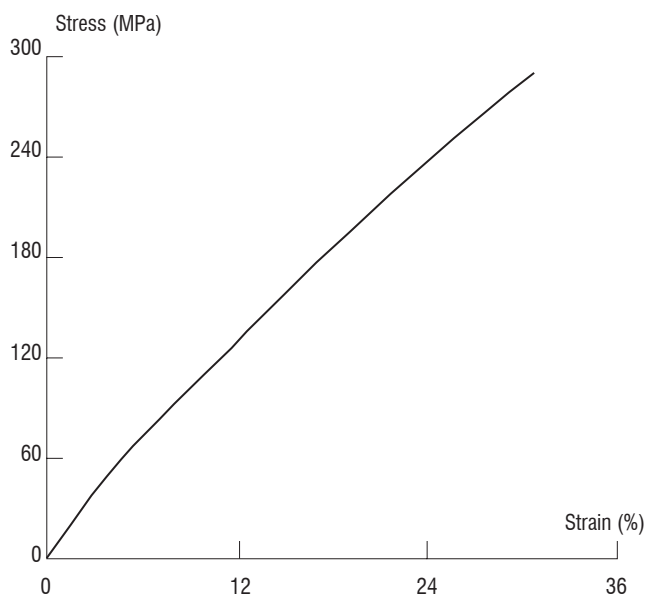


Figure 8 – Tensile stress-strain curves for Nextel TM 610/alumina ceramic composites at room temperature.

Conclusion

To develop CMCs with a low manufacturing cost and better durability in air at high temperatures compared to SiC/SiC composites with carbon interphase between fiber and matrix, oxide/oxide composites based on weak matrix concept without interphase are under investigation at Onera. Oxide Nextel fibers produced by 3M Company (USA) were selected to reinforce a porous alumina matrix. Infiltration technique was used to infiltrate a submicron alumina powder in 2D satin woven fabrics of Nextel 720. The selected alumina powder is able to sinter at a moderate temperature ($\leq 1200^\circ\text{C}$) with limited shrinkage to avoid matrix multicracking. After optimization of the infiltration and sintering conditions leading to a matrix porosity of 25% and a fiber volume fraction of 40%, a flexural strength of 225 MPa is achieved at 1150°C . To avoid reductions in mechanical properties after ageing, additional infiltration of zirconium alkoxide in the porosity was assessed and validated. Indeed, this additive limits the matrix sintering and increases its mechanical strength. In parallel, TBCs were studied to improve lifetime and working temperature. From a thermal simulation point of view, the most efficient TBC is an alumina coating with a porosity of 70% (RBAO). Only one millimeter is necessary to keep the surface of the composite at 1100°C in conditions simulating a combustion chamber with gas at 1500°C . However, debonding of the RBAO TBC from the composite is observed after ageing at 1200°C . This behavior has been correlated to the difference in CTEs leading to thermal stresses higher than the flexural strength of such an RBAO TBC, which is quite low. On the other hand, a 2 mm thick sintered mullite TBC with porosity of 40% is as efficient as an RBAO TBC and no debonding is observed. To improve the fiber volume fraction up to 50%, composite has been manufactured by using vacuum molding of prepregs layers. Using 2D satin woven fabrics of Nextel 610, higher mechanical performances were obtained and are close to those of SiC/SiC composites manufactured by CVI. This investigation has thus shown that oxide/oxide composites have attained sufficient maturity to develop industrial demonstrators for gas turbine components, such as exhaust parts or combustor chambers ■

Acknowledgements

The authors would like to thank Dr. R. Valle for valuable discussions.

References

- [1] M. VAN ROODE, A. SWEDA, K. MORE, J. SUN - *25.000 hour Hybrid Oxide CMC Field Test Summary*. Proceedings of ASME Turbo Expo 2008 : Power for Land, sea and air GT 2008, June 9-13, Berlin, GT 2008-51379, 2008.
- [2] O. SUDRE, A. RAZELL, L. MOLLIEUX, M. HOLMQUIST - *Alumina Single-Crystal Reinforced Alumina Matrix for Combustor Tiles*. 22nd Annual Cocoa Beach Conference and Exposition on Advanced Ceramics, Materials and Structures, Cocoa Beach (FL), January, pp. 20-24, 1998.
- [3] M. PARLIER, M.-H. RITTI - *State of Art and Perspectives for Oxide/Oxide Composites*. Aerospace Science and Technology, Vol. 7, pp. 211-221, 2003.
- [4] M.-Y. HE, J.-W. HUTCHINSON - *Kinking of a Crack out of an Interface*. J. Appl. Mech., Vol. 56, pp. 279-8, 1989.
- [5] D. KOCH, K. TUSHTEV, G. GRATHWOHL - *Ceramic Fiber Composites: Experimental Analysis and Modeling of Mechanical Properties*. Composites Science and Technology, Vol. 68, pp.1165-1172, 2008.
- [6] L.-P. ZAWADA, S.-G. STEEL, S. MALL - *Fatigue Behavior of a Nextel 720 / Alumina (N720/A) Composite at Room and Elevated Temperature*. Ceram. Eng. Sci. Proc., Vol. 22, [3], pp. 695-702, 2001.
- [7] M. WEY - *Utilisation de polymères inorganiques oxydes dans l'élaboration de composites à architecture 3D*. Doctoral Thesis, University of Paris 7, 3rd of December, 1993.
- [8] H. FUJITA, C.-G. LEVI, F.-W. ZOK - *Controlling Mechanical Properties of Porous Mullite /Alumina Mixtures via Precursor-Derived Alumina*. J. Am. Ceram. Soc., Vol. 88, n° 2, pp. 367-375, 2005.
- [9] W.-D. BRENTNALL, M. VAN ROODE, P.-F. NORTON, S. GATES, J.-R. PRICE, O. JIMENEZ, N. MIRIYALA - *Ceramic Gas Turbine Development at Solar Turbines Incorporated*. Progress in ceramic gas turbine development, Vol. 1, chap. 2, pp.155-192, 2002.
- [10] D.-A. STEWART, D.-B. LEISER - *Characterization of the Thermal Conductivity for Fibrous Refractory Insulations*. Proceedings of the 9th Annual Conference on Composites and Advanced Ceramic Engineering and Science Proceedings, Vol. 6, issue 7/8, pp. 769-792, 1985.
- [11] N. CLAUSSEN - *Processing, Reaction Mechanisms and Properties of Oxidation Formed Al₂O₃ Matrix Composites*. Journal de Physique IV-C7 (3), pp. 1327-1334, 1993.
- [12] S. BERTRAND, T. MICHALET, A. GIRAUD, M. PARLIER, A. BATAILLE, R. DUCLOS, J. CRAMPON - *Processing, Microstructure and Mechanical Strength of Al₂O₃ Ceramics Reaction Bonded*. Ceramics International, Vol. 29, pp. 735-744, 2003.
- [13] T. MICHALET, M. PARLIER, F. BECLIN, R. DUCLOS, J. CRAMPON - *Elaboration of Low Shrinkage Mullite by Active Filler Controlled Pyrolysis of Siloxanes*. J. Eur. Ceram. Soc., Vol. 22, pp. 143-152, 2002.
- [14] D. DEMANGE, A. BOUVET - *Experimental and Software Tools to Forecast Radiative and Conductive Thermal Transfer in Partially Transparent Material Deposited on Rotating Blades for Turbine Engine*. Aerospace Science and Technology - AST, Vol. 8, n° 4, pp. 321-331, 2004.
- [15] S. TIMOSHENKO - *Analysis of Bimetal Thermostats*. J. Opt. Soc. Amer., Vol. 11, pp. 233-255, 1925.
- [16] R. VALLE, D. LÉVÊQUE, M. PARLIER - *Optimizing Substrate and Intermediate Layers Geometry to Reduce Internal Stresses and Prevent Surface Crack Formation in 2D Multilayered Ceramic Coatings*. J. Eur. Ceram. Soc., Vol. 28, pp. 711-716, 2008.
- [17] M.-B. RUGGLES-WRENN, S.-S. MUSIL, S. MALL, K.-A. KELLER - *Creep Behavior of Nextel 610/Monazite/Alumina Composite at Elevated Temperatures*. Comp. Sci. Techn., Vol. 66, pp. 2089-2099, 2006.
- [18] K. -A. KELLER, TAI-IL MAH, T.-A. PARTHASARATHY, C.-M. COOKE - *Fugitive Interfacial Carbon Coatings for Oxide/Oxide Composites*. J. Amer. Ceram. Soc., Vol. 83, pp. 329-336, 2004.
- [19] D.-B. MARSHALL, J.-B. DAVIS - *Ceramics for Future Power Generation Technology: Fiber Reinforced Oxide Composites*. Current Opinion in solid State and Materials Science. Vol. 5, pp. 283-289, 2001.
- [20] C.-G. LEVI, J.-Y. YANG, B.-J. DALGEISH, F.-W. ZOK, A.-G. EVANS - *Processing and Performance of an All-Oxide Ceramic Composite*. J. Amer. Ceram. Soc., Vol. 81, pp. 2077-2086, 1998.
- [21] C.-G. PAPAKONSTANTINOY, P. BALAGURU, R.-E. LYON - *Comparative Study of High Temperature Composites*. Composites: part B, Vol. 32, pp. 637-649, 2001.

Acronyms

CMCs	(Ceramic Matrix Composites)
WICs	(Weak Interface Composites)
NOXICC	(Novel OXIde Ceramic Composites)
TBCs	(Thermal Barrier Coatings)
WMCs	(Weak Matrix Composites)
TEOS	(Tetraethoxysilane)
RBAO	(Reaction Bonded Aluminium Oxide)
RBM	(Reactive Bonded Mullite)
CTE	(Coefficient of Thermal Expansion)
CVI	(Chemical Vapor Infiltration)



Michel Parlier Holding an Engineering Diploma from ENSCI (Ecole Nationale Supérieure de Céramiques Industrielles) and having graduated in Materials Science from the University of Paris, he received his Doctorate Degree in Metallurgy (Mechanical Behavior of Materials) from ENSMP (Ecole Nationale Supérieure des Mines de Paris) in 1984. Head of the High Temperature Composite Materials Unit at Onera (Composite Materials and Structures Department), he has been involved in the development of sintering techniques of ceramic powders with specific additives (hot-pressing, reaction bonding, hot isostatic pressing); Chemical Vapor Deposition (CVD) for densification of composites and coatings; Ceramic Matrix Composites (CMC) development (glass-ceramics, oxides and silicon carbide); Oxides derived from Sol-Gel; Silicon carbide derived from organosilicon precursors, low density fibrous thermal insulation; Melt-Growth Composites (MGC) processing routes; thermal, mechanical and microstructural characterizations.



Marie-Hélène Ritti is a research engineer working in the Composite Materials and Structures Department (DMSC). After obtaining her Master's degree from the University of Limoges, she joined Onera in 1982. She is mainly involved in the development of Ceramic Matrix composites (CMC) and other oxides materials.



Aurélie Jankowiak After graduating from ENSCI in 2005, she received a PhD in Materials Science from the University of Limoges (2008). She has been working since 2009 in the Composite Materials and Structures Department of Onera. Her research field is mainly focused on high temperature materials for functional applications (combustion chambers, engine blades, leading edge).